CRANFIELD UNIVERSITY

ISIDRO SERGIO DURAZO CARDENAS

DEVELOPMENT OF POROUS-CERAMIC HYDROSTATIC BEARINGS

SCHOOL OF INDUSTRIAL AND MANUFACTURING SCIENCE

Ph.D. THESIS

CRANFIELD UNIVERSITY

SCHOOL OF INDUSTRIAL AND MANUFACTURING SCIENCE

Ph.D. THESES

ACADEMIC YEAR 2002-2003

ISIDRO SERGIO DURAZO CARDENAS

DEVELOPMENT OF POROUS-CERAMIC HYDROSTATIC BEARINGS

SUPERVISORS: J. CORBETT, D.J. STEPHENSON

OCTOBER 2003

Abstract

Porous-ceramic hydrostatic bearings have been recently developed. These bearings have demonstrated an exceptional overall performance when compared with conventional technology bearings. However, despite all the benefits, porous-ceramic hydrostatic bearings have yet to find widespread acceptance due to the problems found in tailoring the bearings geometry and size to suit precision engineering applications, while producing porous-structures with consistent and reproducible permeability.

Using a series of fine grades of alumina powders in combination with maize starch granules, a new method for the manufacture of porous-ceramic bearings has been developed, based on the starch consolidation technique. By employing this method, it has been demonstrated that is possible to manufacture bearings of different geometries and shapes, with consistent and reproducible properties. The new method also proved to be low cost and environmentally sound.

The performance of the new journal bearings has been investigated in a highly instrumented test-rig, and a comparable performance to that of previous porous-ceramic journal research has been observed.

In a direct performance comparison between a porous-ceramic hydrostatic journal bearing and a conventional hydrostatic bearing of the same size, the porous-ceramic bearing demonstrated a significant performance improvement in terms of stiffness, power consumption and thermal performance.

In previous research, water lubrication proved to significantly improve the spindle thermal performance. However, water lubrication is feared to promote corrosion within the spindle components. In the present research, the effects of water lubrication in porous-ceramic bearing systems were investigated. As a result, it has been demonstrated that corrosion in typical machine-tool materials can be effectively controlled by using inhibitors and low cost surface coatings. On the other hand, it has been also demonstrated that undesirable foaming, air entrainment and microbial growth can potentially develop in water/inhibitors lubrication systems. In this sense, the use of low viscosity oils proved to offer a comparable performance.

Acknowledgments

The author wishes to take this opportunity to express his most sincere gratitude to the following people for all their help and advice during the period of this degree:

Professors John Corbett and Dave Stephenson, for giving the author the opportunity to collaborate in their prestigious precision engineering research programme. The author is also grateful for their advice and guidance throughout this research, as well as the provision excellent research facilities and materials.

Mr. John Hedge for his rapid and dexterous dealing of all technical aspects emanated from this research, and also for his always friendly approach. The author also wishes to thank Mr. Tim Pryor and Mr. Andrew Baldwin for their rapid response to the project requirements, even though these usually had little to do with their own everyday duties.

Mr. Mike Pierce from Cranfield Precision for his enthusiasm and interest in the project, and also for entrusting the author with some very expensive equipment. The author also wishes to thank Mr. Paul Commley from the same company for his help with the precision measurement of the bearings.

CONACyT (Mexico), for covering the author's tuition fees as well as living expenses, always with the highest standards of reliability and service.

In this part, the author wishes to express his gratitude to those with no direct input in the conclusions reached in this research programme, but their indirect input was equally invaluable.

Margaret Norwich and Lynne Badr from the community development office, for all their help and attentions towards the author and his family. They, together with Mrs Carla Barker from the housing office have certainly succeeded in making Cranfield felt like home.

The author wishes to express his gratitude to his family: Isidro, Esther, Yaya and Erubiel for their unconditional love, support and honesty example, providing that invisible safety net that makes finding the courage to take the leap, easier.

The author cannot begin to express his gratitude to his greatest friend and wife, Adriana. Her contribution is far beyond simply understanding and encouragement. Adriana has always provided the author with the most inspirational examples of professionalism, achievement and love.

Providing a short list of the many friends with whom the author has shared this wonderful experience would have been unfair. To those, the author hopes to personally express his gratitude in the near future.
And to you my friend, who are holding this thesis with no scientific interest whatsoever.

Sincerely,

Isidro S Durazo

Table of contents

List of tables

List of figures

Nomenclature

Symbol	Meaning (units)
α	slip coefficient (dimensionless)
β	bearing feeding parameter (dimension less)
γ_w	surface tension of water (N/m)
ϵ_0	eccentricity ratio (dimensionless)
δ	densification (fraction, dimensionless)
η	absolute viscosity of the fluid (Ns/m^2)
κ	viscous permeability coefficient (m^2)
ΔL	compact length change from sintering (mm)
Δp	pressure drop in (Pa)
Λp	bearing speed parameter
λ_s	bearing speed parameter (dimensionless)
ν	kinematic viscosity of the fluid (m^2/s)
ξ_o	open porosity fraction
ρ	density of the test fluid
ρ_g	green density (g/cm^3)
ρ_s	sintering density (g/cm^3)
ρ_w	density of deionised water (kg/m^3)
ρ_w	density of water
ς	total porosity (%)
σ_y	dimensionless permeability factor
σ	non dimensional permeability (dimensionless)
Φ	fractional increase in mass flow rate (dimensionless)
ψ_v	viscous permeability coefficient in m^2
ψi	inertial permeability coefficient in m^2
ω	angular velocity of the shaft
ω	angular speed of the journal (rad/s)
A	area of the test piece normal to the fluid flow in m^2
a	empirical constant
B	bulk density of the test piece (g/cm^3)
B_R	specimen's relative density (%)

b	empirical constant
C	mean radical clearance of bearing (m), (μm)
c	Kozeny constant (c =0.58 for an angular grained powder)
D_f	specimen's OD after sintering (mm)
D_g	green compact diameter (mm)
D	bearing diameter
d	empirical constant
d_{ave}	average pore size
d_w	alumina powder mean particle size
$d_{pore\ max}$	maximum circular-capillary-equivalent pore diameter (m)
E	modulus of elasticity
E_R	relative modulus
e	eccentricity (μm)
e	thickness of the test piece in m
g	gravitational acceleration constant (m/s^2)
H	thickness of the porous bushing (m)
h_w	height of the water column above the specimen (m)
$\overline{K}_{static}$	non-dimensional static stiffness
k	proportionality constant
Lf	fired length of the specimen
L_0	initial compact length (both diametrical and longitudinal in mm)
Lp	plastic length of specimen (mm)
m	empirical constant
m_2	mass of the dried test piece (g)
m_3	mass of the fully impregnated test piece (g)
m_c	critical mass of rotor (κ)
$\overline{m}_c$	non-dimensional critical mass parameter
m_w	mass of the fully impregnated test piece suspended in water (g)
p_1	absolute gas pressure upstream the specimen (Pa)
Ps	supply pressure (N/m^2)
Ps	lubricant supply pressure
$\overline{Q}$	dimensionless flow rate Q lubricant volume flow rate (m^3/s)
R_e	Reynolds's number (dimensionless)
R	journal radius (m)
S	specific surface area
S_{dia}	diametrical shrinkage
St	total linear shrinkage (%)
S_{th}	longitudinal shrinkage

Sv	starch volumetric percentage (%)
s	starch volumetric content (%)
T	tortuosity, actual flow path in relation to thickness (T= 1/P)
U	surface velocity (m/s)
W	steady state load on bearing (N)
W_p	lubricant pumping power (W)
X	modulus of elasticity
X_0	full dense material modulus of elasticity

1 Introduction

1.1 Background

By virtue of their overall performance, porous-ceramic hydrostatic journal bearings present themselves as a viable solution to the newest severe demands for higher accuracy and overall performance levels required by spindle bearing systems.

Amongst the currently available bearing technologies, oil hydrostatic bearings are the precision engineers' preferred choice for applications requiring maximum stiffness. However, their medium term accuracy is limited by heat generation caused by the oil viscous shear. To this effect, thermal distortion and drift are considered major sources of error in higher precision manufacture [1] [2].

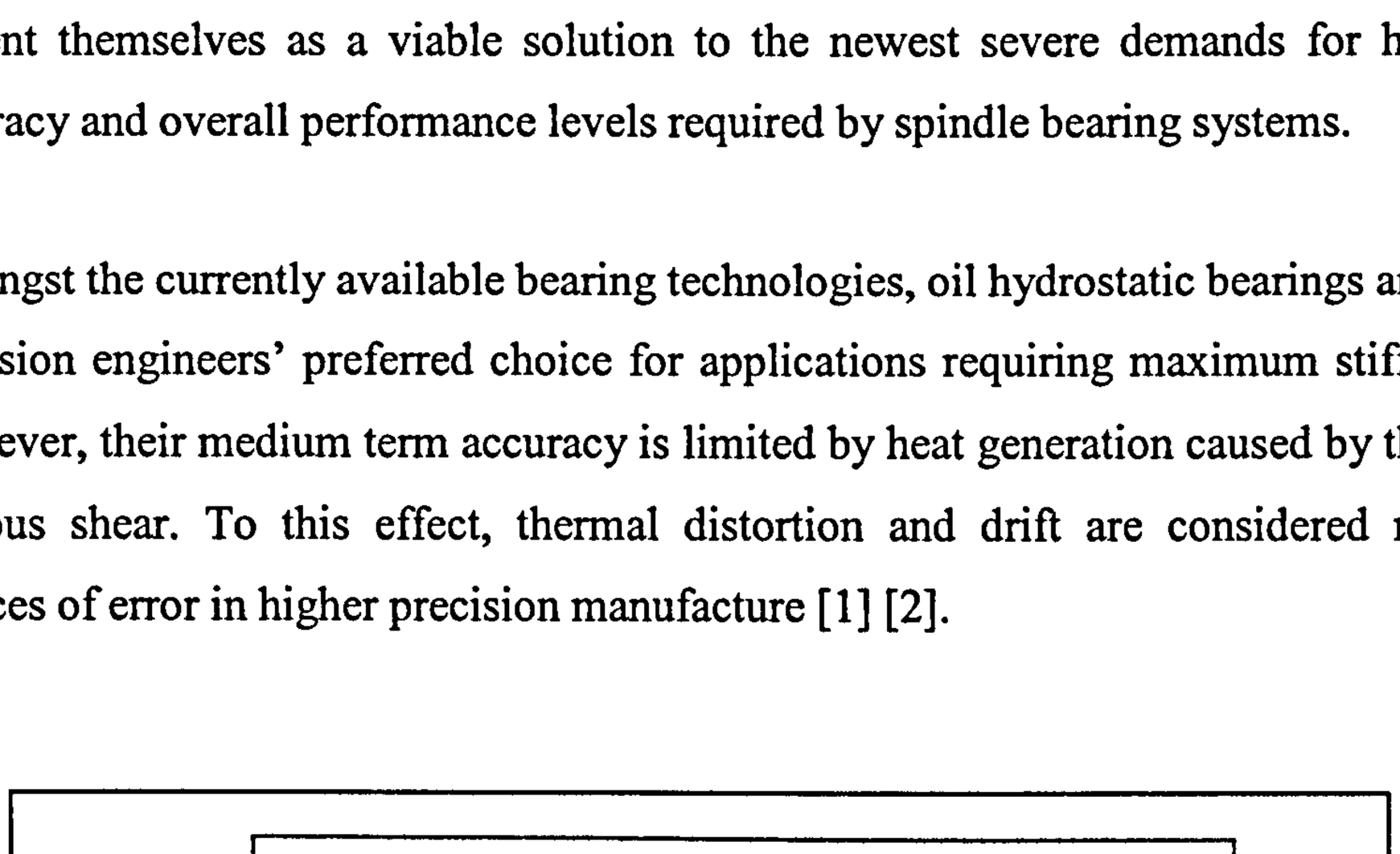

Figure 1- Direct stiffness comparison: Porous-ceramic water hydrostatic bearing Vs a conventional hydrostatic bearing (from reference [3]).

Recently developed porous-ceramic hydrostatic journal bearings have demonstrated an optimized overall performance when compared to conventional oil hydrostatic journal bearings [3]. For example, Figure 1 illustrates a direct stiffness comparison between these two bearing technologies, as presented by Almond [3].

The use of a porous material as a bearing material allows a multitude of feeding restrictors to be uniformly distributed over the entire surface of the bearing, providing the best pressure distribution and thus the highest load capacity and stiffness, as is shown in Figure 1. Superior damping characteristics also result from the use of a porous material, due to its ability to absorb energy oscillations [4].

Unlike hydrostatic bearings, and as a result of their improved pressure distribution, porous-ceramic hydrostatic bearings do not require hydrostatic 'pockets'. Hence, their stiffness via their hydrodynamic-component is maximized; while simplifying their design. In addition, the absence of pockets permits the spindle to reach higher speeds before the onset of turbulence. The effect of the stiffness hydrodynamic-component can be observed in Figure 1, being particularly noticeable above 10, 000 rpm.

A further advantage of porous ceramic hydrostatic bearings is that they can be lubricated with water without corroding; offering the following benefits:

- A lower viscosity than typical hydrostatic bearing oils, which directly reduces friction and heat generation.
- A higher specific heat than oils, making it easier to control the temperature of the bearing assembly and machine.
- Water lubrication overcomes environmental concerns associated with the use of oil and its disposal.

As a result of a comprehensive research programme and a performance comparison study, Almond [3] examined the benefits of porous-ceramic hydrostatic journal bearings over conventional oil hydrostatic journal bearings, clearly demonstrating the

potential benefits from this new technology. A summary of his findings is presented Table 1.

Parameter	Conventional hydrostatic bearing	Porous-ceramic hydrostatic bearings	Improvement factor (%)
Static stiffness (N/μm)	113	188	66
Lubricant flow rate (lpm)	7.5	1.4	80
Pumping power requirement (W)	875	47	95
Friction power (KW)	1.2	0.33	72
Lubricant temperature rise (°C)	6.5	2.5	62
Hybrid stiffness (N/μm)	113	286	52

Table 1-Bearing performance comparison: conventional hydrostatic Vs porous-ceramic water hydrostatic at 10, 000 rpm (from reference [3]).

1.2 Problem identification

Despite the numerous and significant advantages offered by porous-ceramic water hydrostatic journal bearings, these have not yet been completely embraced by precision engineers and machine-tool designers. Certain aspects of both their manufacture and operation must be further developed or improved before their widespread acceptance and application.

The first problem is concerned with the porous bearings' manufacturing method. The current method consists of the vibration packing of powders followed by hot isostatic pressing (HIPing). This has proved to be successful for the production of 50 mm ID x 50 mm long journal bearings. However, a significant level of machining is required and HIPing is a relatively expensive process. Also, it is difficult to process fine powders and avoid agglomeration, which results in a non-uniform permeability. The ability to use a range of powders is important in order to control pore size and pore distribution. In addition, it becomes more difficult to achieve uniform permeability as the size of the components increase. Hence there is a need to establish an optimized

alternative porous ceramic manufacturing route that would enable larger and more cost effective bearings to be produced.

A second problem exists in the scepticism found in using water as a lubricant. Although water lubrication benefits are widely acknowledged, there is a certain hesitancy for their use because water is feared to promote corrosion within the spindle assembly and auxiliary equipment components. The addition of corrosion inhibitors may potentially alleviate this problem. However, corrosion inhibitors are also feared to induce certain non-desired secondary effects such as foaming or bacterial growth. Thus, a thorough assessment of the effects of water lubrication including corrosiveness, the addition of corrosion inhibitors, foaming and bacterial growth in porous-ceramic hydrostatic bearing systems must be conducted.

1.3 Project aim

The aim of this project was to expand and enhance Cranfield University's porous-ceramic bearing manufacturing capability. This was achieved by:

- Developing an optimized manufacturing route capable of producing reproducible, uniform porous structures for larger bearings, suitable for their incorporation with the one of project's industrial partner spindle assemblies.
- The assessment of water lubrication robustness for porous-ceramic hydrostatic bearing systems.
- Employing low viscosity oils as lubricant in porous-ceramic hydrostatic bearing systems.

1.4 Structure of the thesis

In order to achieve this project's aim, chapter 2 starts by reviewing the available bearing technologies, leading to the description of the porous ceramic hydrostatic bearings' principle, main advantages and finally, to their latest developments.

In chapter 3, potential techniques for manufacturing porous-ceramics are reviewed. The aim of this review was to discover elements within the available literature that would allow the ascertainment of each of the techniques' suitability for the present project's applications. This eventually led to the identification of the starch consolidation technique as the most viable. The techniques reviewed included slip casting, injection moulding as well as direct consolidation techniques.

In chapter 4 the details of the bearing manufacturing process are given. Also, the porous-ceramic bearings' property measurements and characterisation methods are discussed and selected. A second section in chapter 4 discusses the measurement methods to find the porous-ceramic hydrostatic journal-bearing performance parameters, as well as describing the test rigs' capabilities. Finally, a third section deals with the experimental procedure for the water lubrication robustness assessment, in terms of minimizing corrosion and foaming.

Chapter 5 presents the results and discussion for the experimental procedures detailed in chapter 4. Finally the conclusions for the present project are presented in chapter 6, along with the recommendations and future work.
Calibration certificates, data sheets and drawings are included in the appendices.

2 Literature review

2.1 Background & introduction

Manufacturing is changing rapidly. The processes, equipment and systems used to design and produce everything from computer chips to aerospace components are undergoing dramatic changes in response to new customer needs, competitive challenges, and emerging technologies.

Recent advances in material and manufacturing sciences, engineering and business practices now enable companies to produce new and better products more quickly and at a lower cost.

As manufacturing continues evolving, more changes and challenges are expected in the future [5].

The precision engineering & machine tool development fields are not left out from manufacturing undergoing changes. Manufacturing's constant evolution demands higher accuracy at higher removal rates from such disciplines.

Amongst the material removal processes, grinding operations are of particular interest because of their ability to machine the hardest materials and to produce a better surface finish. In 1993 Taniguchi [6] predicted machining accuracy to approach 1μm by the year 2000 for 'ordinary' grinding operations. Today, the newest grinding machines have already achieved that level of accuracy, while some exceptional ones achieve even better performance. For example, requirements of less than 1 μm for flatness with surface finishes in the order of 0.010 μm R_a are not uncommon for the electronics industry [7].

In search for higher removal rates and improved surface finish, several machining techniques have recently emerged: high efficiency deep grinding (HEDG) [8], creep feed grinding [9], ductile mode grinding [10], and electrolytic in-process dressing (ELID) [11]. Thanks to the development of grinding techniques alongside improved

machine-tools, grinding is no longer regarded as a finishing process only, but it is also used as a bulk stock material removal process. However, because of the great forces involved during the material removal operation and to be able to keep up with the new accuracy and finishing requirements, the need for an improved stiffness loop in the machine-tool is commonly noted for these new emerging techniques.

Within the overall machine-tool stiffness loop, the importance of the tool-spindle stiffness has been acknowledged at Cranfield University [12]. At the same time, the need for new machine-tool concepts required to meet the new demands for improved machining operations has been noted. This has led to several years of research concerned with the development of very stiff and thermally-stable porous ceramic bearings for spindle applications [3] [13].

Traditionally, tool-spindles have been supported in rolling element bearings. However, these have gradually been giving way to aerostatic and hydrostatic bearings, owing to their better overall performance. Weck [14] *et al* tabulated the relative benefits for various spindle technologies, and these comparisons have been reproduced in Table 2.

	Type of bearing				
	Roller	Hydrodynamic	Hydrostatic	Aerostatic	Magnetic
High durability	+	+	++	++	++
High accuracy	+	+	++	++	++
High damping	-	+	+	θ	+
High rigidity	+	+	++	θ	+
Easy lubrication	++	θ	-	θ	-
Low friction	θ	-	-	++	++
Low price	++	θ	θ	θ	-

Very favourable (++)	Favourable (+)	Medium (θ)	Not favourable (-)

Table 2- Comparison of bearing spindle technologies produced by Weck (adapted from reference [14].

Recent figures for tool-spindle stiffness have been quoted at 400 N/μm [15] for a newly developed spindle that uses hydrostatic bearings lubricated with water.

Tool-spindle stiffness is typically measured in terms of deflection for a given force applied. However, the magnitude of the tool-spindle stiffness is for the most part determined by the design intent for such a machine-tool. Thus, selecting the appropriate machine elements is essential for improved machines; bearings being critical elements to tool-spindle performance.

2.2 Review of bearing technologies

The choice of bearing systems is ever increasing, with innovations constantly appearing and with those already established being improved upon. The theory and proper understanding of bearing systems is of fundamental importance in the design of precision machines and indeed to any system that contains rotating or moving parts.

In choosing a bearing system the designer must consider a great number of factors related to the characteristics, performance and requirements of the available technologies. Generally speaking choice is always the best compromise. Some of those factors as listed by Slocum [1] are:

- Speeds and acceleration limits
- Accuracy
- Vibration and shock resistance
- Damping capability
- Thermal performance
- Required life
- Environmental sensitivity
- Range of motion
- Repeatability
- Stiffness
- Friction
- Cost
- Designability
- Manufacturability
- Applied loads
- Resolution
- Preload
- Weight
- Maintenance
- Availability
- Mounting

In the following sections, the main characteristics and limitations of current bearing systems used for precision machine applications are described.

2.2.1 Rolling-element bearings

The rolling-element bearing technology is well established as it has enjoyed several centuries of development. Indeed, its origins can be traced back more than two thousand years, to roman times [16].

One of the great advantages of rolling-element bearings is their relatively low cost and they are readily available from specialist manufacturers in a wide range of dimensions and for wide range of applications, speeds, and loads. As a consequence, there are many millions of these bearings in operation throughout the world

In the rolling-element bearings working principle, the relative motion between the stationary and the moving elements is facilitated by a set of rolling elements in contact with the bearing outer and inner rings. Rolling elements commonly used are balls, rollers and needles.

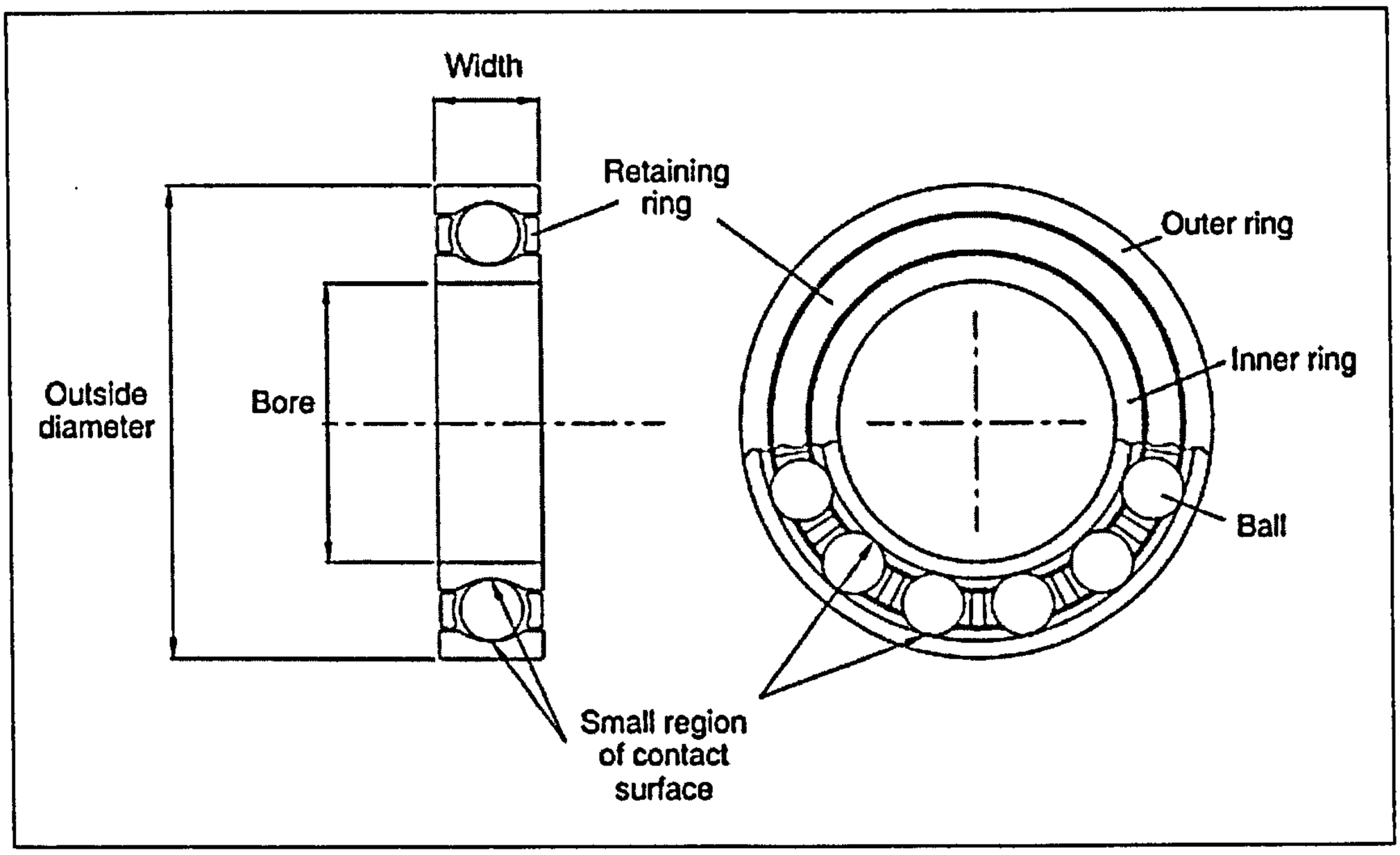

Figure 2-Typical rolling-element bearing (ball bearing) elements. Sketch reproduced from reference [17].

However as a result of their own working principle, rolling-element bearings do posses certain limitations, in particular when devised for manufacture at higher levels

of precision. The overall accuracy of the relative motion achieved by this type of bearing depends on the perfect geometry of its rolling elements and the contact surface roughness and waviness. Weck *et al* [18] produced a comparative study of spindle bearing technologies, where the effect of these was measured in terms of work-piece accuracy. The findings showed that an aerostatic spindle with a 50 nm asynchronous error was able to produce a surface finish of 3.6 nm Ra. In contrast, an equivalent ball-bearing solution with an asynchronous error motion of 300 nm produced a surface finish of 122 nm Ra. From this study it is clear that much improvement is still needed in rolling-element bearing technology in terms of its asynchronous error motion and its relation to surface finish.

Furthermore, despite of the use of very strong steels in their construction, all rolling-element bearings do have a finite life due to fatigue. The reason for this is that the load is exerted in very small area (Figure 2); resulting in relatively high contact stresses that cause the eventual bearing failure. It follows that, increasing the bearing speed increases the magnitude of the contact stresses with the square of the speed, due to the effect of the centrifugal force. This not only increases the wear at the interface, but effectively sets a limit to the speeds that rolling-element bearings can achieve.

Much effort in this field has gone into attempting to improve the overall bearings' performance through the adoption of new stronger materials. For instance, recently developed ceramic hybrid bearings, which incorporate ceramic rollers, have shown significantly improved performance over traditional rolling-element bearings and higher attainable speeds [19]. Ceramic balls are lighter than steel balls and as a result, the useful life of the bearing is improved [20]. And because their surface finish is almost perfectly smooth, they exhibit lower vibration levels, while running at lower operating temperatures.

However, despite all of the limitations mentioned above, rolling-element bearings are still widely found in high-speed applications where large cutting forces and high stiffness are required. As in the case presented by Slocum [1] where rolling-element

bearings were employed in a Cincinnati Milacron high speed machining centre (20, 000 rpm spindle). The very specific design and operation requirements: excellent thermal performance coupled with very high stiffness and cost effectiveness; ruled out other alternatives. Hydrodynamic systems were disregarded because of heat generation, aerostatic bearings because of their crashing susceptibility and porous graphite aerostatic and magnetic bearing systems were considered too expensive.

It is worth noting, nonetheless, that newly developed precision machine-tools now offered in the market, tend to incorporate in their designs aerostatic or hydrostatic bearings systems more often, in order to enable their superior performance.

2.2.2 Aerostatic bearings

In aerostatic bearings, the load is supported by a thin film of air supplied at high pressure by an external source, via restrictors. In comparison with rolling element bearings, with aerostatic bearings there is no contact between supported and supporting members as these are completely separated under all working conditions by the lubricant air film. Consequently, minor surface irregularities have very little disturbing effect. In addition, no wear is observed.

Aerostatic bearings are widely available and can be classified according to their geometry: cylindrical journal, circular thrust, annular thrust, conical and spherical. Aerostatic bearings can be also classified according to the type of flow restrictor used. The most common restrictor is a circular feed hole. The restrictor can, however take the form of a narrow slot, a capillary tube or the porosity of a sintered powder produced pad or bushing.

General performance characteristics of aerostatic bearing spindles are shown in Table 2. In general, the advantages of aerostatic bearings can be summarized as follows:

- Superior accuracy. Aerostatic bearings average out local irregularities, resulting in minimal run out.

- Low friction, which gives low power loss and cool running characteristics.
- Very high rotational speeds.
- Virtually no wear, and therefore infinite life.
- Low noise and vibration levels.
- Capability of operating at very high and very low temperatures.
- Air availability.
- 'Clean' operation.

Some disadvantages of aerostatic bearings include:

- Instability. Instability or 'pneumatic hammer' is a phenomenon associated with the compressibility of gases and the consequent delay between clearance changes and the response of the pressure changes in the restrictor's recess. Reducing the recess volume alleviates the problem, but at the same time reduces the load capacity of the bearing.
- Moderate stiffness.
- Support equipment. Operation of aerostatic bearings requires an external source of compressed air. In addition, appropriate maintenance routines are critical for this system in order to prevent foreign contamination from clogging the bearing's flow restrictors.

Comprehensive reviews of aerostatic bearings principle, design and applications can be found in publications by Slocum [1], Powell [21] and Stout & Rowe [22] [23].

Porous aerostatic bearings

An interesting approach is that of porous aerostatic bearings; where the bearing's set of restrictors take the form of a multitude of finite pores distributed over the entire bearing's surface. In this way, not only the expensive and tedious work of drilling the orifices is avoided, but a more uniform pressure distribution is achieved; which in turn maximises load capacity and stiffness characteristics [1]. Improved stability and damping characteristics have been suggested also [24].

The theory of porous aerostatic bearings is based on Darcy's flow through porous media law [25]. Numerous papers concerned with porous aerostatic bearing fundamentals, analytic models and performance characteristics have been published. Amongst those publications comprehensive reviews have been presented, first by Sneck [26] in 1968, followed by subsequent updates by Majumdar [27] in 1976 and Kwan & Corbett [28] in 1998.

Despite the great advantages offered by porous aerostatic bearings, the availability of porous material with predictable permeability has continued to hamper their widespread application [29] [30]. Recent research efforts at Cranfield University [30] [31] have tried to address this problem through the use of ceramics, successfully producing uniform structures with controlled permeability; hence suitable for this application. This work is briefly reviewed below.

Porous ceramic aerostatic thrust bearings

Kwan [30] first conducted research in order to develop a suitable ceramic material for its application in the manufacture of porous aerostatic bearings. Several porous aerostatic thrust bearings, single and double layer structures of 40 mm OD x 6mm thickness, were successfully produced by a combination of several ceramic manufacturing routes that included capsule free hot-isostatic pressing, slip casting and tape casting.

A double layer approach was able to eliminate the stability problem that the single layer 7 μm alumina layer substrate had exhibited. Here, the first layer consists of a 23 μm alumina substrate fabricated by HIPing, which provides the bulk of the mechanical properties. The second layer consists of a fine pressure restricting layer made form 0.5 μm alumina powder fabricated by slip casting. These two layers were bonded together by hot pressing a tape cast strip of 0.5 μm alumina between them. The static load characteristics and the pressure profile on the bearings tested agreed well with published theories.

Roach [31] followed Kwan's work investigating several ceramics manufacturing routes in order to simplify the manufacture method proposed by Kwan. Roach focused his work on the ceramic injection moulding and slip casting techniques, processing a number of samples that proved both manufacturing methods to be reproducible and cost effective.

Roach suggests that by using fine powders, 4μm or smaller, the void volume at the bearing's surface is reduced, therefore the stability problem is eliminated, as is the need for an extra restrictor layer. Single layer bearings produced by both manufacturing techniques proved to be stable, while exhibiting a static performance that agrees well with the published theories for porous thrust bearings.

Both Kwan [30] and Roach [31] present comprehensive reviews on porous aerostatic bearings, in particular on aspects of their manufacture and the use of porous ceramic materials.

2.2.3 Hydrodynamic bearings

In hydrodynamic bearings the load is supported on a film of lubricant. The relative motion between the supported and supporting members creates the necessary pressure distribution to support the load. Both the pressure and the frictional power loss in this film are a function of the lubricant's viscosity in combination with the geometry and the shear rate imposed by the bearing conditions [32]. Hydrodynamic bearings are commonly found in the form of either journal or thrust bearings. Figure 2 shows the pressure distribution in a typical hydrodynamic journal bearing.

As a consequence of their own working principle, hydrodynamic bearings do experience some rubbing when the shaft starts to rotate as well as when it stops rotating. In practice, there are also other circumstances in which wear takes place [33]. For example, the large friction heating raises the temperature and causes oxidation of the oil and corrosion of the bearing's surfaces. Deterioration of the bearing's surfaces can lead to solid particles circulating in the oil which increases the wear rate.

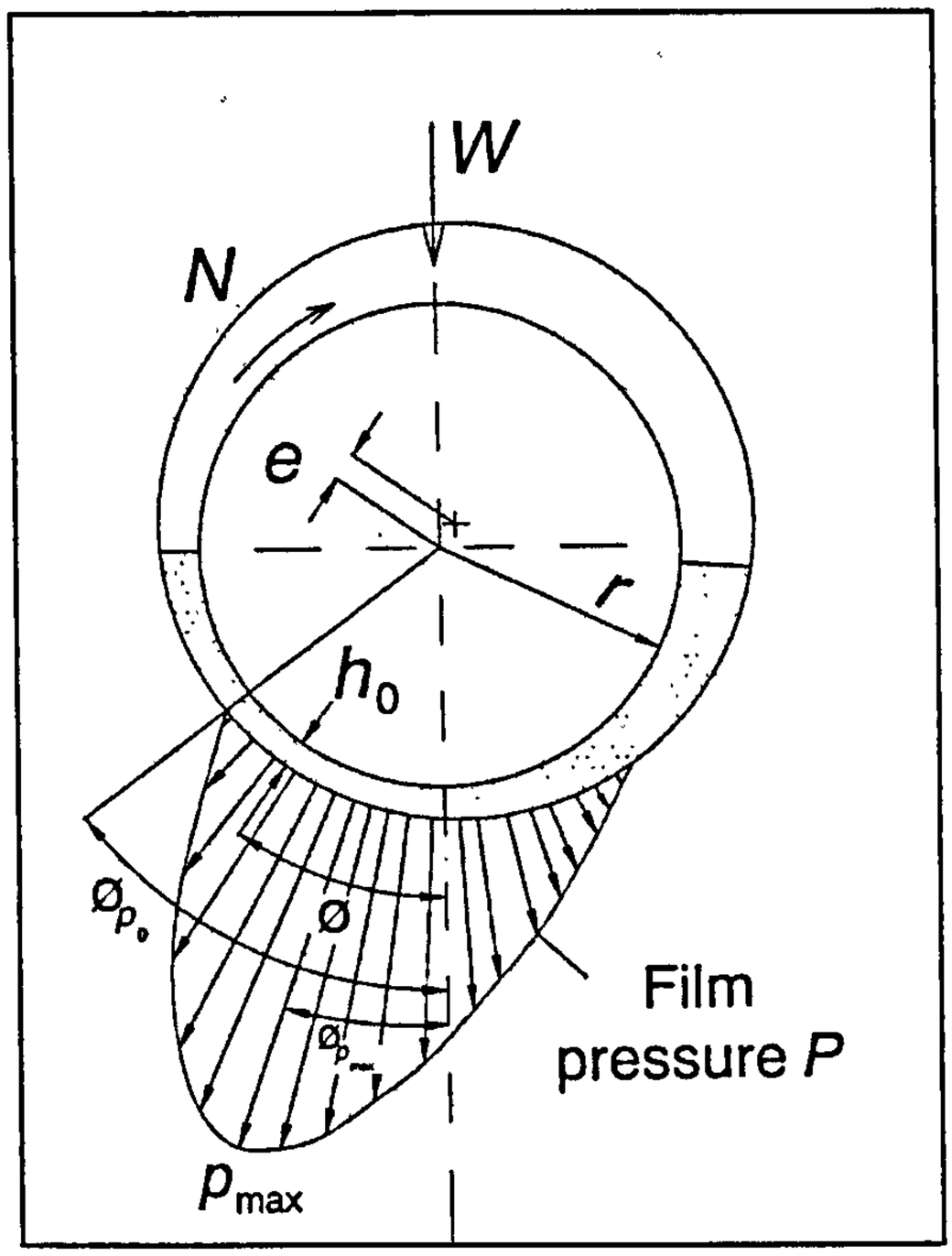

Figure 3-Pressure distribution in a typical hydrodynamic journal bearing; from reference [17].

Nonetheless, hydrodynamic bearings do posses certain advantages that make them attractive to a number of applications such as: hydroelectric generators, turbines, centrifugal compressors, turbochargers, electric motors, oil pumps, etc. General performance characteristics of hydrodynamic bearing spindles are shown in Table 2.

The theoretical analysis and performance characteristics for hydrodynamic bearings are based on the well known Reynolds equation [34].

Fluid film lubrication-Historical perspective

At the beginning of the nineteenth century, an understanding of the mechanism of lubrication was primitive. In 1883, Beauchamp Tower presented his first report on lubrication [35], in which he reported the accidental discovery of substantial pressures in the oil film in journal bearings. This is one of the best known landmarks in the history of tribology. It provided the experimental basis and conceptual stimulus for the well known analytical study by Osborne Reynolds [34], which is

considered as the foundation for the understanding of fluid film lubrication. For the Reynolds' equation has indeed become the starting point for most theoretical analyses, including hydrodynamic bearings, as well as porous hydrostatic bearings.

2.2.4 Magnetic bearings

Magnetic bearings are a non-contacting technology; where the supported member is completely separated from the supporting member by magnetic suspension. The system achieves equilibrium via a closed loop control measuring the air gap and using it as a feedback parameter.

Magnetic bearing systems usually comprise of three basic technologies [36]:

- *Bearings & sensors* are the electromechanical hardware by which input signals are collected, and supporting forces are applied to the machine.
- *The control system* provides the power and control electronics for signal conditioning, calculation of correcting forces, and resultant commands to the power amplifiers for each axis of control.
- *Control algorithms* are the software programs used in digital magnetic bearing system control including the processing of the input signals after conditioning, and calculation of the command signals to the power amplifiers.

Because of their principle, magnetic bearings can be designed for a wide range of applications. For instance, SKF-Revolve [36] has designed and manufactured radial actuators with load capacities from 50 to 25,000 N for shaft diameters ranging from 9 mm to 230 mm. These are installed on machines that have rotational speeds ranging from 1,800 rpm to 100,000 rpm. SKF-Revolve has also designed 'canned' radial bearing designs for hermetically sealed applications and radial bearings for high temperature applications up to 220°C.

Magnetic bearings utilize a non-contacting technology, so they possess negligible friction and wear, as well as higher reliability. In addition, because lubrication is

eliminated, these bearings can be incorporated into processes which are sensitive to contamination, such as vacuum chambers.

Another great advantage of magnetic bearings is that many desirable characteristics for spindle performance, such as higher speeds, load carrying capacity, stiffness and accuracy, can be designed to virtually limitless levels. This however, comes at a price. Magnetic bearing systems are generally custom designed for the application and thus as yet are not available off the shelf. Furthermore, magnetic bearing systems are complex systems and their performance depends on the quality and performance of their components. Hence, the initial investment cost is usually higher than the competing technologies [1].

Magnetic bearing systems have virtually infinite life, however the control system can be affected by power outages or component failure; thus auxiliary rolling element bearings must be incorporated. Other aspects to be taken into account are the size and weight of magnetic bearings which are much larger in comparison with most other bearing systems, as well as the significant amounts of heat generated by this type of bearing.

2.2.5 Liquid hydrostatic bearings

In liquid hydrostatic bearings, the load is transmitted from the supported to the supporting member through a liquid film, by virtue of pressure maintained by an external pump [37]. There are five basic types of hydrostatic bearings: single pad, opposed pad, journal, thrust and conical. Figure 4 shows a typical hydrostatic journal bearing under load.

Basically, a hydrostatic bearings' operation principle is the same as that of aerostatic bearings, the main difference being the use of a liquid film instead of an air film to support the load. Conventionally, oil is used for this purpose; although there may be occasional circumstances where water is preferred.

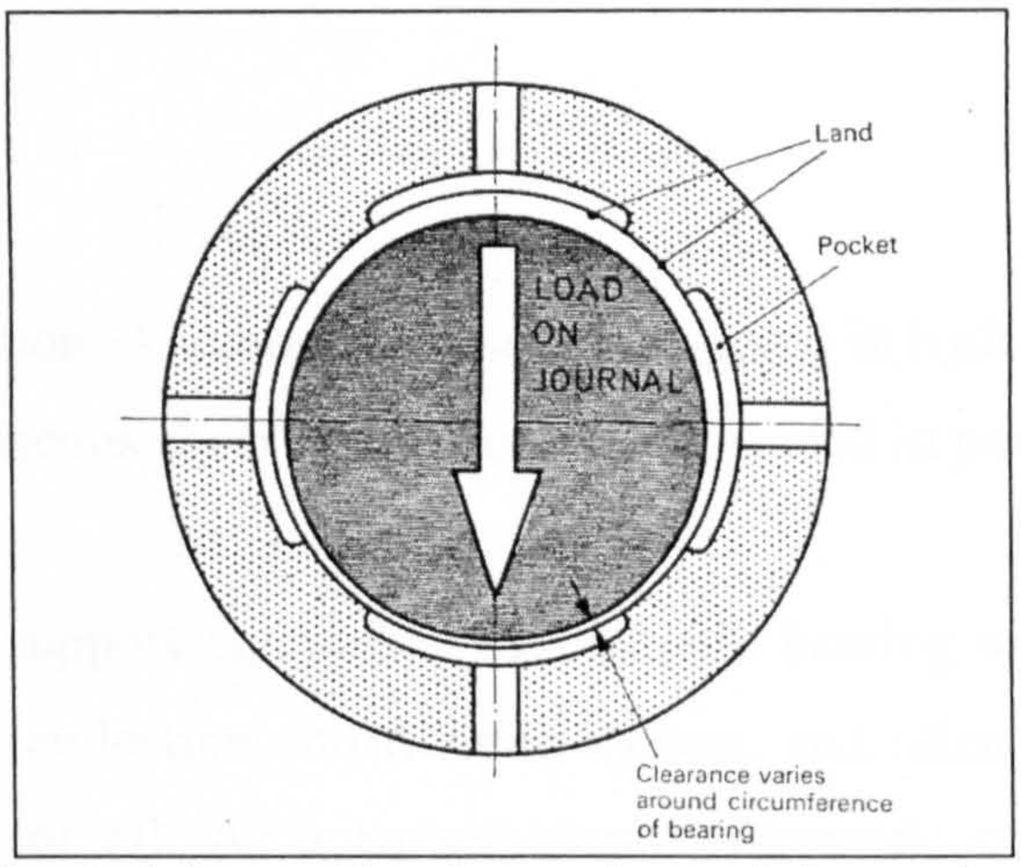

Figure 4-Typical hydrostatic journal bearings under load; from reference 34.

There are certain advantages of using liquids over air. The most evident is that liquids are not compressible; hence the pneumatic instability (hammer) effect is non existent. Consequently the restrictors' recesses (pockets) are generally much larger than those in aerostatic bearings. Pressure builds up in these pockets, more efficiently supporting the load. In practice, liquids can be also raised to higher supplied-pressures than air; and as a result, hydrostatic bearings can be designed to be stiffer and to sustain higher loads than aerostatic bearings.

Another difference between the physical properties of liquids and gases resides in their viscosity. Liquids possess higher viscosities than air, consequently allowing for larger bearing gaps, which makes hydrostatic bearings less susceptible to crashing. In general, the advantages and disadvantages of hydrostatic bearings can be summarized as follows [1]:

Advantages:

- Virtually infinite stiffness that can be a maintained over an exceptionable wide range of speeds and loads.
- Averaging effect. Small micro-roughnesses and wavinesses are averaged out, resulting in minimal run-out.
- Virtually no wear, as there is no-sliding motion.

- High load capacity.

Disadvantages:

- Heat generation. A temperature rise is observed in hydrostatic bearings. This is due to the viscous shear and the energy expended in pumping the fluid through the bearing.
- The use of support equipment. Hydrostatic bearing systems require a pump, distribution, collection and filtering system, and often a means to control the temperature of oil. As a consequence, hydrostatic bearing systems may be expensive.

By virtue of their overall performance (Table 2) hydrostatic bearings have become the preferred choice among high precision engineers, in particular for heavy duty applications. Examples of recently developed state of the art precision machines incorporating hydrostatic bearings are the Cranfield Precision's Nanocentre and the large optics diamond turning machine (LODTM) developed by the Lawrence Livermore National laboratory in the USA [1].

Nonetheless, in view of the new demands for accuracy, hydrostatic bearings systems do possess a crucial shortcoming: heat generation. Thermal distortion is catalogued as a major source of error on the overall accuracy of machine-tools [1] [2]. In this respect, Corbett [12] has noted the need for new bearing concepts in order to cope with the continued drive for improved bearing performance.

2.2.6 Porous hydrodynamic bearings

Porous hydrodynamic bearings, also referred as 'porous bearings', are commonly found in electrical motors, household appliances and audio equipment. These are manufactured mainly from bronze powders by powder metallurgy techniques. The procedure essentially involves powder compaction at high pressures followed by sintering. Finally, the sintered bearings are re-pressed with sizing tools for improved dimensional accuracy and surface finish [38]. Porosity values usually attained range

from 10 to 40%. Lubricant is normally supplied once by impregnation and the bearing operates in the hydrodynamic lubrication regime.

Although this technology dates back to the early 1920's [38], the first mathematical model to investigate its mechanism of lubrication was developed by Morgan and Cameron [39] in 1957. Modifying Reynolds's equation to account for the porous effect, they produced approximate numerical solutions for the film pressure and load capacity in narrow hydrodynamic bearings.

In addition, Morgan and Cameron [39] also explained the oil circulation mechanism within the porous bearing and found the bearing's porous wall acted as an oil reservoir from which the bearing gap was filled with lubricant. Another discovery Morgan and Cameron presented is the 'pore closure' phenomenon. Pore closure occurs in the porous wall around the region of the load line whenever there is physical contact between the rotating shaft and the porous bearing. They concluded that the pore closure phenomenon would be present when the bearing is operating under extreme conditions, such as overloading or overheating. Pore closure changes the permeability of the porous wall, and therefore affects the bearing's performance. Ever since Morgan and Cameron published their analysis, numerous investigations have followed, improving upon the theory to include new operating conditions; amongst these Murti [40], for instance, further developed Morgan and Cameron's model producing more comprehensive solutions, while Conry and Cusano [41] dealt with the stability characteristics.

However, further research [42] [43] into the operation of porous bearings suggests that in practice, the bearing gap is not always completely filled with oil as required for fully hydrodynamic lubrication, but rather that porous bearings operate in the boundary or mixed film lubrication regime. As a consequence, porous bearing performance is compromised and cannot be always predicted accurately [44].

The manufacturing procedures for porous hydrodynamic bearings are very similar to those for conventional porous gas bearings and porous hydrostatic bearings; hence

their importance within the context of the present research. However, the main difference between the three technologies resides in their lubrication principle, and as a consequence, the ranges of application for porous hydrodynamic bearings and externally pressurized bearings are very different. Hydrodynamic porous bearings are best suited for low cost applications, where a relatively high degree of reliability is not required.

2.2.7 Porous hydrostatic oil bearings

Externally pressurized liquid lubricated porous bearings come as a natural development of conventional oil hydrostatic bearings; whereby the much desired performance characteristics noted in porous aerostatic bearings resulting from a more uniform pressure distribution, such as maximised load capacity and stiffness, are added to the intrinsic benefits of liquid hydrostatic lubrication.

The porous wall and its multitude of minute restrictors simplify the bearing design by avoiding the conventional restrictors and pockets. By doing away with the latter, the utilization of the hydrodynamic pressure in the lubricant film is also improved; while allowing higher speeds to be reached before the onset of turbulence. Furthermore, it has been suggested that [4], due to the presence of a permeable surface adjacent to the clearance space, these bearings exhibit better damping characteristics than conventional liquid hydrostatic bearings.

The concept of liquid lubrication and its analysis in externally pressurized porous bearings was first published by Howarth [45] [46] for a thrust bearing configuration. Similarly to porous aerostatic bearings theory, liquid lubrication theoretical analysis for externally pressurized porous bearings is based on Darcy's law for flow through porous media.

Steady state performance analysis of journal bearings

The theory and analysis for porous hydrostatic journal oil bearings has been mainly developed by a group of researchers at the Indian institute of technology Kharagpur in a series of progressive theoretical papers. In the first of these papers, Majumdar and Rao [47] set to find analytical solutions for the pressure distribution, load capacity and oil flow rate. Here, similarly to most bearing theories, non dimensional values were employed to characterize the bearing design. These non dimensional values would be employed also to examine some aspects of bearing's performance such as load capacity ($\overline{W}$) and attitude angle (ø) in a parametric study presented in the same paper. The 'bearing feeding parameter' (β), for instance, takes into account the bearing geometry, permeability and gap:

Equation 1

$$\beta = \frac{12 \cdot k \cdot R^2}{C^3 \cdot H}$$

β	bearing feeding parameter (dimensionless)
k	viscous permeability coefficient (m^2)
H	thickness of the porous bushing (m)
C	radial clearance or bearing gap (m)
R	journal radius (m)

The 'bearing speed parameter' (λ_s), also called 'bearing parameter' (represented as Λp in Rao's paper), is a dimensionless form of the shaft speed parameter, similar to the Sommerfield number used in plain bearing design.

Equation 2

$$\lambda_s = \frac{6 \cdot \eta \cdot \omega}{P_s \cdot (C/R)^2}$$

λ_s	bearing speed parameter (dimensionless)
η	absolute viscosity of the fluid (Ns/m^2)
ω	angular speed of the journal (rad/s)
Ps	supply pressure (N/m^2)

The dimensionless load parameter was defined as:

Equation 3

$$\overline{W} = \frac{4 \cdot W}{L \cdot D \cdot P_s}$$

$\overline{W}$	Load parameter (dimensionless)
W	load on bearing (N)
L	length of the bearing (m)
D	shaft/bearing diameter (m)

The parametric study presented by Majumdar and Rao showed the load capacity improved with an increasing bearing speed parameter, demonstrating an increasing hydrodynamic pressure component (Figure 5). Also, the attitude angle was noted to increase approaching asymptotically to 90° with an increasing bearing speed parameter. Unfortunately, no work was discussed with regard to journal stiffness in this paper, and no attempt at experimental verification appears to have been made.

Further refinement was later achieved by Chattopadhyay and Majumdar [48] by including the Beavers and Joseph slip-flow criterion [49] as well as considering directionally anisotropic permeability in their steady state analysis. A parametric study was also conducted to asses the effect of the various design parameters, including the bearing speed parameter (λ_s) and the slenderness ratio (L/D), upon the

bearing load capacity, friction coefficient and oil feed rate; expressing their behaviour as a function of the bearing feeding number (β).

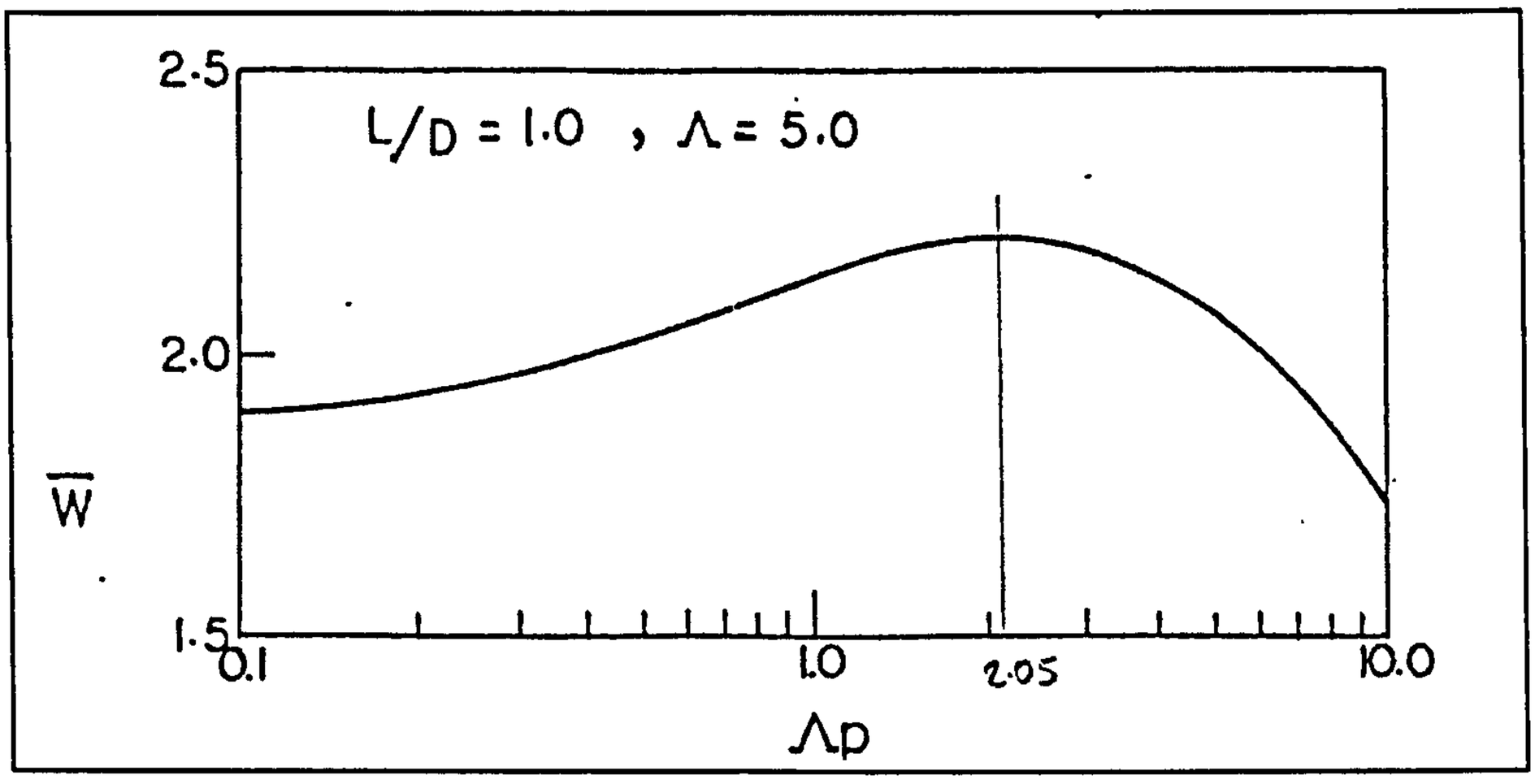

Figure 5-Porous hydrostatic oil journal-bearings load capacity's hydrodynamic pressure component; from reference 47.

Slip flow, within the context of externally pressurized porous bearings, arises from the fact that porous materials do not have a solid boundary, but are bounded by a series of interconnected pores and particles; as opposed to a nominally solid defined boundary that runs along a line touching the outermost peaks.

Traditionally, the flow through the porous media and the flow that entered the bearing gap would be considered as separate systems. In reality, because of this non solid porous boundary, there is no such clear distinction between the two flow regimes, giving place to slip flow at the pore gap boundary (Figure 6). The presence of slip flow, generally leads to a lower resistance to fluid flow within the bearing clearance, with a resulting increase in flow rate.

The slip flow coefficient as defined by Beavers and Joseph [49] is shown in the mass flow equation below:

Equation 4

$$\Phi = \frac{3 \cdot (\sigma + 2\alpha)}{\sigma \cdot (1 + \alpha\sigma)}$$

Φ	fractional increase in mass flow rate (dimensionless)
σ	non dimensional permeability (dimensionless)
α	slip coefficient (dimensionless)

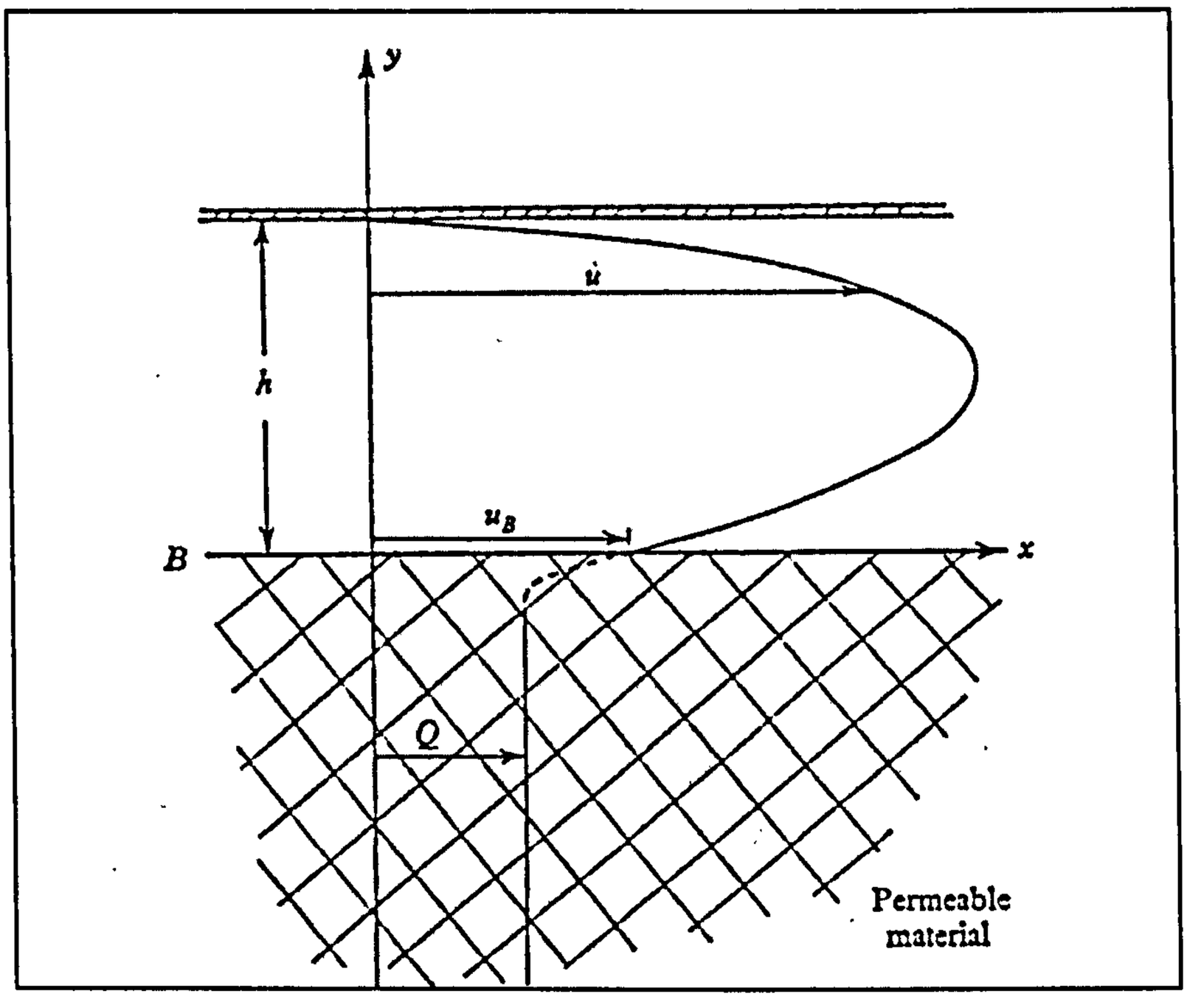

Figure 6-Slip flow over a permeable block; from reference [49].

However, as a result of their study Chattopadhyay and Majumdar concluded that 'for all practical purposes the effect of slip flow is not remarkable'. In the same manner, they concluded that 'the effect of permeable anisotropy is insignificant for eccentricity ratio values below 0.70'. Based on their parametric study, the authors also conclude that the optimum value of the bearing feeding parameter lies between 1 and 3 for most finite porous bearings.

Dynamic performance analysis

A third paper by Chattopadhyay *et al* [50] was concerned with the analysis the dynamic characteristics of porous hydrostatic journal bearings. They investigated the stiffness and the damping coefficients and the effects the various design parameters had on these. For this analysis, the journal was assumed to exhibit an elliptic orbit about its mean steady state position (Figure 7). In addition, the lubricant was assumed to be an incompressible fluid of constant viscosity and the effect of velocity slip was also accounted for.

A parametric study of the stiffness and damping coefficients was undertaken by keeping the slenderness ratio (L/D) and the bearing speed parameter (λ_s) fixed at unity. From this study it was noted that the 'direct' stiffness factors, i.e. those that considered the force component acting in the same direction as the resulting deflection, reached peaks for bearing feeding parameter (β) values between 0.9 and 1.7. However, in the case of the 'direct' damping coefficient, this reached its peak at about 0.3; much lower compared to the optimum 'direct' stiffness parameters. Chattopadhyay and Majumdar also noted that increasing λ_s resulted in an increase of the dynamic coefficients. Finally, they concluded that 'the effect of slip on the dynamic characteristics of porous hydrostatic bearings is at best marginal, when practical values of the slip parameters are considered'.

Whirl instability is a phenomenon peculiar to journal bearings and occurs when the speed exceeds a certain value, which for any given design is dependent on the mass and stiffness of the shaft. This condition manifests itself as a non synchronous motion of the journal centre, severely affecting bearing performance; and potentially leading to shaft-journal rubbing.

Chattopadhyay *et al* describe their investigation into porous-hydrostatic oil journal-bearings' whirl stability, in another theoretical paper [51]. Here, a rigid rotor was assumed to be rotating in a finite externally pressurised porous oil journal bearing. In this analysis, a modified Reynolds equation was written considering the effects of

directionally anisotropic permeability of the porous matrix. Again, the Beavers and Joseph criterion for velocity slip was also taken into account.

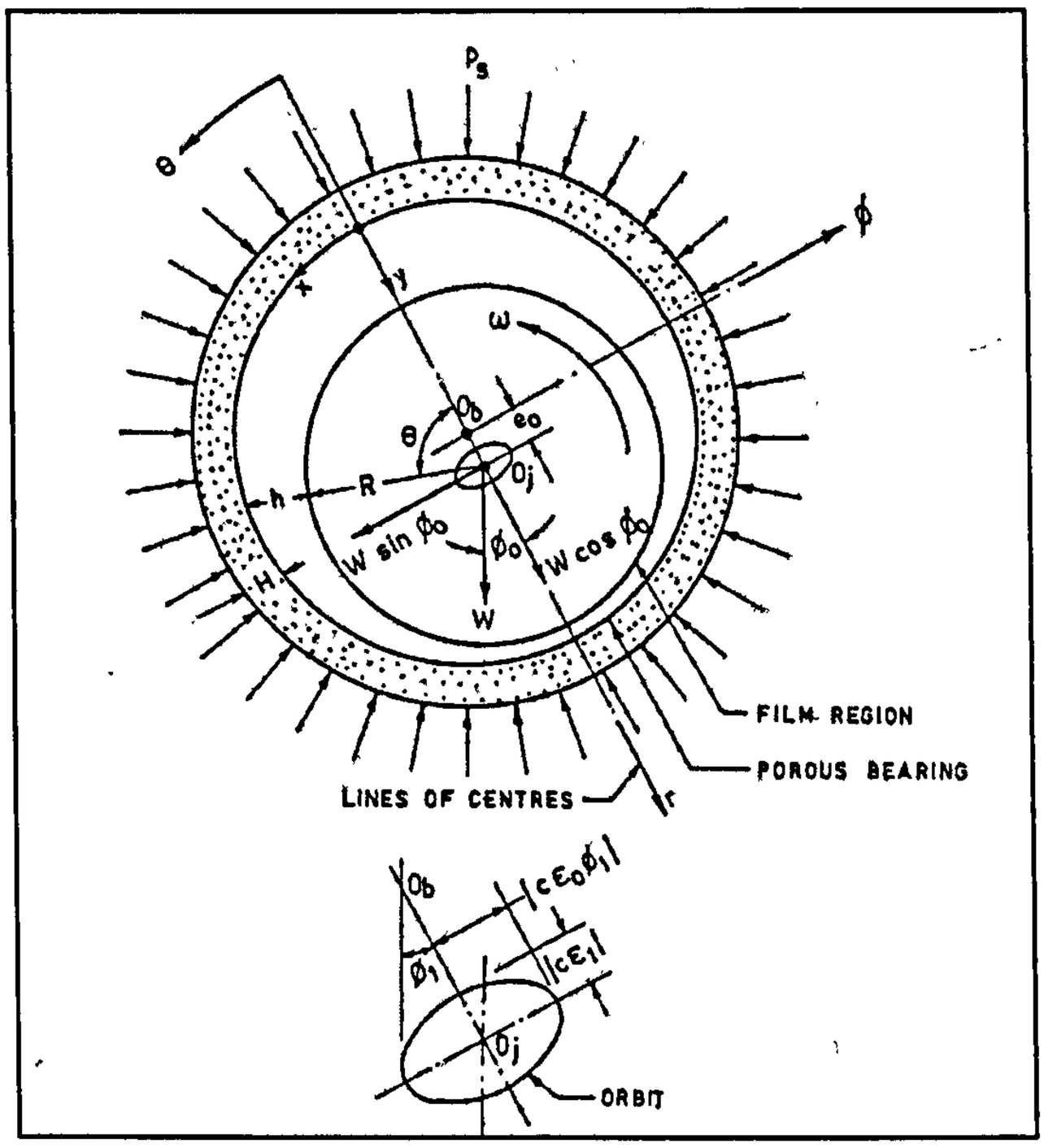

Figure 7-Chattopadhyay dynamic analysis schematic, from reference 48.

The threshold values of whirl instability are given in terms of a non-dimensional critical mass parameter ($\overline{m}_c$) and its variation, presented in the form of graphs, was examined in relation to the bearing feeding parameter with the speed parameter, the slenderness and eccentricity ratios, slip coefficient and permeability factor.

Equation 5

$$\overline{m_c} = \frac{m_c \cdot C \cdot \omega^2}{W}$$

$\overline{m}_c$	non dimensional critical mass parameter
m_c	critical mass of rotor (k)

C	mean radial clearance of bearing (m)
ω	angular velocity of the shaft (rad/s)
W	steady state load on bearing (N)

In this study, Chattopadhyay predicted some particularly important stability characteristics. For instance, their study showed that a bearing would be stable at all speeds for eccentricity ratio values below 0.2; or slenderness ratio values below 0.5. In general, stability is seen to increase for most of the study conditions when the bearing feeding parameter (β) $\geq$1; with the exception of the bearing speed parameter (λ_s). At first, Chattopadhyay noted that for lower values of β corresponding to any values of λ_s stability curves were relatively flat. However, at higher values of β and at higher values of λ_s, stability curves have a tendency to drop; whereas for $\lambda_s = 1$, the stability curve ascends asymptotically to infinity (Figure 8).

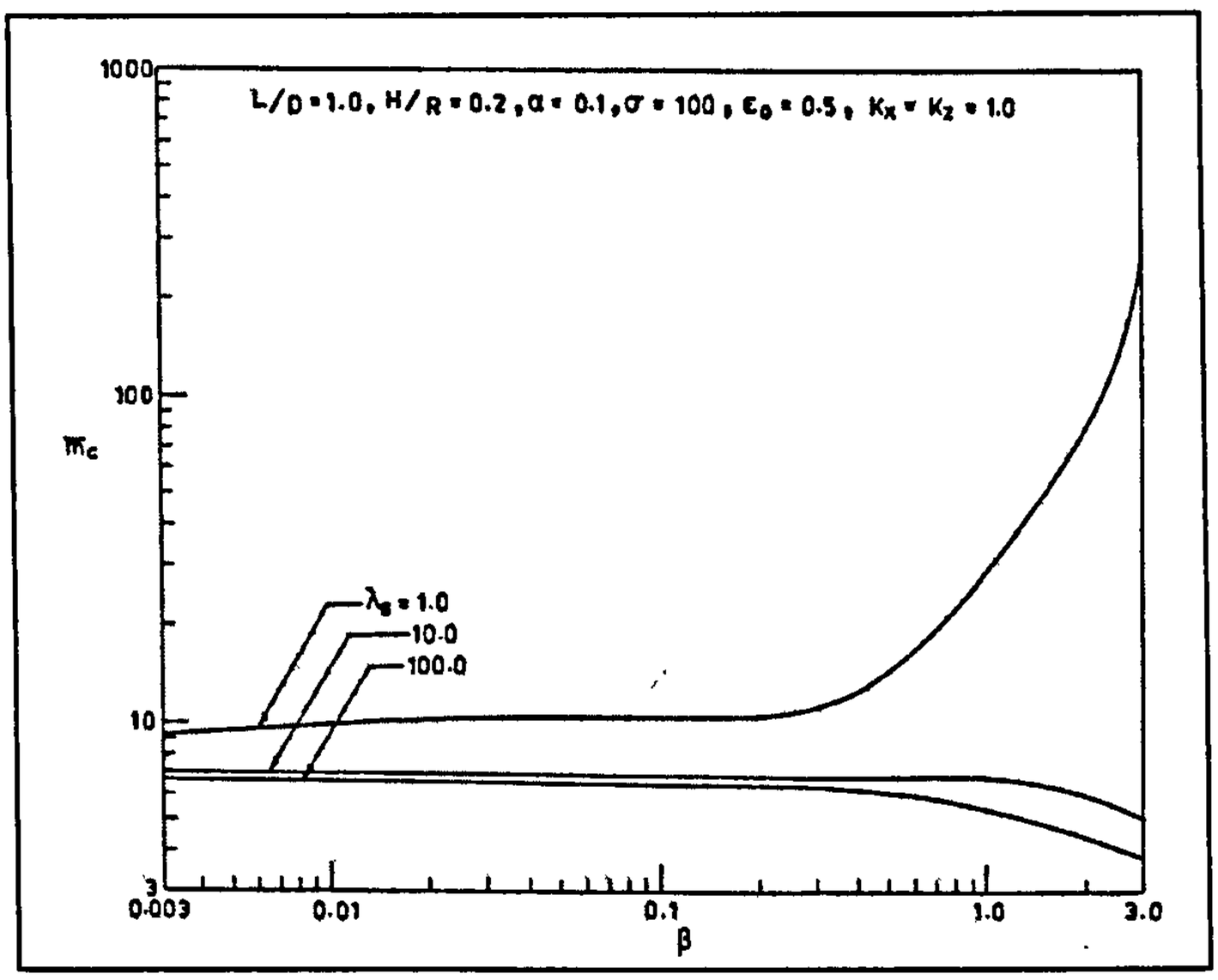

Figure 8-Chattopadhyay (reference [51]) variation of the critical mass parameter with the speed parameter.

The effect of anisotropic permeability on the stability characteristics is described as 'meagre'. Slip flow is seen to slightly increase stability; although, for practical values of the bearing radius-clearance ratio (R/C) its effect is very small. Stability was also noted to marginally increase with the R/C ratio.

For bearings operating at high speeds with low viscosity lubricants it is quite reasonable to expect large Reynolds' numbers and hence flow turbulence within the bearing clearance. Kumar and Rao [52] investigated this phenomenon, aiming to study the effects of turbulence on steady state behaviour in terms of load capacity, friction coefficient and flow. Reynolds' number, as presented in this new study is given by the Equation 6.

Equation 6

$$R_e = \frac{U \cdot C}{\nu}$$

R_e	Reynolds' number (dimensionless)
U	surface velocity (m/s)
ν	kinematic viscosity of the fluid (m^2/s)

Transition from the laminar to the turbulent regime is commonly acknowledged to occur between a R_e of 1000 and 2000. Kumar and Rao included in their analysis Reynolds' numbers ranging from 1000 to 50, 000 for a parametric study that was carried out by varying the bearing feeding parameter (β), slenderness ratio (L/D), bearing speed number (λ_s) and the bearing wall thickness-radius ratio (H/R); as well as considering anisotropic permeability. From this study Kumar and Rao observed the load carrying capacity to increase considerably with increasing Reynolds' numbers (Figure 9). However for higher values of β (β>0.3) the load capacity is sharply reduced. This trend is particularly noticeable for the higher R_e.

Kumar and Rao observed that generally, the effect of turbulence increases the load parameter, frictional drag and flow rate. Further results of their parametric study also showed that by increasing the L/D ratio, the load capacity and flow rate also increased. Interestingly, they also noted a reduction in the friction coefficient. The

effect of anisotropic permeability on the performance of the bearing is considered negligible.

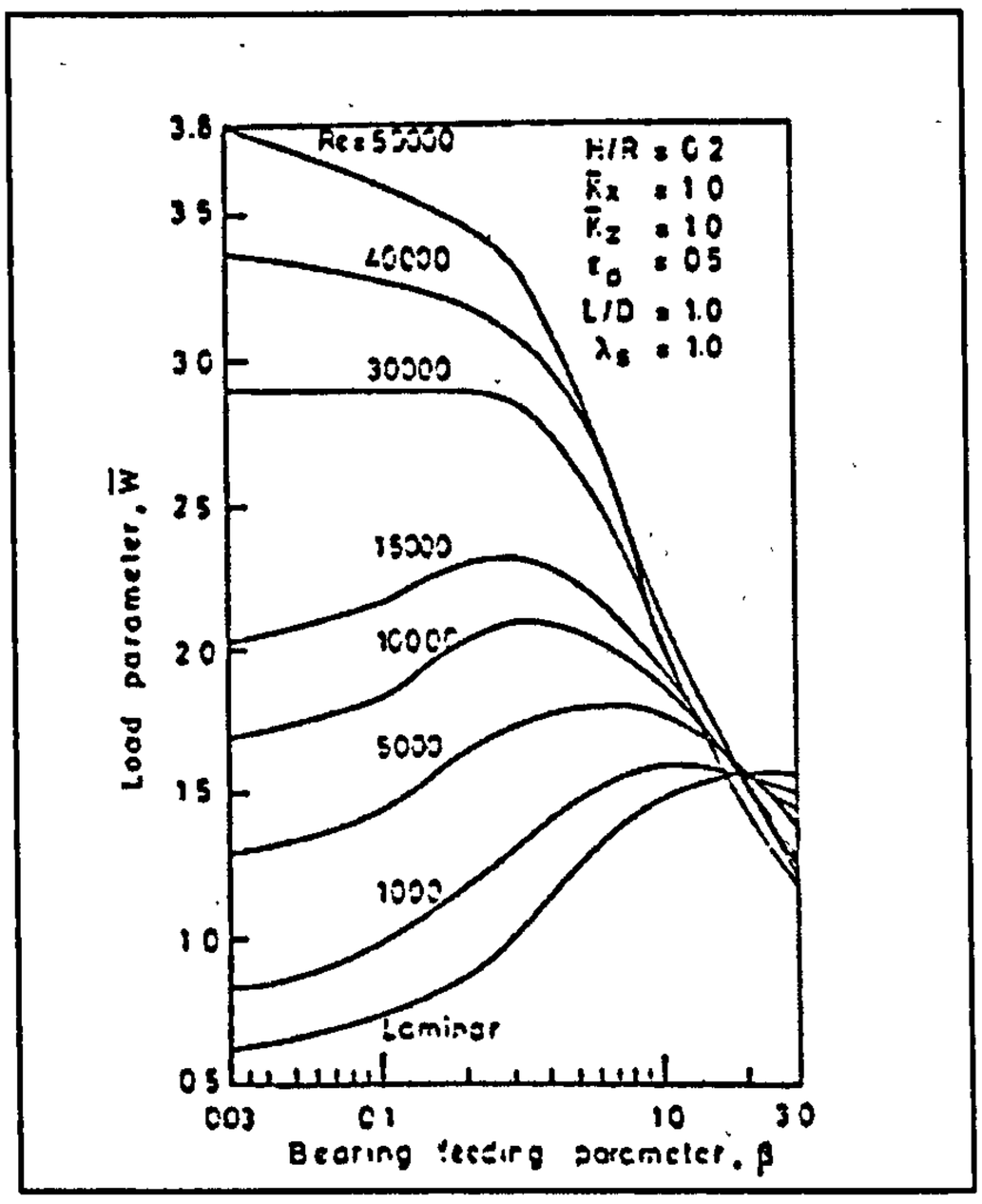

Figure 9-Kumar's load parameter vs. feeding parameter for various Reynolds' numbers.

In conclusion, they stressed the benefits of higher L/D ratios and suggest designing with a β value of 0.3 for optimal bearing performance. In this respect, Almond [3] noted $\beta \leq 0.3$ not to be the most appropriate for ultra-precision applications because the marginal fluid film formed at this β value might cause the bearing to exhibit unpredictable performance characteristics.

Last in the series of progressive papers concerned with porous hydrostatic journal bearings, is a paper presented by Kumar and Rao [4]. Dealing once more with low kinematic viscosity lubricants, Kumar and Rao investigated the theoretical stability characteristics of hybrid porous journal bearings with a turbulent fluid film. They used a modified Reynolds' equation and considered the anisotropy of permeability and the unsteady state of the journal.

A parametric study of bearing stability was conducted; expressing the threshold values of instability in terms the non-dimensional critical mass parameter ($\bar{m}_c$) (Equation 5) and by varying the Reynolds' number (R_e), bearing wall thickness-

radius ratio (H/R), slenderness ratio (L/D), eccentricity ratio (ε_0) and the bearing speed parameter (λ_s); in relation to the bearing feeding number (β). As a result of their study, Kumar and Rao noted that, for values of β between 0.01 and 0.1 the effect of turbulence on the stability was negligible; however for higher values of β, the effect of turbulence was significant. Stability also deteriorated with an increasing R_e (Figure 10).

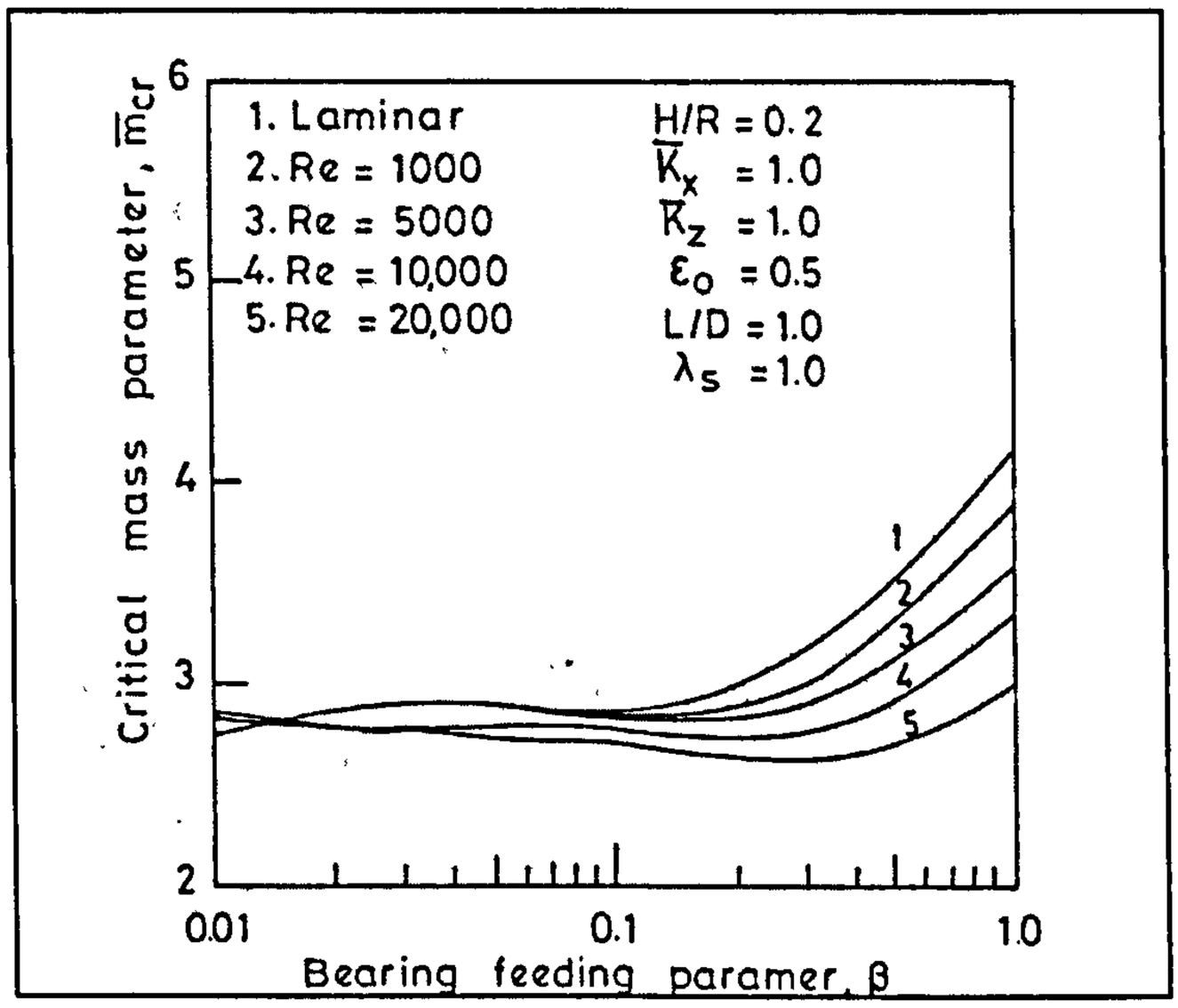

Figure 10-Kumar's (reference [4]) critical mass parameter vs. feeding parameter for various Reynolds' numbers.

Increasing λ_s was noted to adversely affected stability, agreeing with the trends observed by Chattopadhyay *et al.* [51] in their stability investigation. This effect is probably attributable to the effect of turbulence at higher speeds. In general, lower values of β, of around 0.1, are seen to improve the stability of turbulent hybrid bearings; as indeed the authors recommend for stability optimised bearing design. However as Almond noted [3], this is probably in conflict with practical values of β for ultra-precision engineering applications.

Further details concerning the theory of porous hydrostatic journal bearings can be found in Almond's research theses [3].

The porous material challenge

As with porous aerostatic bearings, despite the great advantages offered by porous hydrostatic bearings, the difficulties in producing two identical bearings of specified permeability and porosity; in addition to a decrease in permeability due to local deformation caused by the pressurised fluid has continued to hamper their widespread application, and this has been indeed stressed by Kumar and Rao [4] [52]. Furthermore, the alteration in the properties of bearing stock material due to pore closure caused by machining operations for bronze and graphite has been also noted by Howarth [46] and Kwan [30], respectively.

In a recent research effort at Cranfield University [3], researchers have tried to address this problem through the use of ceramics, successfully producing uniform structures with controlled permeability, which are suitable for precision engineering applications.

2.3 Present state of development of porous ceramic hydrostatic bearings

Porous hydrostatic journal bearings have been recently developed and tested at Cranfield University [3]. These were manufactured to near net shape with ceramic materials (alumina) through capsule free hot isostatic pressing (HIPing). Amongst other advantages, ceramic materials offered long term stability and stiffness, low coefficient of thermal expansion and virtually non-corrosiveness as well as having the ability of being machined without any noticeable pore deformation or closure. Table 3 shows a comparison of materials properties, including alumina.

Property	Steel	Bronze	Graphite	Alumina
E-modulus (GPa)	200	110	20	410
Flexural strength (MPa)	620	515	50	600
Rel. density	7.8	8.8	1.7	3.8
Thermal. Exp. Coefficient (10^{-6} k^{-1})	11.6	17.8	1	5.4
Thermal conduct (wm^{-1} K^{-1})	52	84	5-90	30
Dimensional stability	Poor	Poor	Moderate	Good
Wear resistance	Moderate	Moderate	Poor	Good
Corrosion resistance	Good (if stainless)	Good	Good	Excellent

Table 3-Comparison of materials properties: Alumina, Steel, Bronze and graphite; from reference [30].

Based on the analytical studies developed by Majumdar and his co-workers (previous section), mathematical models were initially developed to design an optimised bearing for ultra-precision applications. Some of the fundamental design variables, used on the Cranfield work, were predetermined using practical bearings dimensions; which were contemplated for this research's specially designed test-rig. As a result, the internal diameter was determined to be 50 mm, the length of the bearings was set to 50 mm (L/D = 1) and a wall thickness of 6 mm was chosen.

Majumdar's mathematical models revealed an optimum permeability of 1×10^{-14} m^2 (Figure 11). Further modelling at Cranfield, based on the Kozeny theory was carried out, accounting for this permeability requirement, in order to calculate the porous matrix target density and average pore-diameter [3].

With regard to the porous-ceramic journal bearing manufacture, the influence of the processing parameters as well as powder size on both fluid flow through the bearing and the mechanical properties of the porous ceramic structures were investigated and identified. The optimum powder size was found to be a bimodal mixture 60% 13μm – 40% 1 μm.

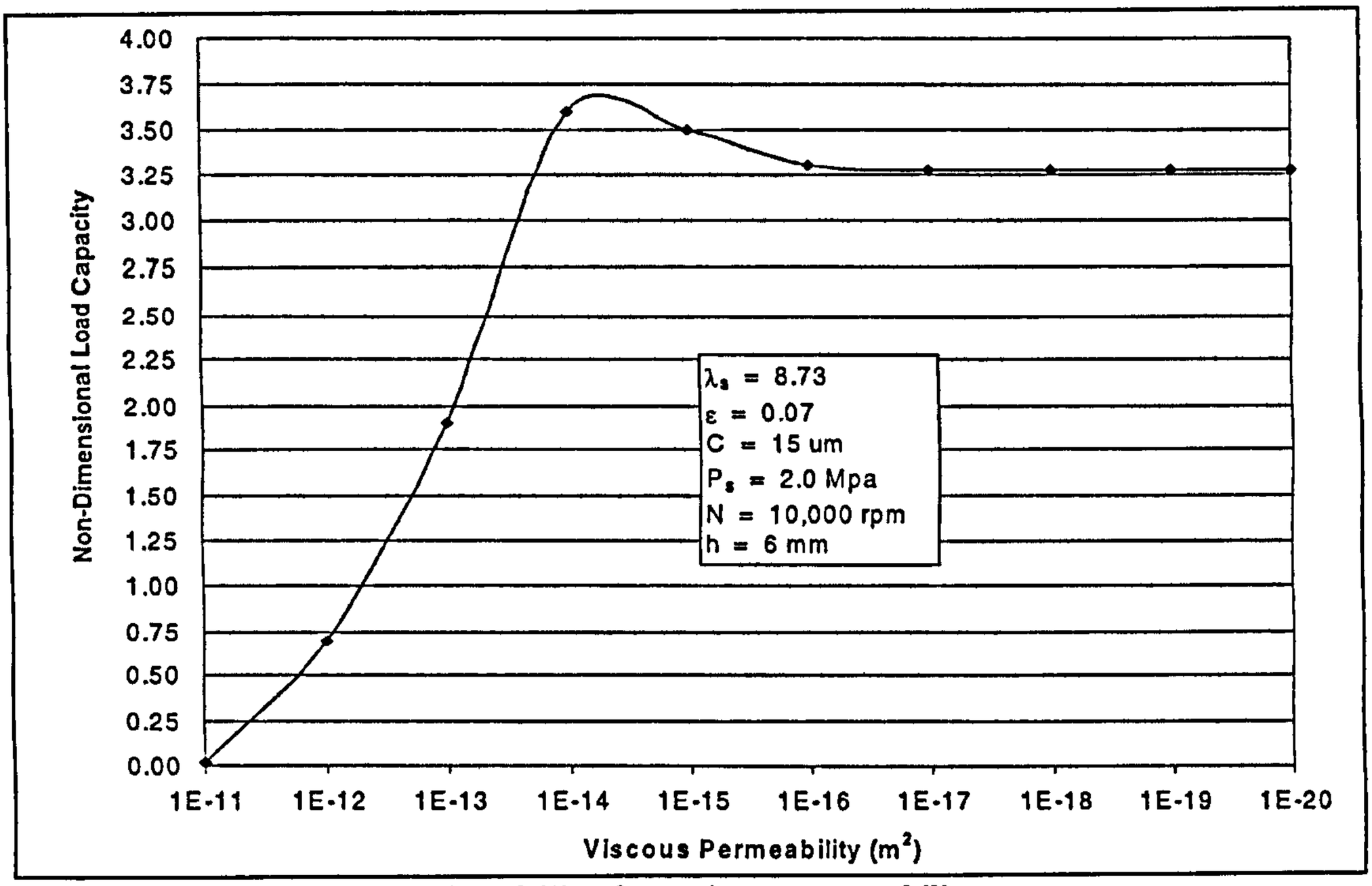

Figure 11-Almond's theoretical modelling for optimum permeability.

During performance testing, these bearings were lubricated with water, which in turn brought the following benefits:

- A lower viscosity than typical hydrostatic bearing oils, which in turn reduced the viscous friction and subsequent heat generation.
- Higher specific heat capacity than oil, making it easier to control the temperature of the bearing assembly and machine.
- Overcoming environmental concerns associated with the use of oils.

Specially-designed fully instrumented test-rigs were manufactured in order to measure the permeability of the ceramic bearings, as well as to measure some of the most important aspects of bearing performance such as bearing stiffness, fluid flow, temperature increase, friction losses, fluid film pressure and temperature maps; from static conditions and up to 14, 000 rpm.

2.3.1 Porous-ceramic water hydrostatic journal bearings: experimental performance

A comprehensive performance-testing programme for porous ceramic water hydrostatic bearings has been recently undertaken at Cranfield University [3]. This programme along with a direct comparison study against a conventional hydrostatic bearing with similar operating conditions; highlighted the following advantages of porous ceramic hydrostatic bearings:

- 66% greater stiffness than a comparable conventional oil hydrostatic bearing.
- A reduction of 62% in temperature rise when compared to a comparable conventional oil hydrostatic bearing of the same dimensions (Figure 12).
- Stability at speeds of up to 14, 000 rpm.
- The energy required to drive a spindle assembly was reduced by 72%.
- The pumping power requirement was reduced by 95%.
- The use of these bearings resulted in a cleaner and safer environment, through the elimination of oil.

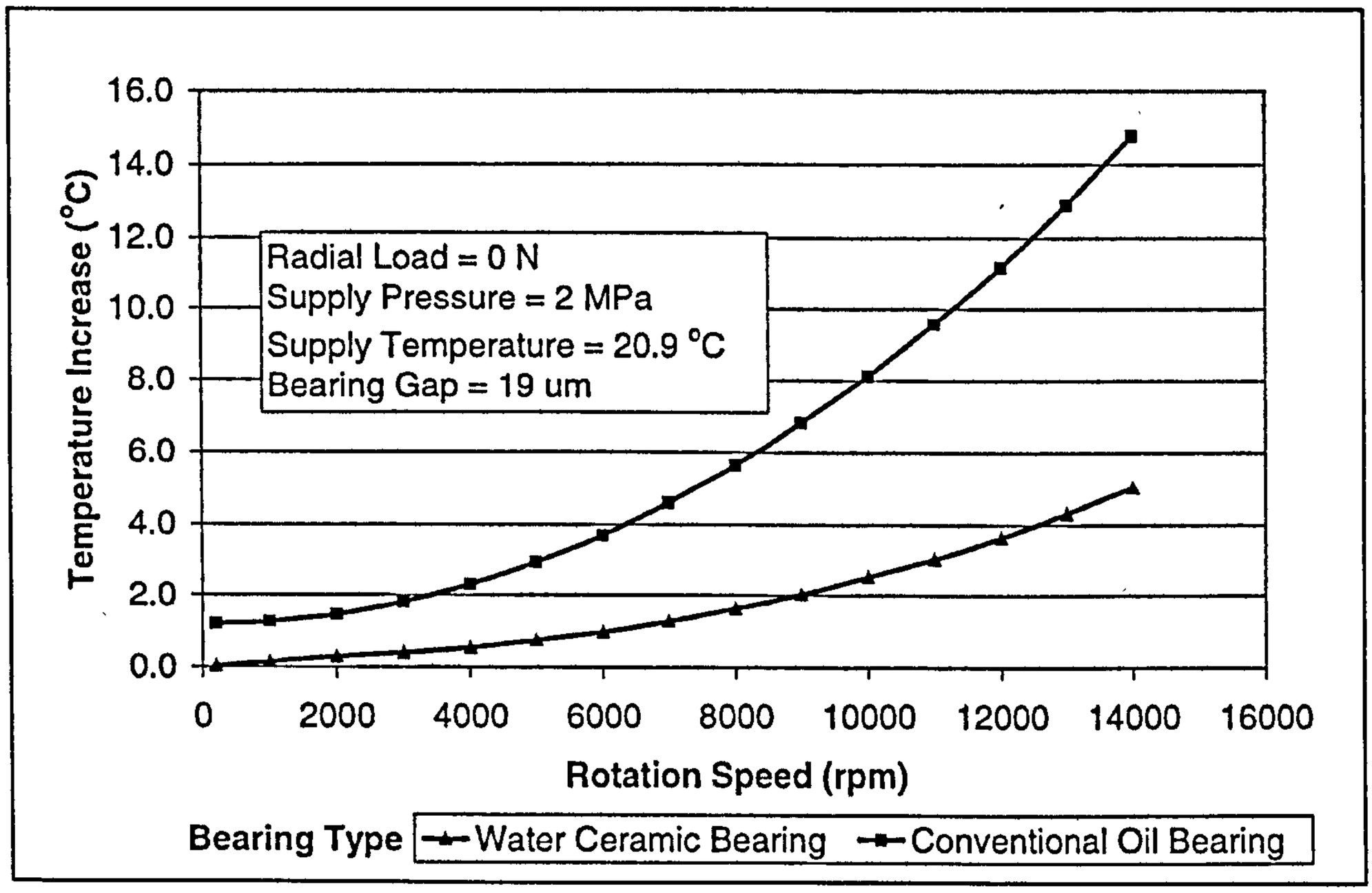

Figure 12-Almond's temperature rise results.

Interestingly, the results obtained by Almond in his research programme constitute the first experimental set of data concerning porous hydrostatic journal bearings. At the time of writing, their proper incorporation and the verification of the existing theoretical research based on these data, was still pending.

2.3.2 Porous-ceramic water hydrostatic journal bearings technology: current challenges

Within the context of the much needed bearing new and emerging-technologies, the advantages of porous-ceramic water hydrostatic bearings are numerous and are certainly significant. However, there are certain aspects of both manufacture and operation that might require a certain degree of development or improvement before they are completely embraced by precision engineers and machine-tool designers.

The current method of production consists of the vibration packing of powders followed by hot isostatic pressing (HIPing). This has proved to be successful for the production of 50mm ID x 50 mm long journal bearings. However a significant level of final machining is required and HIPing is a relatively expensive process. Also, it is difficult to process fine powders and avoid agglomeration which results in a non uniform permeability. The ability to use a range of powder sizes is important in order to control pore size and pore size distribution. In addition, it becomes more difficult to achieve uniform permeability as the size of the components increase [53]. Hence there is a need to establish an optimised alternative porous ceramic processing route that would enable larger and more cost effective bearings to be produced.

In addition, although water lubrication benefits are widely acknowledged, its use keeps meeting a certain scepticism because water is feared to promote corrosion within the spindle assembly and auxiliary equipment components. The addition of corrosion inhibitors, as recommended by Almond [3], require a thorough assessment as they might induce certain non-desired secondary effects, such as foaming or bacterial growth.

3 Review of techniques for producing porous ceramics

3.1.1 Introduction

In this chapter, several potential manufacturing techniques are reviewed, outlining their main features, advantages and disadvantages. The aim of this review was to find the elements within the available literature that would allow the ascertaining of each of the techniques' suitability for the manufacture of porous ceramic structures, with a range of porosities, pore size distribution and mechanical properties.

Selecting a fabrication method that is simple and inexpensive to use yet able to produce complex shapes is one of the keys to the successful manufacture of ceramics [54].

For the particular case of the present research project, there were a number of factors taken into account for the selection of the most advantageous fabrication method. From technical and industrial points of view, several requirements must be met:

- Journal bearing geometry attainment. Hollow cylinders of up to 90 mm in ID with a typically L/D ratio from 1 up to 2 and wall thickness of 10mm must be produced with relative ease.
- Ability to control porosity. Accurate control of porosity values must in turn yield adequate and accurate and consistent values of permeability, Young's modulus, etc. which may directly influence the bearing's performance.
- Repeatability.
- Cost effectiveness. Bearings must be produced at a lower cost than previously proposed manufacturing routes.
- Geometry and porosity control flexibility. The ability to tailor bearings to different dimensions and properties, as required by the machine-tool designer.

- Environmentally sound and safe. In line with recent manufacturing trends, the manufacturing technique must be safe and preferably should not produce residual toxic chemicals. It must also be as energy efficient as possible.

Some ceramic manufacturing techniques have already been investigated in previous research efforts at Cranfield University [3] [30] [31] that were concerned with the manufacture of externally pressurized porous ceramic bearings. These techniques, along with some other potential routes are outlined in the following pages.

3.1.2 Slip casting

The slip casting mechanism, processing and its applications to porous ceramic bearings have been extensively reviewed by Roach [31] in a parallel research project. These are not being repeated here. However, with the purpose of putting the slip cast processing technique into this research context, its main advantages and disadvantages are listed [55].

Advantages:

- Relatively low capital costs.
- Relatively complex shapes can be achieved.

Disadvantages:

- Limited production rate because of long settling and drying times.
- Difficulties in achieving close tolerances and relatively good surface finishes.
- Relatively short mould life. With use, the pores of the mould become increasingly choked; as a result, capillary forces decrease gradually. This not only increases moulding time but could also changes the quality of the castings produced.

During the course of his research, Roach also attempted the manufacture of a porous journal bearing of similar dimensions to the bearings produced in previous porous ceramic journal bearings research (50 mm ID, 62 mm OD), through *rotational slip casting*. Here, a split porous cylinder filled with slip (Al_2O_3-0.5 μm) was continually rotated for 24 h at 200 rpm until all the slip fluid was taken up by the mould material. The specimens were produced to a 'primitive' stage, suggesting that more work needed to be carried out to be able to reach an acceptable quality level.

From this trial, Roach noted that across the specimens' walls two ceramic layers could be distinguished. These he argues, 'mark the point where the rate at which the removal of water from the slip is no longer controlled by the capillary action of the mould, but instead by the powder deposited on the mould wall that the water must first pass through'.

There are also practical limitations to the approach used by Roach. The moulds are relatively large in size (160mm in OD needed to produce a 50mm ID journal). Proper process tuning might result in high rotational speeds of the moulds, which might be dangerous.

The successful manufacture of large (thin wall) ceramic tubes through centrifugal casting has been recently reported by Kyung *et al* [56]. Here, the slip (0.5 μm) was poured into a tubular steel mould and set to rotate at 2500 rpm for 20 minutes, followed by drying and sintering operations. Density is reported to be close to 100% of the theoretical value.

3.1.3 Injection moulding

Again, with the purpose of manufacturing porous ceramic aerostatic bearings, Roach [31] also reviews the mechanism and processing of ceramic injection moulding, successfully producing a number of ceramic thrust bearings. The main advantages and disadvantages of ceramic injection moulding are outlined [55].

Advantages:

- Offers the possibility of producing components of complex geometry.
- Large quantities.
- Very good surface finish and tight tolerances.

Disadvantages:

- High initial tooling costs.
- Slow binder removal, which may take more than a week depending on the binder content and the geometry of the component.
- It requires extensive trial-and-error procedures to determine the proper moulding conditions and minimize defects.

Roach reports binder removal times of around 24 hours for his porous ceramic thrust bearings (typically of 46mm in diameter by 6mm in thickness). The thermal debinding operation used heptane to facilitate the removal of the binder wax component.

In order to demonstrate the versatility of this technique, Roach also attempted the manufacture of small ceramic journals (25 mm ID, 25mm long and 5mm wall thickness) through ceramic injection moulding, successfully producing a small number of them. Debinding cycle times for these journal bearings were not reported. However, longer than 24 h debinding cycle times would be anticipated for the larger journal bearings required for the present research project.

3.1.4 Hot isostatic pressing (HIPing)

HIPing processing entails the simultaneous application of elevated temperature and isostatic pressure on the surface of a part or the sealed capsule of a powder body. The pressure media is usually an inert gas, typically applied at 500 to 3000 bars, which is pumped into a pressure vessel.

Near net shape of complex geometry parts can be achieved by HIPing. Typically, for conventional metal-powders HIPing, the capsule is made of sheet metal. In the case of ceramics processing, powders are encapsulated in glass containers. Ceramics can be 'HIPed' also by *Sinter-HIPing* [57] processing. Here, already sintered ceramic parts, typically from 92 to 96% of the theoretical density, are further sintered via un-encapsulated HIPing, in order to reduce closed porosity. These arrangements however, yield parts with very low porosity which are therefore inadequate for the manufacture of porous ceramic bearings. An alternative HIPing process, *capsule-free HIPing* [58] has been investigated and successfully applied to the manufacture of porous-ceramic bearings by both Kwan [30] and Almond [3].

Capsule-free HIPing of porous ceramics

The capsule-free HIPing technique differs from the conventional HIPing in that the powders, in the form of a green compact, are not held in a sealed container, but rather a porous one or none at all (provided that the green compact has sufficient strength to allow handling and shape retention during sintering). This allows the pressuring gas to penetrate the pores throughout the process. The high pressure gas within the pores serves two purposes. Firstly, the powders are sitting in an isostatic environment, and as such the points of contact between particles are subjected to the same isostatic pressure. As this pressure is normally much higher than atmospheric (about 2000 bar), the increase in contact pressure enhances surface diffusion during sintering, resulting in an improved neck growth between particles and hence mechanical strength [59]. As sintering progresses, however, the presence of high pressure gas within the pores helps to prevent their complete closure, bringing about the reduction in closed porosity and improving consistency in open porosity.

However, HIP processing does posses certain disadvantages. Firstly, there is a high capital cost incurred in acquiring the machine and its components. Operational costs are also relatively high because of the low throughput (relatively slow consolidation cycle) and labour intensive process. Encapsulation, leak testing and vibratory packing are both time-consuming and critical operations.

A recent economic assessment of the HIPing powder process [60] suggests that larger pressure vessels as well as shortening the consolidation cycle would improve the overall manufacturing costs of HIPing. Over time, HIPing vessels have indeed increased dramatically in size, as noted by Mashl [61]. This practice however, could be hazardous as the stored energy in HIP vessels under pressure is very high. Safety codes for the design and manufacture of vessels must be strictly followed.

From a processing point of view, inhomogeneous densification can occur in large and complex geometries at the HIPing stage, if the temperature and pressure are not uniform over the dimensions of the sample, leading to undesirable shape changes [62].

3.1.5 Ceramic extrusion

Extrusion is shaping by forcing a cohesive plastic material through the orifice of a rigid die [63]. A lineated extrudate with a controlled cross section is formed which is then cut to length to form a product. In terms of the equipment used, there are three basic extruder categories: ram or piston, pug mill-auger and screw fed plasticator. These, as well as further details of each of the processing techniques are discussed by Ruppel [64].

In general, extrusion is a very productive forming technique that is used for the mass production of tubes, rods, honeycombs and profiles of numerous shapes. However, extrusion has certain limitations and cannot be used to fabricate all products, being best suited for fabrication of shapes that are of constant cross section and can be linearly formed.

Conventionally, large amounts of polymer binders and organic additives are employed to impart suitable flow properties and wet strength to the ceramic paste for extrusion. Presumably, the ejected extrudate must have adequate strength to survive handling without slumping or deformation.

For ceramics extrusion, the characteristics of the final fired product usually dictate the choice of raw material. Particle shape and particle size distribution profoundly affect packing. Thus, by altering particle packing, the product density is also altered. In the particular case of extruding porous products, a distribution of sizes that does not pack closely is selected [65]. Other factors, such as the mechanics and interactions between the ceramic filler and the binder solvent can also control particle packing, or density [64]. For instance, the extrusion of ceramic membranes with tubular geometry has been reported by De Jong *et al* [66]. Here, thin porous ceramic tubes with an outer diameter of 14 mm and lengths of up to 1200 mm were successfully extruded by mixing alumina powders with particle sizes of 25, 0.4 and 0.02 μm; using carboxymethylcellulose as the binder. Porosity is reported to range from 35 to 40%, while average pore-size and permeability are reported at 6μm and 30 ($l/h \cdot m^2 \cdot bar$) respectively.

The tubes produced by De Jong *et al*, however, are far too thin to concur with the requirements for the present research project. Evidently, further development would be necessary to bring this technique up to the required process capability. This implies running a significant number of trials in order to establish the optimum processing conditions for every potential bearing geometry proposed. This procedure is often long and might be expensive as well [67].

Although De Jong does not report significant defects or process related problems, there are certain known limitations for the processing of large extruded parts. For example, during the sintering stage, large or long parts may need to be fixtured in order to maintain their straightness, roundness and to cope with large dimensional shrinkage [64]. Another problem that might arise with larger particle-size distribution pastes is a tendency for phase separation during extrusion [65].

In practice, some of the processing difficulties encountered in ceramics extrusion include: uniform dispersion of particulate powder into the viscous binder, uniform distribution of moisture through the matrix and the elimination of hard agglomerates. Further processing problems might occur at the drying and sintering stages. For

example, solvent/binder removal might form cracks and undesired pores if they are not burnt-out properly. Also, large amounts of shrinkage can disrupt dimensional stability, causing warpage.

Other aspects to be considered are the high investment costs related to the acquisition and tooling of the equipment.

3.1.6 Polymeric sponge method

In the polymeric sponge method [68], water, binder (usually potassium or sodium silicate) additives and fine ceramic particles (typically <45 μm) are mixed to prepare a ceramic slurry. The slurry is then forced to penetrate a sponge. After infiltration, the slurry excess is removed to be followed by a drying operation (above 100 °C, for up to approximately 6h). The sponge and organics are removed in a subsequent burnout operation that takes place above 350 °C for approximately 6 h. A sintering operation, finalizes the processing. The pore size of the sponge determines the pore size of the final product. Sponge materials used include polyurethane, cellulose, polyvinyl chloride, polystyrene and latex.

Ceramic bodies of very high porosity, ranging from 70 to 90% [69], are obtained with this method. As a consequence, ceramics obtained through this route are not as strong as might be required for porous ceramic journal bearings.

3.1.7 Direct consolidation techniques

There is a new family of forming techniques in which ceramic slips are forced to consolidate in an impermeable mould referred as *direct consolidation techniques* [70]. In these newly developed techniques, the particle structure of the slip is consolidated without powder compaction or removal of liquid, resulting in ceramic bodies with very good homogeneity and improved properties. Typically, direct consolidation techniques, do not require specialised equipment and are relatively simple processing methods, where near-net shape manufacture is emphasised. *Gel-*

casting, hydrolysis-assisted solidification, direct coagulation consolidation as well as *starch consolidation* form part of this new family. These techniques are briefly reviewed below:

Gel casting

In gel casting, a concentrated slurry of ceramic powder in a solution of organic monomers is poured into a mould and then polymerised in situ to form a green body. The gelation process is triggered by the action of a catalyst added to the slurry before casting [71]. The green body is then demoulded, followed by air-drying, binder burnout and sintering operations. The technique is simple and inexpensive, it is also flexible, and allows the production of complex geometries of very good green strength. However, there are certain concerns regarding the toxicity of the monomers employed.

Recently, some research has been undertaken to develop low toxicity gel-casting systems [72]. Although, this has improved the toxicity of the technique, the monomers used in this technique can still be harmful. Another disadvantage of the gel-casting technique is the high degree of shrinkage during densification, typically of around 23%, which might result in distortion in the fired parts.

Direct coagulation consolidation (DCC)

In the direct coagulation consolidation technique, an aqueous electro-statically stabilised ceramic suspension, free of agglomerates and of low viscosity is prepared. This suspension is then cast into a mould where it coagulates to form a stiff wet green body. Coagulation is achieved by changing the pH of the suspension and/or by creating salt directly inside the suspension using a controlled time-delayed reaction [73]. Coagulation takes place at ambient temperature and typically takes from 10 to 90 min. In general, coagulation time is a function of the temperature and the enzyme concentration. After coagulation the formed body is dried and then sintered to finish the processing. Near net shape of complex shaped parts can be achieved through DCC.

Organic additives are used (less 0.5 wt %). Typically, urea and urease are used as the substrate and as the catalyst respectively, generating ammonia as a result of the chemical reaction.

Hydrolysis assisted solidification (HAS)

The process is based on thermally activated hydrolysis of aluminium nitride (AlN) powder added to a highly loaded ceramic suspension. During the hydrolysis of AlN, water is consumed and ammonia is formed, which in turn may increase the pH of the suspension [74], resulting in coagulation of solid particles; both effects result in a rather fast solidification of the slurry within the mould.

Typically, the slurry is cast or injected in a heated mould. Hydrolysis is accelerated between 45-60 °C. Coagulation times, which is a function of the solids loading and AlN addition, ranges from a few seconds to a few minutes. After consolidation the ceramic body is demoulded, dried and sintered.

Drawbacks of this technique [75] include limited time and temperature stability, heat transfer during solidification and the need for additional equipment to collect and neutralise ammonia.

Direct consolidation techniques advantages and disadvantages

Rak [75] has outlined and tabulated the main advantages and disadvantages for some of the newest ceramics manufacturing techniques, and these have been reproduced here in Table 4, for the direct consolidation techniques.

Process	Advantages	Disadvantages	Commercialisation	Remarks
Direct coagulation casting	Excellent rheological properties, no size/wall thickness limitations	Expensive additives, poor green strength	Yes	Solidification by coagulation, excellent mechanical properties of final products
Gel-casting	Widely acceptable, no size/wall thickness limitations	Low solidification rate, low green density	Yes	Solidification by gelling, used for dense and porous ceramics
Hydrolysis assisted solidification	Simple, fast, no size/wall thickness limitations, high green density	Poor green strength, additional equipment required to collect and neutralise residual ammonia	Yes	Solidification by hydrolysis

Table 4-Direct consolidation techniques main benefits and drawbacks; adapted from reference [75].

3.1.8 Manufacture of porous ceramics by the starch consolidation technique

Another member of the direct consolidation techniques is the starch consolidation technique (SC) [70]. This technique is based on the gelling ability of starches in water. By mixing ceramic powder and starch in a water suspension, pouring it into a mould and heating it up to 60-80 °C, the starch particle will swell by water uptake. This swelling act removes water from the slip causing the ceramic particles to stick together and, consequently, consolidate into a solid body. As the starch granules swell they also act as a binder adding strength to the consolidated body which enables demoulding prior to drying. After burnout of the starch and sintering of the ceramic matrix a material is obtained with a porosity corresponding to the original amount, shape and size of the starch particles. Lyckfeldt reports porosities ranging from 23 to 70% after sintering, depending on the starch amount and characteristics. Microstructure studies conducted, report pores to be spherically shaped ranging from 10 to 80 μm in diameter [70].

From a processing point of view, the greatest advantage of the SC technique over the previously described techniques is the systematic approach for controlling the microstructure of the ceramic. This is achieved by controlling the original slip composition regarding the total solids loading and the amount of starch present, and also by the degree of densification attained during the sintering stage.

An interesting aspect of starches is that they are environmentally friendly. Starches are extracted from seeds of cereal grains (corn, rice, etc.), certain roots (potato, tapioca) and also from the pith of the sago palm. Starches consist of granules with a size in the range of 5 to 100 μm.

Another advantage of starches is that they are very cheap, and because they are widely used as components and/or processing aids in the manufacture of adhesives, textiles, paper, food, pharmaceuticals, and building materials, they are readily found.

According to the literature reviewed for the present research project, the first recorded use of starch for ceramics processing is in a paper presented by Bonekamp [76] in 1989. Here, potato starch was used as the pore former for a slip casting experiment. Bonekamp observed that, by increasing the amount of starch, the specimens' porosity increased. Lyckfeldt [77] presented another paper in 1994, apparently unaware of Bonekamp's work, where potato and maize starches were used for pore forming and control of porosity for the experimental slip casting processing of thermal insulation materials. Starch as pore former for dry pressing manufacturing of ceramic samples has also been reported in 1996 [78].

The use of an impermeable mould on a slip (alumina-starch) casting process and the thorough characterisation of the entire processing route were first reported by Lyckfeldt [70], effectively creating the starch consolidation technique. A few SC related papers have recently appeared in specialised publications. The purpose of these papers has been mainly to report on the technique characterisation, development and improvement [79] [80] [81] [82] [83] [84] at laboratory level. A few other papers, based on experimental results, report on potential applications for the SC technique, such as medical implants [85] and membrane manufacture [86].

However, at the time of writing, no specific tailored applications have been tackled and/or reported yet. It is also worth noting that in all published work the alumina particle size has been limited to submicron levels (0.5 and 0.7 μm).

Further to the already described advantages of the SC technique, and as result of a potential joint research venture between Cranfield University School of Industrial and Manufacturing Science and Industrial Research Ltd (New Zealand) two ceramic bearing samples were produced by the SC technique. One of them in the form of a disc, 50 mm in diameter and 7 mm in thickness, and the other in the form of a journal bearing of 76 mm ID, 75 mm in length and 5 mm in wall thickness. Permeability measurements performed [31] on the disc proved to be very near the range of interest for porous ceramic bearings.

Although, the research venture did not consolidate at the end, the ceramic specimens produced proved the versatility of the SC technique and confirmed it as a potentially viable technique for manufacturing porous ceramic journal bearings, as this technique complies with the majority of the requirements previously noted.

The work developed by Lyckfeldt [70] for the SC technique would eventually form the foundation for the manufacture of porous ceramic bearings for the present research project.

Porous-ceramic bearings manufacture by the starch consolidation technique

The present review has been focused towards processing techniques in which the ability to comply with the project processing requirements was at least presumed. The great number of new processing techniques constantly being developed and the improvement of those already established are not overlooked. However, some of them have not reached the level of development to enable them to sufficiently control the level of porosity and/or pore size. For some of the other techniques, hollow cylinder geometry attainment is intrinsically difficult, because of the nature of their

principle. A good example of this is *tape casting* [55], which is a more adequate technique for the manufacture of flat artefacts.

The potential suitability of the starch consolidation technique (SC) has been proven already, as noted by Roach [31] and detailed in a previous section of the present review. This technique's versatility, as well as the clear and systematic way in which the level of porosity and pore size are controlled was of particular interest for the manufacture of externally pressurized porous-ceramic bearings. The subsequent incorporation of alumina size powders of 1, 2, 3 and 4 μm, as well as the tailoring of the processing conditions for specific applications for porous ceramic bearings, would demonstrate the originality of this research project; while broadening the scope for the SC technique.

4 Experimental procedures

4.1 Manufacture of Bearings by starch consolidation (SC) technique

As a result of a critical assessment of porous-ceramic manufacturing techniques, reviewed in the previous chapter, the starch consolidation (SC) technique was identified as the most feasible route for the manufacture of porous-ceramic hydrostatic bearings.

Figure 13 illustrates the procedure followed in the processing of porous-ceramic hydrostatic bearings for the present research project. This procedure is also described in the following sections.

Material requirements

In the first instance, the material requirements were set to be those found to be optimum in previous research [3], for the design of an ultra-precision porous hydrostatic journal bearing of 50 mm ID by 50 mm long and a 6 mm wall thickness. These requirements are:

- A permeability value of 1×10^{-14} m^2.
- A fractional porosity of 20%.
- A pore size of 3μm.

A further advantage was that specially-designed fully-instrumented test-rigs from previous research could then be used to measure permeability, as well as certain aspects of bearing performance, such as static and rotational stiffness and temperature rise.

Previous theoretical analyses and experience [3] [30] [31] have acknowledged a common permeability target for practical porous-ceramic hydrostatic bearings applications of around 1 x 10^{-14} m^2. Hence, this value has been taken as the permeability target. In this respect, nonetheless, a well defined range of values around this target is also considered important, in order to provide for specific design needs.

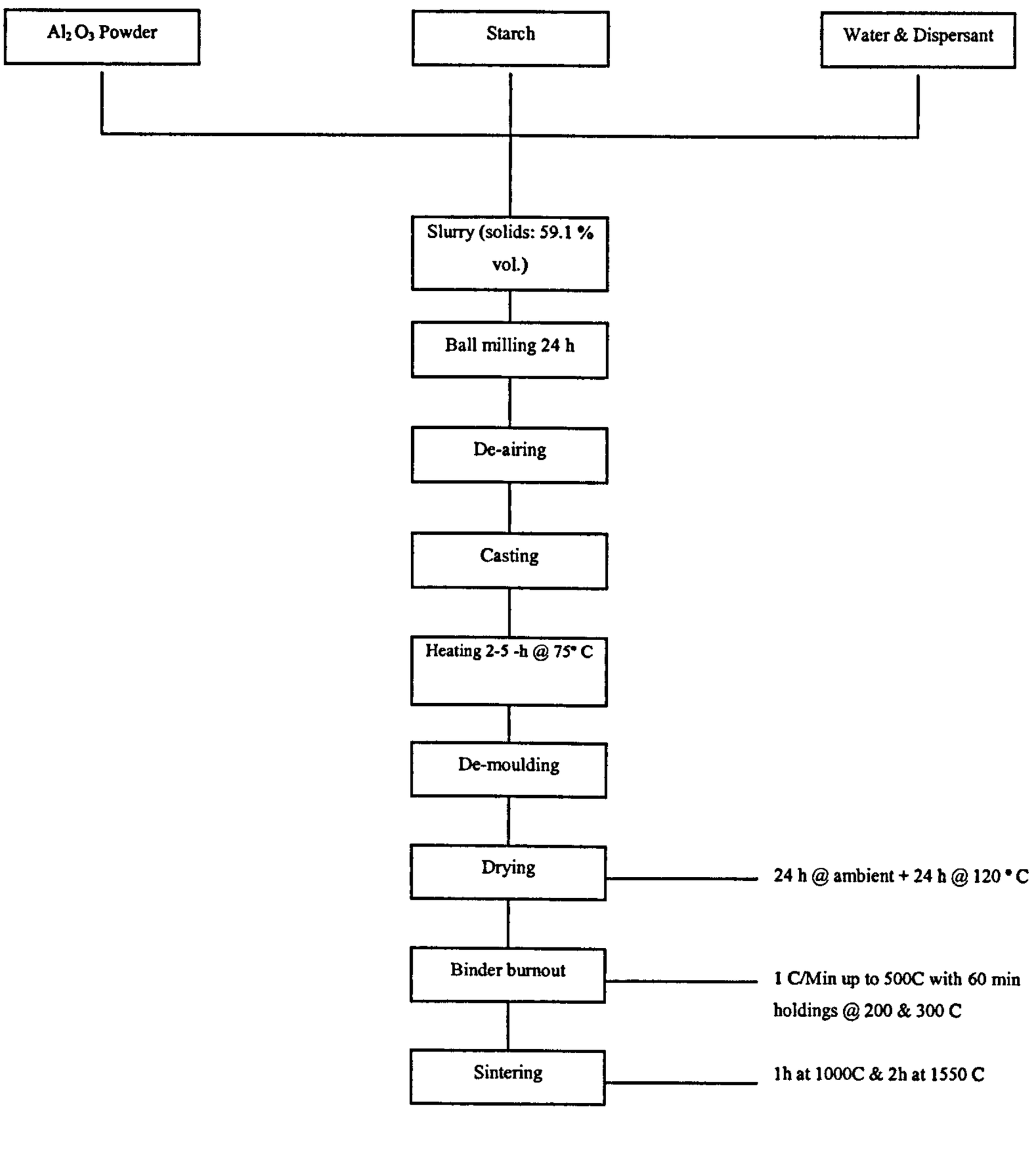

Figure 13-Current research's starch consolidation technique flow chart.

4.1.1 SC Processing experimental procedures

Initially, the procedure outlined by Lyckfeldt [70] was adapted and followed, achieving the successful manufacture of discs (thrust bearings) of 46 mm OD by 6 mm in thickness. Besides being a relatively simple geometry, discs could be produced using moulds readily available from previous research programmes [30] . The raw materials, including alumina powders of various sizes as well as maize starch were also readily available from previous research projects within SIMS. Preliminary permeability measurements conducted on these discs using an existing test-rig [30], BS 5600 [87] compliant; as well as non destructive Young's modulus measurements [88] confirmed this technique's applicability for porous bearings applications. This subsequently led to attempting the manufacture of a hollow-cylinder (journal geometry).

Slip preparation

Ceramic slips were prepared with alumina mono-sized powders. All powders, including starch were dried at 120°C for 24h before the slip preparation.

The total solids loading was set to 59.1 volumetric %; as this was the highest solids loading achieved by Lyckfeldt [70]. At this level of solids, Lyckfeldt's experiments proved consistent throughout their processing, yielding controlled porosity characteristics as well as the highest density values. In addition, higher viscosity levels were expected; and therefore lower levels of shrinkage and deformation.

Based on maize starch and alumina densities of 0.56 and 3.98 g/cm^3 respectively, an excel spreadsheet was developed for the calculation of the slip formulation for a given amount of alumina and/or starch content. In order to facilitate the slip preparation and the overall SC processing, a form expressing the required raw materials proportions in grams could be generated and plotted from this spreadsheet. A copy of this form can be found in appendix 2.

Once the slip's starch content and alumina size was defined, the required raw materials were weighed and poured into a 1-litre ball-mill pot. The slip was then ball-milled for 24 h at 66 rpm using cylindrical grinding media in various sizes (∅ 15.5, 7.5, 5 mm). Then the slip was de-aired.

De-airing was implemented in the SC processing to avoid the entrainment of air, which formed undesirable air 'bubbles' within the consolidated ceramic body. This operation was conducted in a vacuum oven with only the pump running (thermostat off), and carefully opening-shutting of the oven's inlet valve to facilitate the collapsing of air-ceramic slip bubbles. De-airing times were restricted to a maximum of 10 min to avoid the ceramic slip particles settling; although in practice, most of the observed air bubbling collapsed in about 5 minutes.

Experiments with different alumina sizes and starch vol. % contents

In previous SC research [70] [83] [81], alumina powders have been restricted to submicron levels (0.5-0.7 μm). However, it has also been suggested that [70], the characteristics of starch consolidated ceramic structures such as porosity and pore size distribution are directly related to the amount of starch in the slip as well as the degree of densification achieved during the sintering stage. Therefore, by incorporating a range of alumina particle sizes, achieving different levels of particle packing and therefore different levels of densification during the sintering stage, it should be possible to broaden the range of applications of the SC technique.

In order to assess the effects of the alumina size and the amount of starch, an experiment was undertaken, where a number of ceramic slips was prepared by varying the alumina particle size. Alumina sizes included were 0.5, 1, 2, 3, 4 and 7 μm. A second variable was the starch amount added to the ceramic slip, and this was varied in 10% vol. increments ranging from 10 to 60%.

The experimental response was assessed by measuring the bearings' permeability, pore size distribution, Young's modulus, density, shrinkage as well as rheological studies.

Table 5 shows typical ceramic/starch slip formulations with varying volumetric starch % contents for a fixed alumina quantity (500 g).

	Starch volumetric content (%)					
Material	10%	20%	30%	40%	50%	60%
Alumina	500	500	500	500	500	500
Starch	7.816	17.58	30.15	40.901	70.351	105.527
De-ionised Water	96.60	108.675	124.20	144.901	173.881	217.351
Dispex A40	2.031	2.070	2.12	2.187	2.281	2.422

Table 5-Typical ceramic-starch slip formulations (grams) for varying volumetric starch % contents, based on a 59.1 volumetric % (total solids loading) for 500 g of alumina.

The ceramic and organic materials used throughout this research project are listed in Table 6. Datasheets for these materials can be found in the appendices.

Material	**Producer**	**Particle size average (μm)**	**Surface area (m^2/g)**
Maize Starch 03401	CERESTAR	10-20	--
Dispersant Dispex A40	Allied colloids ltd	--	--
Al_2O_3 (RA 45E)	ALCAN	0.5	7.5
Al_2O_3 (RA 7)	ALCAN	1	2.9
Al_2O_3 (RA 10)	ALCAN	2	2.2
Al_2O_3 (RA 15)	ALCAN	3	3.7
Al_2O_3 (RA 12)	ALCAN	4	1.8
Al_2O_3 (MA4LS)	ALCAN	7	0.7
De-ionized water	--	--	--

Table 6- Raw materials used in the slips' formulation for the manufacture of porous ceramic bearings.

The range of powder sizes investigated here paralleled those previously used for porous ceramic hydrostatic bearing investigations [30] [3] [31]. The actual powder batches used were the same as supplied and used previously, and at that time particle size measurements were made. This work was undertaken on a micrometrics 5100 Sedigraph machine. Details of the procedure can be found elsewhere [30]. Any

reference to a powder size contained within this research programme refers to the nominal powder size as specified by the manufacturer.

Figure 14 shows maize starch particles used for the present research.

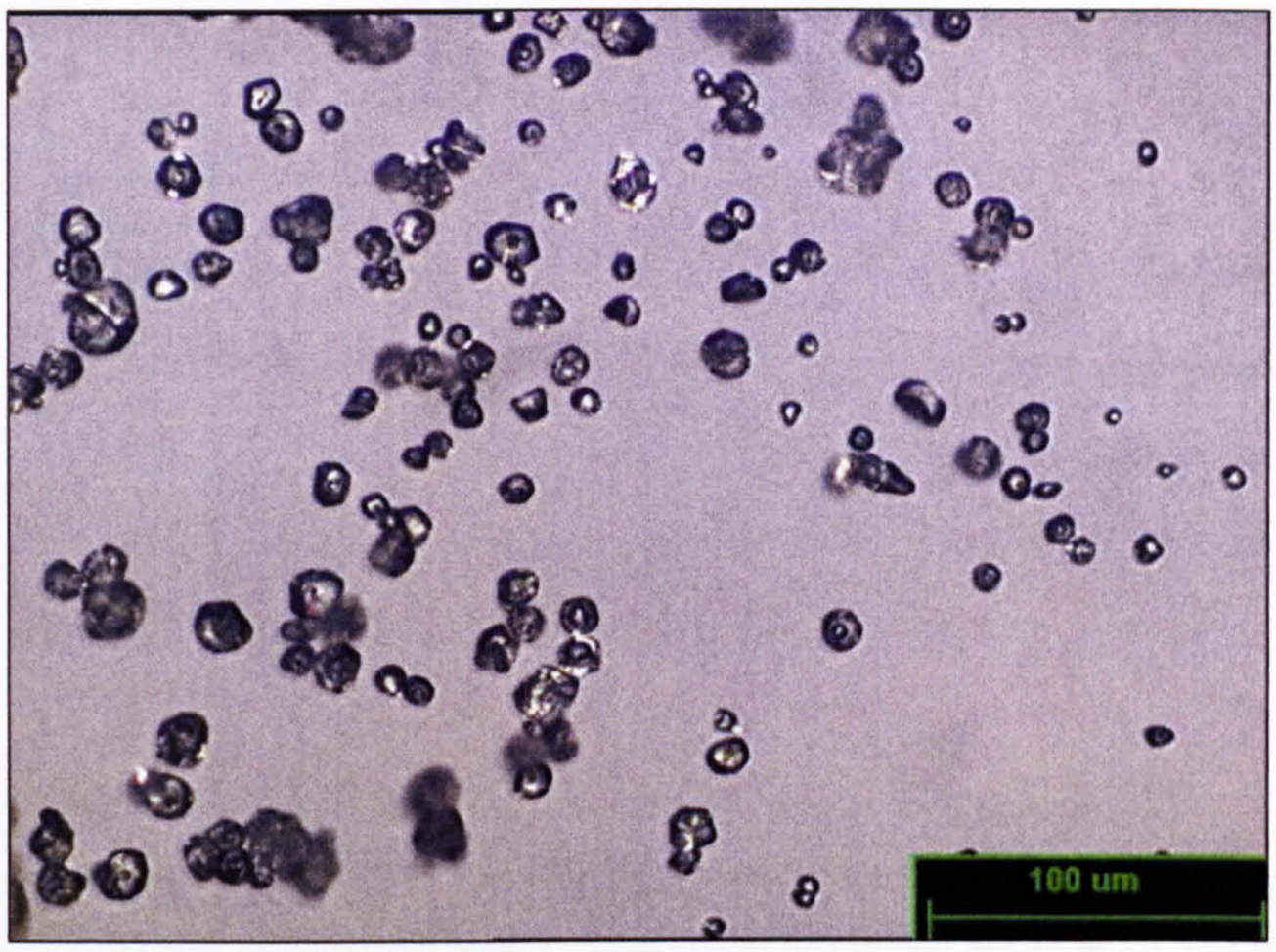

Figure 14-CERESTAR maize starch 03401 particles, used in the present research.

Rheological measurements

Rheological measurements were considered as a quality-control tool, for monitoring and controlling the consistency and behaviour of the alumina-starch slip.

These measurements were conducted using a controlled stress *CVO Bohlin instruments* rheometer; with a cup and bob configuration and a pre-set gap of 150 μm. The experimental conditions were similar to those described and used by Lyckfeldt [70]. Steady shear measurements of viscosity at various shear rates ranging from 1-500s^{-1} and at a constant temperature of 23°C were conducted. Before measurement, all slips were exposed to a pre-shearing at 500s^{-1} for 1 min, followed by a 30 s rest.

Experiments with journal geometry

Discs are relatively simple shapes. In going from discs to a journal geometry some problems were anticipated. In order to investigate these, a relatively simple steel mould was designed, based upon the geometry used by Almond [3], 50 mm ID, 50 mm long and a 6mm wall thickness.

On the initial trials, de-moulding became a problem as the journals stuck to the mould core which resulted in large cracks. The high temperature that was achieved by the solid steel core was believed to be the main cause, as the ceramic body looked to be 'over dried'. This problem was overcome by machining a hole through the mould core centre and lids, enhancing the heat transfer.

Figure 15-Typical 4-part aluminium mould for the manufacture of journal bearings.

A second optimized mould made of aluminium was manufactured. The new mould had tapered walls (2˚) to facilitate the ejection of the casting. Shrinkage factor values were calculated (see below) and taken into account for the mould dimensions.

As a result of aluminium's higher thermal conductivity, forming times were reduced by 33%. In addition, aluminium is of lower density than steel, making handling of the mould during processing easier. Aluminium was chosen as the mould material over alternatives such as glass or plastic because it possesses good strength and machinability. Figure 15 shows a typical aluminium mould for the casting of journal bearings. Typical mould detail drawings are shown in appendix 1.

Mould preparation

Prior to casting, the mould walls were spay-coated with a non-silicone release agent. In addition, a small amount of white silicone was applied on the mould assembly's mating surfaces, in order to avoid slip leakages.
A Datasheet for the release agent used is shown in appendix 2.

Once the forming stage was finished, moulds were washed with water/soap. If necessary, moulds were sand-paper polished.

Forming

The slip is poured into the moulds and then heated in an air-circulating oven at 65-75 °C; forming times varied from 2 to 5h depending on the slip amount and size of the component. During this stage, the mould's lid was kept on, in order to minimise the evaporation of water before and during solidification.

Once consolidation occurred, the bearings were hard enough to be de-moulded without any major deformation.

De-moulding

The de-moulding of discs was easily achieved. However, the de-moulding of journal bearings presented some challenges.
The most critical step was the removal of the mould's core. This needed to be accomplished without damage and before shrinkage on of the part occurred. De-

moulding jigs were devised to facilitate the removal of the core and the ejection of the bearing.

The most successful procedure for the de-moulding of journal bearings proved to be the following sequence (Figure 16):

i. Removal of the mould's lid and base.
ii. Locating the core ejector jig.
iii. Core removal. At this stage, because of the tapered mould walls, the mould-casting was turned upside-down. The core is then ejected by thrusting it against the core ejector jig and the casting. This step of the procedure was conducted with the aid of a hydraulic jack assembly press; as this provided a mechanism for the control of the ejecting force; and hence avoided deformation.
iv. Casting removal. Once the core is removed, the casting is 'pushed' out of the mould's sleeve, using a casting 'pusher' jig. This step is again carried out with the aid of the hydraulic jack assembly press.

Figure 16- De-moulding procedure sequence. From left to right: 1-lid and base removal, 2-core removal, 3-casting ejection, 4-completed procedure.

Drying

The first samples dried according to the Lyckfeldt scheme (at 120°C for 24h immediately after de-moulding); cracked inevitably. The high water content in the mixture was believed to be the main cause. In order to overcome this, reducing the water content in the slip mixture was attempted. However this was not achieved, as the slip invariably solidified at de-airing. The alternative was to devise a different way of drying the ceramic bodies. This was accomplished by letting them dry at ambient temperature until they had lost a great percentage of their moisture. Typically, this took about 24h and it was determined by weighing the discs every 8h, accounting for a weight loss of approximately 8.5-18 % depending on the starch content. The samples were then dried for 24h at 120 °C, in an air-circulating oven.

Binder Burnout and Sintering

Usually, the furnace processing step was carried out by integrating the burnout, pre-sintering and sintering operations. The starch was burned out at a slow temperature rate (1°C/min) up to 500°C, with holdings for 1h at 200 and 300°C. Pre-sintering and sintering were conducted at the same temperature rate for 1h at 1000°C and 2h at 1550°C respectively.

A Pyrotherm box furnace, fitted with a Eurotherm 818 controller was used for this part of the process. The temperature's top limit for this furnace was 1550 °C. Throughout this research's experimental runs, the sintering temperature was kept constant at this value; as this ensured the maximum densification achievable for the ceramic matrices produced.

Figure 17 shows the sintering profile employed for the present research project.

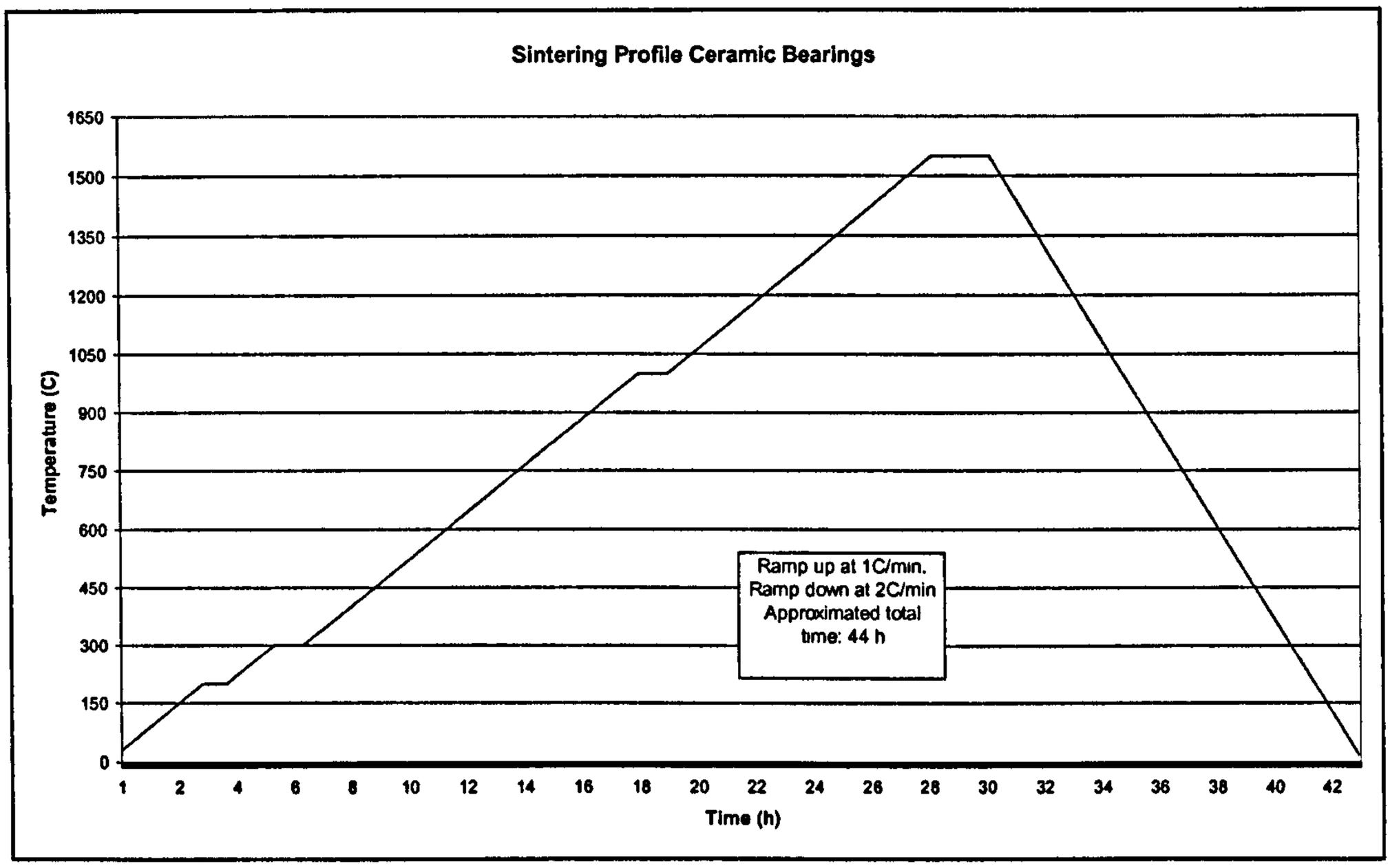

Figure 17- Sintering temperature profile for the manufacture of porous ceramic bearings.

Linear shrinkage

Ceramic round bars were produced in order to calculate the fired linear shrinkage, in accordance with ASTM C326-82 [89]. The purpose of this experiment was to obtain values of shrinkage under the various processing conditions to enable the proper determination of the moulds' dimensions, so as to produce a predetermined size of the fired component.

These round bars were 25 mm in diameter by 120 mm in length. Shrinkage reference lines 100 mm apart were marked. After drying the bars, the distance between the lines was measured to the closest 0.1 mm (L_p) with a digital vernier. The samples then continued their processing in accordance to the procedure outlined in Figure 13. After firing, the distance between the reference lines was measured (L_f) and recorded.

The firing linear shrinkage was calculated as a percentage of plastic length as follows:

Equation 7

$$S_t = \frac{L_p - L_f}{L_p} \times 100$$

St	total linear shrinkage (%)
Lp	plastic length of specimen (mm)
Lf	fired length of the specimen (mm)

Grinding of bearings

Although bearings were produced to near net shape, they still required some degree of grinding to achieve final size and geometry.

Diamond-grinding operations were carried out by a ceramics specialist, under specifications laid down in previous research. Further details can be found elsewhere [3].

4.2 Porous-ceramic bearings properties measurement

4.2.1 Density & porosity measurements

Density measurements on alumina-starch sintered journals and discs have been conducted via a modified version of BS EN ISO 2738:2000 [90]. This technique is based on the Archimedes' principle and involves weighing the porous samples in three different conditions: dried, fully water impregnated while suspended in distilled water, and finally free-standing fully water impregnated.
This method was preferred over the simpler mass/geometry method because, in addition to being more accurate, it also provides more information of the porous structure properties, such as open and closed porosity.

The modified BS version was developed at Cranfield University in a previous research effort [30], specifically to address the shortcomings in the BS standard in relation to porous alumina bearings. Two changes resulted, firstly the choice of oil for impregnation was rejected in favour of deionised water, and secondly, the vacuum degassing of the sample and impregnation of liquid procedure was changed.

The use of oil to prevent corrosion was not necessary for ceramic specimens. In addition, alumina has a good affinity with water, and as such, improved wetting was expected.
The changes to the vacuum degassing stage were found necessary due to incomplete impregnation of the samples, leading to incorrect density measurements. The solution was to vacuum degas the sample and liquid at the same time, until no further bubbling was seen, then letting the degassed bearing enter the liquid. The surface tension effect was then minimized, leading to full penetration of the pores upon re-pressurisation to atmospheric pressure. This modified procedure is reported to be 29% more accurate, in terms of impregnation, than the standard procedure. Further

details of this modification as well as its theoretical justification can be found in Kwan's [30] thesis.

In order to ensure consistency, the following procedures were observed:

- The specimens were dried at 120°C for 24h before testing.
- Vacuum evacuation time was set to 15 minutes, longer if required (until no bubbles were seen).
- All the weighing was carried out on a calibrated Sartorious Type 1712 balance, capable of resolving down to 1μg.

The weighing part of the procedure can be summarized as follows:

1) Dry weighing, obtaining m_2.
2) Full impregnation-water suspended weighing, to obtain m_w.
3) Full impregnation-free standing weighing (excess water wiped off), to obtain m_3.

From this set of data, and taking into account water's density (ρ_w), the test-piece bulk density, and open porosity were calculated:

Equation 8

$$B = \frac{m_2 \cdot \rho_w}{m_3 - m_w}$$

Equation 9

$$\xi_o = \frac{m_3 - m_2}{m_3 - m_w} x100$$

B	bulk density of the test piece (g/cm^3)
ξ_o	open porosity percentage (%)
m_2	mass of the dried test piece (g)
m_3	mass of the fully impregnated test piece (g)
m_w	mass of the fully impregnated test piece suspended in water (g)
ρ_w	density of water (g/cm^3)

4.2.2 Permeability measurements

Permeability is one of the most important properties in the design and manufacture of porous bearings. The bearing permeability coefficient is translated into a design parameter, via the bearing feeding parameter or bearing number, and it is directly related to the bearing performance.

The bearings' permeability was expected to be controlled and varied by altering the processing conditions, with regard to the alumina powder size, as well as the amount of the starch the original slip was prepared with.

A concise discussion on the different methods and best practices for measuring permeability coefficients has been published by Cliffel [91].

Permeability measurement in its simplest form, involves passing a fluid of known physical properties through a specimen of known, uniform cross section and thickness. The out-flowing fluid is collected, and the flow rate measured. By varying the inlet pressure, a set of measurement points of pressure difference across the specimen and their corresponding flow rates can be obtained, from which the permeability coefficients can be calculated.

For the present work, permeability measurements have been conducted in accordance to standard BS 5600 [87], using test rigs from previous research projects. These rigs were specifically designed for the permeability measurement of journal [3] and thrust bearings [30] [31].

For the calculation of the permeability for viscous flow Darcy's law is employed [87]:

Equation 10

$$\frac{\Delta p}{e} = \frac{Q \cdot \eta}{A \cdot \psi_v}$$

At higher flow rates, laminar flow progressively breaks down. In order to compensate for this, an extra term (inertial permeability) is added to Darcy's law. Equation 10 becomes Equation 11, which is known as the Forchheimer's equation.

Equation 11

$$\frac{\Delta p}{e} = \frac{Q \cdot \eta}{A \cdot \psi_v} + \frac{Q^2 \cdot \rho}{A^2 \cdot \psi_i}$$

Δp	pressure drop (N/m^2)
Q	volume flow rate (m^3/sec)
A	area of the test piece normal to the fluid flow (m^2)
η	absolute dynamic viscosity (Ns/m^2)
ρ	density of the test fluid (kg/m^3)
e	thickness of the test piece (m)
ψ_v	viscous permeability coefficient (m^2)
ψi	inertia permeability coefficient (m^2)

This equation is presented in the BS 5600 procedure in the following form:

Equation 12

$$\frac{\Delta_p \cdot A}{e \cdot Q \cdot \eta} = \frac{1}{\psi_i} \cdot \frac{Q \cdot \rho}{A \cdot \eta} + \frac{1}{\psi_v}$$

The calculation of results is carried out by plotting $\frac{\Delta_p \cdot A}{e \cdot Q \cdot \eta}$ against $\frac{Q \cdot \rho}{A \cdot \eta}$; the intercept of this line on the y-axis gives the reciprocal of the viscous permeability ($1/\psi_v$), and the slope of this line gives the reciprocal of the inertial permeability ($1/\psi_i$).

The standard also covers sample preparation, test equipment design and the selection of test fluids, amongst others.

Permeability measurements on journal bearings

A permeability measurement apparatus specifically built for journal geometry was available from a previous research project [3]; and this was used for the present research journal-bearing permeability measurements (Figure 18). This equipment was designed and operated in accordance with BS 5600 [87] recommendations; and it was capable of accommodating journal bearings ranging from 38 and 60mm in length, a maximum of 80mm in OD and a minimum of 36mm in ID. Because this test-rig was originally designed for liquid test fluids, such as water, all metallic parts were manufactured from stainless steel.

In its basic operating principle, the pressurised test liquid is supplied to the permeability test-rig vessel. After passing through the bearing, a two way valve either directs the liquid to the main reservoir, or for a timed period, into a tank for mass flow measurement.

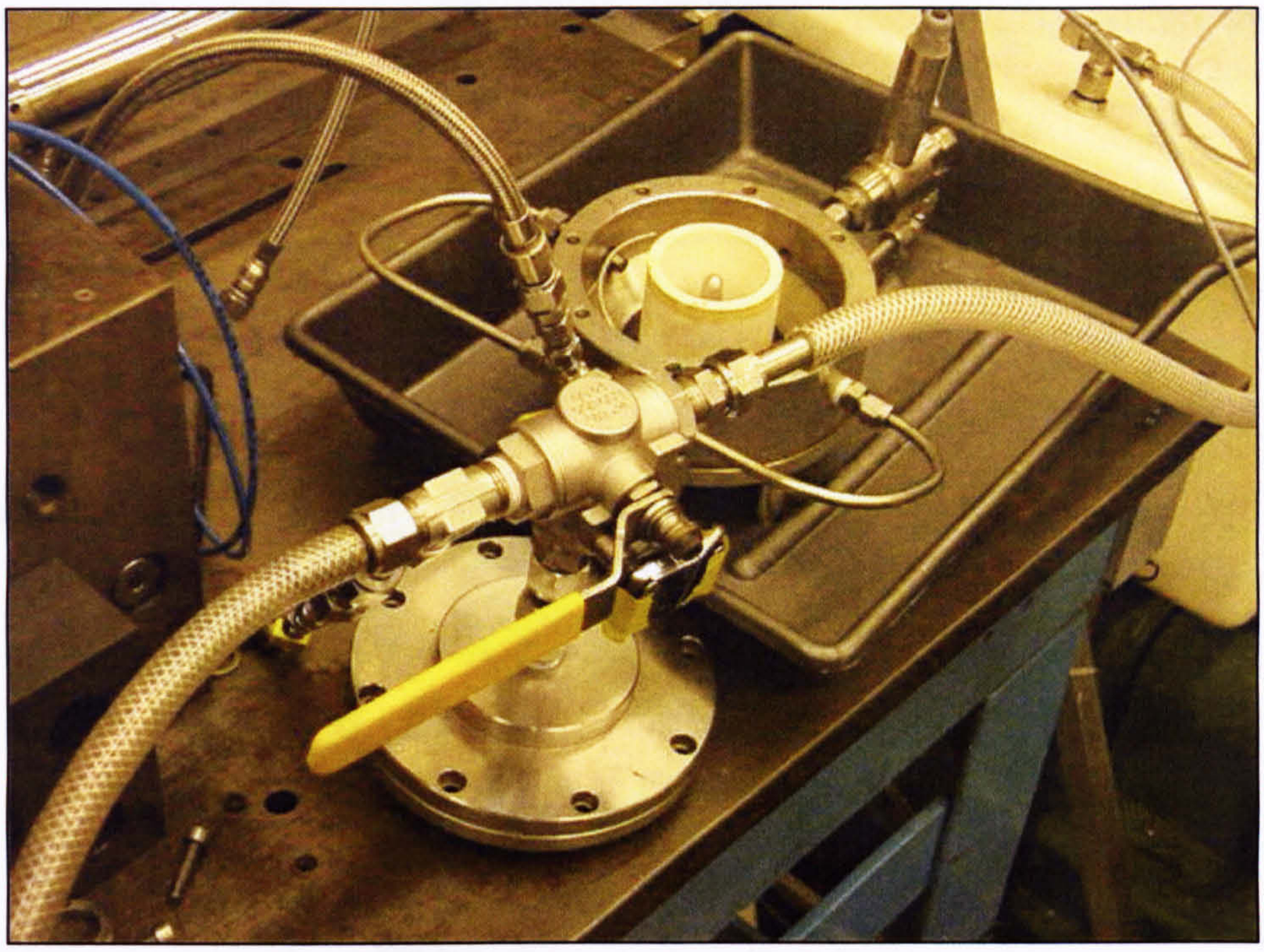

Figure 18-Porous-ceramic journal bearings permeability test rig.

Measurement procedure

During the test rig operation, the test fluid was forced through the ceramic shell from the outside at pressures ranging from 0.05 to 1MPa. A differential pressure sensor connected across the shell was used to measure the pressure drop. The outflowing test liquid was then collected in a weighing tank for mass flow measurement. A previously calibrated Sartorious type 1474A balance was used. In addition, the fluid's inlet and outlet temperature was also measured via K type thermocouples, to allow calculation of the compensated density and viscosity values. Figure 19, shows a schematic of the permeability test-rig operating principle.

Ten pressure drop Vs volume flow readings were usually taken; and these used in conjunction with the equations and the procedure described in the BS 5600 standard to calculate the permeability coefficients, via a specially developed excel spreadsheet.

Each of the shells tested was ground to final dimensions. In order to ensure consistency, the shells were subjected to full flow rate purging within the test equipment for one hour.

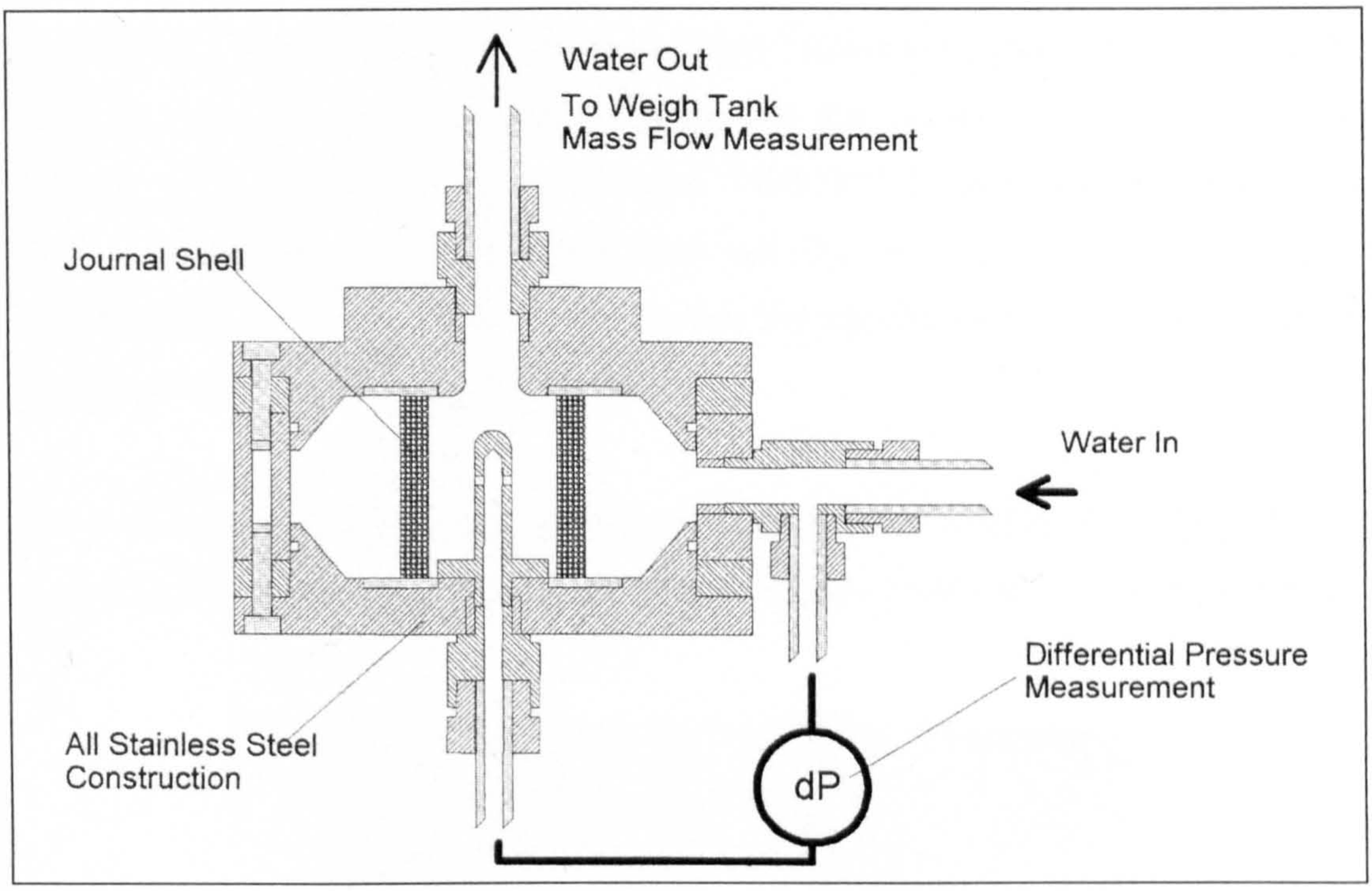

Figure 19- Porous-ceramic journal bearings permeability test rig operating principle, from reference [3].

Owing to the importance of permeability as a bearing property, permeability measurements were performed twice for each bearing, in order to confirm the first measurement. A third measurement would take place only if the second measurement did not match the first one. This condition applied to the thrust bearings' permeability measurements too.

The permeability apparatus described has a reported [3] permeability accuracy of ± 0.001 μm^2. Due to its importance within the procedure, the calibration of the differential pressure sensor was successfully double checked using a Druck 601 digital pressure indicator serial No 8159/92-7.

Further details of the design, manufacturing and calibration procedures for this test rig can be found in Almond's thesis [3]; these are not being duplicated here.

Permeability measurements on thrust bearings

Permeability measurements on thrust bearings (discs) were conducted using another permeability test-rig specifically designed for this purpose in previous research projects [30] [31], in accordance with BS 5600 [87]. In this rig, compressed air is used as the test fluid. Air is supplied dried and filtered to the test rig via a computer controlled pneumatic regulator at the base of the rig; the air then passes through the bearing centre, and is ejected at the top.

The main body of the test rig is made of Perspex tube (Figure 20). The test rig is capable of holding discs of 46 mm in diameter with a maximum thickness of 8 mm.

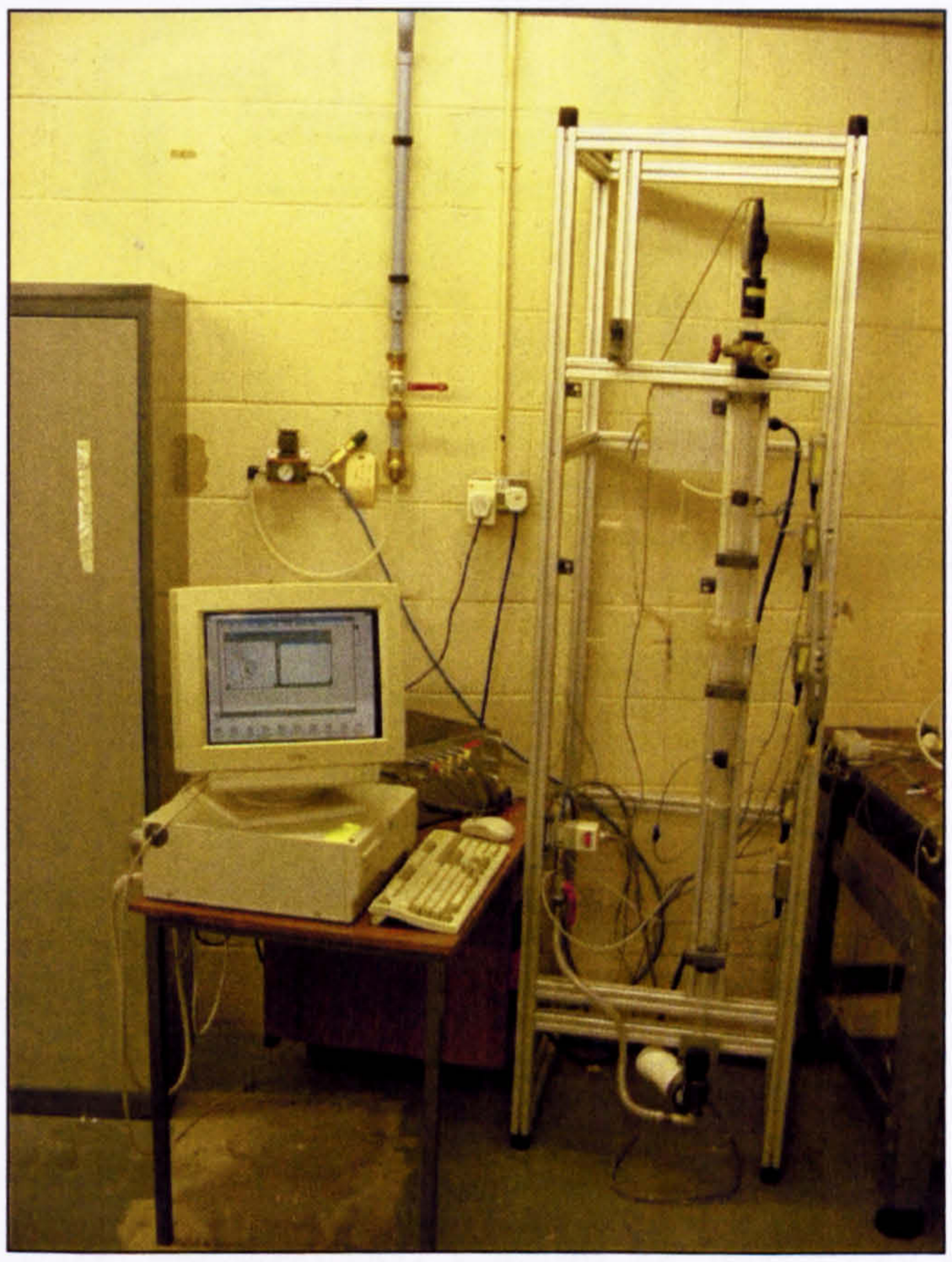

Figure 20-Porous-ceramic aerostatic bearings permeability test rig.

An arrangement of flow meters, pressure sensors and K type thermocouples placed on the rig and attached to a data acquisition card/computer were used to monitor and capture the pressure drop across the bearing along with the air temperature, ambient pressure, ambient temperature, volumetric flow rate, and pressure downstream. The computer used a LabView 4.1 computer programme suite to perform the testing semi-automatically.

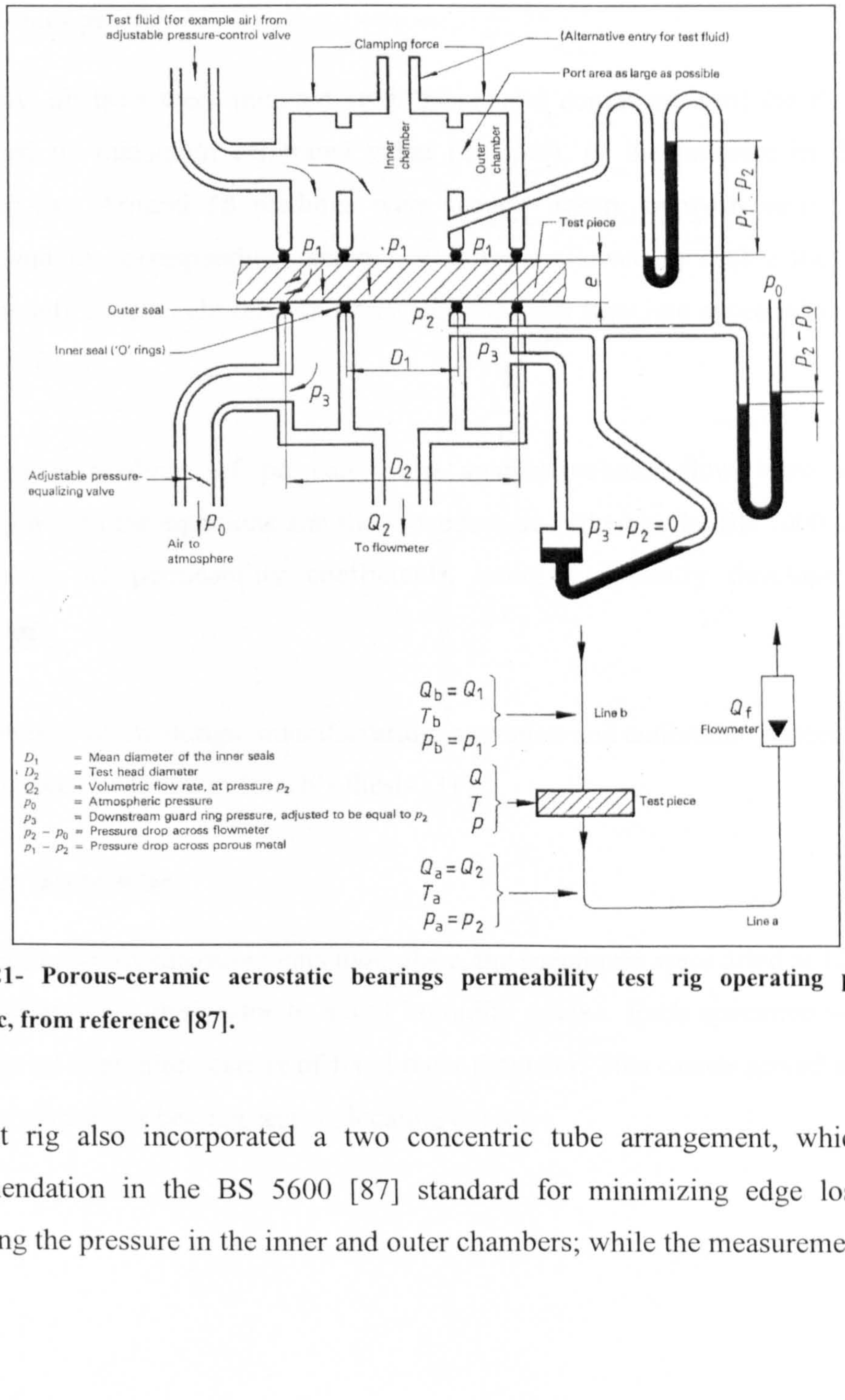

Figure 21- Porous-ceramic aerostatic bearings permeability test rig operating principle schematic, from reference [87].

The test rig also incorporated a two concentric tube arrangement, which is a recommendation in the BS 5600 [87] standard for minimizing edge losses by equalising the pressure in the inner and outer chambers; while the measurement takes

place. Figure 21 illustrates the permeability measurement principle for thrust bearings

The porous-ceramic aerostatic bearings permeability test rig was designed in such a way that, with a small amount of alteration it could also be used for the bubble test, a simple test used to determine the largest through pore size; as well as performing the water expulsion method used for pore size distribution measurement.

Measurement procedure

Essentially, all tests were initiated at 0.75-bar, and continued until the flowmeter approached its maximum calibrated value (20 lpm), or the pressure in the tube reached 5-bar. Around 18 readings were usually taken; between each pressure increase and its corresponding reading, 30 s were allowed to enable the flow to achieve steady state conditions. In every case the final flow rate exceeded the initial by a factor of 10.

The eventual readings of pressure drop against volume flow were used in conjunction with the equations and the procedure described in the BS 5600 standard to calculate the permeability coefficients, using a specially developed excel spreadsheet.

Further details of the design, manufacturing, operation and calibration procedures for this test rig can be found in Roach's thesis [31].

Specimens' preparation

Before permeability measurements took place, the specimens were dried at 120°C for 24h, and kept in a desiccator to avoid humidity uptake. Each specimen was then 'glued' to an aluminium carrier of fixed outer diameter. This carrier served as outer-edge seal, as well as bearing-test rig locating datum.

4.2.3 Pore Size Distribution

An ideal porous material for externally pressurized porous bearings would not only possess predictable permeability, but equally important, uniformity in pore-size distribution, as this in turn implies a homogenous permeability across/along the bearing's walls.

Measurement methods review

A comprehensive discussion on the different methods for the determination of the structure of porous media is presented by Dullien [92] *et al*, and another interesting review on this subject is by Robens [93] *et al*. Figure 22 illustrates Robens' classification of the different available technologies for the estimation of pore size distribution, which are shown plotted in relation to their range of measurement.

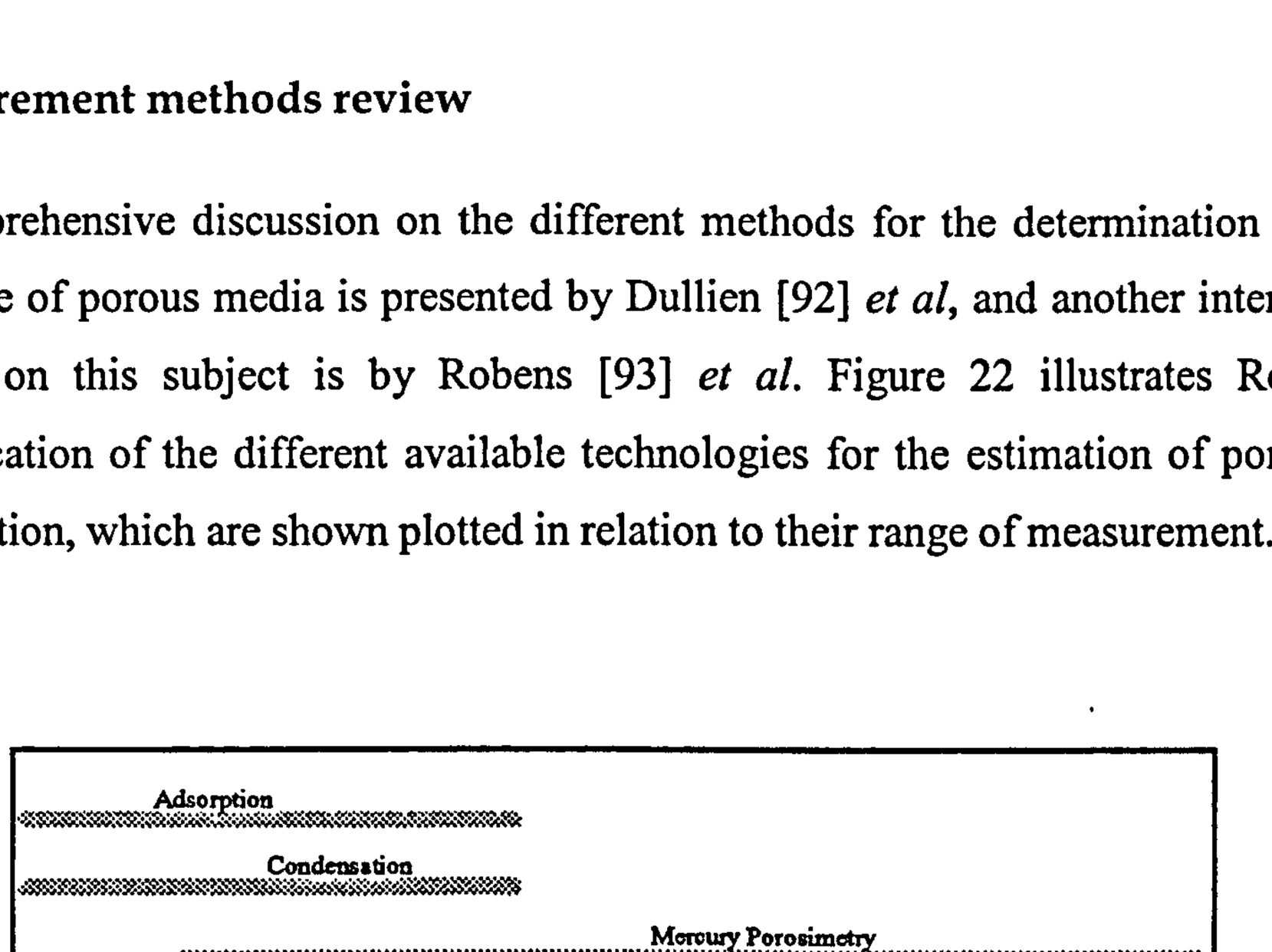

Figure 22- Pore size methods recommended range of application, from reference [30].

The most widely used models of pore structure consist of straight, non intersecting cylindrical tubes, the diameters of which are distributed according to a given distribution function. However, several authors argue [92] [94] that very few real porous media will contain pores of straight cylindrical capillary shape. Therefore the pore size calculated from this principle must considered equivalent.

The most popular method for pore size measurement is mercury porosimetry. This technique is well developed and is applicable to a wide range of pore sizes. Basically, the mercury porosimetry method consists of measuring simultaneously the capillary pressure and the volume of mercury that has penetrated the sample up to that pressure. In relation to this research, its main disadvantage resides in the subsequent failure to remove all mercury from the sample; thus the specimens would be used only once, and would no longer be useful for other tests.

On the other hand, the use of image analysis only reveals pore size information over a relatively small area of the specimen. Other problems include the risk of false porosity due to improper polishing. It does, however, provide useful evidence on the maximum size of pores and their shape.

It is generally acknowledged that the result of any pore size distribution is not an absolute measure, and that this is highly dependant on the measurement method. Clear evidence of this is presented in Dullien's review [92], in which two methods, mercury porosimetry and photomicrography, yield very divergent pore size distributions for the same specimen. In this respect, and as a result from a comparative study of methods for measuring pore-size distribution, Clements & Vyse [95] recommend a combination of methods, liquid penetration combined with microscopy, for the appropriate study of a pore system.

Measuring pore size distribution for SC porous ceramic bearings

For the present research, pore size distribution was assessed by a combination of three adjunct techniques: the bubble-test [96], the dynamic water-expulsion method [97] and SEM studies.

The extended bubble test point and the water expulsion method were used to measure the pores that correspond to the equivalent connecting contact areas or necks between much larger spherical shaped pores created by the original starch particles. On the other hand, The SEM and image analysis investigations visually displayed the overall pore structure dominated by the large pores left by the starch particles.

The bubble test

In the bubble-test [96], the test specimen is fully impregnated with de-ionized water. One surface of the specimen, facing upwards, is further covered with a known column of water (h_w). Pressurized air carefully controlled is gradually passed through the specimen from the bottom surface. The pressure (p_1) at which the first bubble begins to emerge on the top submerged surface, known as the first bubble point is used to calculate the maximum equivalent capillary diameter of the pore:

Equation 13

$$d_{pore\ max} = \frac{4 \cdot \gamma_w}{p_1 + \rho_w \cdot g \cdot h_w}$$

$d_{pore\ max}$	maximum circular-capillary-equivalent pore diameter (m)
γ_w	surface tension of water (N/m)
p_1	absolute gas pressure upstream the specimen (Pa)
ρ_w	density of deionised water (k/m^3)
g	gravitational acceleration constant (m/s^2)
h_w	height of the water column above the specimen (m)

The test rig previously used for the permeability measurement of thrust bearings [30] was reconfigured for this purpose, in accordance with BS EN 24003. The test rig's

original design allowed for the necessary modifications to be carried out with relative ease. Figure 23 illustrates the bubble test principle.

The bubble test, although a relatively simple test to conduct, provides information only on the maximum through pore over one of the specimen's surface. No information on the size and spatial distribution can be obtained.

The bubble test was extended in the present study to provide a qualitative assessment of the uniformity of the spatial distribution of pores. After reaching the first bubble point, the pressure was gradually further increased to cause general bubbling over the entire bearing surface, allowing the visual inspection of the pore distribution uniformity.

The use of the bubble test through the thrust bearing permeability rig implied that only ceramic discs were subjected to it. Discs were dried and impregnated using the procedure previously described for density and porosity measurements; and were also fixed to the aluminium carrier previously used for permeability measurements.

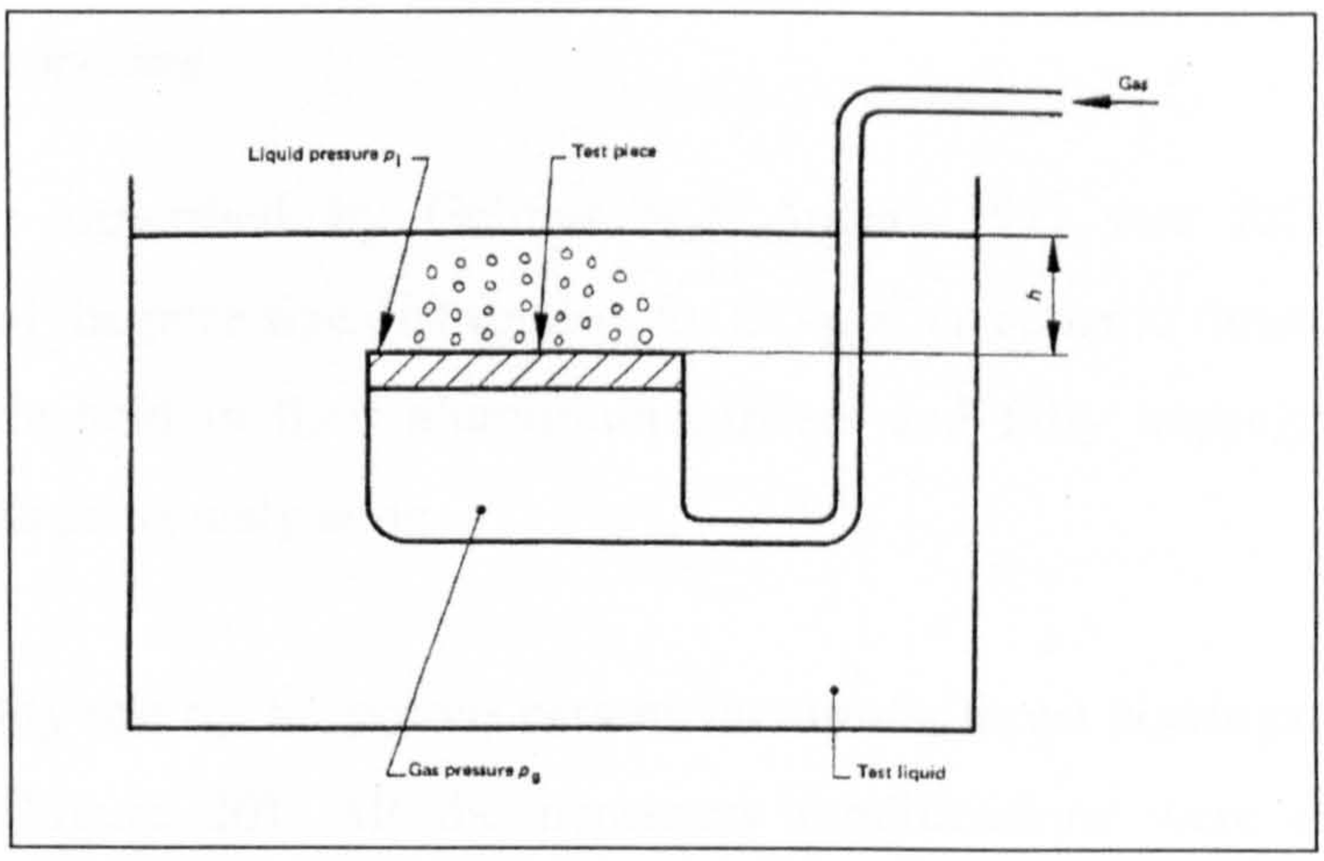

Figure 23- Bubble test principle schematic, from reference [96].

The relatively quick results obtained through the bubble test gave an idea of the magnitude of the pores' size, and the pressures involved; complementing the more thorough water-expulsion test subsequently conducted.

Water expulsion method

In the absence of mercury porosimetry equipment, the water expulsion method [97] was employed. Its range of measurement capability appeared to be adequate, and results from previous bubble test measurements supported this assumption. Furthermore, good agreement with mercury porosimetry results [95] has also been reported.

The dynamic water expulsion method involves passing compressed air, gradually increasing the pressure, through a porous specimen previously impregnated with water. As the pressure increases the surface tension of the water is overcome in an increasing number of pores; thus the water is expelled. These pores are thereafter free for air to flow through. The air pressure supply is gradually increased and the pressure difference across the specimen, as well as, the steady state airflow rate is monitored. The equivalent pore size corresponding to a particular differential pressure, plus the number contributing to the increase in airflow rate, can be determined. Details of the mathematics for this method can be found in the paper by Gelinas and Angers [97].

Measurement procedure

The procedure described by Gelinas and Angers [97] was followed for the measurement of the pore size distribution for SC porous ceramic thrust bearings. The specimens were held in their aluminium carriers and fully impregnated with de-ionised water as previously done.

The permeability test rig for porous ceramic aerostatic thrust bearings was employed for this test (Figure 20). All the necessary modifications were carried out, as described by Kwan [30]. Further details of the rig's operation, modification and calibration procedures are described by both Roach [31] and Kwan [30].

The starting air flow pressure was set at 0.9 of the first bubble point pressure for each specimen. Around twenty five measurements points were taken at equal pressure increments. Flow was allowed to settle for 40 seconds after every pressure increase,

as recommended by Kwan [30]. The test-rig's computer software allowed the flow rate to be monitored to ensure steady flow was achieved.

An excel spreadsheet was developed and permitted the calculation of the results in accordance to the Gelinas and Angers procedure [97].

SEM micrography & image analysis

A further study concerned with the pore morphology of the porous journal bearings was conducted using scanning electron microscopy (SEM), complemented by image analysis. In this study the effects of the alumina powder size, as well as the amount of starch in the original slip, were investigated in relation to the overall pore structure.

From each shell, one centre section was acutely sliced as shown in Figure 24, in order to expose a surface extending through its wall. The specimens were then mounted in resin and polished using progressively finer diamond paste. Following the specimens' preparation SEM micrographs were taken.

A computer image analysis exercise was undertaken for selected journal bearings, using the previously taken micrographs. Fractional pore surface area and average equivalent pore diameter estimates could then be made.

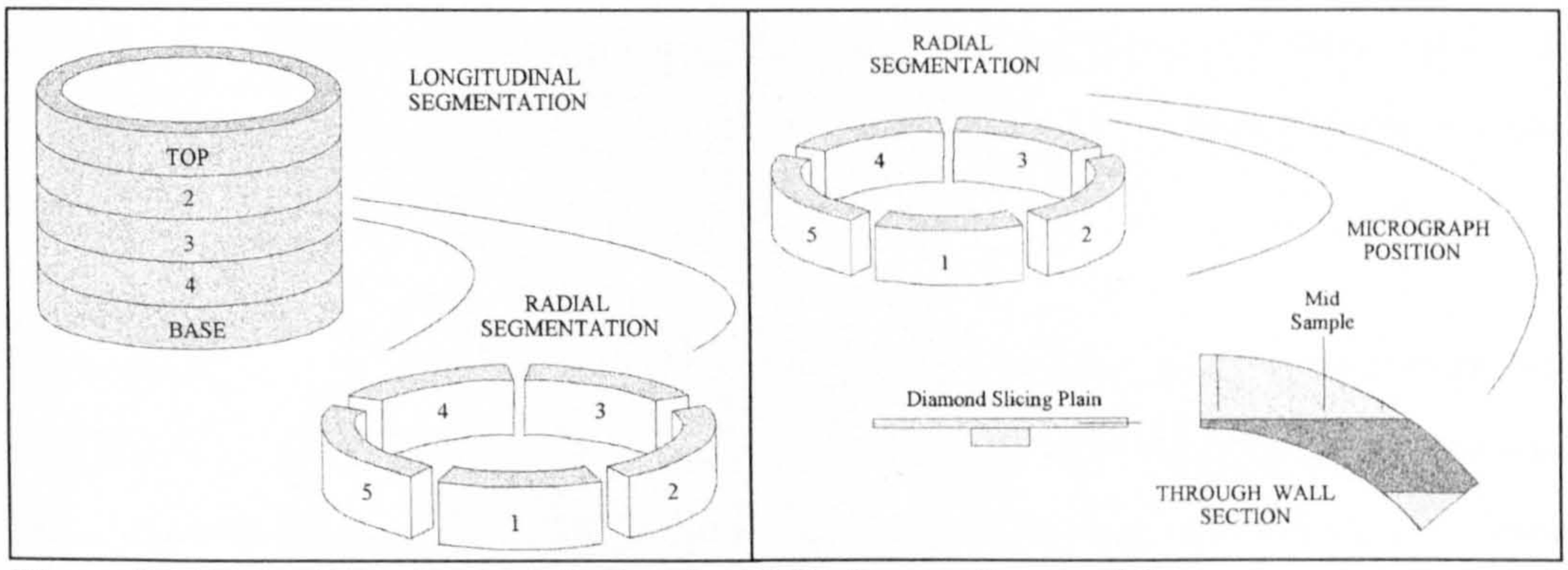

Figure 24- Journal bearings' sectioning for SEM; from reference [3].

4.2.4 Measurement of Young's and shear moduli

The mechanical properties of a material determine its structural performance in applications where the material is required to sustain a load [98]. Hence the importance of the Young's and Shear moduli measurements for porous-ceramic bearings. Typical Young's modulus for dense ceramics has been quoted at around 410 GPa [99]. However, it is also commonly accepted that an increasing level of porosity in a given ceramic matrix would negatively affect its elastic constants. In this sense, in addition to being capable of producing bearings with adequate porosity values, the manufacturing route must also be capable to produce the same bearings with adequate mechanical properties.

Measurement of the modulus of elasticity

For ceramic materials, the modulus of elasticity (E), or Young's modulus, is traditionally measured by two techniques [98]. The first involves direct measurement of strain as a function of stress, plotting the data graphically and measuring the slope of the elastic portion of the curve. This technique can be conducted accurately at room temperature using strain gauges, but is limited to the temperatures above which strain gauges can be reliably attached.

A second method for determining the modulus of elasticity is based on the measurement of the resonant frequency of the specimen. Formulas that relate this frequency and the specimen's geometry, shape and mass are then used for the calculation of E. In this regard, a comprehensive review of formulas for the moduli calculation is presented by Morell [100].

Most ceramics posses a relatively low-strain to fracture ratio; therefore resonance frequency techniques are sometimes preferred over strain-stress measurements. Several techniques exist depending on the nature of the excitation and detection method. These are discussed at length by Davis [101]; several other authors [102] [103] have undertaken experimental comparisons for the different techniques, including the impulse excitation [104] and the ultrasonic pulse techniques [105] with generally very good agreement between the results for each technique.

Measurement of elastic and shear moduli for SC porous-ceramic bearings

For the present research bearings, the impulse excitation technique was used for measuring the E modulus. This technique is based on the analysis of a transient of the specimen resulting from a mechanical impact. A Lemmens Grindosonic MK5 machine was readily available. This device when attached to a computer running EMOD version 9.15 [106] software allowed the calculation of E and the shear (G) moduli, as well as Poisson's ratio, starting from the specimen's mass, dimensions and natural frequency. A great advantage of this method is that it is non-destructive. This enabled the specimens to be used for subsequent tests, such as permeability or pore-size distribution.

The Lemmens Grindosonic machine is capable of calculating the elastic properties for a variety of geometries, including discs, bars and cylinders. Unfortunately, there was no provision for journal geometry (hollow cylinder) in the software. In the absence of this, relative moduli values were calculated. The evaluation of the elastic properties was then carried out by comparing the squares of the resonant frequencies. Relative moduli evaluation is a common practice for complex geometries and in cases where no moduli formulas can be used [104].

In addition, measurements were performed on SC discs. These provided a quantitative measure of the moduli, serving for the comparison and evaluation of the elastic constants in relation to the published porosity-moduli theories.

Measurement procedure

The specimens were dried and kept as described previously in section 4.2.2. For the actual measurement, the specimens were supported on foam strips and a piezo-electric probe was placed as indicated in the Grindosonic machine manual [88] for each case; as illustrated in Figure 25 and Figure 26 for journal and disc bearings, respectively. The vibration was induced by striking lightly with a small hammer. The frequency of this vibration was displayed on the Lemmens machine, and once

consistent readings were obtained, the data was entered into the computer for the moduli calculation.

To ensure true and consistent measurements, the moduli for steel and aluminium duplicate journal and thrust bearings were verified using the same measurement procedures and equipment.

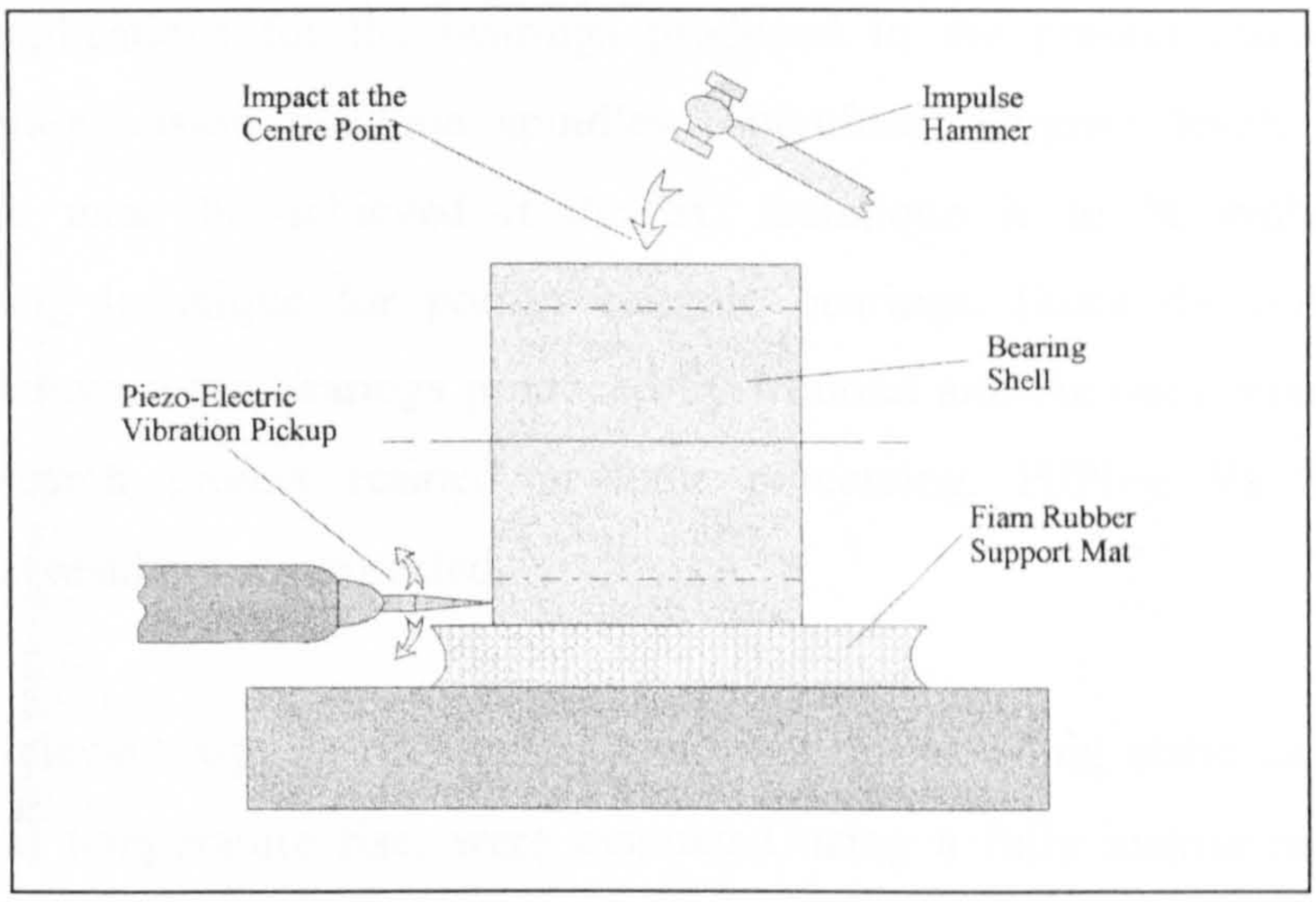

Figure 25-Schematic diagram of the Grindosonic moduli measurement procedure for journal bearings (reference [3]).

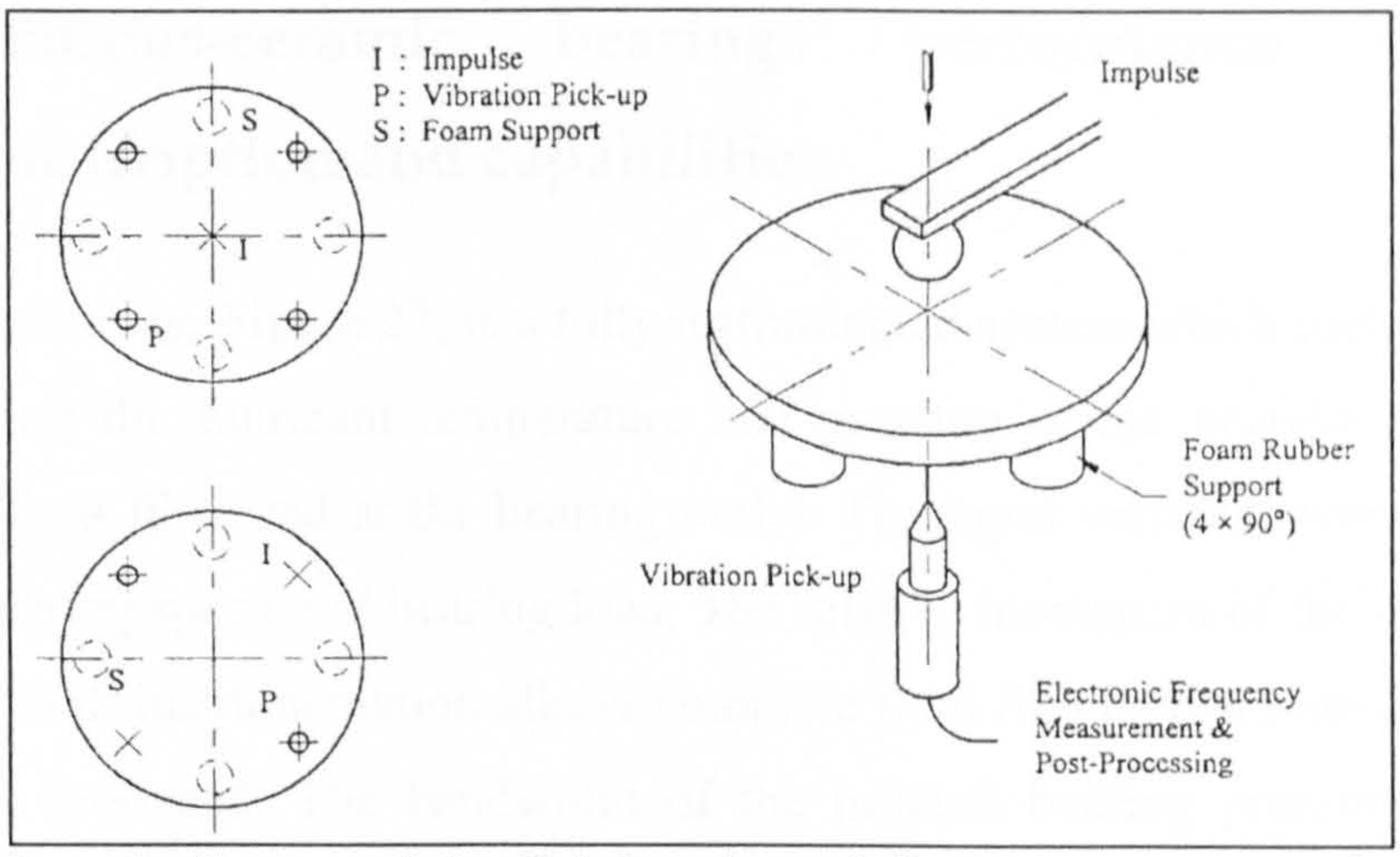

Figure 26-Schematic diagram of the Grindosonic moduli measurement procedure for thrust bearings (reference [30]).

4.3 SC porous-ceramic bearing performance

The potential benefits of the porous-ceramic hydrostatic journal bearings have been already demonstrated by Almond [3] and have been also discussed in a previous chapter of this thesis.

Potential applications for the bearings produced in the present research project include ultra-precision machine spindles. Therefore adequate levels of bearing performance must be achieved if the SC technique is to be embraced as a manufacturing technique for porous ceramic bearings. Since the only apparent difference between the bearings produced by Almond and the ones produced in the present research project resided in their processing, HIPing Vs SC, similar performance results were expected.

The most relevant aspects of bearing performance, including static and rotational stiffness and temperature rise, were evaluated using a fully instrumented test-rig, designed and built specifically for this purpose in a previous research project [3]. This test rig is described in the following sections.

4.3.1 Porous-ceramic bearings performance test rig description and capabilities

The bearing test-rig, Figure 27, is a fully instrumented system which includes sensors for measuring the lubricant temperature and pressure at the bearing inlet points, within the fluid film, and at the bearing outlet. The input variables were the supply pressure, bearing speed and bearing load. The relative movement of the bearing shell over the in-shaft instrumentation allows complete fluid film temperature and pressure maps to be produced. The bandwidth of the in-shaft bearing pressure sensors is sufficient to allow full 360° pressure profile plots at 16, 000 rpm. Figure 28 and Figure 29 illustrate the test rig's housing and in-shaft instrumentation, respectively.

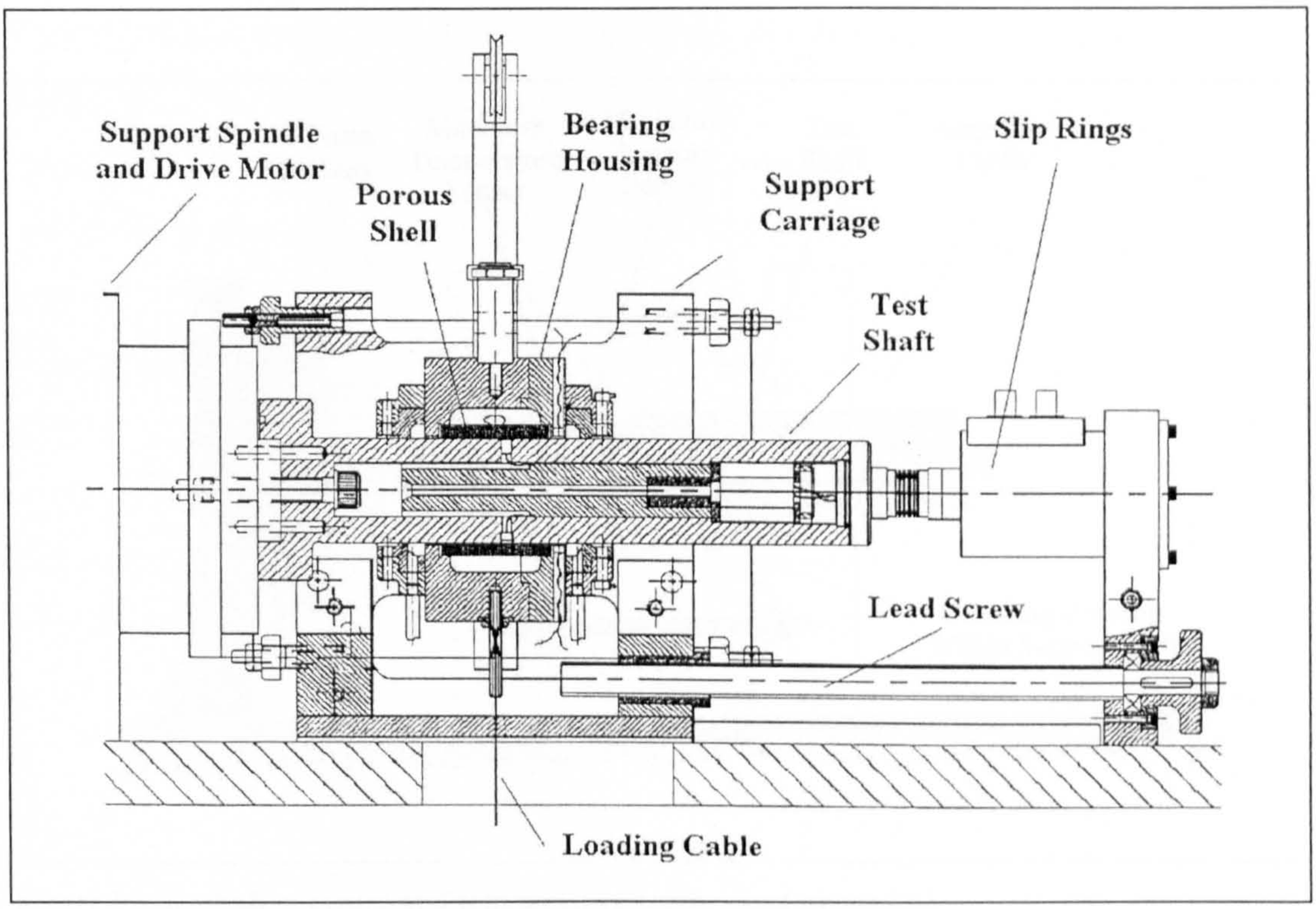

Figure 27-Porous-ceramic hydrostatic journal bearings performance test rig (reference [3]).

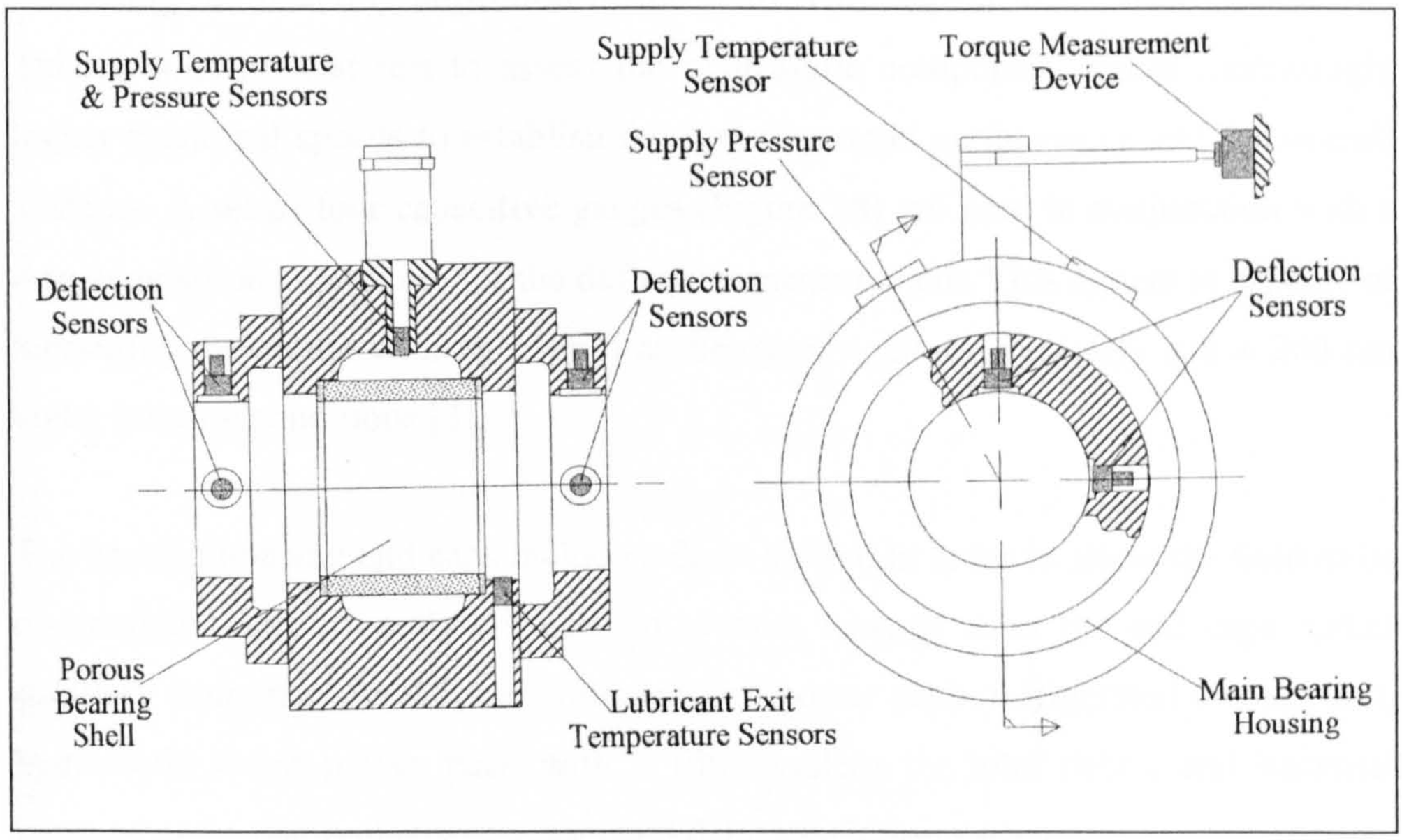

Figure 28- Bearing housing's sensor placement (reference [3]).

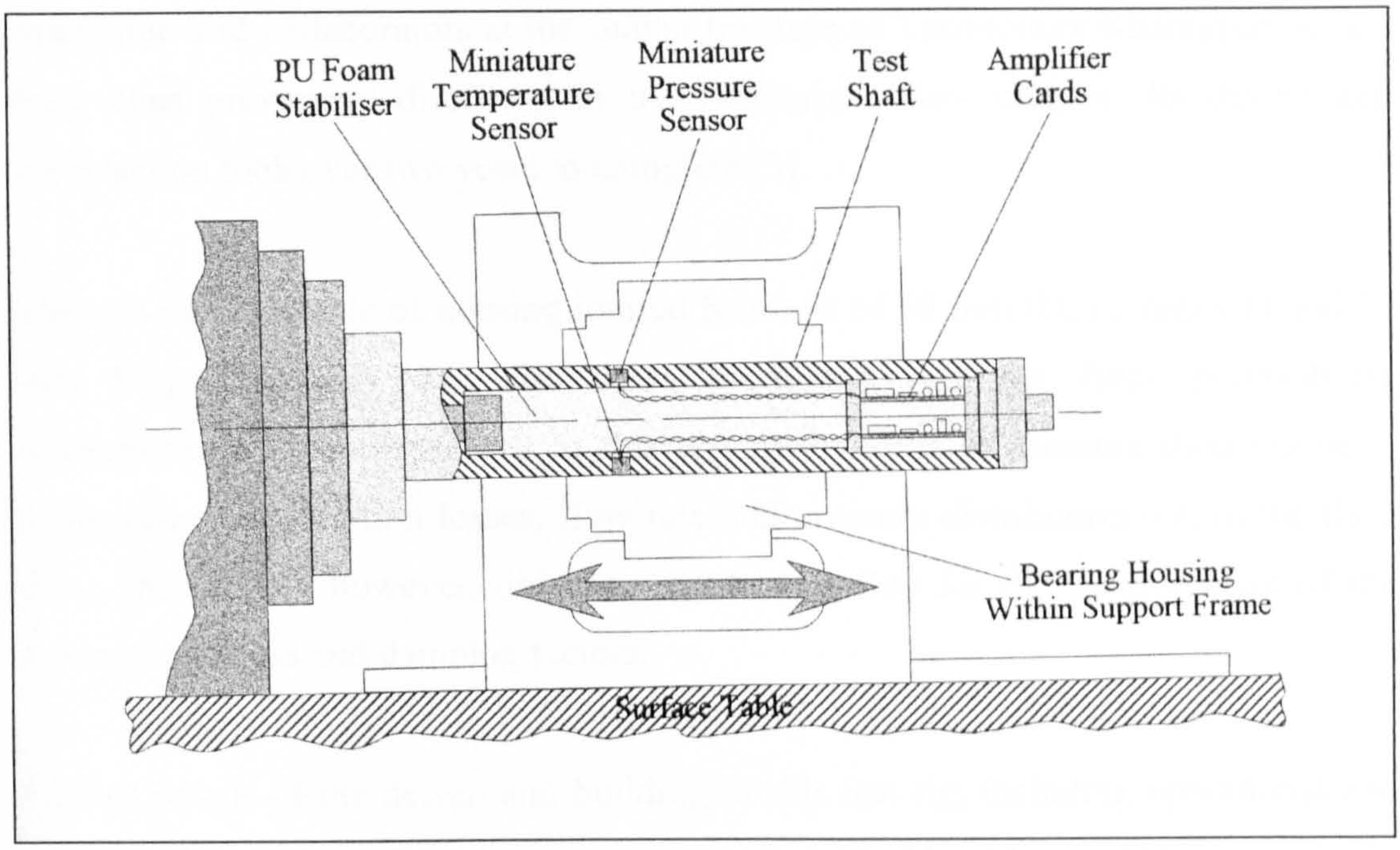

Figure 29- In-shaft pressure and temperature sensors (reference [3]).

Bearing stiffness is measured by applying a dead weigh load using a cable and measuring the resulting deflection of the shaft with respect to the bearing housing. This is done both at rest to assess the hydrostatic component and at increasingly higher rotational speeds to establish the hydrodynamic performance and the overall stiffness. A set of four capacitive gauges (Figure 28) are used in conjunction with a data acquisition subroutine for the deflection measurement. This system is capable of measuring deflection with an overall accuracy of ± 20 nm statically and ± 200 nm under rotating conditions [3].

The bearing housing end caps include a drain system in order to allow the fluid to be re-circulated and air seals are used to prevent leakage from the end caps. Other ancillary equipment includes a hydrostatic oil power pack, refrigerated cooling unit, hydrostatic water power pack with a filter system for total debris and bacterial removal and a comprehensive automated data acquisition system.

The porous-ceramic journal bearings performance test-rig is unique apparatus in its design and operational capabilities, in the sense that it provides accurate

experimental verification for the theoretical models and analyses developed by Majumdar and collaborators at the Indian Institute of Technology Kharagpur, which have been previously discussed in the literature review chapter. Its design and construction took over two years to complete [3].

The test-rig is capable of housing journal bearings of 50 mm ID, 62 mm OD and 50 mm long (appendix 1). The most promising bearings from permeability measurements were transferred to this test-rig in order to measure their stiffness, temperature rise, friction losses, flow rate and pressure-distribution within the fluid film. The test-rig, however, did not provide a facility for the measurement of the dynamic stiffness and damping factors.

Further details of the design and building of this test rig, including operational and calibration procedures have been extensively described by Almond [3], and these are not duplicated here.

Oil lubrication

In previous research [3], porous ceramic journal hydrostatic bearings have been lubricated with water. For the present research project, and at an industrial sponsor's request, water lubrication was changed to low viscosity oil lubrication. This request was in response to a potential specific design application/solution for one of their customers, which resulted in an order for a porous-ceramic hydrostatic bearing spindle. Although at this point the parallel corrosion and foaming tests indicated that their effects could be effectively controlled, water lubrication was seen as a disadvantage because the manufacturers of standard ancillary and auxiliary equipment had not specifically developed their components for water lubrication; hence their effectiveness under these conditions could not be guaranteed long-term. Low viscosity oils would be used instead, because of their potential for an improved thermal performance over more common machine-tool oils.

In the first instance, BP's *Energol HP0* was chosen as lubricant. However, due to unavailability, this was later changed to *Dielectric 180*, from the same company.

Datasheets for these lubricants are provided in appendix 2. Density and viscosity measurements were performed in accordance with BS standards 4699 [107] and 188 [108], over a range of temperatures. The results from these measurements were then input in the relevant bearing performance calculations. A plot from these measurements can be found in appendix 2.

The change in the lubricant resulted in some minor alterations made to the rig. For example, the original electrical conductive level switch used in one of lubricant tanks had to be replaced with a float-switch, due to the poor electric conductivity of oils. Silicone piping within the rig was also replaced with an oil resistant plastic piping.

Porous-ceramic hydrostatic bearings had been never been tested for performance or permeability with oil as the lubricant, and this constituted another area of originality for the present research.

Journal bearing experimental preparation

Permeability measurements

Prior to performance testing, permeability measurements for each of the journals tested were undertaken with the relevant oil as the test fluid, as described previously within this chapter. This again provided an opportunity to compare these coefficients against the permeability coefficient values previously obtained with water as a test fluid.

Journal measurement and Gap

Measurement of the journal shells was carried out at the industrial sponsor's metrology laboratory, taking advantage of their ample range of facilities and expertise in metrology. A Talycentre machine was used for measurement of the journal shell radius, run-out, and concentricity in five different planes with an accuracy of ± 0.1 μm. The Talycentre machine metrology records for the shells tested can be found in appendix 4.

The test shaft nominal diameter was 49.970 mm. This was double-checked with a previously calibrated Tesa Digitmaster micrometer with a resolution of ± 1 μm. The bearing radial gap was then determined by simply deducting the test shaft radius from the bearing's average bore radius.

4.3.2 Porous-ceramic hydrostatic journal-bearings experimental performance measurement

Measurement of static stiffness

Hydrostatic stiffness testing of the bearing shells was carried out for a series of radial load values ranging from 0 to 100 N. These tests were typically conducted at fixed supply pressures of 0.25, 0.50, 1.0 and 2 MPa. The bearings were positioned in the centre of their working section under non-rotating conditions and a simple static stiffness calculation was performed from a deflection measurement under a known load. Deflection was measured with respect to the shaft in the same direction as the applied loads using a capacitive sensor array. The radial load was increased in 10 N steps for each of the supply pressure settings. The obtained data was then plotted, in order to asses the significance of the bearing stiffness in relation to the bearing design-parameters such as eccentricity ratio and the bearing feeding parameter.

Measurement of static flow rate

Flow rate was measured using a weight tank and the balance used in the permeability measurements exercises. The lubricant inlet and outlet temperatures were also measured to permit density and viscosity corrections. Flow rate tests were conducted in static conditions, with fixed supply pressures of 0.25, 0.50, 1.0 and 2 MPa under no load conditions. The flow-rate results from the different shells could be then examined in relation to the bearings' permeability and gap; in order to ascertain the effects of these.

Pumping power

Power consumption is an important factor to consider when assessing the economic performance of a bearing system. The pumping power component of this is a simple product of the lubricant flow-rate and the supply pressure.

Equation 14

$$W_p = P_s \cdot Q$$

W_p	lubricant pumping power (W)
Q	lubricant volume flow rate (m^3/s)
P_s	lubricant supply pressure (Pa)

Hydrostatic pressure distribution maps

The test rig provided a facility for the generation of the hydrostatic pressure maps. The different pressures were measured using the automatic logging routines developed in the data acquisition software in conjunction with the in-shaft instrumentation. Longitudinal sweeps were used, during which the carriage was driven over its entire length with pressure measurements triggered every 1mm. the data from each sweep was logged into the computer's hard drive, and the process repeated with the test shaft fixed at positions between 0 and 360° in increments of 45°. Each full film pressure map therefore comprised 8 sweeps, each consisting of 51 pressure measurements.

Fluid film pressure maps were recorded for a number of different operating conditions. Four supply pressure settings fixed at 0.25, 0.50, 1.0 and 2 MPa were used, and radial loading was varied over a further five fixed values of 0, 25, 50, 75 and 100 N. In all, these variations provided a set of twenty different operating conditions for each shell tested.

Measurement of rotational stiffness

In this part of the testing, supply pressures of 1 and 2 MPa were used for each experimental bearing shell, and fixed radial loads of 0 to 100 N were applied in 10 N steps. Each test was carried out in the centre of the test section over six different speed settings from 100 up to 10, 000 rpm. The rotational stiffness was therefore examined under each of 132 different individual operating conditions with respect to pressure, load and speed.

Experiment preparation

Prior to testing a warm up period of one hour running at the selected test speed (rpm) was observed. This allowed the conventional oil hydrostatic bearings in the drive spindle to reach a stable operating temperature. Once the testing started, the lubricant temperature was also monitored to allow corrections of the density and viscosity values where appropriate. The same observations applied for subsequent experiments, such as temperature rise testing or hybrid pressure distribution.

Flow rate measurement

In addition to the static flow measurements, flow rate under rotational conditions was also measured, in order to investigate the effects of angular velocity. The supply pressure was set to both 1 and 2 MPa for each tested bearing. No load conditions were maintained with the bearing positioned in the centre of its test section, with rotational speeds ranging from 100 to 8,000 rpm.

A weight tank and the balance previously used for permeability measurements were employed for this part of the testing. In the same manner, the lubricant inlet and outlet temperatures were also measured to permit density and viscosity corrections.

Temperature rise measurement

Friction power is dissipated within a fluid film bearing as heat energy, and this causes a corresponding increase in the lubricant temperature. This absorbs a

proportion of this heat energy, and by carefully engineering the lubricant can remove a significant amount of the unwanted heat with minimal temperature increase to the machine structure.

For this experiment, supply pressures were set to 1 and 2 MPa, and the spindle was run for one hour under no load conditions, to allow the lubricant's temperature to reach a stable condition. The temperature difference between bearing's inlet and outlet could then be measured and subsequently studied in relation to the non-dimensional bearing speed parameter (λ_s).

4.4 Direct experimental performance comparison: porous-ceramic hydrostatic technology Vs conventional hydrostatic technology

In order to validate the performance results obtained during the present research project, a direct experimental comparison between a porous-ceramic hydrostatic journal-bearing and a typical hydrostatic journal bearing (conventional technology) was carried out. The industrial sponsor provided a typical 5-recess hydrostatic journal that was equivalent in size to the SC ceramic journals used in the performance test programme of the present research.

The hydrostatic journal bearing was manufactured in such a way that it could be fitted directly into the porous-ceramic journal bearing performance test-rig. The bearing was then subjected to static and rotational stiffness, flow rate and temperature rise tests, conducted using the same procedures previously described. The results from this exercise were then compared against the results of a porous-ceramic journal bearing under the same testing conditions, and using the same lubricant. To ensure the fairest comparison, the porous ceramic journal's bore was carefully re-ground to allow the bearing gap for both bearings to be the same.
Details of the design for both bearings can be found in Table 7.

Characteristics	Porous-ceramic hydrostatic	5-Recess hydrostatic
Journal diameter (m)	0.05	0.05
Journal length (m)	0.05	0.05
Wall thickness (m)	0.006	N/A
Viscous permeability (m^2)	2.7×10^{-14}	N/A
Radial gap (m)	2.65×10^{-5}	2.65×10^{-5}
Bearing feeding number β (N-D)	1.71	N/A
Axial land width (m)	N/A	2×10^{-3}
Number of pockets	N/A	5
Resistance ratio	N/A	1.5
Circumferential land width (m)	N/A	3×10^{-3}
Pocket depth (m)	N/A	2.5×10^{-4}

Table 7-Direct performance comparison: porous ceramic hydrostatic and 5-recess hydrostatic journal bearings characteristics.

4.5 Water lubrication: investigation into the corrosion, foaming and air release characteristics for porous-ceramic hydrostatic bearing systems

The benefits of water lubrication in relation to porous-ceramic hydrostatic journal-bearing technology have been already demonstrated by Almond [3]. In this context, potential secondary effects, such as corrosion, had not been yet thoroughly studied.

The addition of corrosion inhibitors to the water used as a lubricant is a natural development. Conventional water based coolants with added corrosion inhibitors are of particular interest, because they could serve both purposes in a machine-tool. However, these could potentially bring about some other secondary effects, such as foaming or bacterial growth. Hence the need for further studies on the corrosion behaviour on the likely found materials in machine-tools, as well as possible foam formation.

4.5.1 Corrosion testing

The objective of the corrosion test was to ascertain whether conventional materials employed in the manufacture of machine tools were suitable for their incorporation in systems where porous-ceramic hydrostatic bearings are lubricated with water and with the addition of corrosion inhibitors.

Available corrosion tests

Published corrosion studies related to machine-tool components are scarce. Amongst the literature reviewed, only the Institute of Petroleum's IP 125 [109] deals with the monitoring of the corrosiveness of aqueous cutting fluids. Here, steel millings are placed on the clean surface of a cast iron plate and the test fluid is poured on them. After 24 h the millings are removed and the surface of the plate is examined for

corrosion. Results are reported by citing the number of pits found as well as estimates of the percentage of the test area stained and its intensity.

A different approach was taken by Menke [110] for a study derived from the corroding of steel surfaces discovered on machine-tools with inactive short periods. In this particular case, the level of corrosion protectiveness for all of the fluids involved in the machine tool operation, including oils and water-based coolants, was analysed by first coating low carbon steel coupons with the relevant fluid, followed by salt-spray corrosion testing in accordance to ASTM-B117 [111]. Results were expressed in the time taken for corrosion to develop. In these tests, markedly low times were observed for the particular case of the water-based coolants.

Another test method developed at NACE, NACE TM0169-95 [112], deals with the corrosion testing of metals by immersion of the metal test-piece into the corroding solution for a pre-determined amount of time. The experiment's response is measured in terms of the specimen's mass loss and the depth measurement of pits formed, if any. The specimens' mass loss can be then translated into the appropriate corrosion rate units.

NACE's TM0169-95 and other similar tests are widely used for assessing the corrosion resistance of metallic materials [113]. It is also a versatile test in the sense that allows the test equipment components to be modified in order to better suit the needs of a particular investigation. A further advantage is that results expressed in corrosion rates can be more easily related to any previous test results. These advantages tied to its simplicity made NACE's TM0169-95 the most attractive corrosion test for the present research.

Corrosion test procedures

The corrosion test was conducted in accordance with standards NACE's TM0169-95 [112]. The industrial partner provided a sample of a material to be tested, cast iron gr.250 by BS 1452[114], which is commonly used by pump and auxiliary systems manufacturers in their components. This was machined to produce a number of corrosion test coupons of 25 x 50 x 3 mm with a 0.3 μm surface finish.

Initial experimental runs

In the first series of runs, water was used as the corroding solution in order to determine the factors that have more impact on the corrosion resistance of the BS 1452 grey cast iron gr. 250 [114]. The results from these initial runs were then used as benchmark values for the subsequent inhibitors' experimental runs.

In order to obtain the maximum valid information for the minimum use of resources, a 3-factor half fraction 2-level experiment design [115] was used for the initial tests. The control variables used were defined as close as possible to the operating conditions within a spindle system. Usually in the porous-ceramic hydrostatic journal-bearing performance test-rig, the lubricant operational temperatures have been found to range from ambient to a maximum of about 31 °C. Therefore, the temperature variable was set at 22 °C and 40°C for low and high values, respectively. Lubricant flow is expected to happen, and to simulate this condition the stirring speed has been set to 0 and 600 rpm. A third variable was the water type, tap and de-ionized. Although the current bearing performance test rig utilises de-ionized water as the lubricant; in practice, production machines' coolant tanks are more likely to be replenished with tap water.

Table 8 shows the corrosion test variable definition table. Table 9 shows the details of the corrosion test initial experimental runs.

Experimental factors					*Response variable*	
Code	**Name**	**Low**	**High**	**Units**	**Name**	**Units**
A	Water type	Tap	De-ion	---	Corrosion rate	mm/year
B	Temperature	22	40	°C		
C	Stirring speed	0	600	rpm		

Table 8-Corrosion test variable definition table.

Run	A	B	C
1	Low	22°C	600rpm
2	High	22°C	0 rpm
3	Low	40°C	0 rpm
4	High	40°C	600rpm

Table 9-Corrosion test experimental runs.

Further details of the test design, materials and equipment are as follows:

1. Substrate material: cast iron gr.250 by BS 1452
2. Control variables:
   - Inhibitor used.
   - Temperature of the solution.
   - Stirring speed.
3. Exposure time: initially set to 120h in accordance to standard and preliminary tests.
4. Equipment used:
   - 1 litre capacity flask.
   - Bibby HB 502 hot plate/magnetic stirrer with the following characteristics:

     i. Maximum temperature: 450 °C.

     ii. Speed range: 0-2000 rpm.

   - K type thermocouple, attached to an electronic Tempcon 1200 reader. This arrangement was double-checked against a previously calibrated thermometer.
   - Sartorious 5-digit electronic balance.
   - Digital calliper.

Experimental runs with machining coolants and corrosion inhibitors

Once the effect of the variables was identified, a series of experimental runs adding the corrosion inhibitors under the most severe conditions was prepared, using the same test equipment.

Two commercially available coolants containing corrosion inhibitors and a galvanic corrosion inhibitor were readily available from within SIMS for testing (Figure 30). These were diluted to the manufacturer's recommendation, shown in Table 10. The inhibitors' datasheets are provided in the appendices.

Inhibitor	Manufacturer's recommended dilution	Use
Dowell	1:50	Machining coolant
Thaumakool	1:65	Machining coolant
Nalco 2536	1:100	Industrial galvanic corrosion inhibitor

Table 10- Coolants and galvanic corrosion inhibitor available for corrosion testing.

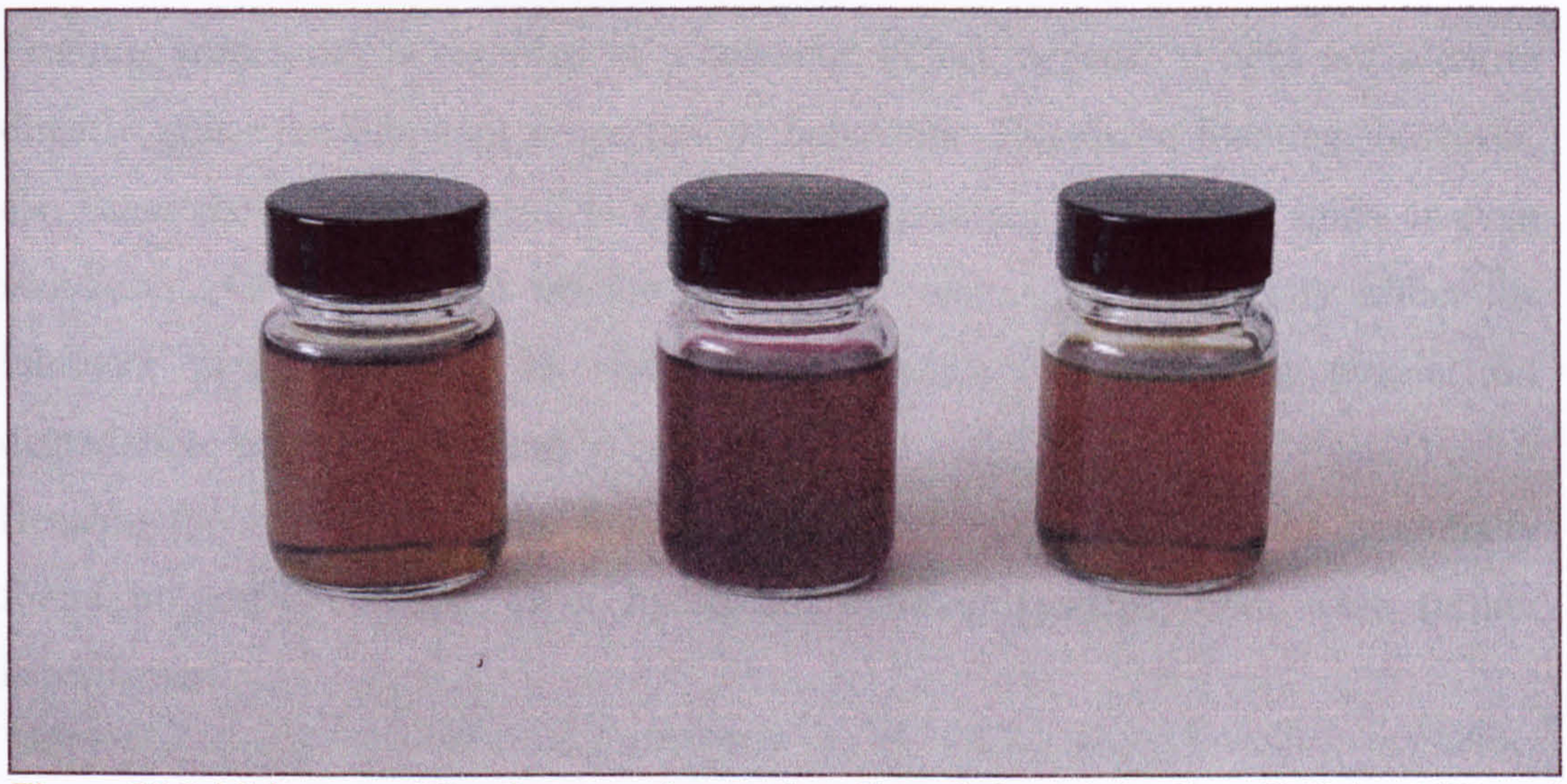

Figure 30-Inhibitors used for the corrosion testing. From left to right: Dowell, Nalco 2536 and Thaumakool.

4.5.2 Foaming test

Coolants and inhibitors often contain detergents and additives. Hence, it was reasonable to expect some degree of foaming if these were added to the water in a porous-ceramic bearing spindle system.

Technically, the term 'foaming' refers to a large amount of air enclosed in thin films of oil to form a low oil content structure on the surface of the oil [116], although the term is also indiscriminately used to describe the air entrainment phenomenon. In difference with foaming, air entrainment is a phenomenon in which a smaller amount of air is dispersed throughout the bulk of the oil in the form of extremely small bubbles. The two phenomena are considered separate, because the practical problems arising from both are quite different, although they maybe obviously related.
Paradoxically, in trying to control the foaming phenomenon through the addition of certain silicone-based anti-foam agents, an adverse effect on the air release rates has been noted [117].

Foaming sometimes is regarded as a cosmetic defect, because it does not seem to directly affect the lubricant properties or behaviour. Excessive foaming, however, can cause the oil level control to malfunction, resulting in lubricant spills or even starvation. Air entrainment on the other hand, not only can directly affect the lubricant properties such as viscosity or density [117], causing general oil degradation, but it can also lead to cavitation.
Because the two phenomena, foaming and air entrainment, could be potentially found in porous-ceramic water hydrostatic bearing systems, both were further investigated.

Methods for measuring foaming

When considering foaming tests it is found that the ASTM D892 [118] method is universally used. This method provides an empirical rating of the foaming characteristics of a lubricant under specified temperature conditions. Basically, the method consists of blowing a metered volume of dry air through a diffuser immersed

in the test-liquid for a period of five minutes. The results are reported as foam volume, in mm, at the end of the blowing and settling periods for three or more sequences.

Methods for measuring air release properties

The number of standard methods for measuring air release properties of oils is limited. Amongst these the most widely known and accepted is the ASTM D3427 [119] test. Through this test, the ability of a lubricant to release entrained air at a controlled temperature can be determined. Compressed air is blown through the sample for 7 minutes, and the time taken to release the entrained air is recorded. The value of the entrained air is determined from sample measurements with a density balance.

Other less used methods for measuring air release properties are the Deutsche shell air release and the AEG air release tests, which are described in more detail by Claxton [116]. Because these methods are either less accurate and/or their results are more dependant on the operator's interpretation than the ASTM D3427 test, their utilization here was not further pursued

Finally, other researchers have also designed their own custom tests [117] seeking to duplicate more closely the real operational conditions for a given application. The same can be said for foaming tests.

Foaming and air release properties procedures

For the present research project, the analysis of the formation of foam and release of entrain air was conducted via three different routes. Foaming was assessed through ASTM D892 [118], whereas air release properties were measured via ASTM D3427 [119]. In addition to these standard tests, a custom test was also conducted using the porous-ceramic hydrostatic journal-bearing performance test-rig, to observe the foaming and air release behaviour of a water-based coolant when used as lubricant in a spindle system.

Foaming test

The foaming test was conducted in accordance with ASTM D892 [118]. A test rig based on the standard's description was put together. Figure 31 illustrates the basic principle and apparatus required for the measurement of foaming.

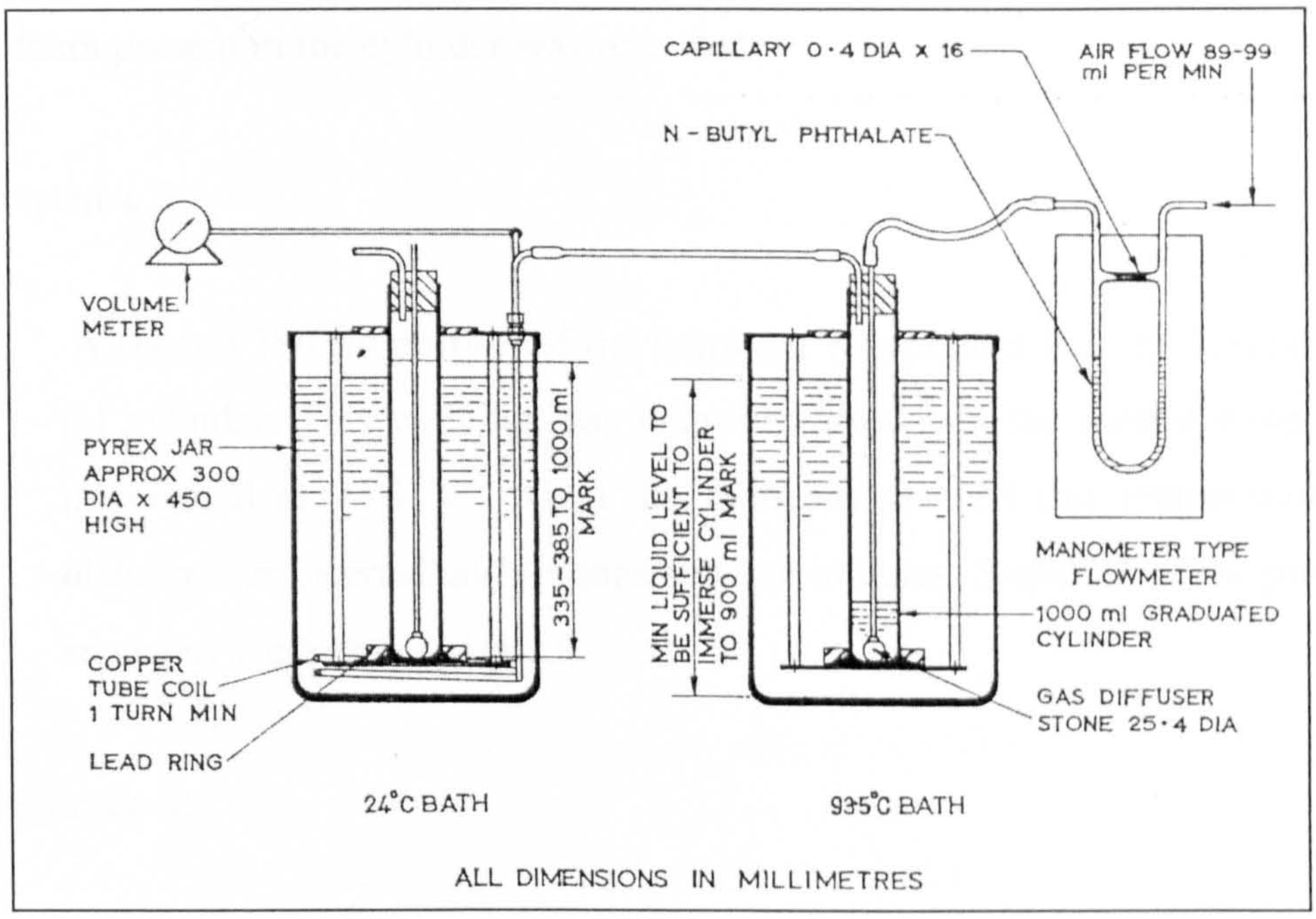

Figure 31-Foaming test basic principle and apparatus, from reference [118].

The required glasswork was custom made to suit the procedure's description; and the diffusers were acquired from an ASTM authorized supplier. The calibration certificates for the diffusers and the flow meters used can be found in appendix 3. The ASTM compliant immersion thermometers were previously calibrated against iced and boiling water.

Procedure

- Sequence 1:

1. 190 ml of previously heated lubricant (to 49 ± 3 °C) was poured into one of the 1000 ml cylinder. The cylinder was then immersed in the water bath.

2. Once the lubricant reached the water bath temperature (24 ± 0.5 °C), the diffuser was inserted and let soak for five minutes.
3. The air was allowed to flow through the diffuser at a rate of 94 ± 5 ml/min for five minutes, timed from the first appearance of air bubbles.
4. The volume of foam present was recorded, immediately after shutting the air.
5. The cylinder was allowed to stand for ten minutes, and again the volume of foam present in the cylinder was recorded.

- Sequence 2:

1. A second 180 ml portion of the lubricant was poured into the second 1000 ml cylinder. This cylinder was then immersed into the second water bath, maintained at 93.5 °C. When the lubricant reached this temperature, the diffuser was inserted and let soak for five minutes. Steps 3-5 of the previous sequence were then repeated.

- Sequence 3:

1. After all the foam from the previous sequence collapsed, the cylinder was transferred to the first water bath and allowed to reach the bath's temperature (24 ± 0.5 °C). The lubricant was then subjected again to steps 3-5 of the first sequence.

Air release properties testing

The air release properties of the water based lubricant were studied in accordance with ASTM D3427 [119]. A test rig based on the standard's description was put together. Figure 32 illustrates the basic principle and the apparatus required for the measurement of foaming.

The thermostat of one of the water baths used for the foaming test provided a facility for water recirculation and this was used for the water jacket in the test vessel. Temperature was monitored with previously calibrated ASTM compliant

thermometers. A copper tube coil (1 m long) was immersed into the second water bath; serving as heater for the air. A previously calibrated thermocouple was used for the air temperature monitoring. Both temperatures, water and air, were set to 25° C, in accordance to the standard test.

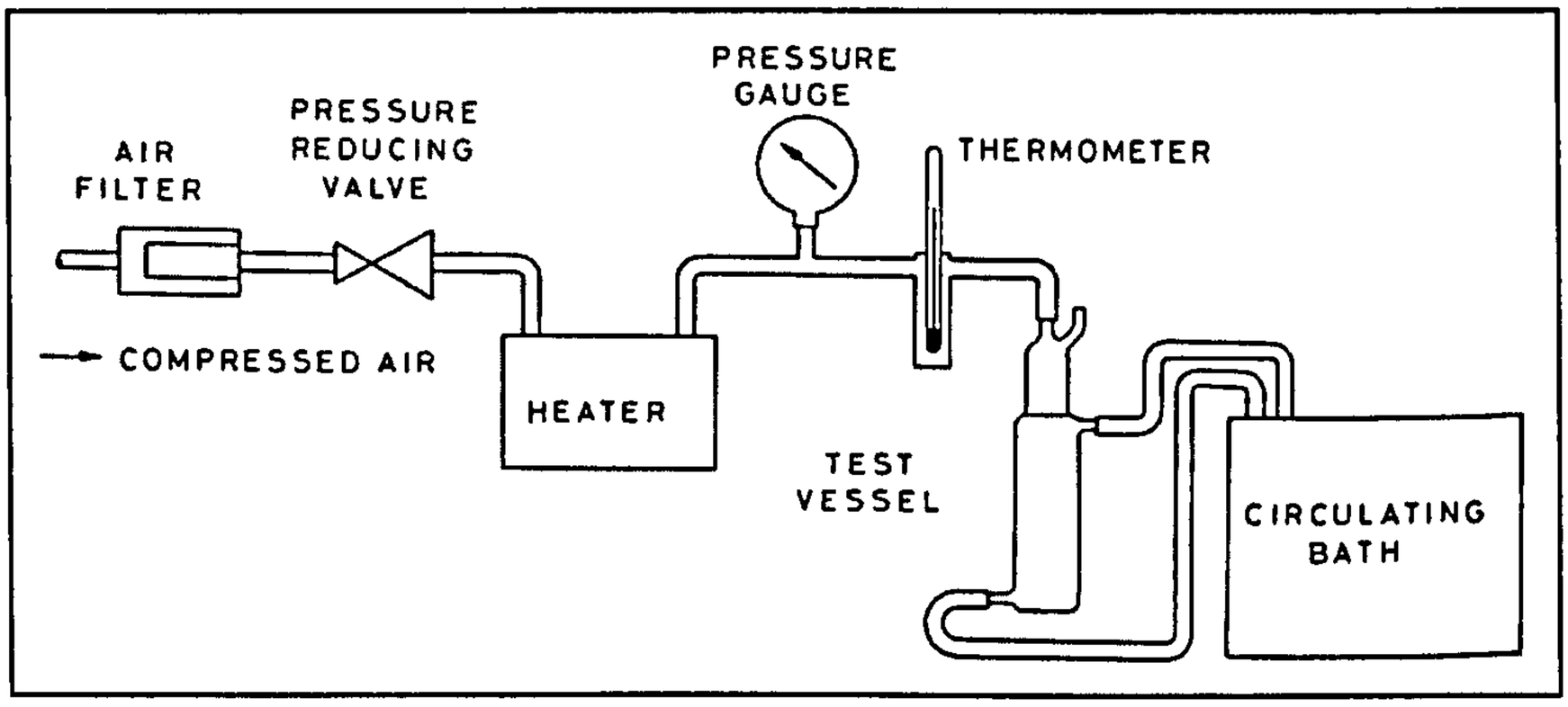

Figure 32-Air release properties basic principle and apparatus, from reference [119].

The required glasswork was custom made to suit the procedure's description (Figure 33). The calibration certificate for the pressure gauge can be found in appendix 3.

Procedure

1. 180 ml of previously heated lubricant (to approximately 35 °C) was poured into the test vessel.
2. Once the lubricant reached the test temperature, the sinker was warmed inside a cylinder submerged on the water bath and hung from the balance's beam approximately 10 mm from the bottom of the vessel.
3. The sinker's weight was recorded.
4. The sinker was replaced with the vessel's air tube. After 5 minutes, air was supplied at 20 k-Pa.
5. After 7 minutes, the air was shut off and the air tube was removed. The sinker was hung again.
6. The time from the shutting of the air until the balance passed the null point was recorded.

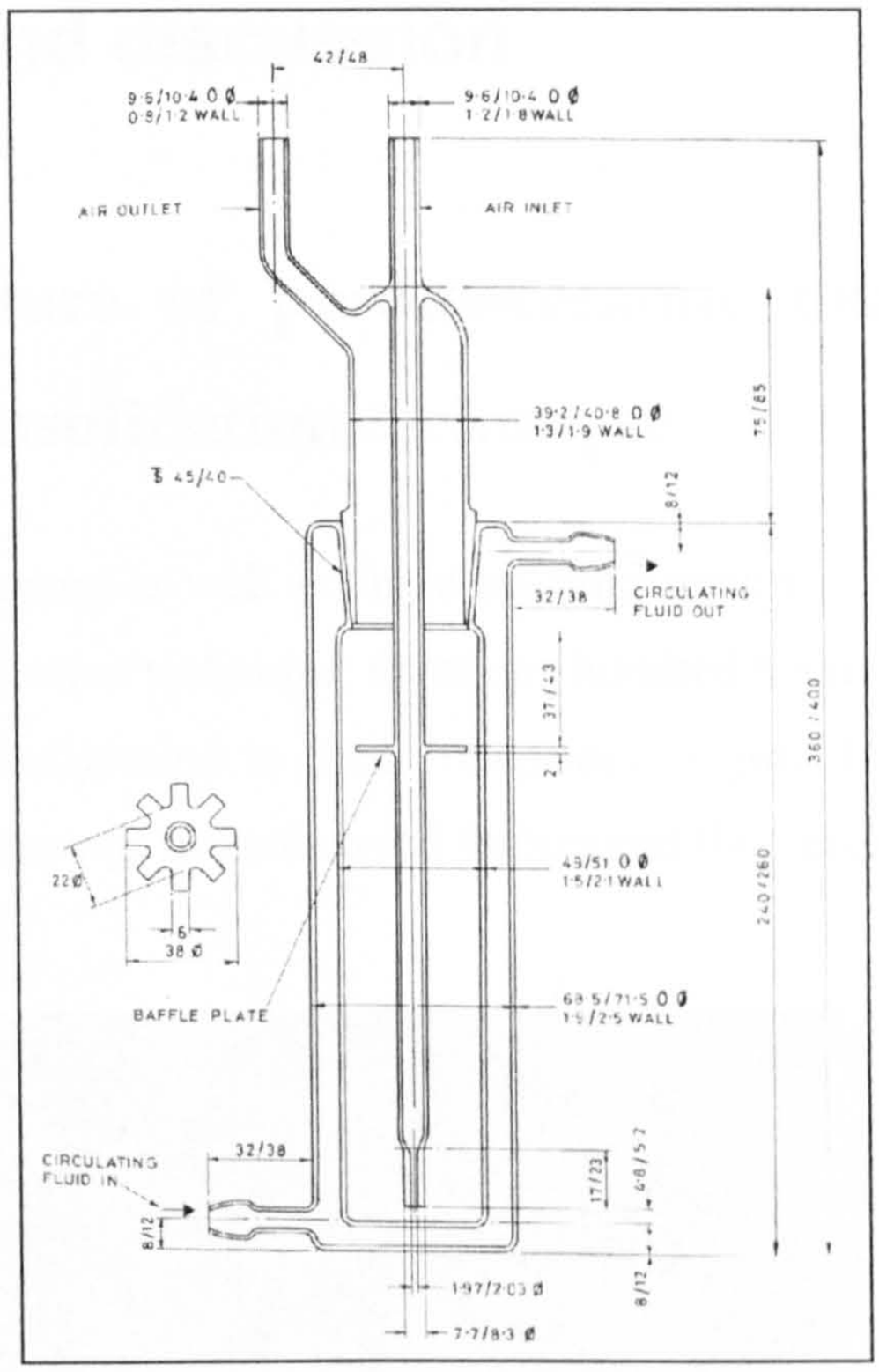

Figure 33-Air release properties test vessel, from reference [119].

Custom foaming test

Dowell, one of the aqueous metal-working fluids used in the corrosion test, was added in a 1:50 dilution to the water on the porous-ceramic hydrostatic journal performance test- rig.

The test consisted of two parts. The first one was to observe the time taken to clear the foam formed on the surface of a sample, as well as on the surface of the return tank. The spindle was run for 1-h periods at different speeds ranging from 1500 to 8000 rpm; in order to observe the range of speeds at which foam forms. Samples were taken from the settling tank, in order to observe possible foam formations closely. The second part of the test was to observe the air release characteristics of the water with added corrosion inhibitors when the spindle is run at higher speeds. The spindle speed was set at 8000 rpm, and samples were taken from the discharge tube in the settling tank. The time to clear the bubbles was observed.

5 Results and discussion

5.1 Manufacture of porous-ceramic bearings by the starch consolidation technique

Journal geometry bearings as well as thrust bearings were successfully manufactured via the starch consolidation technique. Over one hundred bearings of both geometries were manufactured and ground to final dimensions. Figure 34 and Figure 35 show the porous-ceramic bearings manufactured throughout this research.

Figure 34-Porous ceramic journals bearings manufactured by SC technique, 50 mm ID, 62 mm OD and 50mm long.

Once adequate consolidation times were established for each alumina particle size-starch combination, the overall journal bearing-manufacturing success up to the final sintering operation was 78 % throughout this research (over 40 batches). No

reference has been made in this regard in previous porous-ceramic journal bearings research [3]. A success rate of 45-50 %, however, can be inferred from shell HIP moulding records. Hence, the new process developed in the current research has resulted in a significant improvement in reliability.

Figure 35-Porous-ceramic thrust bearings manufactured by the SC technique, Ø 46mm x 7mm thick.

On reviewing the present research's failure causes, it is believed that the success rate could be improved even further in the future. For example, a great percentage of the failed attempts were related to mould leakage at the consolidation stage, which resulted in non-uniform wall thickness and weak castings that cracked in subsequent processing stages. Relatively simple moulds have been employed here, but more sophisticated features such as gaskets or O-rings, could be easily implemented to improve the SC process.

5.1.1 Experiments with different alumina sizes and starch volume fractions

It was expected that through a combination of powder size and starch content a range of porosity levels would be achieved, enabling the tailoring of the bearing porosity to suit particular bearing applications.

Porous ceramic bearings were successfully produced using 0.5, 1, 2, 3, and 4 μm alumina particle sizes. Slips based on 7-μm alumina, however, proved unsuccessful as these invariably segregated before the casting step. Reducing the water content in the mixture proved unsuccessful.

On the other hand, the manufacture of porous-ceramic bearings proved reliable up to a limit of 40 % by volume of the starch content. Beyond this, the ceramic/starch castings, particularly journal bearings, proved to be too soft for demoulding, resulting in deformed or cracked shells. Journal bearings at higher starch contents (50-60 vol. %) were only successfully produced with alumina sizes of 0.5 and 1 μm. This is probably due to the intrinsic better particle packing associated with the smaller particle sizes, giving strength to the casting.

The simpler thrust bearings' geometry resulted in a simpler demoulding process, leading to a higher success rate at the higher end of the starch content. For the particular case of the 0.5-μm alumina, starch contents below 40 % vol. resulted in bearings with a relatively high density and low permeability; and therefore their manufacture at lower starch contents for this alumina size was not further pursued.

Table 11 and Table 12 illustrate the number of bearings manufactured for each combination alumina particle size/starch content, based on a solids loading of 59.1 volumetric %, for journal and thrust bearings, respectively.

Powder size µm	10%	20%	30%	40%	50%	60%
0.5	-	-	1	1	1	1
1	2	2	1	1	1	-
2	1	1	1	1	-	-
3	1	2	1	1	-	-
4	1	2	1	2	-	-

Table 11- Porous-ceramic journal bearings manufactured by the SC technique. Quantity produced by each slip powder composition.

Powder size µm	10%	20%	30%	40%	50%	60%
0.5	-	-	1	2	5	1
1	5	5	1	4	2	-
2	1	1	1	3	1	-
3	1	3	2	4	-	-
4	5	9	3	3	3	3

Table 12- Porous-ceramic thrust bearings manufactured by the SC technique. Quantity produced by each slip powder composition.

The greater amount of thrust bearings produced only reflects the fact that more moulds were readily available for thrust bearings to be cast, as opposed to only one available for 50 mm ID journal-bearings. In addition, a ball-milling pot loaded with approximately 500 g of powders, a standard measure throughout the manufacturing phase, was enough to produce several thrust bearings but only one of the 50 mm ID journal bearings.

5.1.2 SC journal bearings manufacture cost analysis

Tooling costs

The cost of a 5-part set of moulds for a journal bearing geometry of 62 mm OD, 50 mm ID and a length of 50 mm, including additional demoulding jigs, made of aluminium stock was £ 450.00. This was used to produce over 35 castings. In this

exercise, however, in order to provide a basis for comparison with previous research [3], the cost of the tooling is considered to be amortized by producing 25 bearings.

Materials and processing costs

The materials and processing costs for producing a single 50 mm shell are presented in Table 13:

Quantity	Description	Price (£)
1	Raw materials	0.28
1	Tooling cost	18.00
1	Mould cleaning and preparation (£28/hr)	14.00
1	Slip preparation (£28/hr)	28.00
1	Casting and demoulding operations (£28/hr)	28.00
1	Furnace loading (£28/hr)	5.00
1	Consolidation drying and Sintering operations (£20/hr)	493.33
1	Grinding cost	50.00
	Total	636.61

Table 13- Materials and processing costs for porous-ceramic journal bearings manufactured by the SC technique. VAT not included.

A similar analysis has been conducted for the manufacture of the same bearings via HIPing [3] which resulted in an estimate of £1007.32 per bearing. Hence, by changing the processing from HIPing to starch consolidation the cost for manufacture of a journal bearing of 50 mm ID is reduced by approximately 36 %.

Owing to the highest reliability of the SC technique (previous section), further savings can be achieved in relation to the HIPing process in the long run. For example, the cost for completing a 10-bearing lot using HIPing as manufacturing route, under the current conditions, ascends to approximately £ 20,000.00. In contrast, the cost for the same lot would cost approximately £ 8,400.00 using the SC technique, resulting in further 22 % savings.

5.1.3 Manufacture of larger bearings

At a later stage in this research, and in anticipation to the industrial sponsor's requirement for larger bearings, two journal bearings, one with an ID of 80 mm, OD of 96 mm and 62 mm long and a second with an 85 mm ID, a 101mm OD and 82 mm long were manufactured with the same procedure previously described for the 50 mm ID journals. The only difference was an additional half an hour during the consolidation stage to compensate for the additional slip amount (approximately 300 g more of powders than the smaller journal bearings).

Figure 36- Larger bearings manufactured via the SC technique. Journal to the left dimensions: ID of 80 mm, OD of 96 mm and 62 mm long. Journal to the right dimensions: 85 mm ID, a 101mm OD and 82 mm long.

The achievement of these geometries demonstrated the flexibility of the SC consolidation method, while expanding the range for porous ceramic journal applications, as only 50 mm ID journal had been previously attempted [3].

5.1.4 Rheological measurements

Initially, rheological measurements were only intended as a quality control tool for monitoring the ceramic-starch slip consistency. Preliminary trials revealed that slips based on an alumina size of 4 μm and a starch volumetric content of 20 % yielded bearings with near the optimum properties for journal bearings for ultra-precision applications. In parallel with the manufacture of bearings based on these slips, rheological measurements were also conducted. The results of four different viscosity measurements for four different ceramic slips with the same powder combination and processing conditions proved to be relatively close between each other, with their viscosity values ranging from 108 to 124 milli-Pa·s.

On extending the measurements to the different alumina-size combinations, trends started to become noticeable. Figure 37 shows the viscosity values obtained for all the slip combinations of alumina size and starch contents that were subjected to measurements at a shear rate of 100 s^{-1}. Lyckfeldt [70] argues that at this shear rate the hydrodynamic forces dominate and the factors influencing the viscosity are essentially the solids loading, the particle morphology and size distribution.

Over twenty rheological measurements were performed. From Figure 37 it can be observed that viscosity decreased as the starch content increased, for the 0.5, 1 and 2 μm alumina-starch slips. After reaching its lowest value, viscosity is seen to increase again.

A set of results obtained by Lyckfeldt [70] have been added for reference, and these also show a similar trend. Lyckfeldt argues that the increasing amount of starch particles have a much smaller surface area than the alumina particles, and therefore less exposure towards the liquid phase. Hence the reduction observed in the viscosity's trend-lines. For the sudden increase in viscosity observed at the higher starch contents, the water uptake characteristics of the starch particles are cited, along with the possibility of having exceeded the optimum particle packing [70].

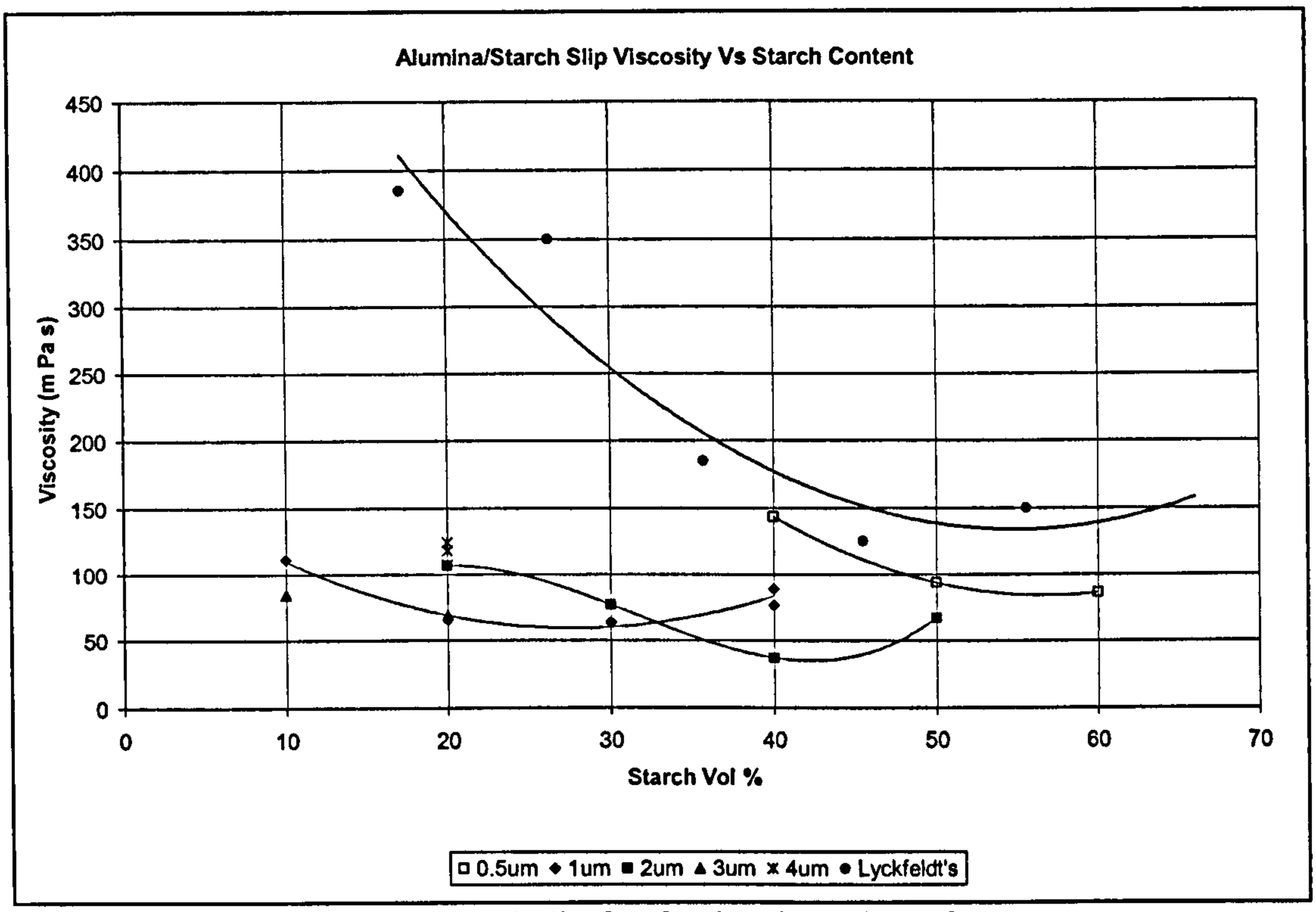

Figure 37- Viscosity of alumina-starch slips by alumina size and starch content.

The present research viscosity trend-lines shown in Figure 37, seem to support Lyckfeldt's justification, not only in relation to the increased amount of starch accompanied by a declining viscosity, but in the sense that the viscosity of the slips also reduced when the alumina powder was substituted with a larger alumina size, and vice versa. For a given solids loading, the number of particles of each larger alumina size is lower, as is the surface area exposed towards the liquid phase; hence the reduction in the viscosity. Table 6 shows the specific surface area for each alumina particle size as provided by the manufacturer.

As with Lyckfeldt's investigation [70], the slip viscosity seems to be influenced by the total exposed surface area of the solids, the possible existence of an optimum particle packing and the water uptake characteristics of the maize starch. The first factor dominates at the lower starch contents, where the decreasing exposure of particle surface area results in a decreasing viscosity. The other two factors seem to

dominate at the higher starch contents, varying for each alumina particle size, at which viscosity seems to increase with increasing starch contents.

Unfortunately, due to a temporary unavailability of the rheometer at the time, extending the rheological studies for the full range of alumina size/starch volume-fraction slips was not possible. However, the number of measurements and the trends observed were considered representative of the alumina/starch slips' rheological behaviour.

Overall, the monitoring of the rheological behaviour was important to ensure the appropriate processing of bearings. The viscosity of an alumina-starch slip needed to be low enough to permit the adequate casting of the bearing without entrapping air, while at the same time, high enough to prevent segregation during the consolidation stage. In this sense, the full range of slip viscosities observed in the present study, (0.143 to 0.037 Pa·s) proved to be successful for the manufacture of porous ceramic bearings.

5.1.5 Linear shrinkage

Linear shrinkage calculations were important at the initial stages of the manufacturing research in order to design the moulds. These measurements were conducted in accordance with ASTM C326-82 [89]. A total of 18 cylinders, Ø 25 x 100 mm long, were processed.

Figure 38 shows the different shrinkage percentages for each of the alumina size/starch content combinations in relation to the volumetric starch content used in each ceramic slip. Although the number of specimens produced for this test, at this stage was limited, two distinctive trends could be observed. The first with the steepest slope, describes the shrinkage behaviour of the 0.5 μm alumina slips at 40-60 % volumetric starch contents. A second trend can be observed for the larger alumina sizes, 1, 2, 3 and 4 μm, describing parallel almost-flat trend-lines for each (trend-lines have been omitted for clarity).

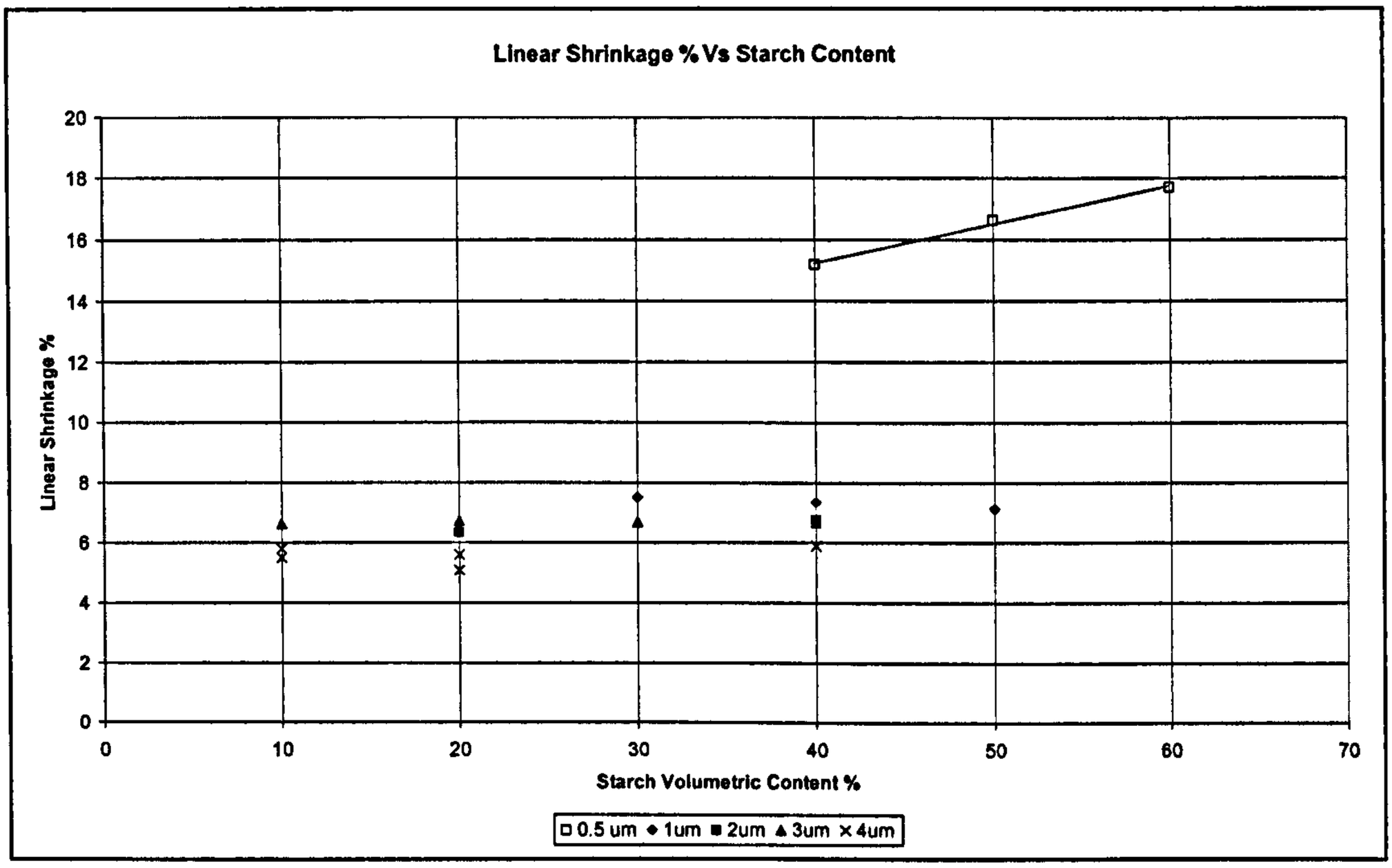

Figure 38- Linear shrinkage of cylinders by alumina size and starch content.

The higher shrinkage rates of the 0.5 μm alumina based cylinders reflect the influence of both the alumina particle size sintering behaviour and the amount of starch. The offset of this alumina size trend-line in relation to the other alumina sizes is mainly a result of the more rapid sintering rate characteristics of the 0.5 μm alumina, for which the density is expected to reach 98% under the selected sintering conditions, according to the manufacturer's datasheet (appendix 2).

On the other hand, the influence of the original slip's starch content on the shrinkage is represented by the trend-line's slope. This, as shown in Figure 38, increases with an increased amount of starch for the 0.5 μm alumina cylinders only. A similar observation was made by Lyckfeldt [70], who used a similar alumina size in his experiments. The reason for this may be that the castings with the higher starch content were naturally less dense, and these would further shrink during firing due to the larger void space existing between the matrix particles.

The larger (from 1 to 4 μm) alumina sizes' trend-lines indicate only a marginal influence of the starch content for the selected sintering conditions. The shrinkage rates for the cylinders produced with these alumina sizes were mainly influenced by

the alumina particle characteristic sintering behaviour, which resulted in lower shrinkage rates for the larger alumina sizes, as expected.

The best fit lines' equations for the shrinkage observed for each alumina particle size were of the form:

Equation 15

$$S_l = a \cdot S_v + b$$

S_l	sintering shrinkage (%)
a	empirical constant
Sv	starch volumetric percentage (%)
b	empirical constant

The results of the curve fitting are summarized in Table 14.

Alumina powder size (µm)	m	b
0.5	0.13	10.17
1	-0.02	8.04
2	0.02	5.93
3	0.001	6.65
4	0.01	5.42

Table 14-Curve fitting results for linear shrinkage by particle size.

Equation 15 together with Table 14 may prove helpful to the porous bearing designer wishing calculate an estimate of the shrinkage values starting from the alumina particle size and the starch content, in order to determine the correct size of the moulds.

Figure 39 shows the cylinders for all the alumina particle sizes for a fixed amount of starch of vol. 40 %. This clearly shows the higher shrinkage of the 0.5 μm alumina cylinder.

Figure 39-Shrinkage test cylinders after sintering. From left to right 0.5, 1, 2, 3 and 4 μm alumina at a fixed starch content of 40%. The further shrinkage of the 0.5 μm alumina is clearly noticeable.

In general, uniform sintering shrinkage reflects uniform densification of the alumina matrix; and consequently uniform properties across the ceramic body. Uniform shrinkage characteristics are very important for porous-ceramic bearing manufacture as an indirect measure of uniform permeability, as this might directly influence the porous bearings' performance. This aspect will be further discussed in section 5.2.2 of the present chapter.

5.1.6 Processing densification and shrinkage

SC bearings were usually furnace-processed in a single operation that included the drying, binder burnout and sintering stages. However, it was also interesting to investigate the densification and the dimensional changes which occurred throughout the processing. Hence, the diametrical and longitudinal shrinkages, as well as the changes in mass were monitored for a specimen lot consisting of fourteen thrust bearing castings, with different alumina particle size and starch content, for which each processing stage was conducted separately. The castings had a typical diameter of 52 mm and a 10 mm thickness. A digital calliper was employed for the bearings' dimensional measurement. Because of their simpler shape, thrust bearing castings had a more uniform geometry than journal bearings casts, allowing for a more accurate investigation.

SC thrust bearings green and sintering density

The green and sintering densities for the bearing lot studied here, are shown in Figure 40 and Figure 41, respectively, in relation to their starch content for each particle size.

The first thing to notice on the green density chart is that increasing starch content results in a decreasing green density. This behaviour was expected, as the lower density (0.56 g/cm^3) starch powder increasingly replaced the denser alumina (3.98 g/cm^3)

On closer inspection of Figure 40, however, the specimens' green density overall behaviour does not reveal any apparent trends in relation to their alumina particle size. Data points are well grouped with relation to their starch content, the maximum difference in densification for two specimens made with the same starch content and different alumina particle being 0.09 g/cm^3. A possible explanation is that the effect of the alumina particle size at this stage of the processing is negligible.

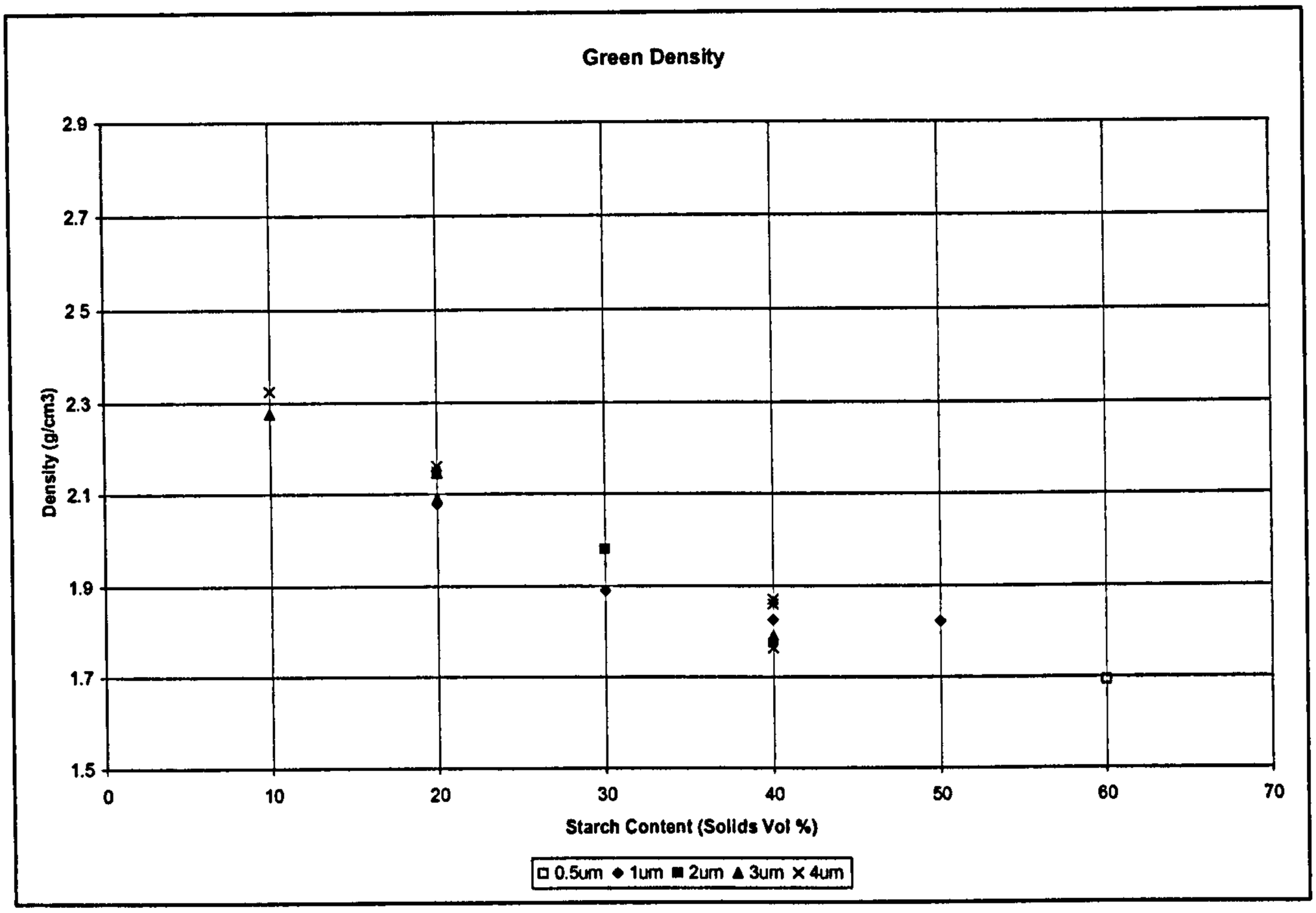

Figure 40-Thrust bearings green density.

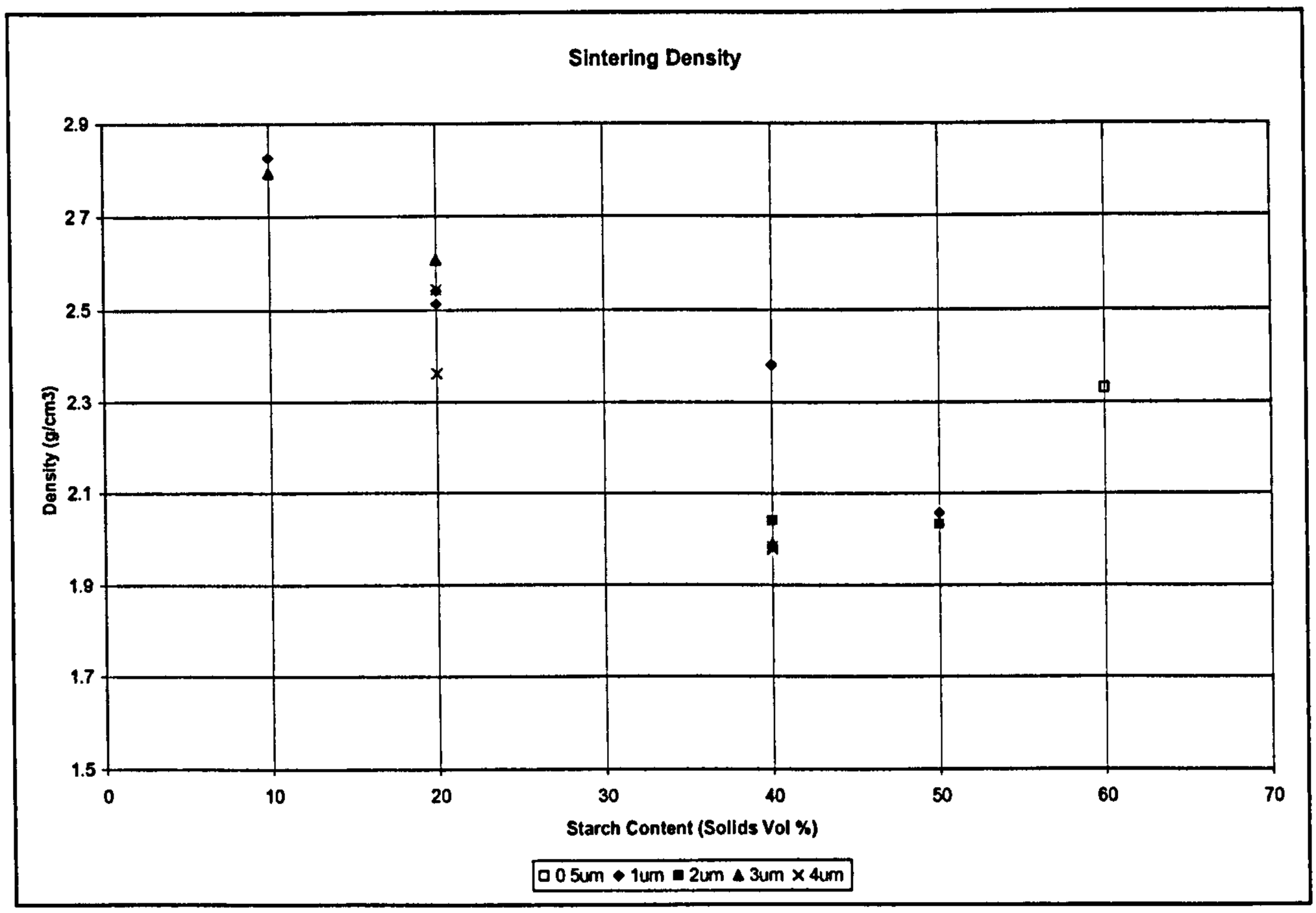

Figure 41-Thrust Bearings sintering density.

Since there is no powder compaction operation associated with this manufacturing procedure, the specimens' green density was expected to be influenced mainly by the slip powders', alumina and starch, particles packing. In this sense, McGeary [120] studied particle packing for binary mixtures and found the optimum packing for an idealized experiment to occur when the ratio between the coarse and the finer particle size diameter was around 7. Below this, the compact density decreased rapidly. On the other hand, higher values of this ratio were observed to have an almost negligible effect.

In this research, powder packing was not conducted in idealized conditions. However it was reasonable to expect a similar packing behaviour as the one noted by McGeary, observing a lower overall density, resulting from the absence of a powder vibration stage. Considering an estimate of 20 μm for the starch particle diameter, then the resulting coarse to finer particle diameter ratio is relatively large for the alumina powders used here (0.5 to 4 μm), ranging from 40 to 5, which is probably beyond the corresponding optimum value. Hence the little effect of the alumina particle size, as observed in Figure 40.

At the sintering stage, however, the effect of the alumina particle size is very noticeable. The specimens' density increased in accordance with each alumina particle size sintering rate, i.e. the specimens based on the finer alumina size reached higher density, for all starch contents.

From Figure 41, it is also noted that density decreases with an increasing starch content, resulting from the larger number of pores left by the starch particles. This was expected, and is in accordance with all the published SC research. A more thorough study looking at the densities achieved in this part of the processing is presented in the 'porous-ceramic bearing property measurement' section of the present chapter.

Densification

Densification of the porous specimens can be defined as the increase in density after sintering:

Equation 16

$$\delta = \frac{\rho_s}{\rho_g} - 1$$

δ	densification (fraction, dimensionless)
ρ_s	sintering density (g/cm^3)
ρ_g	green density (g/cm^3)

The densification values for the set of specimens studied here are shown in Figure 42 in relation to their original slip solids components.

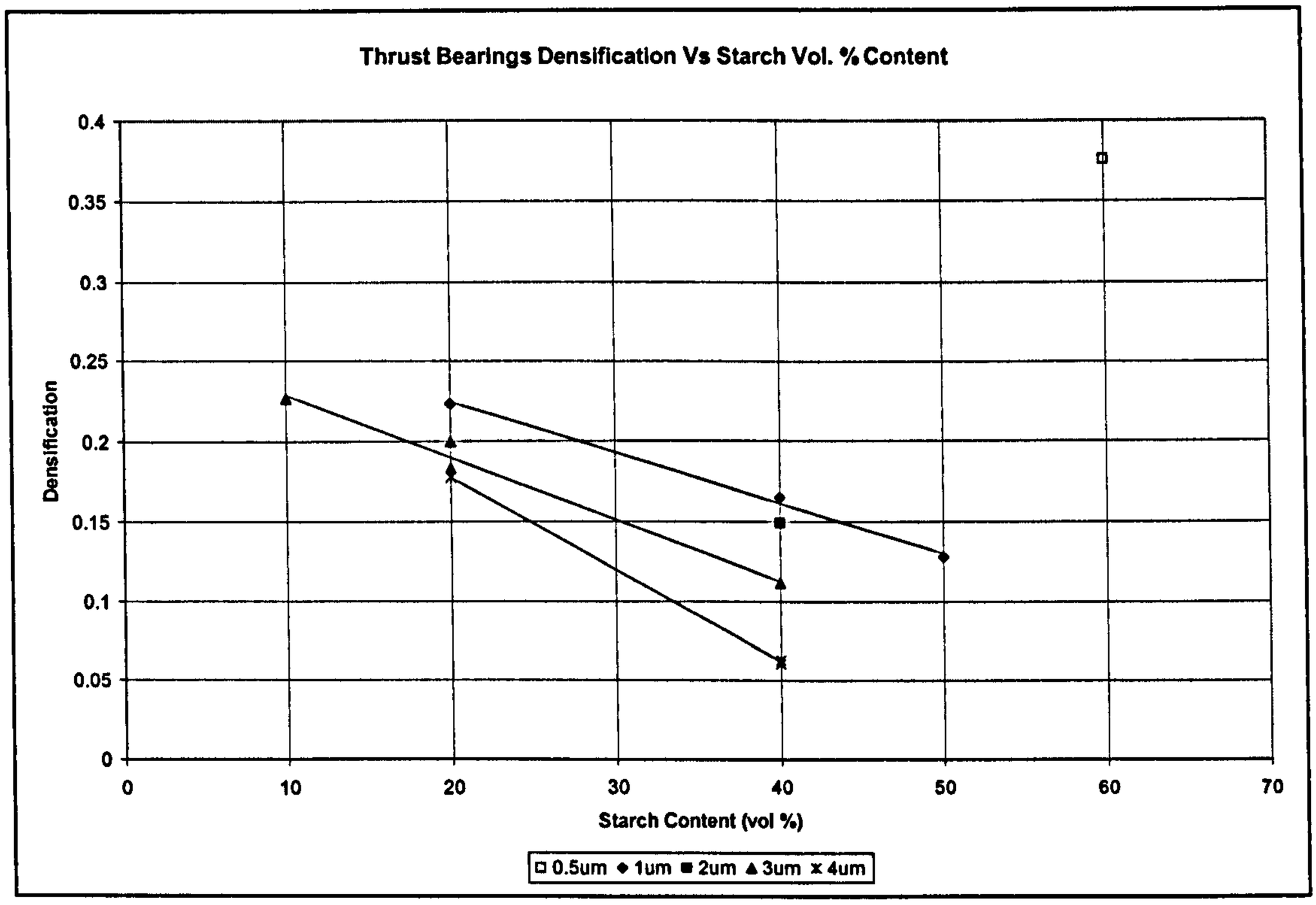

Figure 42-Thrust bearings densification Vs original slip solids components.

As it can be seen from Figure 42, the densification linear trends show a decreasing densification for the increasing starch content. It is also seen that the smaller particle

sizes resulted in a higher densification. Both conditions were expected from the observed behaviour of the sintering density in Figure 41.

Dimensional shrinkage

Dimensional changes that occur after the sintering operation offer a quick assessment as to the degree of sintering that has taken place [121]. The diameter of the green compact and the later sintered specimen were determined by taking four different measurements. Similarly, the specimens' height was determined by taking eight measurements at different places.

Diametrical shrinkage can be defined as:

$$S_{dia} = \frac{D_g - D_f}{D_g}$$

Equation 17

S_{dia}	diametrical shrinkage (dimensionless)
D_g	green compact diameter (mm)
D_f	specimen's OD after sintering (mm)

Longitudinal shrinkage can be defined as:

$$S_{thk} = \frac{th_g - th_f}{th_g}$$

Equation 18

S_{th} longitudinal shrinkage (dimensionless)

D_g green compact thickness (mm)

D_f specimen's thickness after sintering (mm)

In general, shrinkage was of isotropic nature. There was also a good correlation between the diametrical and the longitudinal shrinkages, suggesting good uniformity across the bearings' matrixes; and hence uniformity of the bearings properties, such as density and permeability. This correlation is shown in Figure 43.

The relationship between both measured diametrical and longitudinal shrinkages and densification was generally observed (Figure 44) to have a reasonable correlation with the values obtained through the widely known theoretical relationship [121]:

Equation 19

$$\rho_s = \frac{\rho_g}{(1-\frac{\Delta L}{L_0})^3}$$

ρ_s sintering density (g/cm^3)

ρ_g green density (g/cm^3)

ΔL compact length change from sintering (for both diametrical and longitudinal in mm)

L_0 initial compact length (for both diametrical and longitudinal in mm)

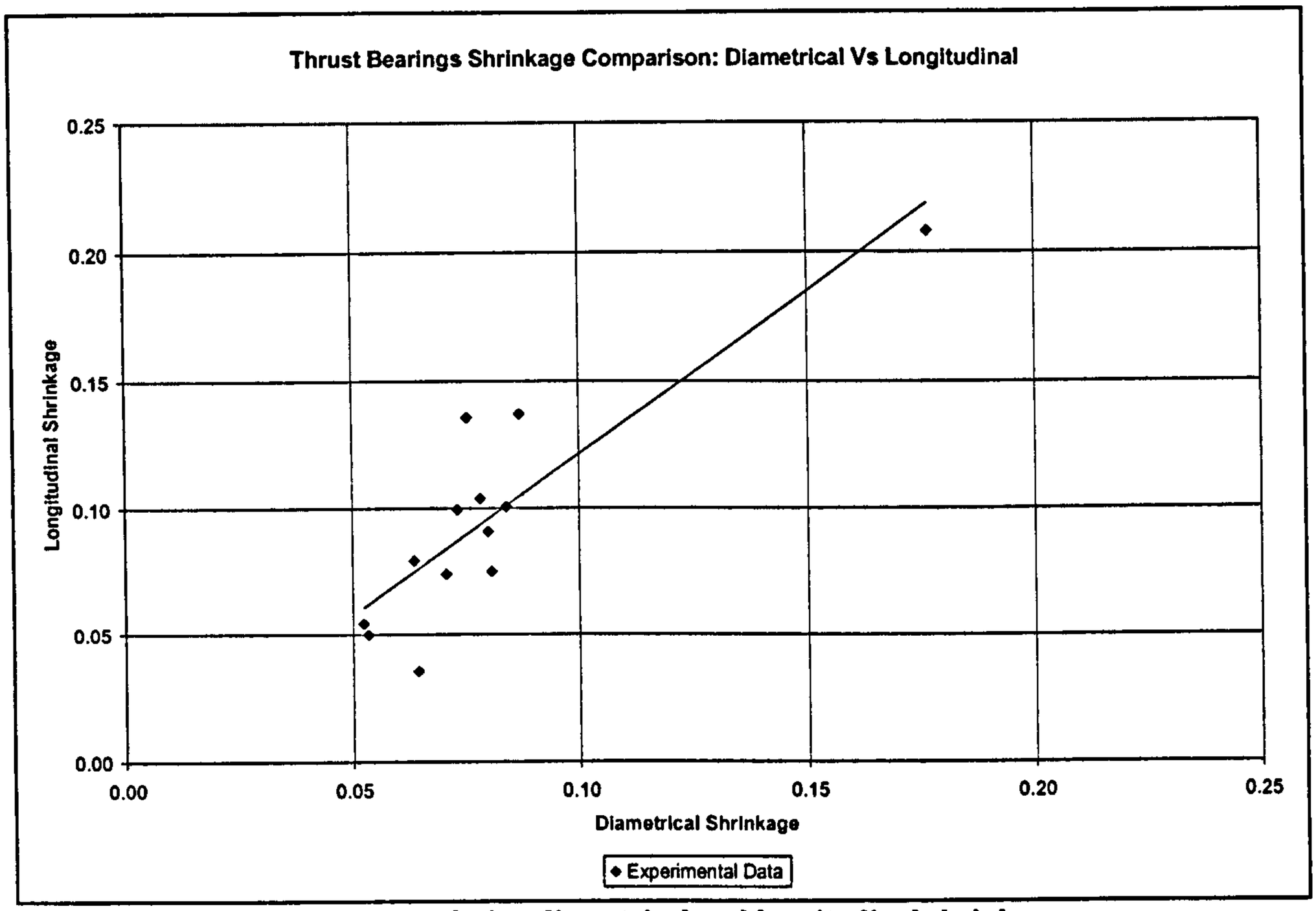

Figure 43-Thrust bearings correlation diametrical and longitudinal shrinkages.

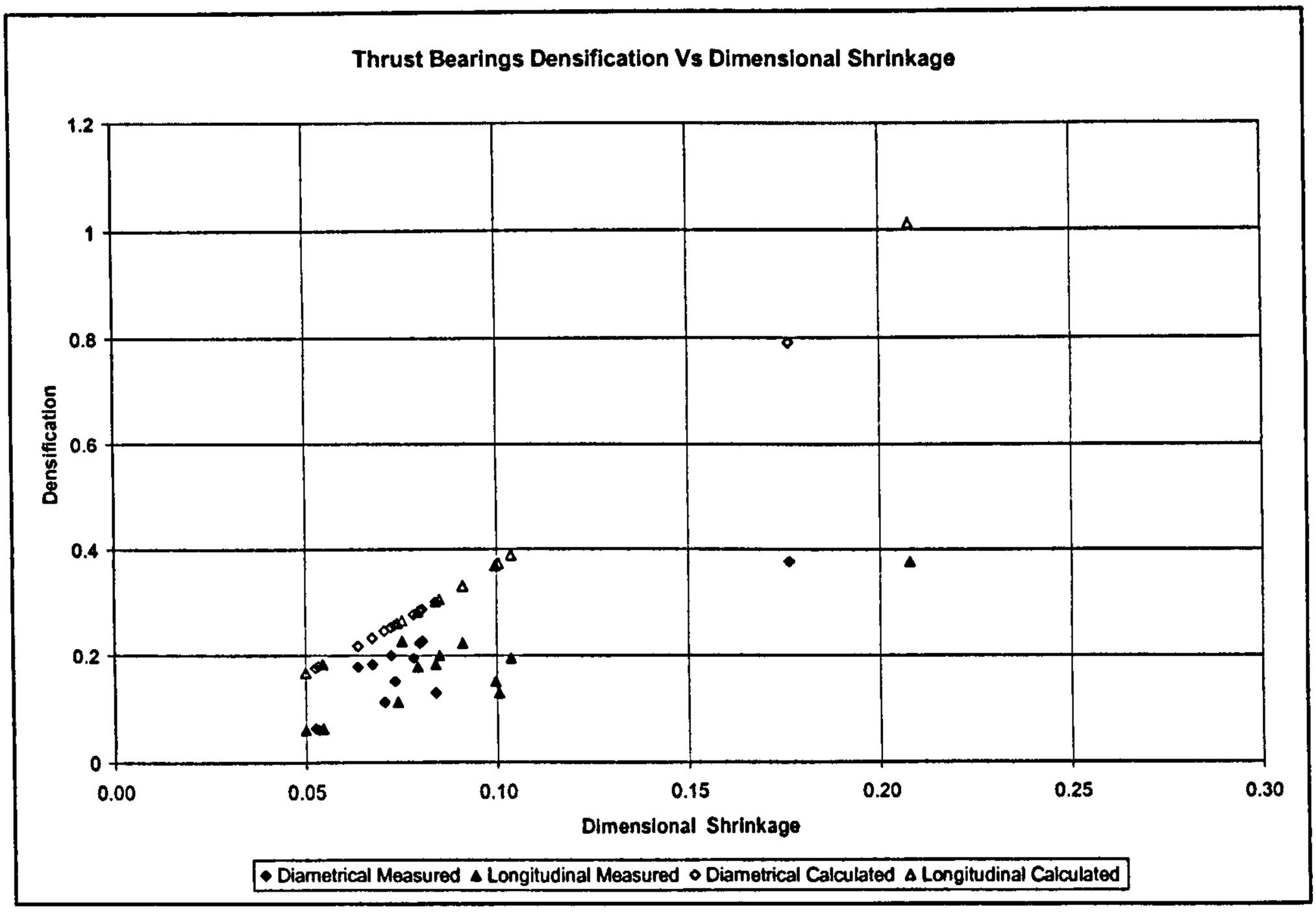

Figure 44- Thrust bearings densification Vs dimensional shrinkage.

At first glance of Figure 44 it is evident that one sample did not adequately follow this relationship for both diametrical and longitudinal shrinkages. This particular specimen was manufactured with a 0.5 μm alumina (60 % vol. starch content). It was believed that the effect of increasing the starch content influenced its divergent behaviour, resulting in a pronounced lower densification from the calculated values.

As shown in the previous shrinkage experiments described in section 5.1.5, the specimens based on a 0.5 μm alumina were the only ones where the effect of the starch content was evident. Typically for this particle size, increasing the starch content resulted in an increasing shrinkage rate accompanied by a decrease in density. As observed before, the castings with higher starch content were naturally less dense, and these would further shrink during firing due to the larger void space existing between the matrix particles. However, this did not necessarily result in higher densification. Hence, densification of such specimens can not be accurately represented through Equation 19.

However on closer inspection of Figure 44, it can be noted that a general deviation exists between the measured (lower) and the calculated figures. This suggests that overall, the addition of starch obstructs the further densification of the ceramic matrix. This is logical, as for the measured densifications, the measured value for ρs is indeed influenced by the amount of starch, resulting from the specimens' increasing change of mass which occurs at the binder burnout stage, causing the noted deviations.

Nonetheless, Equation 19 may be used to estimate either the densification or the shrinkage for SC bearings at lower densification and shrinkage values. However, a more accurate relationship was found by curve fitting the measured values, resulting in a linear equation of the form:

Equation 20

$$\delta = 1.794 \cdot \frac{\Delta L}{L_0} + 0.0093$$

δ	densification (fraction, dimensionless)
ΔL	compact length change from sintering (both diametrical and longitudinal in mm)
L_0	initial compact length (both diametrical and longitudinal in mm)

It is interesting to note that the shrinkage values obtained in the present exercise, Figure 44, are consistent with the previous shrinkage percentages observed in Figure 38. The information obtained in section 5.1.5 was then used to predict the specimens' shrinkage based on a larger sample size. Curve fitting of the obtained values for constants *a* and *b* (Table 14) yields the following relationship:

Equation 21

$$a = -0.0238 \cdot d_w^3 + 0.1833 \cdot d_w^2 - 0.4204 \cdot d_w + 0.2796$$

Equation 22

$$b = -0.5395 \cdot d_w^3 + 4.1821 \cdot d_w^2 - 10.355 \cdot d_w + 14.489$$

d_w alumina powder mean particle size

By using equations 20-22 together with Equation 15, a bearing designer can estimate the densification and shrinkage for SC bearings, based on the initial starch content and the alumina particle size. The magnitude of the maximum error from this set of equations in relation to the measured densification for all the alumina particle size specimens including 0.5 μm was 0.08, providing a more accurate and comprehensive prediction than the one observed by employing Equation 19.

Sintered body microstructure

Scanning electron microscopy was used to examine the microstructure of several SC bearings. The micrographs illustrating this part of the study are presented in section 5.2.3.

SC bearings mass loss at binder burnout

The specimens' change of mass after the binder burnout operation from the green state mass was monitored. At the end of this processing stage the bearings were removed from the furnace and their weight was recorded. It was expected that a mass loss proportional to the amount of starch in the slip would be observed.

From a processing point of view, SC bodies in which starch has been burnout off become 'softer' as well as 'chalky' in appearance; and hence more prone to breaking. Dimensional measurement of the bearings was performed very carefully in order to avoid damaging the specimens. From the green to the 'brown' (after binder burnout) density, dimensional changes were negligible (a maximum of 0.1 mm was measured). Because of this, mass loss at this stage is only considered to reflect the absence of the starch particles. Figure 45 illustrates the mass change expressed in weight mass percentage in relation to the starch content and the alumina particle size. It can also be seen that, at this stage the influence of the specimens' alumina particle has yet to become noticeable.

From Figure 45 it can also be seen that the measured weight loss percentage follows closely the theoretical values originally calculated from the slip formulation. This

suggests that the errors induced at the initial processing stages are minimal, giving confidence in the overall reliability of the SC technique.

A change in mass from the binder burnout to the sintering stage was also observed for all the specimens, although this was very small in magnitude when compared with the mass loss observed in the previous processing stage, ranging from 0.09 to 0.23 g; however no obvious trend was observed. This small mass changes may be related to the final densification achieved at the sintering stage, where a small amount of the remaining porosity is further reduced.

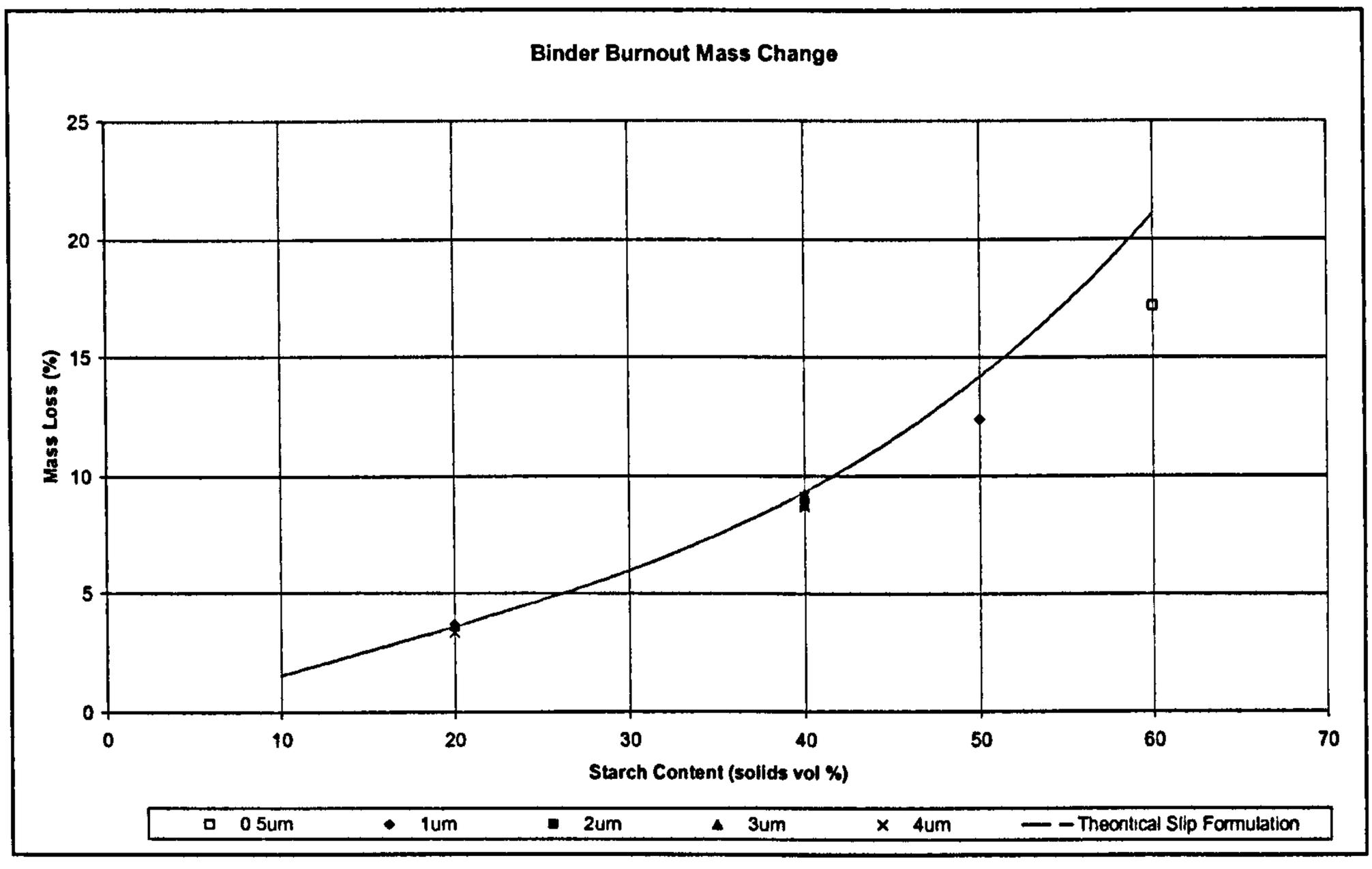

Figure 45-SC specimens weight loss during binder burnout Vs starch content and particle size.

5.2 Porous-ceramic bearings property measurements

5.2.1 Density and porosity measurements

In previous porous-ceramic bearing research [3] [30] [31], the permeability of the bearings as well as the structural properties were noted to vary linearly with their density/porosity; hence the importance of these measurements.

The density of the fired components was measured via a modified version of BS 5600 [90], as described in a previous chapter. The bearings' relative density shown in subsequent figures has been calculated based on a 3.98 g/cm^3 value for full density alumina. Total porosity, on the other hand, can be defined by the following formula:

Equation 23

$$\varsigma = 100 - Br$$

ς	total porosity (%)
Br	specimen's relative density (%)

Journal shell density

Figure 46 illustrates the variation of the relative density with starch content of twenty-six fired 50 mm ID, 62 mm OD x 50 mm-long journal bearings.
Depending on the alumina size and the starch content of the original slips, the density of the journal bearings varied between 51 and 81% of the full density.

From Figure 46, it is quite evident that there is a direct relationship between the bearings' density and the amount of starch present in the original starch. Higher starch content resulted in lower density bearings, and vice versa. Roughly, a decrement of 5% in the bearings' density resulted for each 10 % vol. starch increment. This effect was expected, as the increasing amount of starch burned in a previous processing stage, leaves an increasing number of voids within the ceramic matrix. The same effect has been also reported by other authors [70] [81].

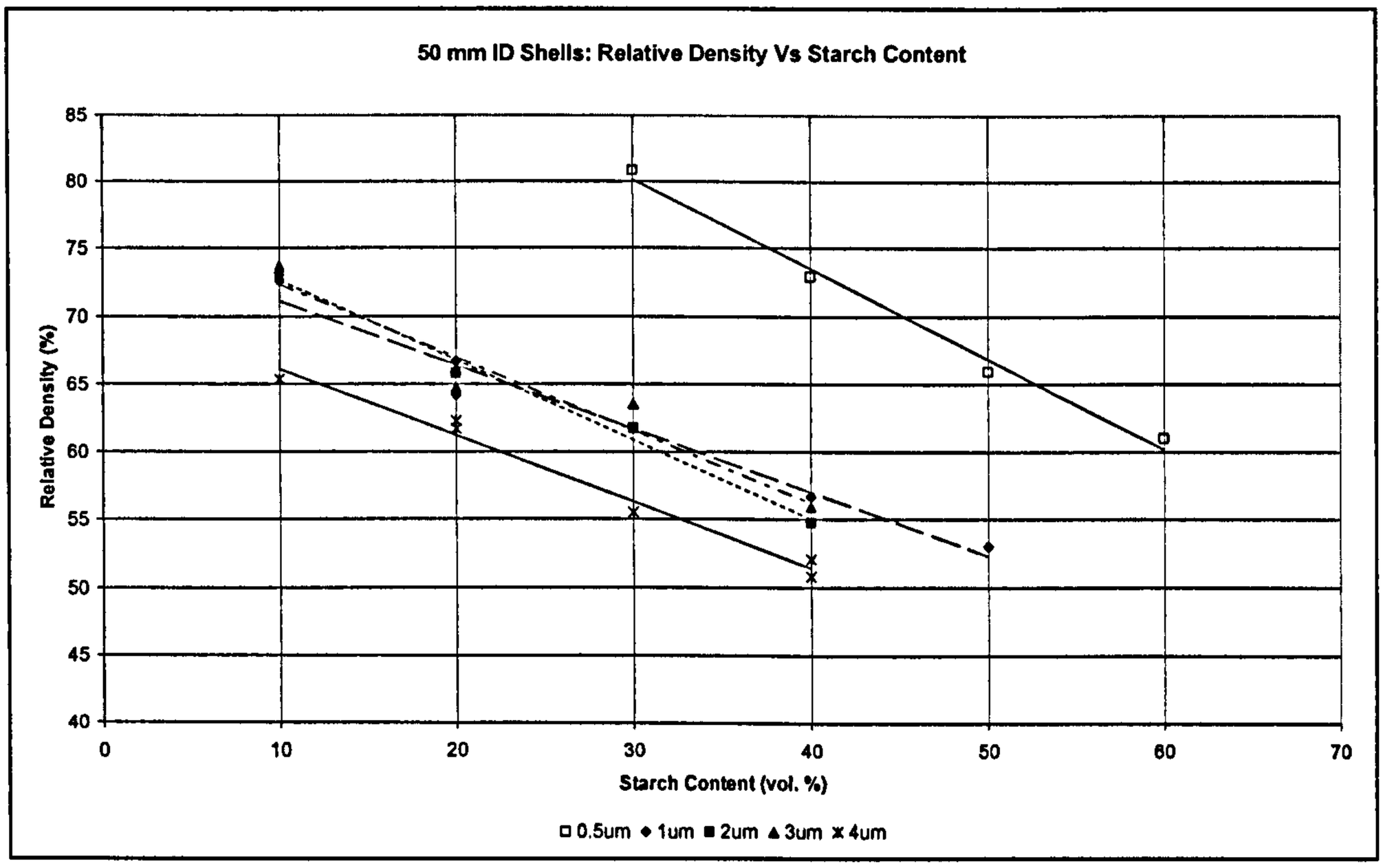

Figure 46-Journal bearings' density trend-lines for each alumina size.

The trend-lines for the different alumina sizes are very similar, the main difference being an offset in relation to each other. As a result, each smaller particle size trend-line has a generally higher y-intercept, and vice versa. This effect is mainly attributable to the sintering characteristics of each alumina particle size at the selected sintering conditions. This is also expected, as usually the smaller alumina sizes achieve higher densification for a given set of sintering conditions.

The best fit lines' equations for the density achieved for each alumina particle size and increasing starch content were of the form:

Equation 24

$$B_R = m \cdot S_v + b$$

B_R	specimen's relative density (%)
m	empirical constant
Sv	starch volumetric percentage (%)
b	empirical constant

The constants results of the curve fitting are summarized in Table 15.

Powder size (µm)	m	b
0.5	-0.66	100.07
1	-0.47	75.77
2	-0.59	78.49
3	-0.54	77.72
4	-0.49	71

Table 15-Journal density best-fit line results by alumina size.

Equation 24 together with Table 15 may prove helpful to the porous bearing designer wishing calculate an estimate of the density values starting from the alumina particle size and the starch content.

In broad terms, it can be established that density is first influenced by the alumina size sintering rate at the chosen sintering temperature and time. A second influence is the addition of starch which can increase the porosity a further 20-25 % depending on the alumina size. The former has the stronger influence at the lowest starch contents, while the latter's influence becomes more noticeable at the higher starch contents.

In the few SC studies published [70] [81], the alumina matrix has been assumed to achieve full densification at the firing stage. Under this assumption, the sintering phenomenon is simplified and the observed behaviour of the specimens' density and porosity are considered only a function of the solids loading and the original amount of starch present in the slip.

In this study, however, because the sintering operation was conducted in air at lower temperature than the required for the full densification for each particle size, this could not be assumed. Because of its complexity, the further ascertaining of the effect of the alumina size and the starch content requires exhaustive examination of the sintering stage and this was not within the scope of the present study.

Thrust bearings density

The results for the density measurements performed on thrust bearings of 46 mm Ø x 7 mm thickness are shown in Figure 47. Over 65 density measurements were conducted. Depending on the alumina size and starch content, density was observed to vary from 49 to 73 %.

From Figure 47 it can be observed that density of thrust bearings behaves in a similar manner to the journal bearings' density. Again, it is obvious the relationship between the density obtained and the starch content in the original slip. As in the case of the journal bearings, the trend-lines are offset in relation to each other with those that correspond to the smaller particle sizes having a larger y-intercept.

Figure 47 also shows measurements performed on thrust bearings at higher starch contents (50-60 vol. %) that were not achievable for journal bearings. This was a result of an easier demoulding procedure of the thrust bearings.

A different trend was observed for the 4 μm alumina density measurements at these higher starch contents. The beyond the 40 % vol. starch content, increasing the starch content did not necessarily result in a decreasing density. This remained at about the same values observed for the 40% vol., but behaving more inconsistently than the readings conducted at the lower starch contents. This concurs with Lyckfeldt's [68] research, in which a similar phenomenon was also observed. Lyckfeldt assumed that

this was a consequence of some minor breakdown of the starch granules during the consolidation stage, resulting in smaller, unstable pores that were excluded during sintering.

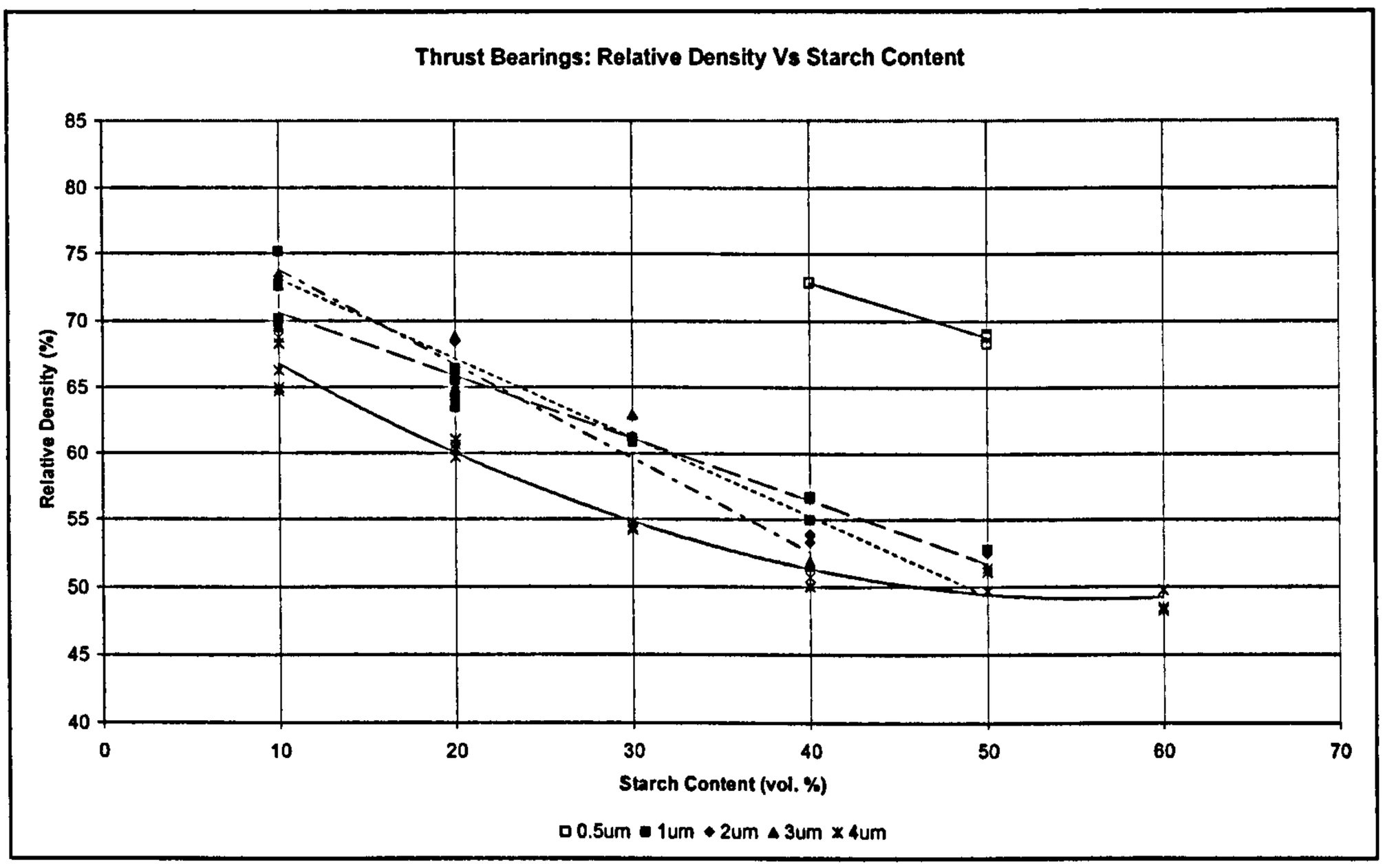

Figure 47-Thrust bearings' density trend-lines for each alumina size.

Geometry and density consistency

Similar density values were observed between journal and thrust bearings manufactured at the same alumina/starch fractions throughout this research. In general, bearings with very similar properties were expected between bearings manufactured within the same slip batch. However, very similar density also resulted from the same formulation slip batches processed separately, regardless of the specimen's geometry. For example, in the case of the 4μm and 20 vol. % starch content slip, more than 6 batches were processed, resulting in more than 10 thrust bearings and two journal bearings. Amongst these, the worst case of measured density repeatability was of 4.1 %. This gave confidence in the SC technique with regard to its overall reliability and repeatability.

Figure 48 shows a comparison of the density results for discs and journals up to 40 vol. % starch content, regardless of the processing batch they belong to. The trend-line is set to y-intercept at zero, and a very good correlation is observed, noting that these measurements include not only experimental errors resulting from the density measurement procedure, but also the possible variations in the sintering furnace and slip composition.

It is therefore postulated that the density of a bearing, journal or thrust, manufactured via the SC technique under the same set of processing conditions, is not affected by its geometry.

From this conclusion it follows that, Equation 24 can be also used to predict the density of a thrust bearing produced via the method developed here. The maximum error resulted from this calculation and the actual measured density on thrust bearings was of 3.52 %.

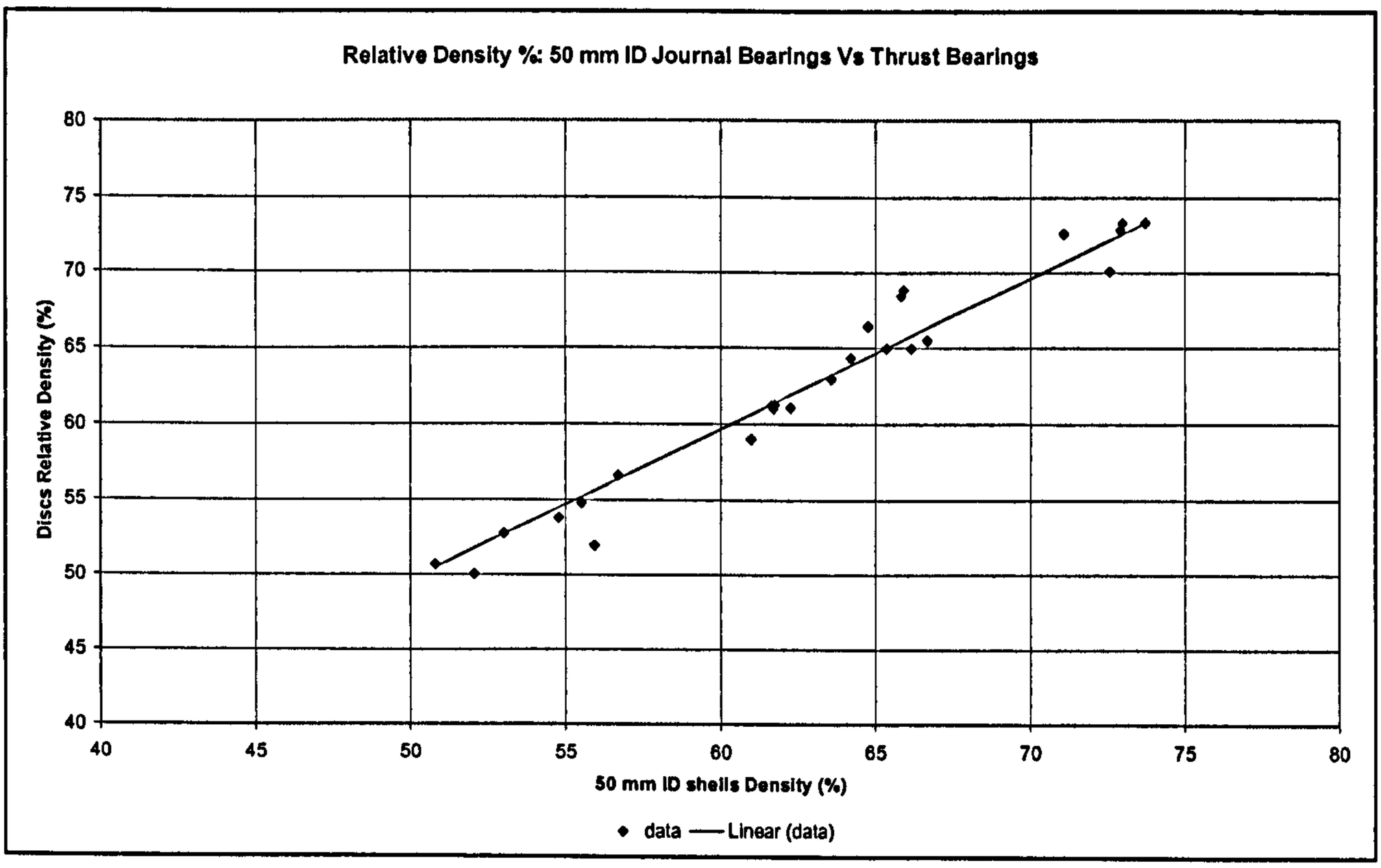

Figure 48-Density comparison: 50 mm ID journals Vs 46 mm Ø x 7mm thrust bearings.

5.2.2 Permeability measurements

Permeability measurements were performed in both, journal and thrust bearings using the procedures and methods described in a previous chapter. Over 86 measurements were performed, using three different test fluids for the journal bearings and air for the trust bearings.

Permeability Vs open porosity

In most published theories, permeability is expressed as a function of porosity. One of the most traditional and well established is the Kozeny theory [94]. In other powder-metallurgy experimental studies, porosity has been also related to the particle size [122] [121,123]; whereas Cliffel *et al* [91] proposed an expression that involved porosity and mean pore size.

In previous porous-ceramic aerostatic bearing research [30] [31], however, the permeability coefficients have been expressed as a power law function of the specimens' open porosity for the different alumina sizes:

Equation 25

$$\psi v = k \cdot \xi_o^{\,a}$$

ψv	viscous permeability coefficient (m^2)
k	proportionality constant
ξ_o	open porosity fraction
a	empirical constant

Subsequent interpolation of these equations resulted in a set of equations that were intended to predict permeability for a given particle size.

In the present research, there is also a very noticeable permeability dependency on the open porosity, as illustrated in Figure 49 for journal bearings. This dependency can be also accurately expressed with an equation of the same form as the one used in previous porous-ceramic aerostatic bearing research [30] [31] (Equation 25).

The following were the values found for each constant/particle size:

Alumina powder size (μm)	k	a
1	3.82×10^{-10}	11.9
2	3.13×10^{-12}	5.91
3	5.23×10^{-12}	6.36
4	2.78×10^{-09}	13.1

Table 16-Curve fitting results for each alumina particle size.

The fact that the best fitted curve type is identical to that of Kwan [30] and Roach [31] gives some confidence in the procedure. However, on closer inspection it was observed that the values for the constants are somewhat different from Roach's set of results for the same particle sizes employed here (1 and 4 μm). For example, in the case of the 4 μm alumina particle size, Roach obtained a *k* value of 1.99×10^{-12} and a value of 5.15 for *a*. These differences may be due to the different set of sintering conditions used in each research. Roach conducted the sintering operation of these particle sizes at a lower temperature, and therefore reached different levels of porosity and permeability; hence the differences observed in the constants' values. Despite these differences, the relationship permeability-open porosity seems to be of the same nature for both researches.

A similar analysis exercise to that of previous porous aerostatic ceramic bearings research was conducted, which resulted in a very accurate fitting with the following equations for k and a:

Equation 26

$$k = 3.1825 \cdot d_w^2 - 15.508 \cdot d_w + 24.218$$

d_w alumina powder mean particle size

Equation 27

$$a = 3.99E-10 \cdot d_w^3 - 2.20E-09 \cdot d_w^2 + 3.43E-09 \cdot d_w - 1.25E-09$$

The previous set of equations can be used to predict permeability based on experimental results starting from the alumina particle size (1-4 μm). The maximum error in relation to the measured permeability was 1.81 m^2 which is within the same order of magnitude. Caution should be exercised in relation with the alumina mean particle size, as the value used here is the one quoted by the manufacturer in data sheets (see appendices).

The correlation between permeability and open porosity, as observed, is quite obvious. However as seen in a previous section, density and porosity have shown to be dependant on the alumina particle size as well as the amount of starch. From a practical point of view, it made more sense to analyse permeability as a function of those variables.

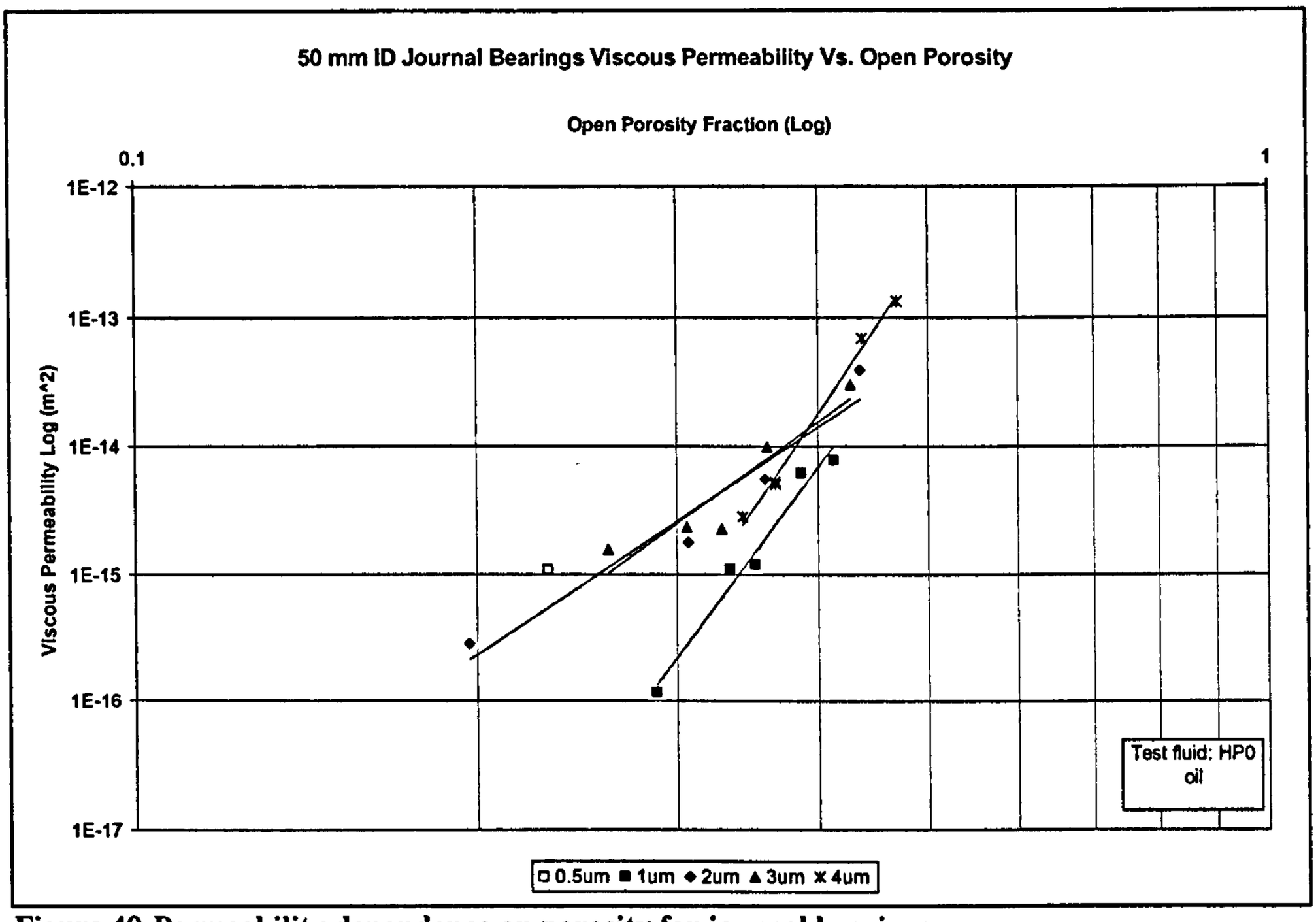

Figure 49-Permeability dependence on porosity for journal bearings.

Permeability Vs Alumina size and starch content

Permeability was observed to vary with the alumina size and starch content in a similar way as density did. Permeability increased with an increasing amount of starch. The trend-lines are also offset in relation to each other, with the larger alumina particle sizes possessing higher permeability values. Again, both effects were expected, given the previously noted effect of both, alumina size and starch content, on the density of the ceramic bodies.

Figure 50 and Figure 51 show the viscous permeability coefficients for the 50 mm ID journal and the thrust bearings, respectively. It is worth noting that the vast majority of the permeability measurements conducted here occurred in the permeability's laminar flow region, meaning that the curve Q Vs Δp was of linear form; thus indicating little significance of the inertial permeability coefficients.

Journal bearings results

The majority of the permeability measurements for the journal bearings were performed using HP0 as the test fluid. The measured viscous permeability coefficient ranged from 1.18×10^{-16} to 1.31×10^{-13} m^2. Figure 50 shows the results from these measurements in relation to the bearings' original slip solids composition.

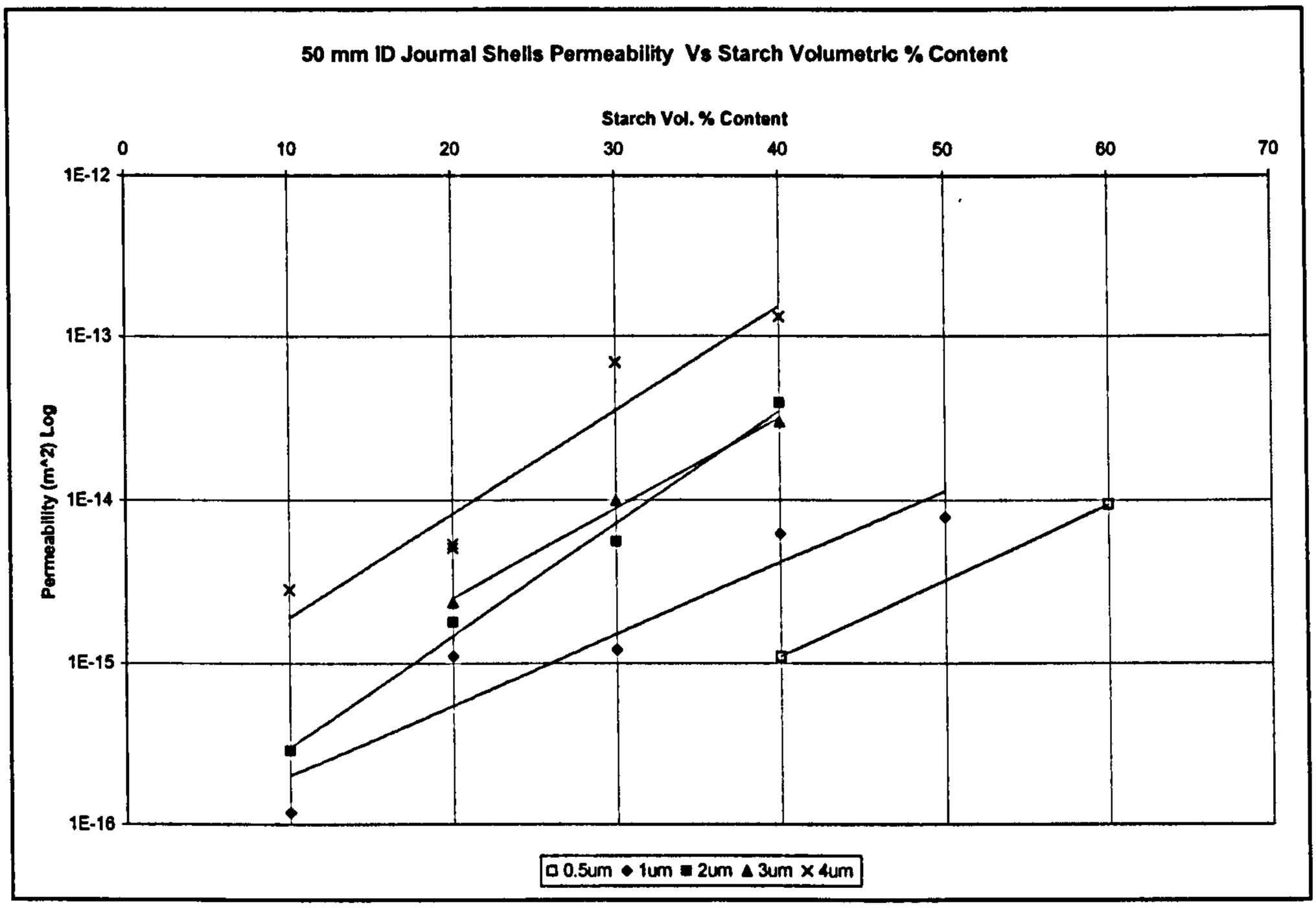

Figure 50-Journal bearings permeability Vs starch content by alumina particle size.

The best fit equations for the trend-lines in Figure 50 are of the form:

Equation 28

$$\psi_v = k \cdot e^{as}$$

ψv viscous permeability coefficient (m^2)

k	proportionality constant
a	empirical constant
s	starch volumetric content (%)

The constants for each alumina size are tabulated below:

Powder size (μm)	k	a
0.5	1.49×10^{-17}	0.1073
1	7.21×10^{-17}	0.1011
2	6.10×10^{-17}	0.1588
3	1.91×10^{-16}	0.1278
4	4.36×10^{-16}	0.1464

Table 17-Curve fitting results for permeability-alumina particle size and starch content.

From this set of equations, and using a similar approach to that of Kwan [30] and Roach [31], a new set of empirical equations can be established taking into account the alumina size and the starch content. The following best-fit equations were found for k and a:

Equation 29

$$k = 4.54\text{E-}17 \cdot d_w^2 - 9.39\text{E-}17 \cdot d_w + 7.76\text{E-}17$$

d_w alumina powder mean particle size

Equation 30

$$a = 0.017 \cdot d_w^4 - 0.1469 \cdot d_w^3 + 0.4122 d_w^2 - 0.4055 d_w + 0.2243$$

The previous set of equations (28-30) may prove helpful to a designer wishing to estimate the permeability of a journal ceramic bearing to be produced through this technique starting from the alumina particle size and the starch vol. %. However, these estimates should be treated with caution, as the alumina size used here was the nominal mean particle size. The maximum error found in relation to the measured permeability was 3.24 m^2 which was within the same order of magnitude (10^{-15}). In order to put the magnitude of this error into context, attention is drawn to Figure 11. It can be observed that, for the permeability values around the optimum permeability target, an error of this magnitude is not expected to alter the ultra-precision bearing design significantly.

Thrust bearings results

Air was used as a test fluid for the permeability measurement of the thrust bearings. The viscous permeability coefficient for these ranged from 1.15 $x10^{-16}$ to 1.04 $x10^{-13}$ m^2. Figure 51 shows the results from these measurements in relation to the bearings' original slip solids composition. Overall, these measurements seemed to agree with the behaviour observed for journal bearings discussed in the previous section.

Figure 51 also illustrates the results from permeability measurements on thrust bearings with the highest starch contents. As with the density results, the permeability of the bearings shows certain inconsistencies for the higher starch contents. For example in the case of the 4 μm alumina, permeability increases with an increasing starch content up to starch content of 40 % vol. At this starch vol. % content, the permeability values are around 9.27 x 10^{-14} for three individual bearings. However, increasing the starch content to 50 % vol. resulted in a permeability decrement to around 4.1 x 10^{-14} for three different bearings. Further incrementing the starch content to 60 % vol. resulted in further permeability inconsistencies. One of two bearings tested possessed a permeability of 6.8 x 10^{-14} and the other 2.6 x 10^{-14}. Similar results are observed for the other the alumina size bearings with exception of the 0.5 μm based bearings, for which increasing the starch content from 40 to 50% vol., resulted in an increasing permeability.

Overall, these results are consistent with the density measurements previously conducted, and they seem also to confirm Lyckfeldt's assumption [70] regarding the breakdown of the starch particles in previous processing steps. The better behaviour of the 0.5 μm powder bearings at the higher starch contents probably reflects the intrinsic better particle packing achieved with this smaller alumina size powder.

It was not possible to produce journal bearings beyond a starch content of 40 % vol. However, based on the evidence of both the journal and thrust bearing measurements it can be concluded that for bearings produced by the SC technique with the current processing conditions and for alumina sizes ranging from 1 to 4 μm the maximum starch content vol. % is 40. Beyond this value, bearings with a controlled permeability can not be consistently produced.

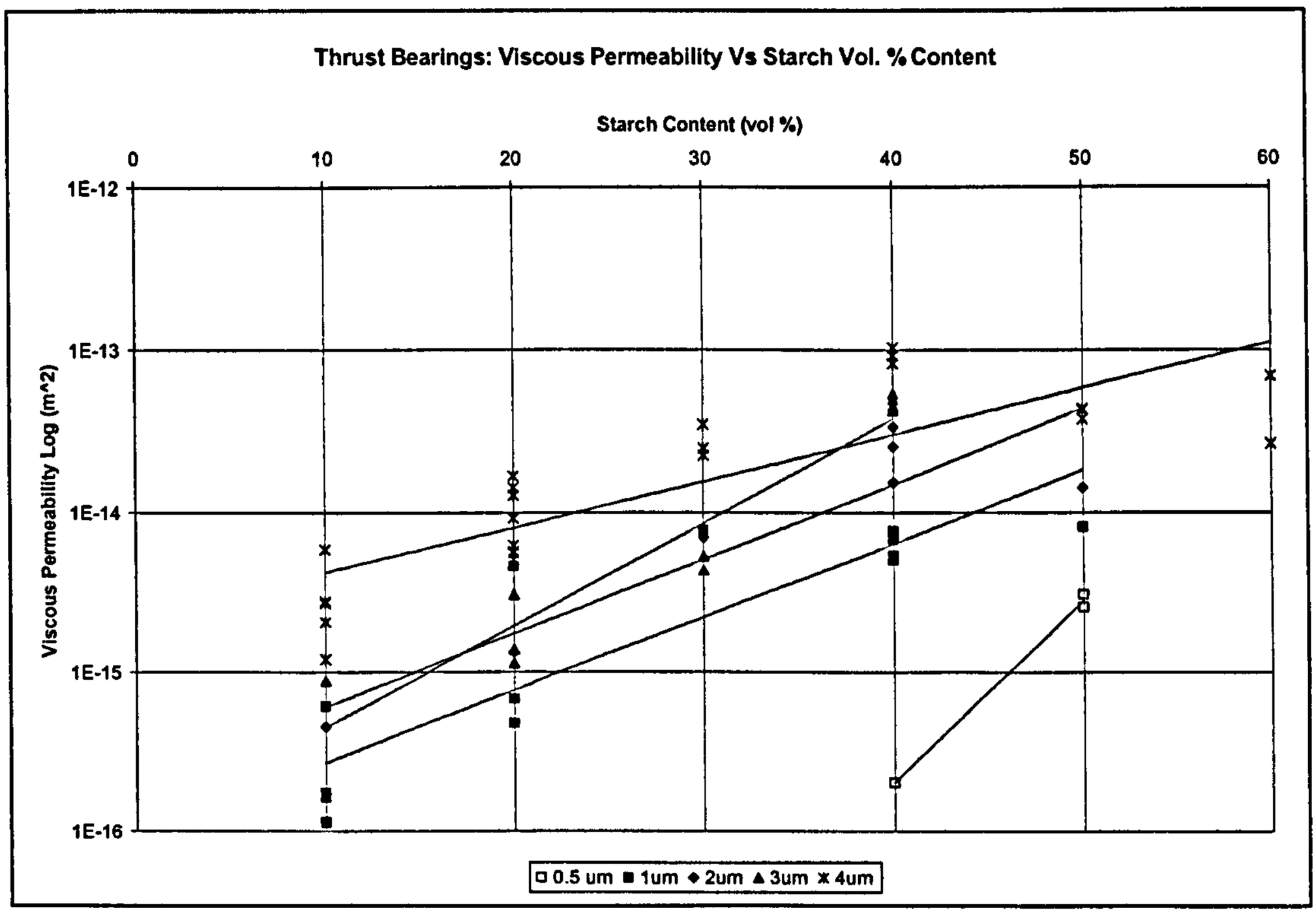

Figure 51-Thrust bearings permeability Vs starch content by particle size.

Geometry and test fluid consistency

Figure 52 illustrates a comparison of the bearings' permeability for both types of bearing, journal and thrust, manufactured with the same processing parameters, although not necessarily belonging to the same processing batch. The lower correlation-factor observed in relation to the density comparison shown in Figure 48, 0.934 as opposed to 0.980, may be attributable to experimental errors resulting from the utilisation of different permeability test-rigs and test fluids for each type of bearing. The maximum error between the measured permeability of journal and thrust bearings was 4.17 m^2, which was within the same order of magnitude.

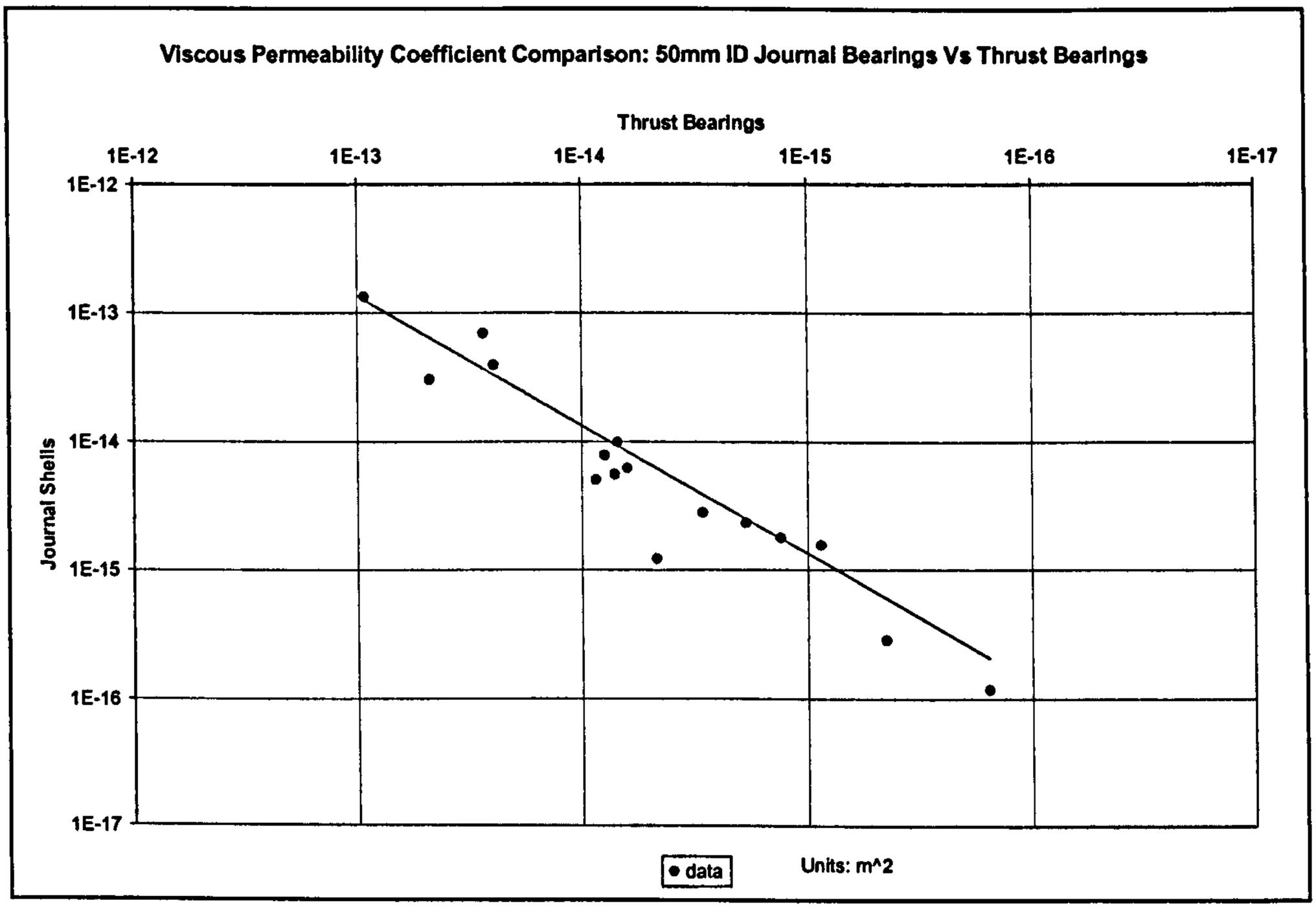

Figure 52-Viscous permeability comparison journal Vs thrust bearings.

By virtue of the observed correlation between the permeability of both types of bearing, it can be established that the permeability of ceramic matrixes produced under the same processing conditions with the method developed here, is independent of their geometry (for journals of 50 mm ID or thrust Ø 46 mm), regardless of the test fluid. Therefore, the use of the set equations 25-27 and 28-30

for predicting permeability can also be extended to thrust bearings. This assumption is supported by Figure 53.

Figure 53 illustrates a comparison of the viscous permeability coefficients measured for both journal and thrust bearings against the predicted values obtained through the use of equations 28-30, for 74 measurements. The line's fit correlation factor was 0.953. A very similar trend is obtained using equations 25-27, the correlation factor for this being 0.930.

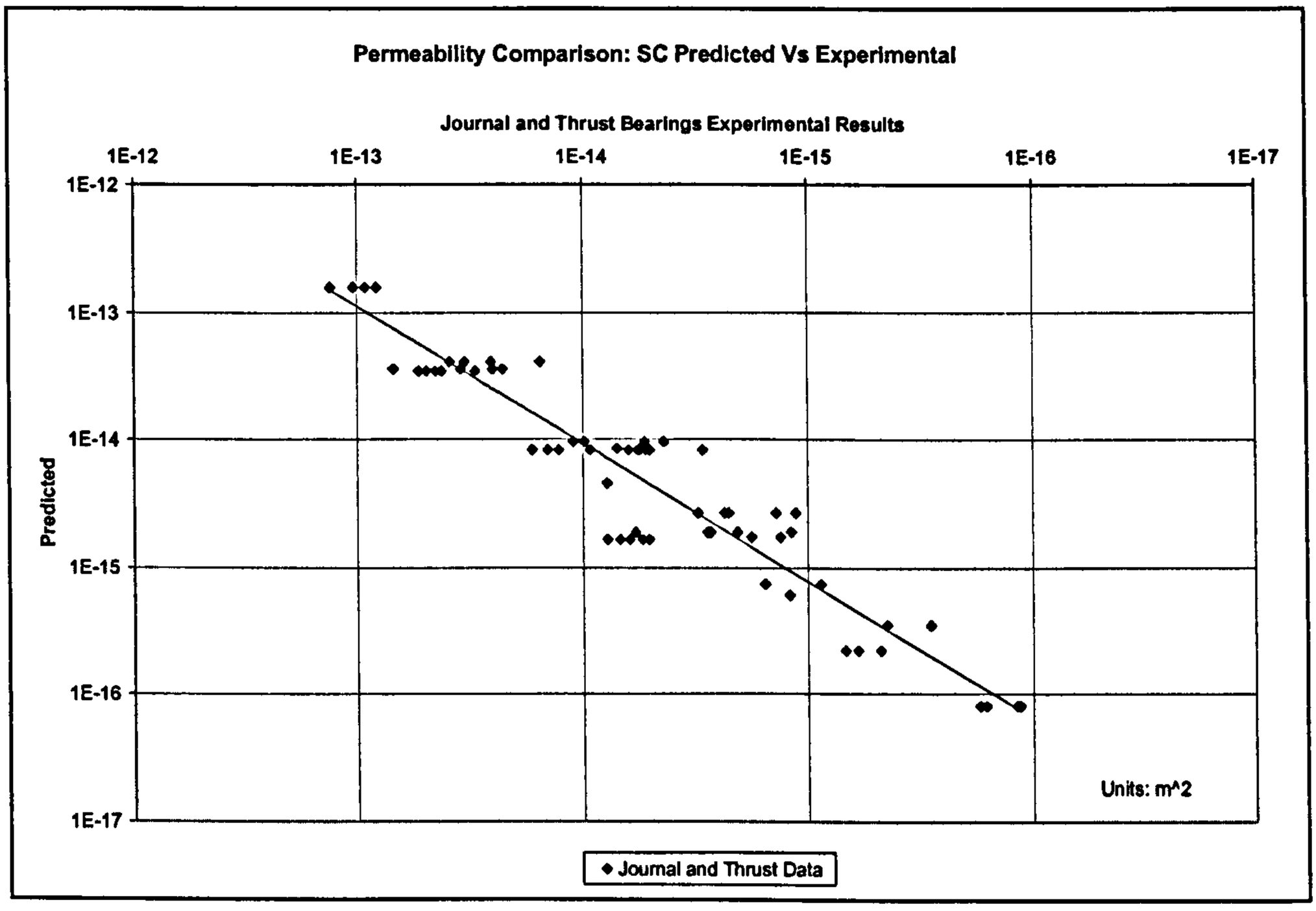

Figure 53-Measured Vs predicted permeability for journal and thrust bearings.

Although the previous sets of equations (25-27, 28-30) have not been derived through rigorous mathematical analysis, these results may provide a designer of porous bearings with a useful tool for predicting permeability. Considering the possible errors induced throughout the processing and permeability measuring, the overall accuracy of these equations is considered acceptable.

Effect of the different test fluids on the permeability of journal bearings

Throughout this research bearings have been produced for several geometries and dimensions. In the case of the journal bearings, *HP0* and *DIE 180* oils as well as water were used as test fluids. Figure 54 illustrates a comparison for the bearings that were subjected to permeability measurements with at least two of the liquid test fluids. The effect of the test fluid on the measured viscous permeability can be observed in Figure 54. Given the correlation factors for each of the charts, 0.999, 0.996 and 999 for a, b and c respectively, permeability was considered the same for any practical purpose. This was expected, as several previous experimental analyses have reached a similar conclusion for the permeability of porous specimens in which the measurements were conducted within the permeability's laminar flow region.

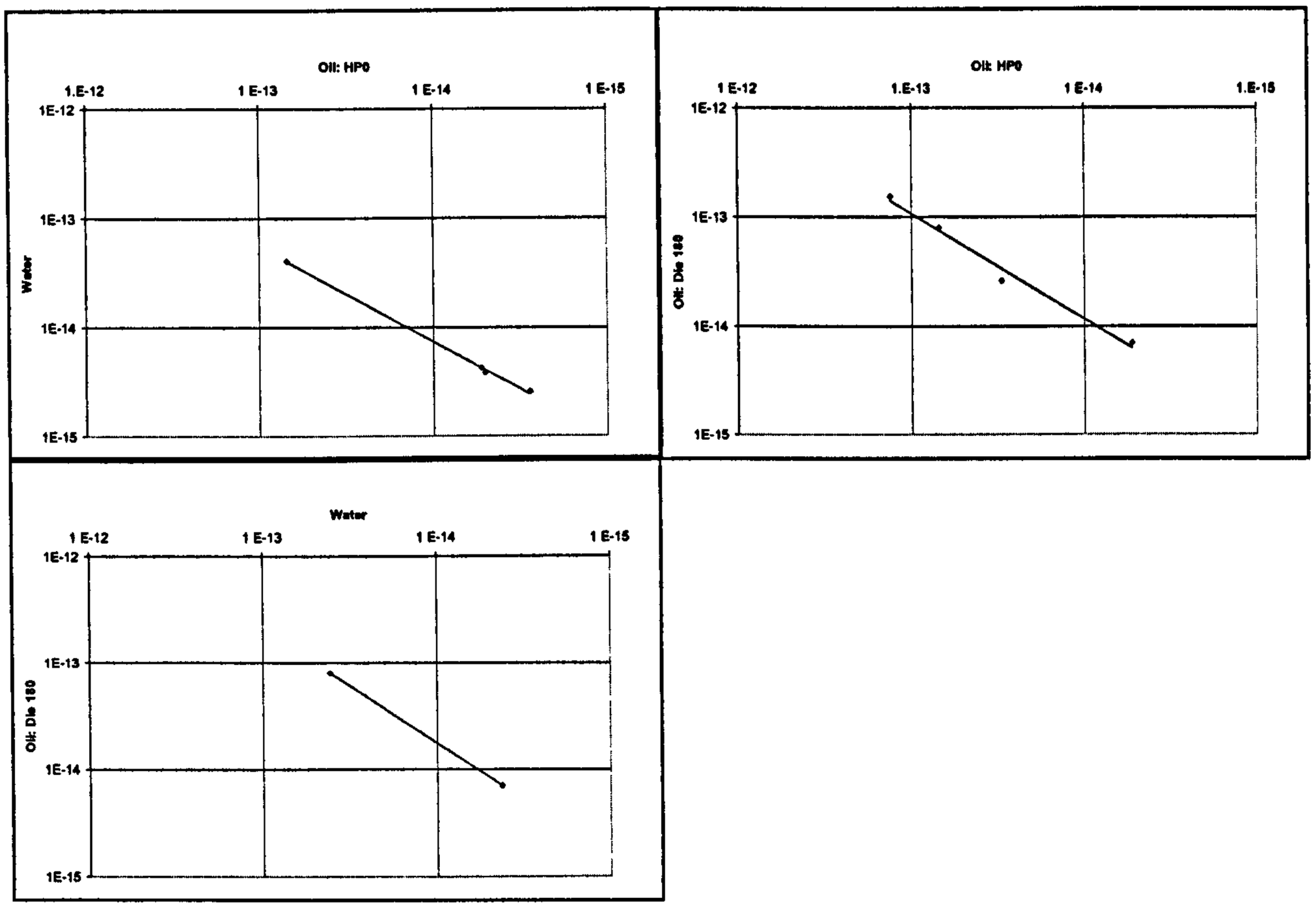

Figure 54- Permeability comparison per test fluid in journal bearings. a) HP0 Vs water, b) HP0 Vs DIE 180, c) Water Vs DIE 180; units in m^2.

Permeability measurements for one of the larger bearings (80 mm ID) shown in Figure 36 were also conducted. Its viscous permeability coefficient is shown in Table 18, along with the coefficients for two 50 mm ID journals manufactured with the

same processing conditions in separate batches. In this particular case, the original ceramic slip solids composition was based on 4 μm alumina with a starch content of 20 % vol.

Specimen	50 mm ID journal # 1	50 mm ID journal # 2	80 mm ID journal
Viscous permeability coefficient (x 10^{-15} m^2)	3.78	4.20	2.65

Table 18-Viscous permeability coefficient for journal bearings made with 4 μm alumina and 20 vol. %. Test fluid used was water.

Overall, the difference between the permeability of bearings with the same specified processing conditions is not very significant, regardless of their size, as seen in Table 18. This suggests that the permeability of the SC bearing matrices it is not greatly affected by the size of the specimen.

Journal bearing shell sectional consistency

Uniform and consistent permeability is of paramount importance for the adequate performance of porous hydrostatic bearings. Direct permeability measurement along and across the bearing wall has not been possible. However, in previous porous ceramic hydrostatic journal research [3] density measurements have been performed longitudinally and circumferentially on sliced bearing rings and the results were used as an indirect measure of uniform permeability. The reasoning for this procedure is based on the observed linear relationship between the permeability and density/porosity of the porous bearings. The same method has been applied here, and this involved slicing the bearings length ways in five segments. The centre ring was further sliced into five 72° segments, as illustrated in Figure 24.

Two 50 mm ID and one 80 mm ID journal bearings were sliced, the resulting segments were subjected to density measurements in accordance with ASTM C20-87 [124]. These bearings were manufactured with an alumina particle size of 4 μm and starch content of 20 vol. %.

Figure 55 illustrates the results obtained with this exercise using longitudinal and circumferential segments. The results for the two shells manufactured via HIPing from previous research [3], one exhibiting the best and the other exhibiting the worst uniformity results, have been added as a reference.

From Figure 55 it can be also observed that in general, SC shells posses a more uniform density than the HIPed shells. This probably reflects the non-uniformities originating at the powder vibration packing operation for the HIPed shells, as well as the more uniform packing of the suspended alumina-starch particles. Almond [3] had already noted the correlation between the vibration powder packing process and the observed density behaviour along the porous wall, which resulted in the higher density observed at the top segments.

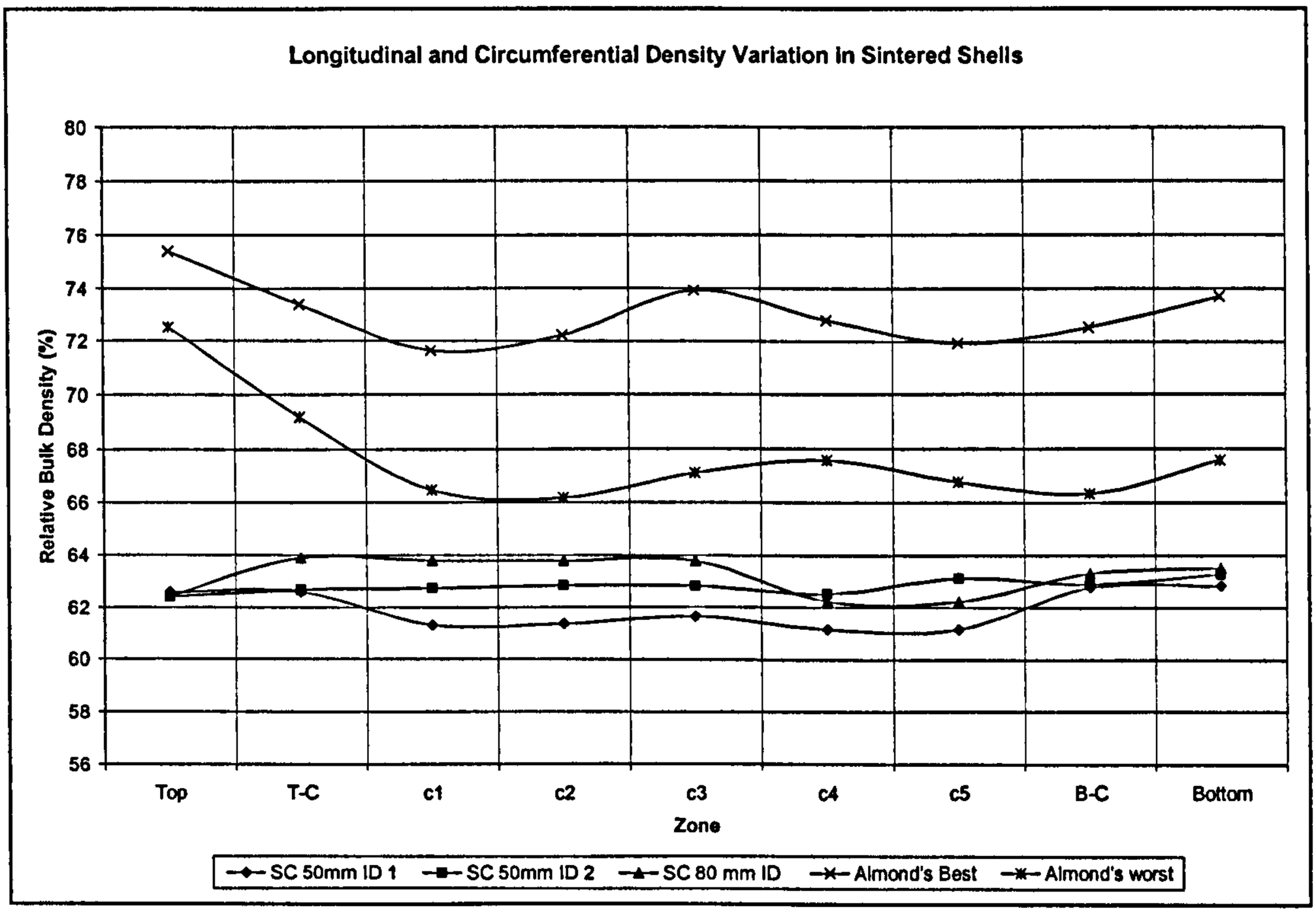

Figure 55-Longitudinal and circumferential density variation for SC shells.

From Figure 55, it is also noted that the density results for these segments correlate well with the previous measured density of un-segmented SC shells. It is also worth noting that, the results for the three SC bearings are consistent, suggesting that the

geometry and size do not exert a strong influence; this was expected from the journal-thrust bearings density comparison.
Overall, the maximum deviation observed for the SC slices within the same bearing was 1.71 %. In contrast, the maximum deviation for the HIPed bearings slices was of 6.21 %.

Generally, HIPed shells achieved a higher overall density, reflecting the nature of this high pressure process.

Uniform shrinkage

The measurement of the bearings' shrinkage during the sintering operation can be also used as an indirect measure of uniform density and therefore of permeability. It is well known that during the sintering operation, the densification of the ceramic matrix is accompanied by a shrinkage that is proportional to the degree of densification. If the occurring shrinkage between the drying and the sintering is measured at different points, then the uniformity at those locations can be presumed. A further advantage is that the bearings used for this purpose could be reused for subsequent testing, as opposed to the previous method.

As with the ASTM procedure for linear shrinkage (chapter 4), reference shrinkage marks were carefully made on the 'dried' journal castings. Dimensional measurements were taken at the locations shown in Figure 56, using a digital calliper before and after sintering. The sintering shrinkages were calculated for each feature using Equation 6. Results of these measurements can be found in Table 19.

From Table 19 it can be seen that in general, there is a good correlation with the linear shrinkage values previously calculated for the design of the moulds. The overall deviations are relatively small (maximum of 1.92 %), which gave confidence in SC processing repeatability. No shrinkage tendencies were obvious. In addition, because of the narrow sample-set no correlation could be established between the deviations' location and the sintering operation. Generally, this operation was

conducted with the bearings standing on top of an extruded ceramic matrix, with the same position as shown in Figure 56.

Results from a similar exercise for thrust bearings were marginally better (a maximum deviation of 1.3 %). This is probably attributable to the smaller and less complex nature of their geometry.

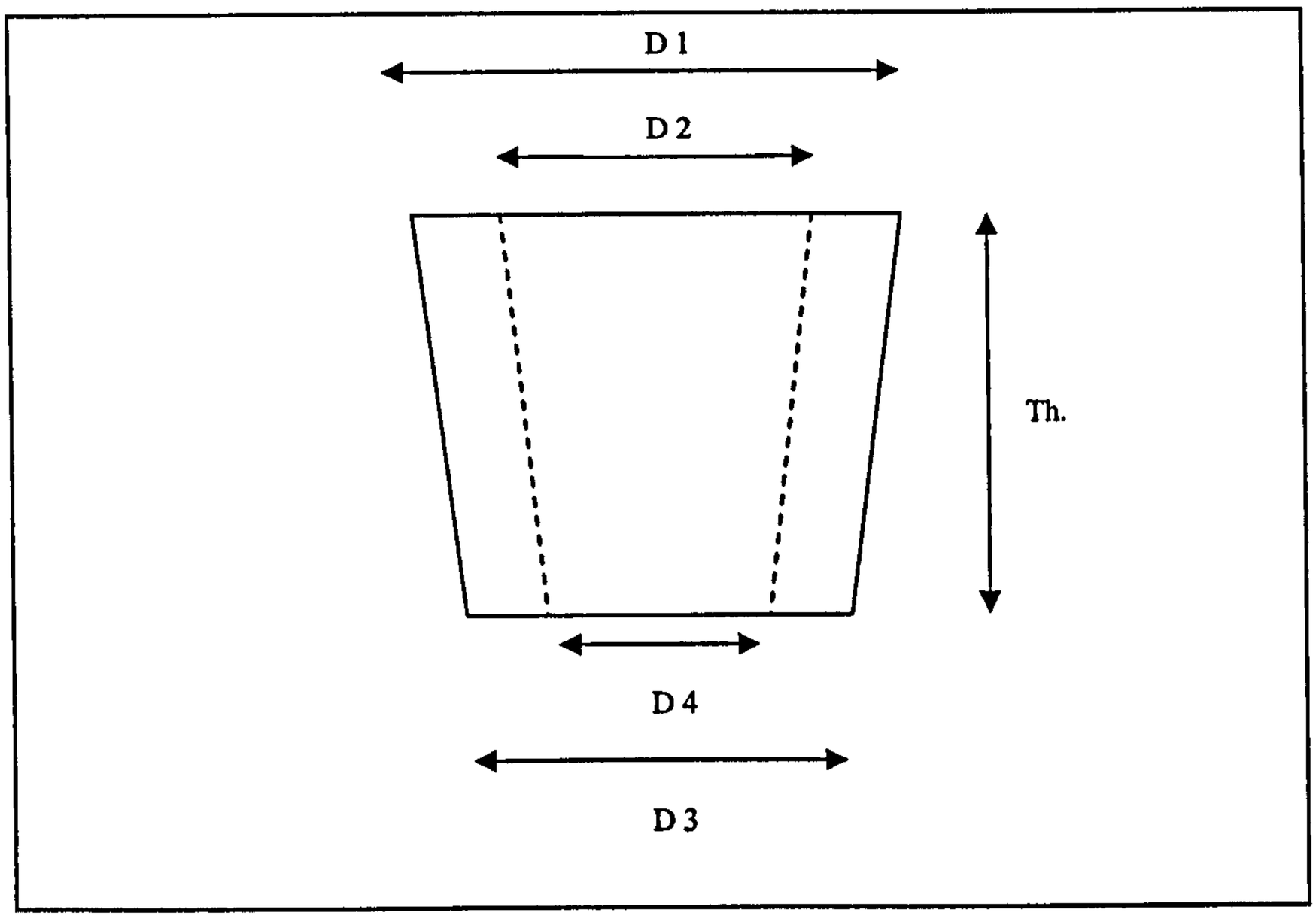

Figure 56- Journal bearings shrinkage feature measurement places.

Bearing #	Alumina size (μm)	Starch content (vol. %)	Th.	D1	D2	D3	D4
112	0.5	50	18.5	18.86	19.3	19.11	17.38
111	1	30	8.25	8.47	---	8.75	7.7
112	1	40	8.06	8.06	8.35	7.42	7.80
111	1	50	7.58	8.33	---	8.88	---
112	3	10	7.86	8.20	8.48	7.82	6.98
112	3	20	7.16	8.09	7.66	7.45	8.44
S4	4	20	5.30	5.28	5.79	5.02	5.29
80 mm ID	4	20	6.21	6.05	6.34	4.92	5.05

Table 19-Measured localized bearing sinter-shrinkage %, by slip solids composition.

Effect of grinding on the permeability the porous wall of SC bearings

At the beginning of the project, it was possible to verify the effect of the grinding operations on the permeability of two SC bearings. The two cast bearings had a very smooth surface finish after the SC processing and in the first instance, only the top and bottom faces were ground flat. The bearings were then fitted in the permeability test rig and measurements were conducted as described in chapter 4, for journal bearings. Once these measurements were completed, the bearings' ID and OD were ground with the techniques described in chapter 4, and new permeability measurements were conducted.

Journal Shell #	S1	S1 (Ground)	S2	S2 (Ground)
Permeability (m^2)	2.26×10^{-15}	2.20×10^{-15}	2.46×10^{-15}	3.06×10^{-15}

Table 20-Permeability measurement results for ground and un-ground shells.

From Table 20 it can be observed that the difference between the permeability of the journal bearings, ground and un-ground, is not very significant. This suggests that the surface pores of the porous wall of a SC bearing are not smeared during, grinding of the bearings, indicating some level of justification over the adoption of ceramic materials for porous hydrostatic bearings.

Caution should be observed, however, as the cast bearing walls were tapered 1° over a bearings' length of 50 mm. The maximum estimated permeability error due to this was 0.02×10^{-15} m^2 (within the same order of magnitude).

5.2.3 Pore size distribution

Bubble test results and discussion

The results from the bubble-test for over twenty measurements are shown in Figure 57, in relation to their alumina-starch slip solids composition.

Roach [31] had already analyzed the practical limitations of the bubble test in relation to the expected pore size and the available supply pressure (around 5 Bar) via Equation 12, suggesting that smaller equivalent pores ($\leq$0.05) expected from the 0.5 μm alumina bearings were not measurable with this method. As a result, the number of specimens for testing was limited to specimens whose expected bubble-test pore was larger than this value; and by refining by trial an error it could be established that the minimum measurable bubble-test pore resulted from a combination of 1 μm alumina and a starch content of 40% vol. Hence excluding measurements for specimens based on a 0.5 μm alumina particle size.

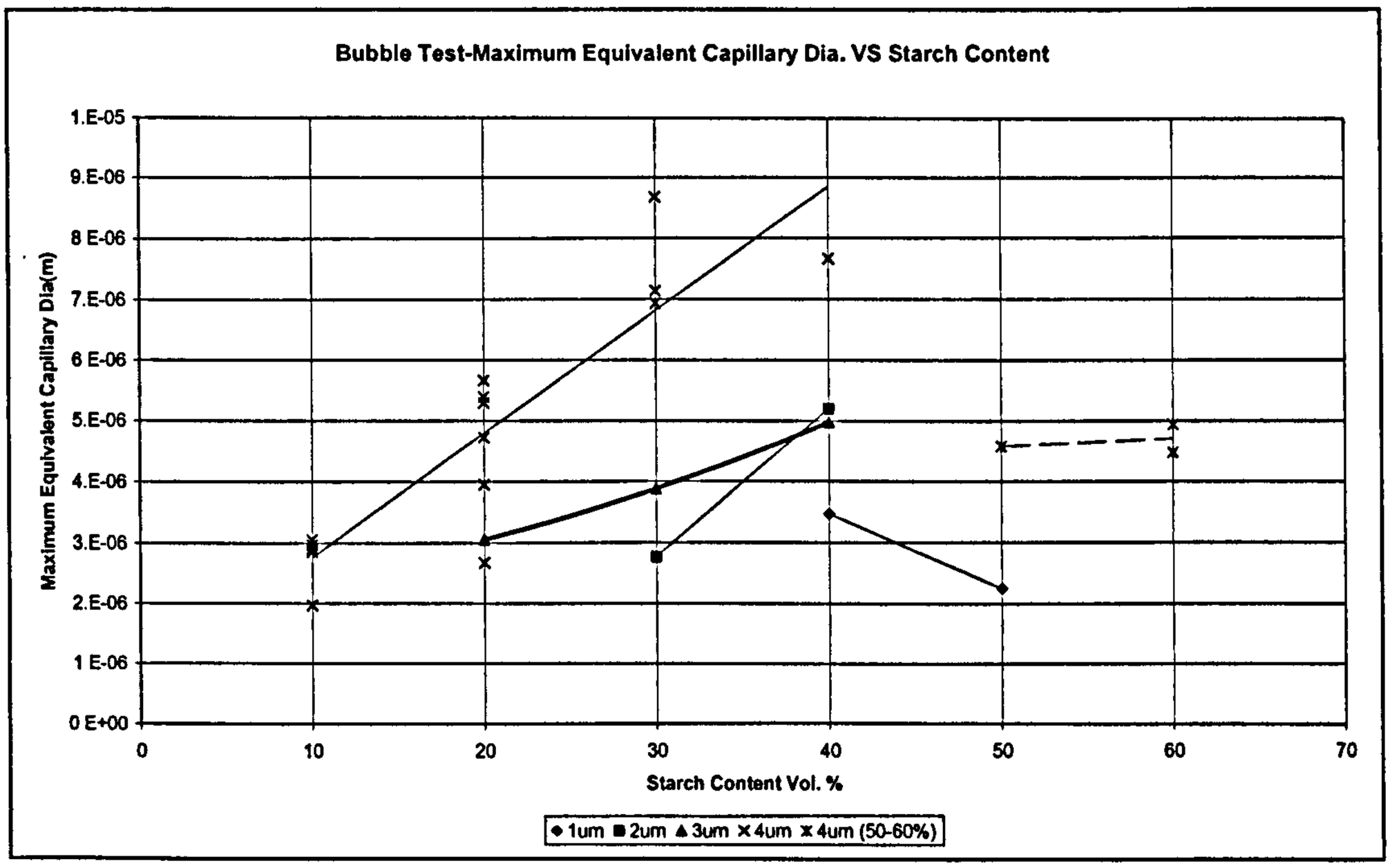

Figure 57-Bubble-test maximum pore size results by starch content and alumina particle size.

In general, the spatial distribution of the specimens was very uniform. More often than not, the first bubble points occurred simultaneously at more than one location, which were also randomly spaced.

From Figure 57 it can be observed that in general, an increment in the starch content resulted in an increment in the pore size. The reason for this is that, with an increase on the amount of starch the number and the degree of contact between the starch

particles also increases, resulting in larger pores. This behaviour has been also observed by other researchers [70] [86]. However, the inconsistencies found during the density and permeability measurements at the higher end of the starch contents (50-60% vol.) were also present during the bubble-test for the 1 and 4μm alumina. For example, for the 4μm alumina, an increment in the starch content from 40 to 50 % vol. did not result in a larger pore size but rather a decrement. A further incrementing the starch content resulted in further inconsistencies. Again, this behaviour is in accordance to what was observed in the earlier density measurements.

In addition it was also noted that generally, the specimens manufactured with larger alumina particle sizes yielded larger bubble-test pores for the same amount of starch. This was also expected as these larger particles yielded higher porosity during the density and porosity measurements performed.

Finally, the bubble test data was also valuable when used for the water expulsion testing, as noted in a previous chapter.

Water expulsion (WE) test results and discussion

Figure 58 shows the results of the water expulsion test in terms of mean pore size against the starch content fraction % per each particle size for twelve different specimens. From Figure 58 it can be observed that the mean pore size increases with an increasing starch content. Also, a larger average pore size was observed for the larger alumina particle sizes, both aspects correlating well with bubble-test results.

The measurements conducted for specimens manufactured at the higher starch contents also reflect some level of inconsistency, which was more noticeable for the 1μm alumina. However, not enough data was available to adequately describe this behaviour. Nonetheless, the results for the range of alumina of 2 to 4 μm describe similar slopes for the best fit lines, proving some level of consistency.

In general for all the tested specimens, the wet permeability curves approached the dry permeability ones, as proposed by Gelinas and Angers [97]; hence validating these results, as was also observed by Kwan [30].

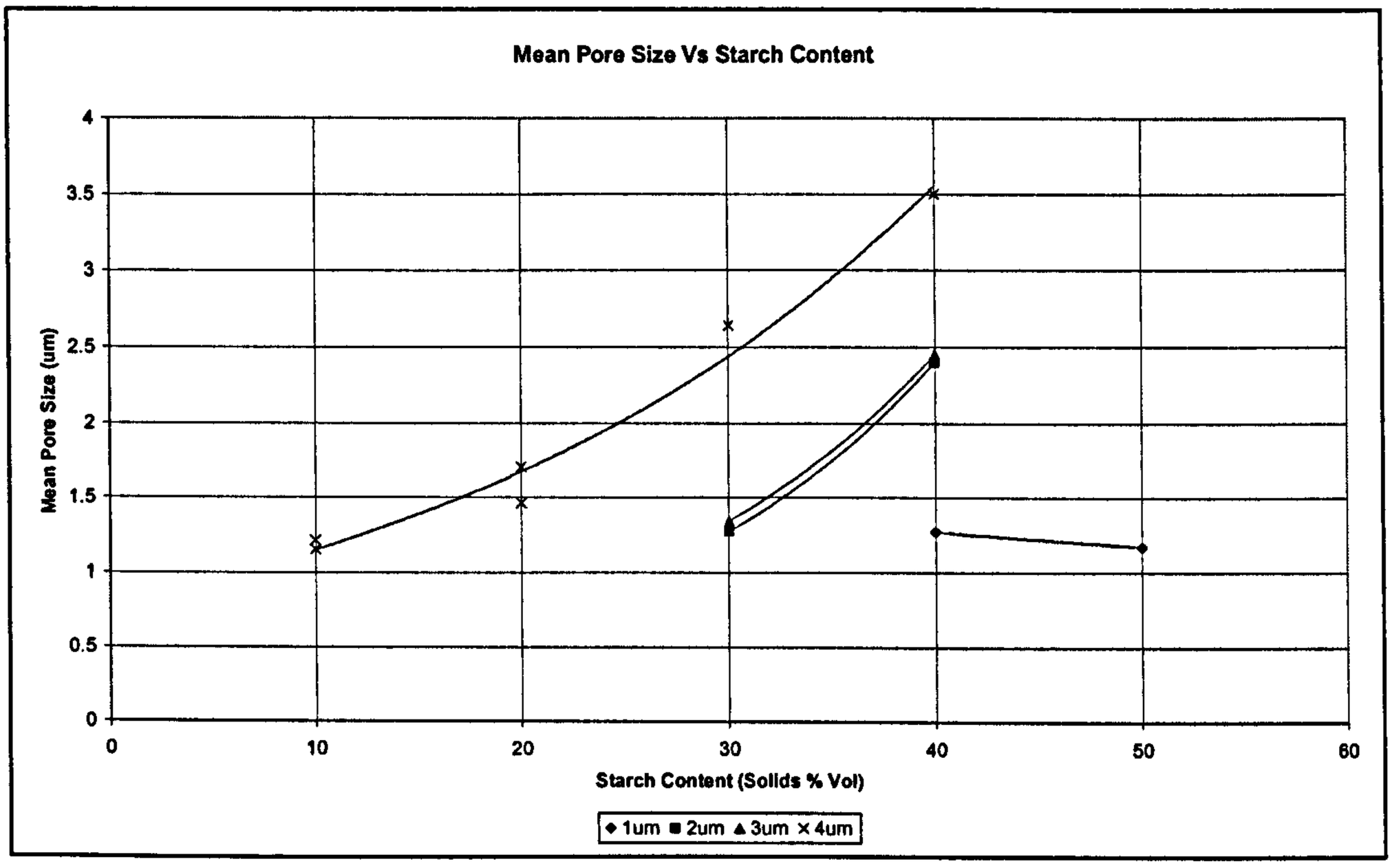

Figure 58-Water expulsion results: Average pore size Vs starch content.

The best-fit lines for the average pore size as a function of the starch content are of the form:

Equation 31

$$d_{ave} = k \cdot e^{as}$$

d_{ave}	average pore size
k	empirical constant
a	empirical constant
s	starch volumetric content (%)

The resultant constant values for each alumina size are tabulated below:

Alumina powder size (μm)	k	A
2	0.1882	0.0636
3	0.2192	0.0603
4	0.7887	0.0376

Table 21- Water expulsion average pore results for k and a.

Figure 59 shows a typical cumulative pore distribution plot for a 1 μm alumina and 50% vol. starch content.

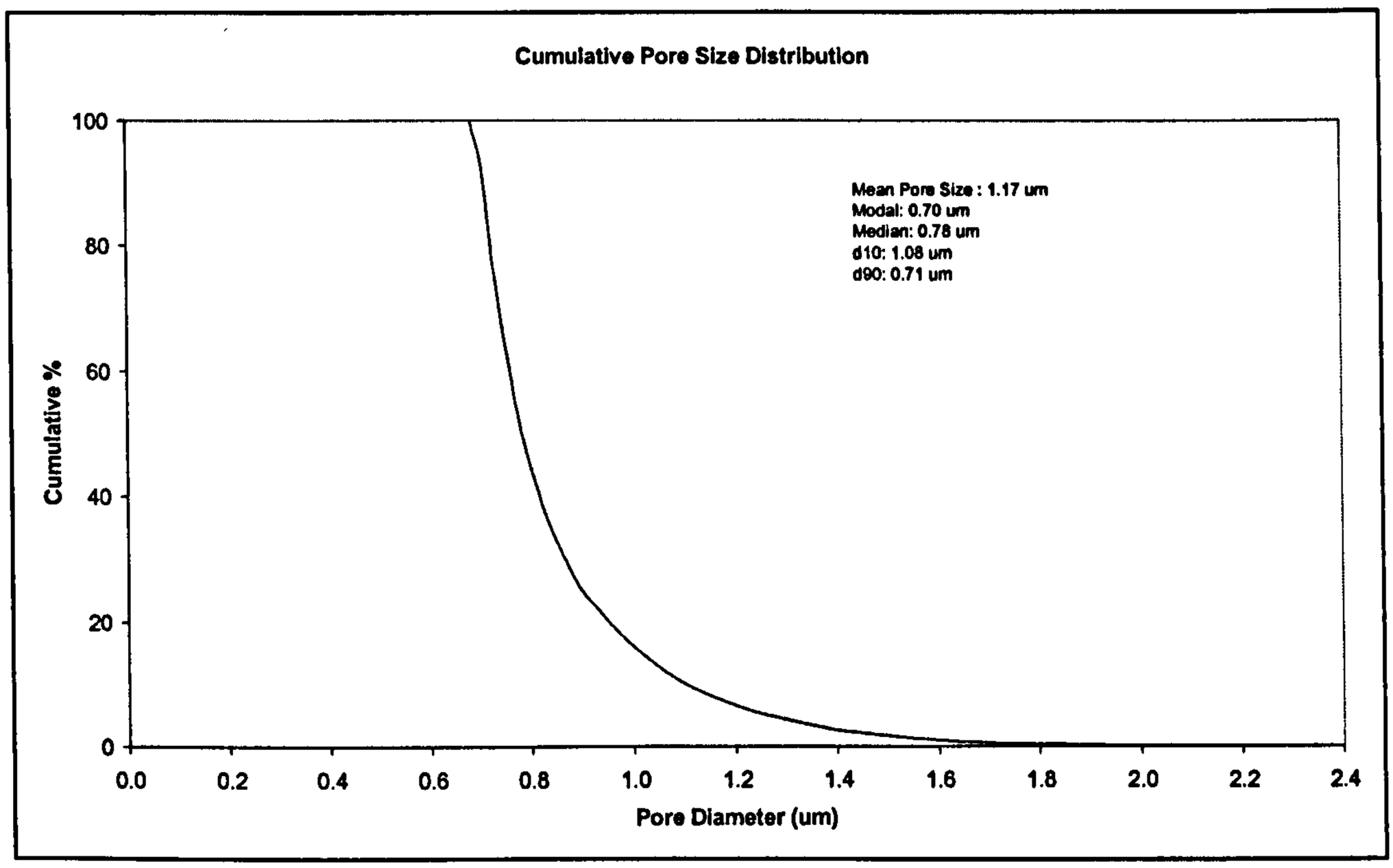

Figure 59- Typical cumulative pore size distribution for the SC specimens.

Pore size Vs permeability of SC bodies

Besides the present work, the only other reference to the permeability of SC consolidated bodies is made by Vasconcelos *et al* [86]. There, diatomite powders were processed into membranes layers via the SC technique using potato starch. Vasconcelos expressed his results in terms of the average pore size against the permeability observed, obtaining a power law curve.

A similar exercise was conducted here and the results are shown in Figure 60, also resulting in a power law correlation for the 2-4 μm alumina particle sizes:

Equation 32

$$\psi v = k \cdot d_{ave}{}^{a}$$

ψv	viscous permeability coefficient (m^2)
k	empirical constant
d_{ave}	average pore size
a	empirical constant

Table 22 shows the values for k and a for each particle size. It also includes the values obtained by Vasconcelos as reference.

Alumina powder size (μm)	k	a
2	5.21×10^{-15}	2.23
3	5.73×10^{-15}	3.24
4	1.58×10^{-15}	1.24
Vasconcelos ([86]) results	2.54×10^{-14}	2.1

Table 22-Pore size Vs permeability resulting values for k and a.

The similarity with the results obtained by Vasconcelos gave confidence in the validity of the best fit lines' equations.

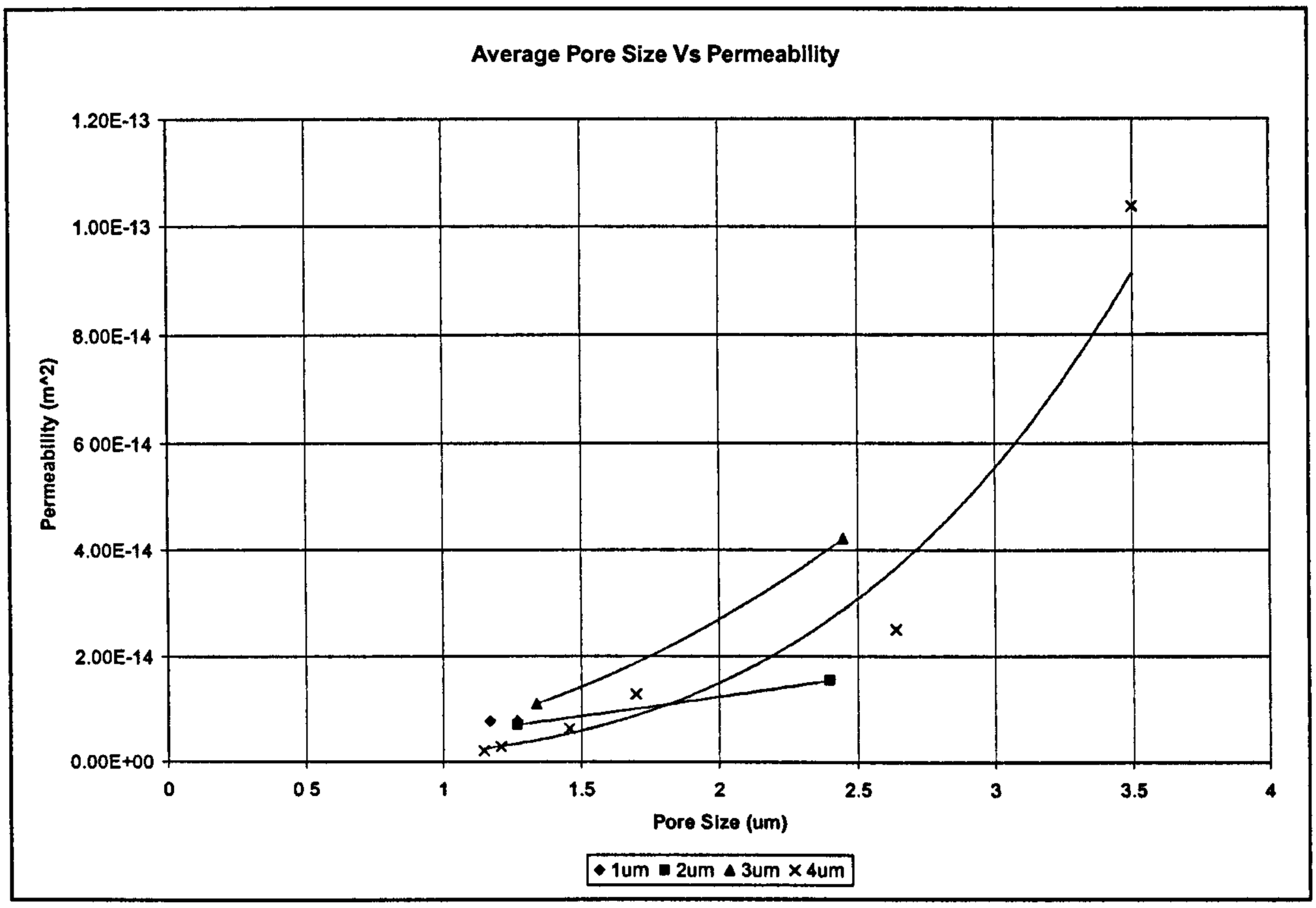

Figure 60-Water expulsion average pore Vs permeability.

From the acquired WE test-data, the modal and median equivalent pore diameter as well as the 10^{th} and 90^{th} percentiles of the cumulative distribution could be calculated. Table 23 presents typical values for the several specimens based on a 4um alumina.

Specimen	Starch vol. %	Average (μm)	Modal (μm)	Median (μm)	d_{10} (μm)	d_{90} (μm)
212	10	1.21	0.58	0.79	1.26	0.58
412	20	1.42	0.75	0.76	1.13	0.65
411	30	2.55	1.17	1.52	2.23	1.20
411	40	3.50	2.18	2.25	3.20	2.05

Table 23-Water expulsion test results for SC specimens.

Overall, the results obtained with the WE technique seemed to correlate well with the results obtained with previous SC research, as well as theoretical results obtained with the Kozeny theory [94]:

Equation 33

$$\psi_v = \frac{c \cdot P^3}{T \cdot S^2}$$

ψv	viscous permeability coefficient
c	Kozeny constant (c = 0.58 for an angular grained powder)
P	fractional open porosity
T	tortuosity, actual flow path in relation to thickness (T = 1/P)
S	specific surface area, internal surface area per unit volume of porous material

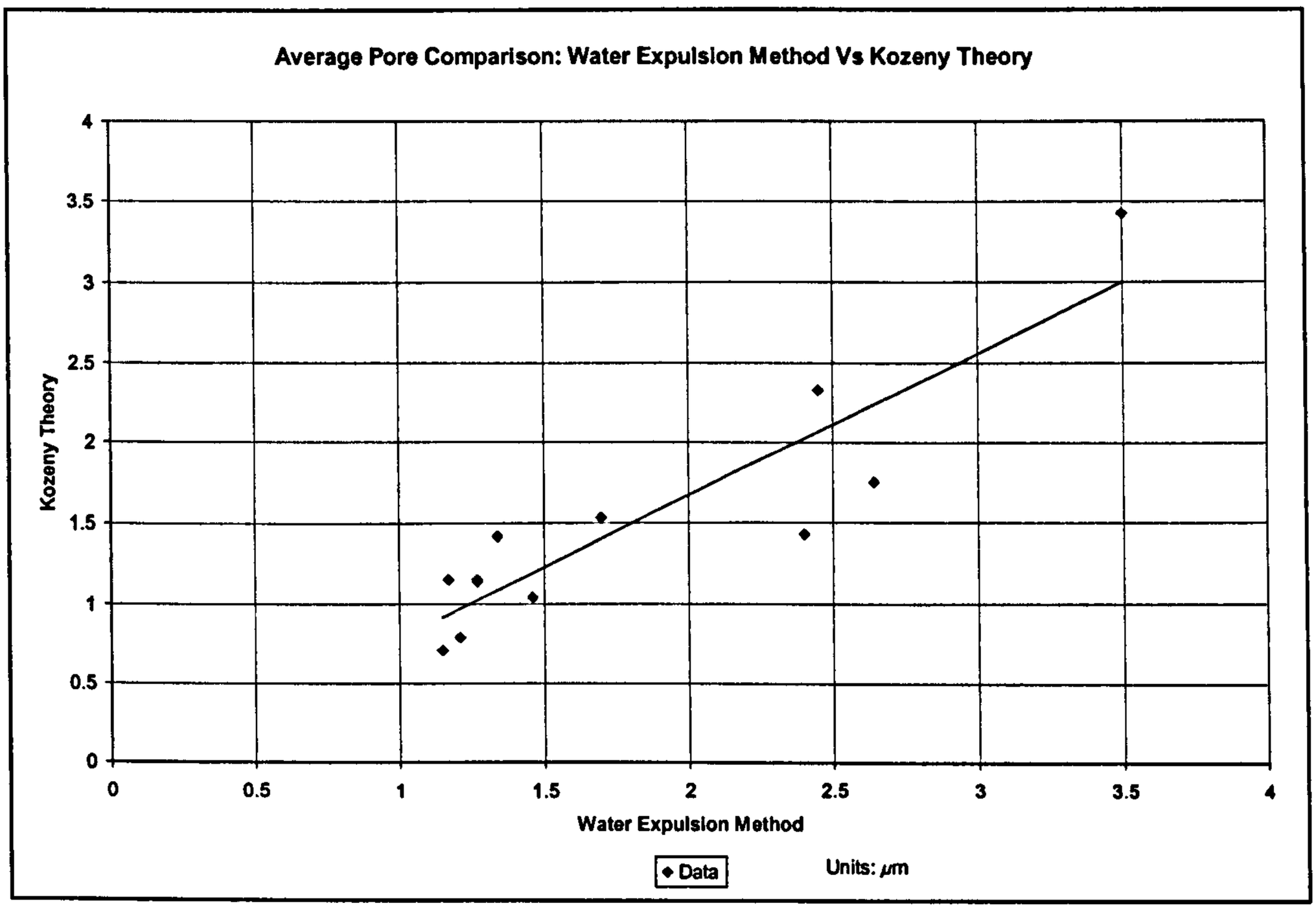

Figure 61-comparison of the measured and theoretical pore size (based on the Kozeny theory) for SC porous alumina samples.

Figure 61 illustrates a comparison between the WE measured average pore size and the theoretical average pore derived from Equation 33 for twelve SC porous alumina

specimens of different permeability. These results show a very good correlation between the measured values and those predicted by the Kozeny equation.

SEM micrography & image analysis

Figure 62 and Figure 63 show typical micrographs of sintered journal bearings and the correlation between the pore size and the starch granules is readily apparent. The pores appear to well dispersed, both in terms of distribution and of separation of individual pores. The microstructures shown in Figure 62 and Figure 63 belonged to journals S1 and S2, respectively. These bearings had been previously used also for sectional consistency and ground and un-ground permeability tests. Because these bearings were manufactured with the same slip composition but from different batches, it was interesting to inspect visually their microstructure in order to investigate if there were any resulting changes.

From Figure 62 and Figure 63 it can be seen that the microstructure of both bearings is very similar. At first glance, the larger pores left by the swollen starch particles seem to dominate, while their even distribution in both specimens was expected from the previous permeability and density measurements, again corroborating the reliability and repetitiveness of the SC technique.

Figure 64 and Figure 65 show the microstructure of a 4 μm (S1) and a 0.5 μm alumina specimens at a higher magnification allowing for a closer inspection. The more advanced stages of the sintering process are more evident for the 0.5 um, neck and grain growth are clearly appreciated. It is also quite obvious that the void left by the starch particle suggest that this have in part obstructed the specimen's further densification. However, it was also apparent that the smaller alumina particle size resulted in smaller pores.

On the other hand the 4 μm alumina specimen, Figure 64, seemed to possess larger starch particle pores, essentially reflecting the lower sintering shrinkage of this particle size for the chosen sintering conditions.

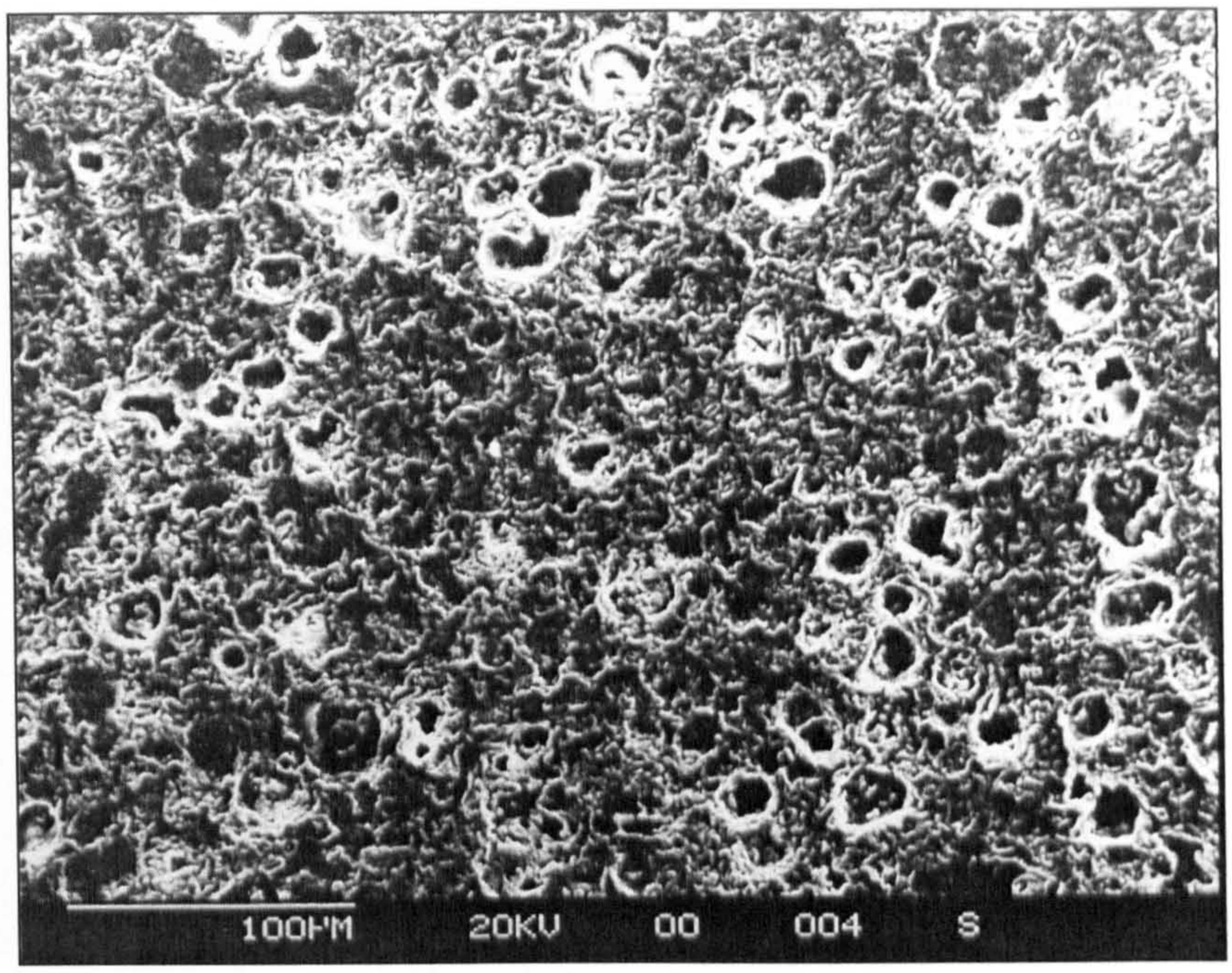

Figure 62-Shell 1 microstructure, made with 4μm alumina and 20 % starch. Permeability: 2.20E-15 m^2, relative density: 61.3 %.

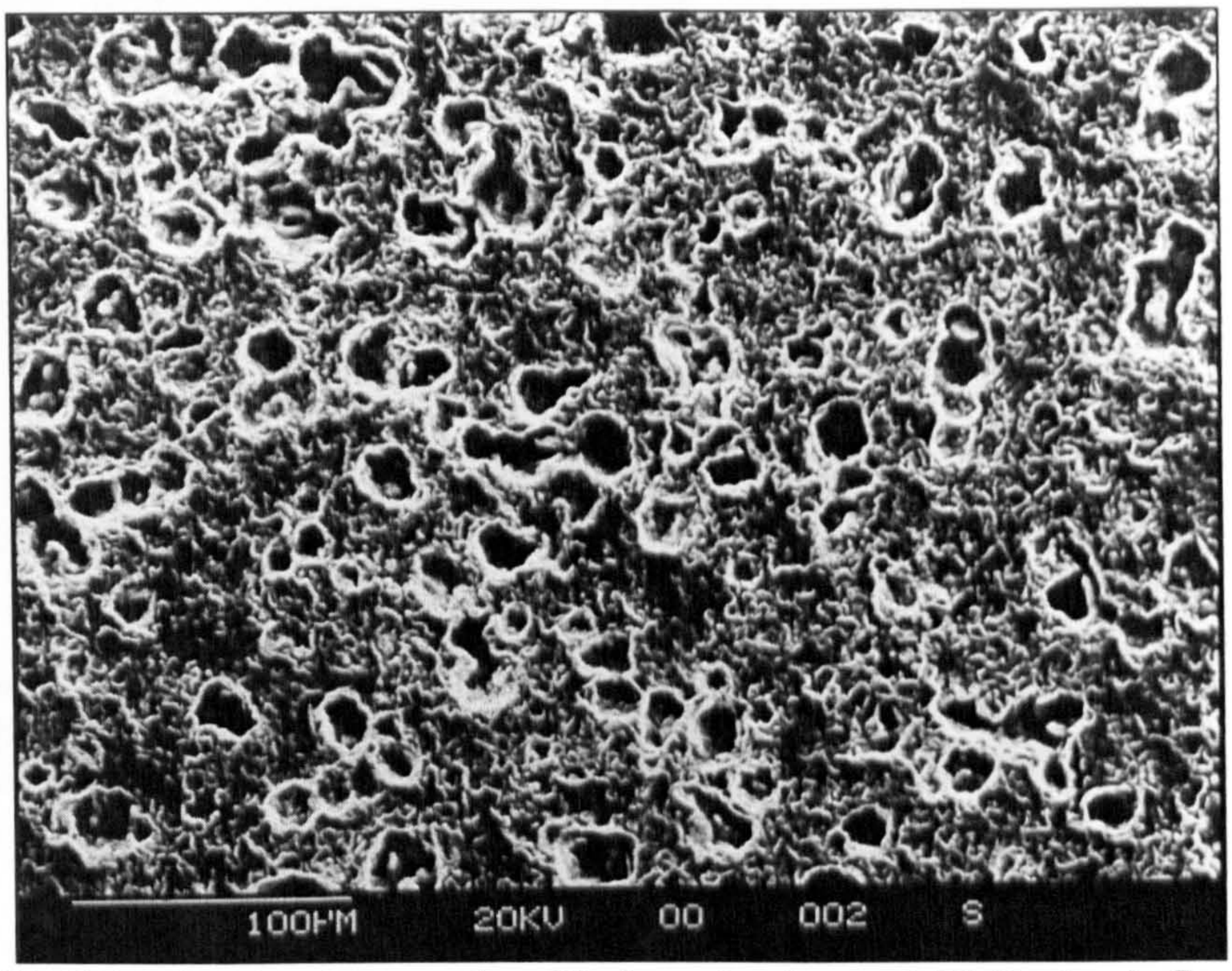

Figure 63- Shell 2 microstructure, made with 4μm alumina and 20 % starch. Permeability: 3.06E-15, density 62.8 %.

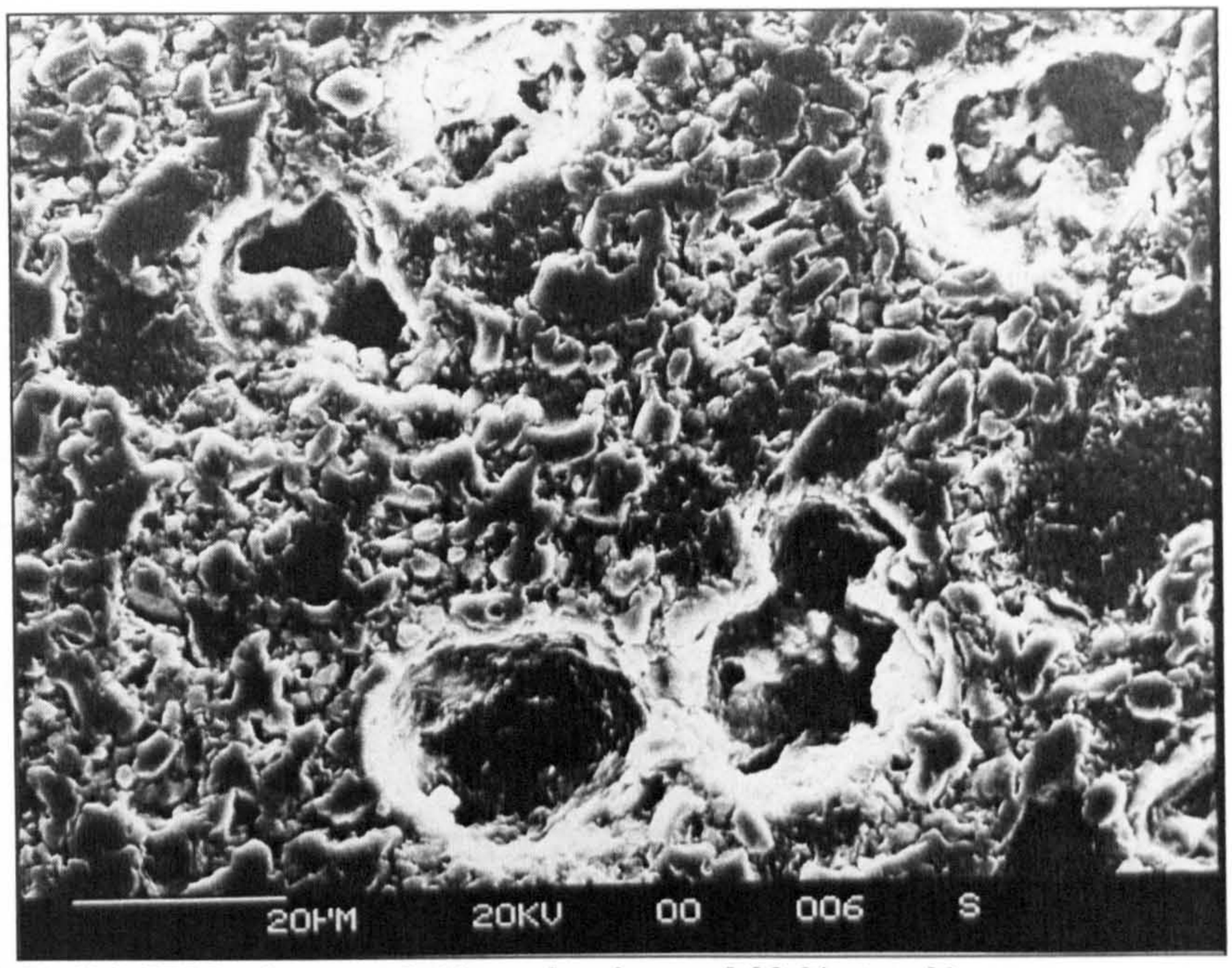

Figure 64-Shell 1 SEM micrograph (4μm alumina and 20 % starch).

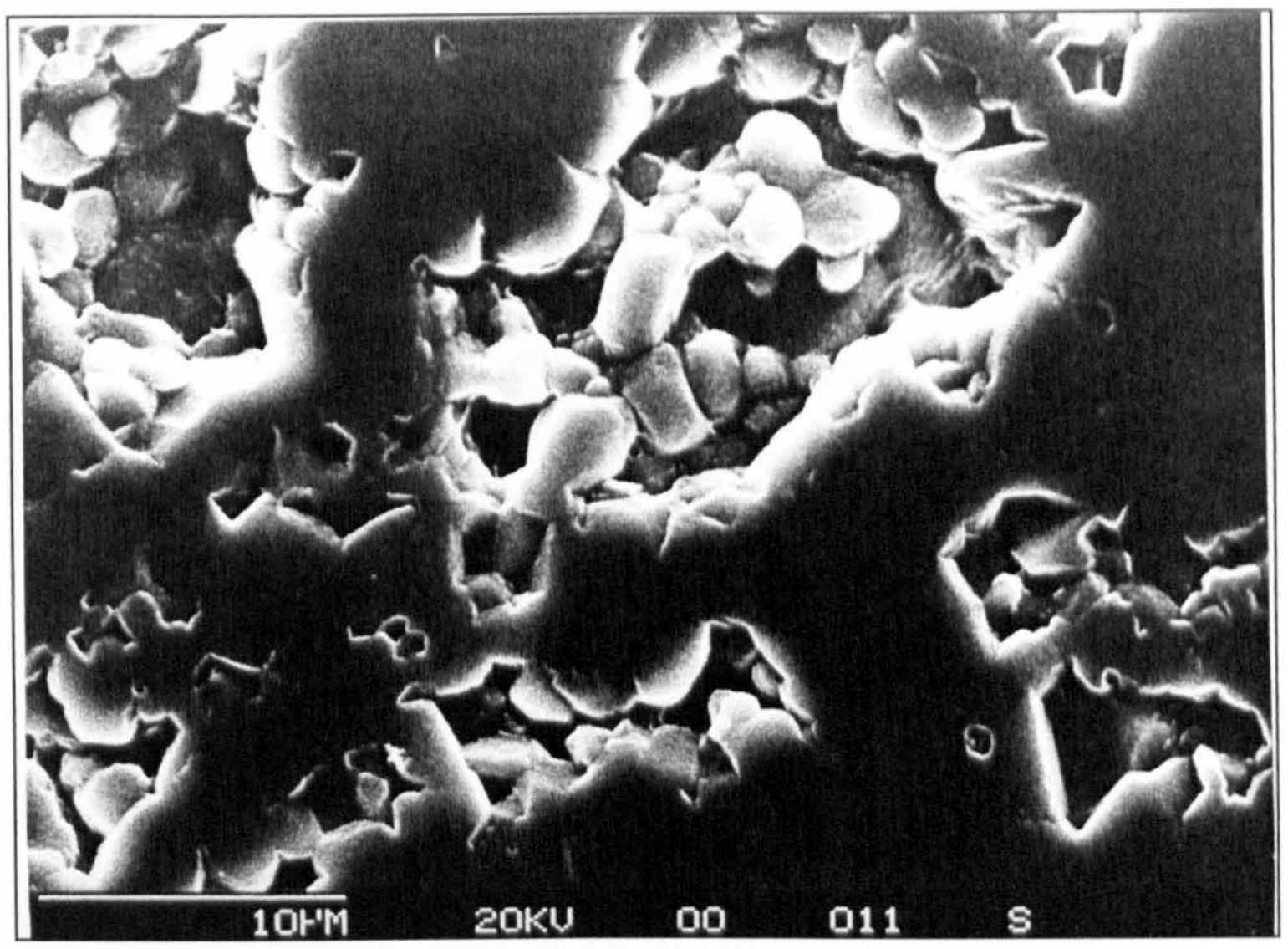

Figure 65-SEM micrograph for a 0.5 μm alumina and 40 % starch thrust bearing.

In general, this part of the porous-ceramic microstructure seems to resemble the appearance of the analytical model proposed by Greskovich and Lay [125], in their study of the grain growth of very porous alumina compacts (relative density ranging from 30 to 95 %); although further studies would be required to categorically conclude this. Overall, the need for a further understanding of the sintering phenomenon for porous solids, beyond qualitative models, has been emphasized by Rahaman [62].

Figure 66 illustrates the Greskovich and Lay's sintering mechanism model.

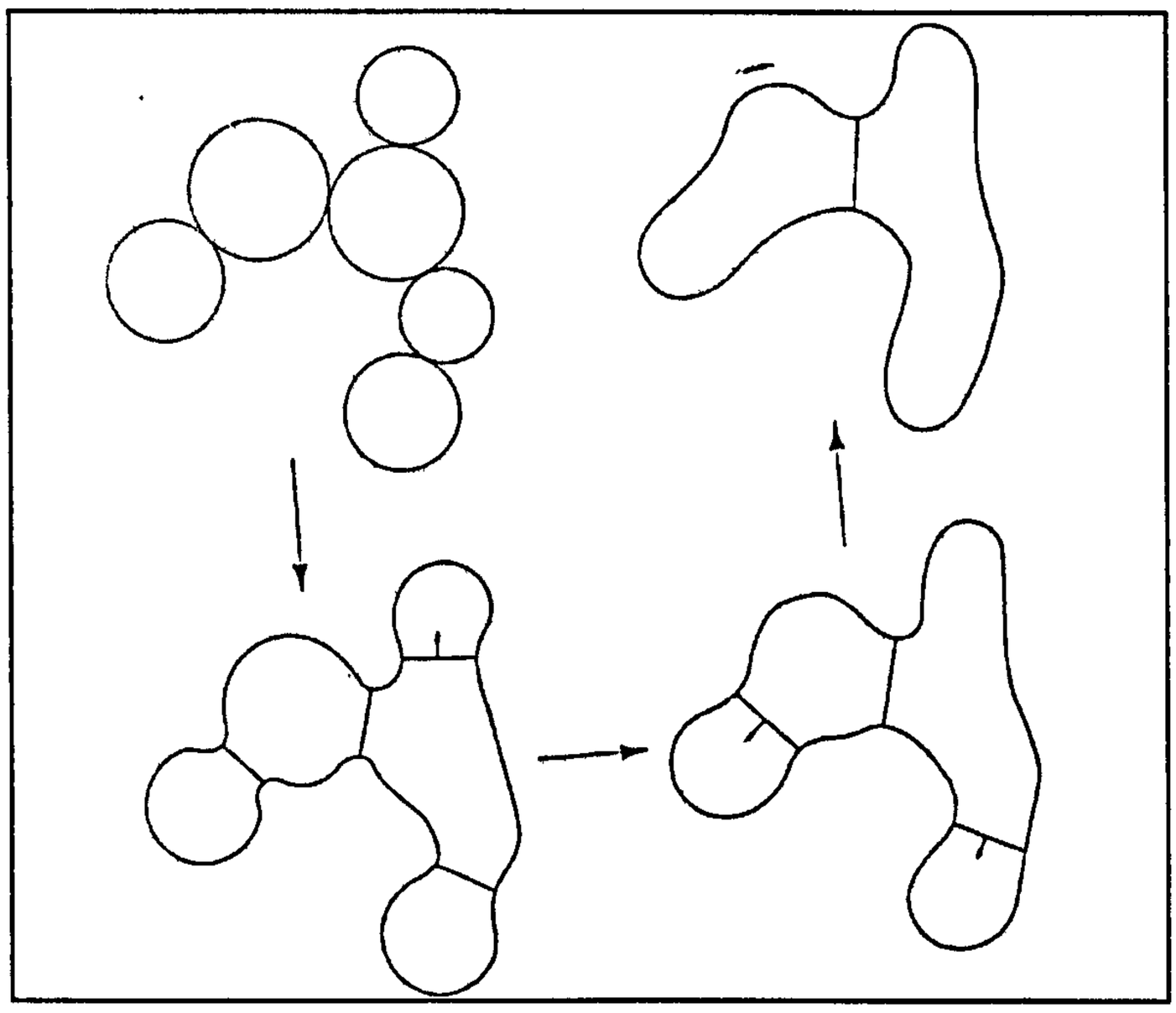

Figure 66- Greskovich and Lay's grain-growth mechanism model for porous solids, from reference [125].

Pore size measurement by image analysis

Computerized image analysis techniques were also used to examine SEM micrographs of the journal bearing structure. The associated software was able to clarify bit-map images taken from these photographs and determine such phenomena as pore surface area, fractional pore surface area, pore count, pore shape and average equivalent pore diameter.

The equivalent pore diameter distribution found for a micrograph showing the microstructure of bearing S2 (4 μm alumina and 20% vol. starch) is shown in Figure 67.

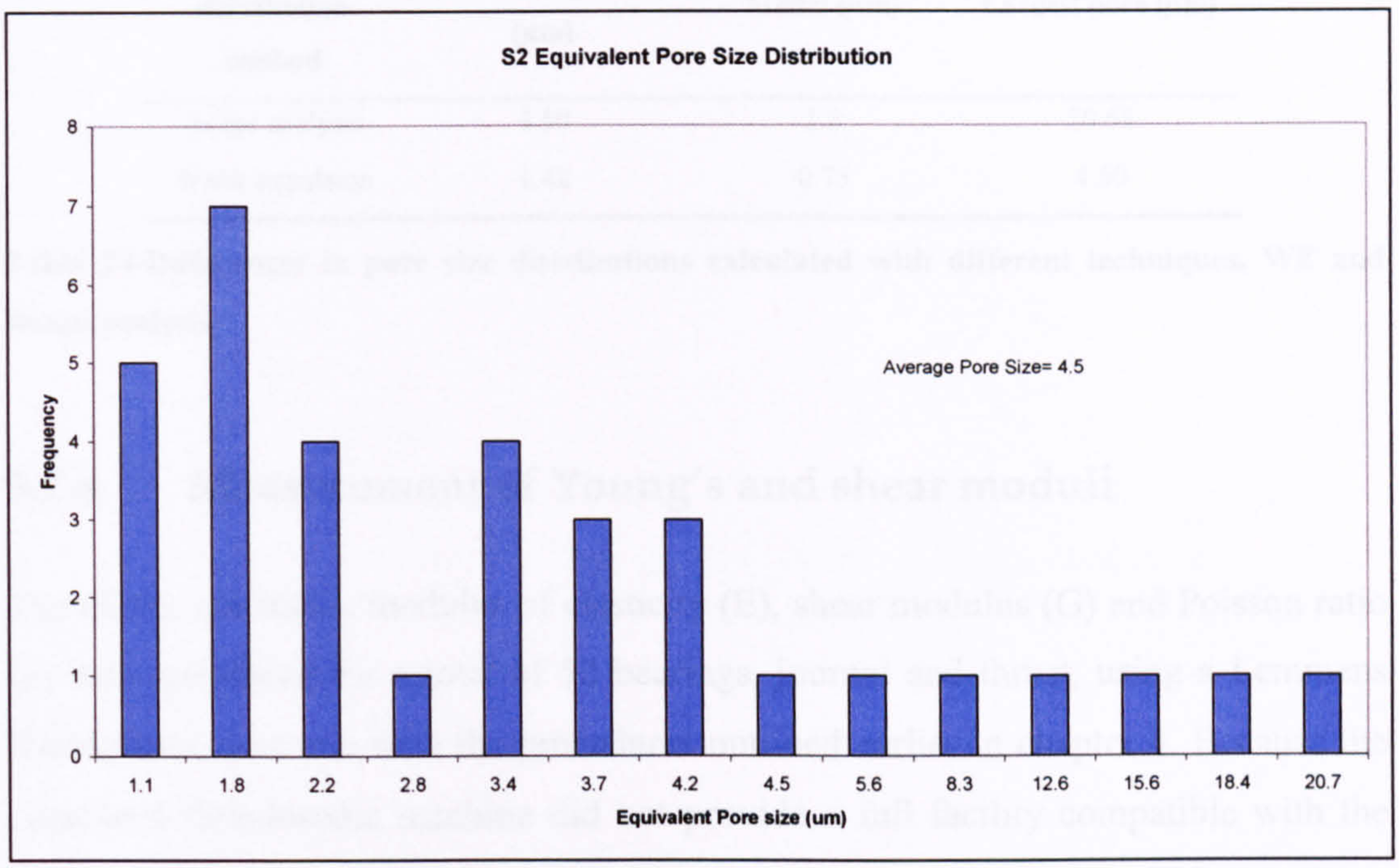

Figure 67-Pore size distribution resulting from image-analysis techniques for specimen S2.

As observed in Figure 67, the image-analysis technique did acknowledge the presence of larger semi-spherical pores (from 8-21 μm), presumably resulting from the location of previous starch particles. These larger pores could not be characterized by the WE method.

Because of the different nature of these two methods, some differences were expected. As reviewed before in the WE method, the equivalent pores were determined as a function of the flow and the pressure differential, whereas in the image analysis method these were estimated based on the morphology of the bearing's inner wall microstructure. Several other researchers [92] [95] have also observed similar results when comparing different techniques for pore distribution. Table 24 illustrates some of the differences found in the pore size distribution for specimens made with the same slip composition and similar densities.

Overall, it was believed that the two techniques complemented each other well, revealing very useful information with regard to the microstructure of SC bearings.

Pore distribution method	Average (μm)	Modal (μm)	Largest pore (μm)
Image analysis	4.50	1.8	20.68
Water expulsion	1.42	0.75	4.50

Table 24-Differences in pore size distributions calculated with different techniques, WE and image analysis.

5.2.4 Measurement of Young's and shear moduli

The elastic constants, modulus of elasticity (E), shear modulus (G) and Poisson ratio (υ) were measured for a total of 52 bearings, journal and thrust, using a Lemmens Grindosonic machine with the procedures outlined earlier in chapter 4. Because the Lemmens Grindosonic machine did not provide a full facility compatible with the journals' geometry, relative modulus has been measured instead. This has been calculated by raising the obtained resonant frequency to the power two [126].

Journal bearing relative modulus results and discussion

The results of the measurement of the relative modulus for seventeen 50 mm ID journal bearings are shown in Figure 68 in relation to their relative density. The density for the measured journal bearings ranged from 52 to 73 %. The results for identical shape and geometry specimens from previous porous-ceramic bearings research [3] have been added here as reference.

From Figure 68, it can be observed that the results from SC bearings agree well with the results obtained in previous research [3] for similar densities, despite the different manufacturing route. Almond fitted a curve with the HIPed data describing the relative modulus-open porosity relationship, resulting in a logarithmic curve with the same form as the one observed by Allison [127]:

Equation 34

$$\zeta = a - (1/b)\ln E$$

ζ	porosity
a	constant
b	constant
E_R	relative modulus

In the present study, however, the best fit curve is one of exponential form:

Equation 35

$$E_R = 1.2688 \cdot e^{0.0551 \cdot B_R}$$

E_R	relative modulus
B_R	relative density (%)

In general, HIPed bearings showed a marginally higher modulus for similar densities and this is probably due to the stiffer bonds between particles achieved through the high pressure HIPing process; although the data points are more scattered than those of the SC bearings. The reason for this may be the variations found in density, which are suspected to have been induced at the powder vibration step, resulting in less uniform microstructures.

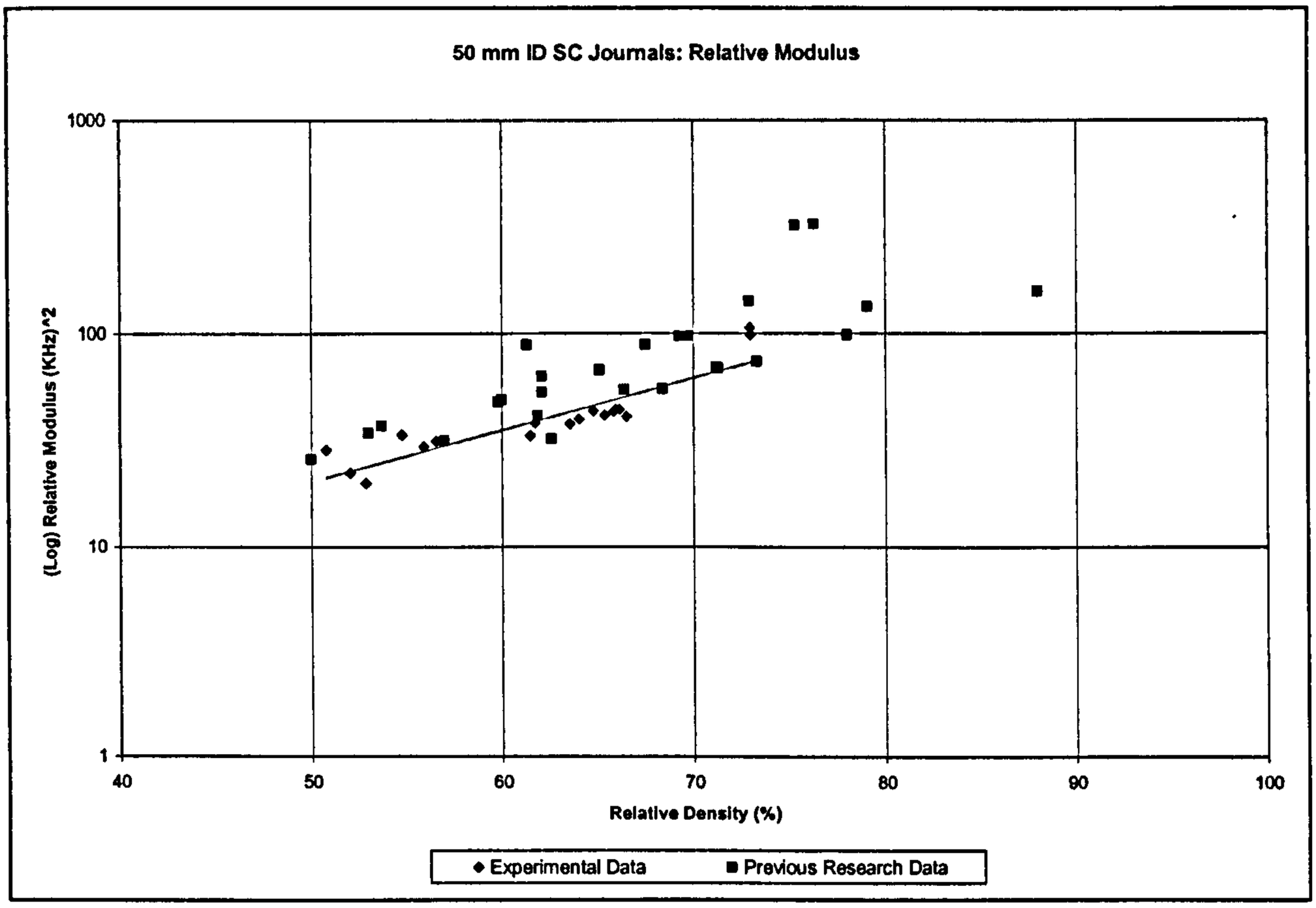

Figure 68- Relative modulus for SC bearings Vs density.

Thrust bearing moduli results and discussion

In addition to the investigation into the relative modulus for porous-ceramic journal bearings, a more quantitative approach was taken by measuring the moduli of thrust bearings, as for this type of geometry the Lemmens Grindosonic machine did provide a full facility for their measurement. In most moduli studies, results are examined in relation to the specimens' porosity or density. As observed before, the differences between the density of thrust and journal bearings were not very significant. This supported the assumption that the measurement of the elasticity and shear moduli by performing these tests on either type of bearing is valid for a SC bearing regardless of its geometry.

At the start of this study, two metallic discs, one made of aluminium and the other made of steel with similar dimensions to those of the SC thrust bearings, were also tested, resulting in a modulus of elasticity of 72.3 and 206.1 GPa, respectively. These were very near the theoretical values for each [128]; hence validating the method and procedure.

Porosity dependency on the Young's (E) and shear (G) moduli

Young's modulus results and discussion

Several authors in the past have attempted to correlate the level of porosity in a body with the resulting Young's modulus. The most widely acknowledged approaches use either an exponential or a power law function to describe this relationship.
Typical of these two approaches are the work of Duckworth [129] and Spriggs [130], where an exponential function was proposed:

Equation 36

$$X = X_0 \cdot e^{-b\zeta}$$

X	modulus of elasticity
X_0	full dense material modulus of elasticity
b	empirical constant
ζ	fractional porosity

Others amongst Wagh [131] used a power law function:

Equation 37

$$X = X_0 \cdot (1-\zeta)^a$$

a	empirical constant

The best fit line for the results of the present research measurements is of a power law form (Equation 37) for each alumina particle size. However, it was observed that all the data points converged well and if all the data points for each alumina powder

were taken together, taking no notice of the powder size or starch content and only of the specimens' porosity, the curve fitting was still very accurate (Figure 69, CF=0.965), simplifying the analysis, as well as allowing a direct comparison with previous research measurements. The effects of the alumina particle size and the starch content on the porosity and density of the bearings have been discussed in a previous section of this chapter.

Over 45 bearings were tested, with total porosities ranging from 30 to 49 % with the elastic modulus ranging from 57 to 177 GPa depending on the specimens' porosity. Figure 69 illustrates the results for all the thrust bearings tested. Typical results for very similar geometry and size bearings from previous porous-ceramic thrust bearing research [30] [31] have been added as reference. Kwan [30] specimens' were produced via HIPing with alumina powders ranging from 0.5 to 63 μm, generally observing well defined modulus results. The specimens presented in Figure 69 belong to specimens produced with 7, 13 and 23 μm alumina.

Roach [31] on the other hand, used several manufacturing routes, such as slip casting and injection moulding. In general, Roach presented more scattered results; and the ones shown here, are those with the highest measured modulus, which were based on a 0.5 μm alumina.

As observed in Figure 69, the modulus of elasticity increased with an increasing density of the specimens. Data points belonging to bearings based on a 4 μm alumina and a starch content ranging from 50-60 % vol. starch have been omitted from this figure, as the inconsistencies observed during the density and permeability measurements were also present in the measurement of the moduli.

As indicated before, the curve fitting for the data shown in Figure 69 was of a power law form, similar to Equation 37. The curve fitting constants obtained in this exercise are shown in Table 25. Kwan [30] and Roach [31] fitted similar curves for aerostatic thrust bearings and the empirical constants they obtained are also shown in this table, as reference.

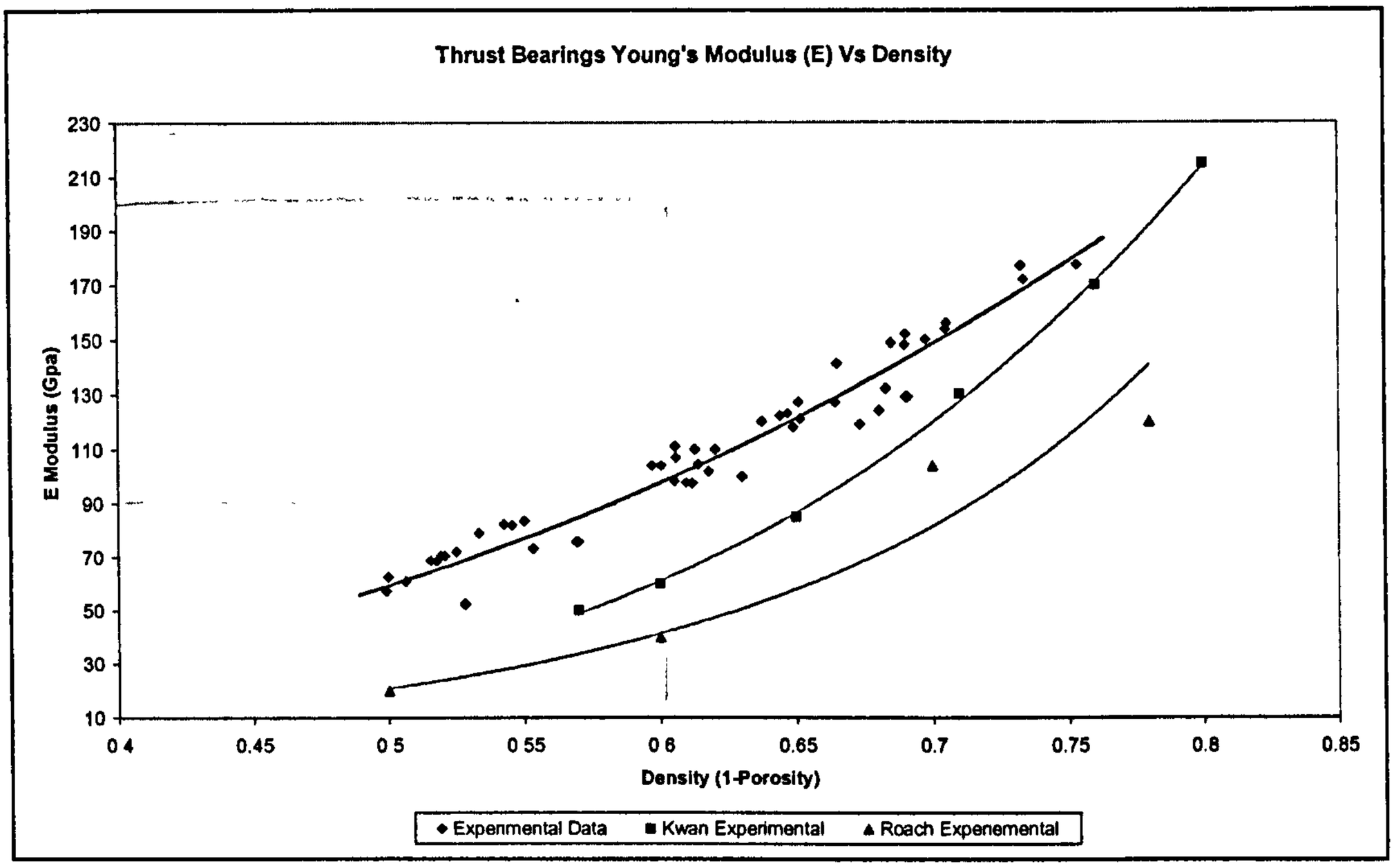

Figure 69-Thrust bearings Young's modulus Vs fractional density.

	Present Research		Kwan (ref 28)		Roach (ref 29)	
Property /Constants	**X_0**	**a**	**X_0**	**a**	**X_0**	**a**
Modulus of elasticity	390.07	2.71	479.7	3.91	276	4.11
Shear modulus	158.01	2.68	193	3.82	135	4.38

Table 25-Modulus and shear moduli experimentally derived elastic constants.

Considering the elastic modulus of fully dense alumina to be 410 GPa [99], it can be seen that the obtained empirical constant for X_0 is relatively close to this value, indicating a very good correlation of the porosity and the resulting modulus. In addition, the value for the empirical constant a is reasonably consistent with the results observed by Wagh [131] for ceramics fabricated without hot pressing or sintering aids (a $\approx$2).

The differences observed in relation to the constant values obtained by Kwan [30] and Roach [31] may be in part due to the different microstructure achieved by the different processing routes. Costa [132] *et al* have conducted research in this field

using a similar piece of equipment, and have noted the discrepancies in the Young's modulus on porous ceramic specimens manufactured with different forming techniques.

Roach [31] has also suggested that another source for the discrepancies observed between his and Kwan's [30] work, may be experimental errors induced by the specimen's surface finish, with the rougher finished samples causing the greatest deviations. At this stage, Roach did not quote any values for any of the surface finish parameters. However, similar deviations were also found at the bearings performance measurement stage, and for this he considered bearings with a R_a of 1.793 and 4.676 μm to be 'better' and 'poor' surface bearings, respectively.

For the present research, the surface finish R_a for a SC thrust bearing was examined using a form Talysurf 120lL equipment, and this was found to be 2.370 μm, which is closer to what Roach considered to be an adequate bearing. On the other hand, R_t was found to be 19.545 μm, whereas Roach observed a minimum of 18.455 and 24.113 μm for the better and poorer bearings, respectively. However, it must be noted that, for the 52 measurements performed here, there was no indication of the occurrence of problems of this nature. Hence, Roach's assumption could not be verified.

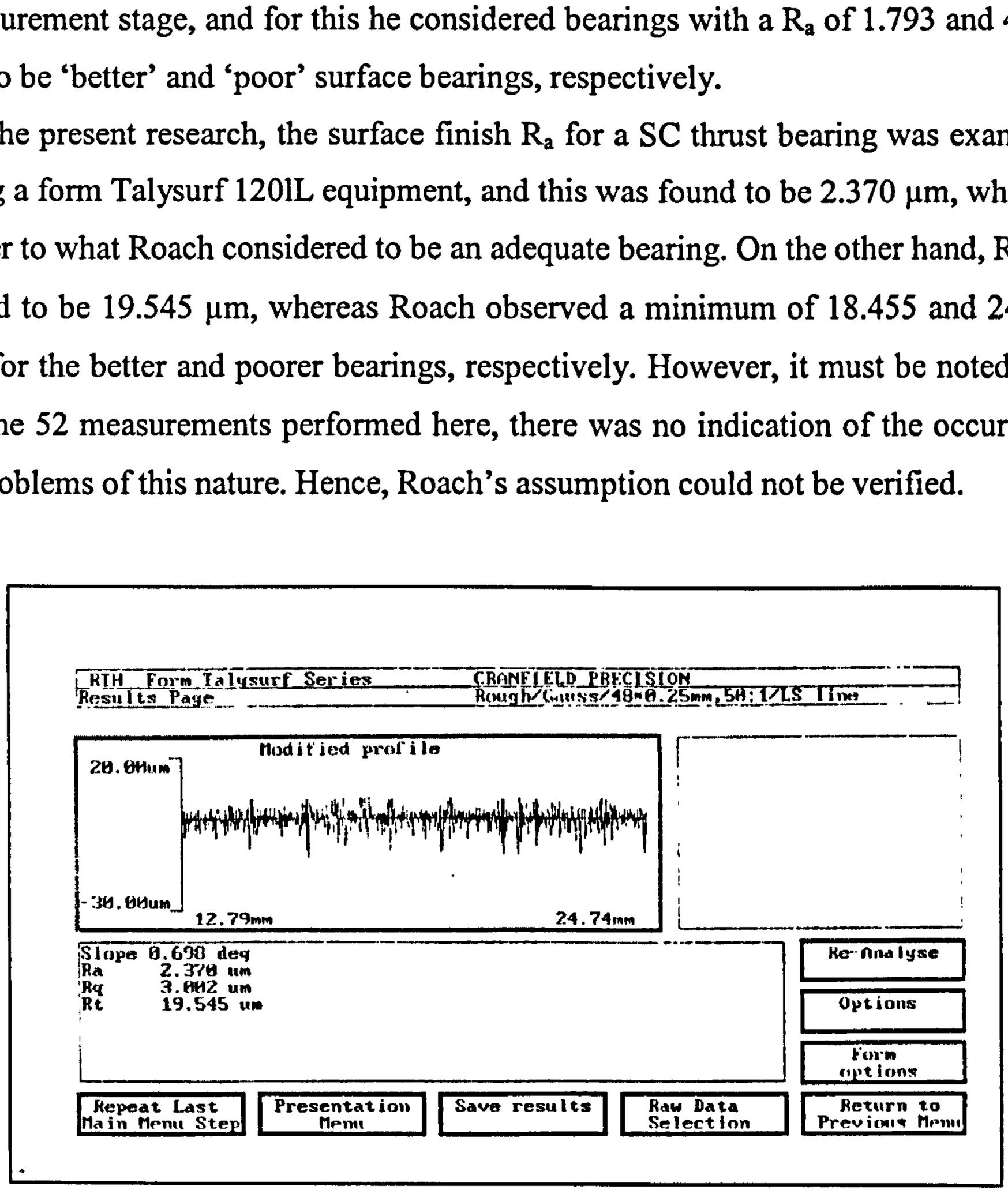

Figure 70- Surface finish profile for a 4 μm alumina size and 20% vol. starch solids content SC trust bearing.

Shear modulus results and discussion

The shear modulus results for all the measured SC thrust bearings are shown in Figure 71 in relation to their density. As with the elastic modulus, the shear modulus increases with an increasing density. This was expected from the previous density and porosity measurements, which indicated an increasing porosity with increasing starch contents.

Curve fitting resulted in a curve of the same type as to that observed for the elastic modulus (Equation 36). The empirical constants obtained through this exercise are also shown in Table 25.

Poisson's ratio values for the thrust bearing measurements ranged from 0.20-0.23. Although, the Poisson's ratio results did not show any obvious trends, the range of values observed here are well within the values expected for ceramic specimens [99].

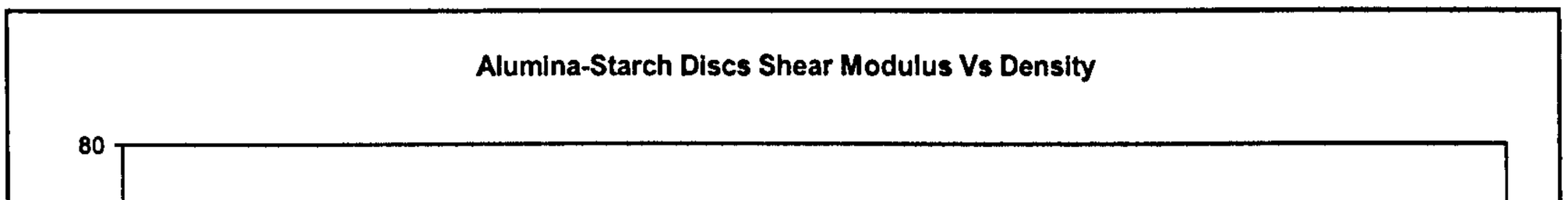

Figure 71-Thrust bearings shear modulus Vs density.

Overall, the magnitude of the obtained values for SC thrust bearings elastic constants are comparable with the results obtained by Kwan [30] for the same range of porosity, and generally higher than the results obtained by Roach [31], despite the presence of the voids left by the starch particles in their microstructure. In this sense, it is interesting to note that because of their nature, the more conventional processing routes employed by Roach, slip casting and injection moulding, are more successfully conducted using a smaller alumina particle size range (usually 0.5 to 1 μm), which generally results in relatively dense bodies. Porosity levels are then controlled by controlling the sintering temperature and time. An increase in porosity, as may be required for the present application, is usually achieved by decreasing these two variables, which in turn results in a lower densification; and hence weaker particle bonds. Conversely, the SC bearings have been sintered at a higher temperature (1550 °C), leading to stronger particle bonds, and their influence is reflected in the higher moduli results, and yet the pores created by the starch particles contribute to achieve the required porosity without compromising too much the structural properties of the bearings.

Kwan [30] on the other hand, used larger alumina particle sizes, but employed HIPing as the sintering route, which resulted in stronger and stiffer bonds. However, for a bearing microstructure achieved like this, an extra ceramic layer to control the pneumatic hammer effect associated with aerostatic bearings may be required [30], accounting for a more complex and expensive manufacture process.

5.3 SC porous-ceramic bearing performance results

5.3.1 SC journal bearing selection for performance testing

The selection of the SC bearings for testing was based on the modelled theoretical requirements for an optimized ultra-precision journal bearing of 50 mm ID specified in previous research [3], and these essentially are:

- Permeability target: 1×10^{-14} m^2
- Sintering density target: 80 %

These requirements have been further discussed in chapter 2. The SC bearings selected for testing and some of their most important properties are shown in Table 26.

Specimen	Alumina particle size	Starch solids vol. content (%)	Permeability (m^2)	Bearing radial gap (μm)	β (dimensionless)
3	4	20	6.69×10^{-15}	19.5	1.19
4	4	20	7.04×10^{-15}	13.35	3.69
3/40	3	40	2.63×10^{-14}	26.5	1.71

Table 26- Characteristics of bearings chosen for performance testing.

The measured permeability values for the SC bearings selected for testing are around the optimum for this application as estimated by Almond [3]. The bearing's radial gap is also a very important parameter in the bearing performance. The determination of this has been detailed in the chapter 4.

On the other hand, the bearing feeding parameter (β) is a porous-bearing design parameter derived by Majumdar [47] and in its definition involves other parameters such as the bearing's gap, permeability and dimensions. This has been more

thoroughly reviewed in chapter 2. Chattopadhyay and Majumdar [48] found β to be around 1.3 for the optimum load capacity of porous-hydrostatic bearings. The characteristics for the conventional hydrostatic journal bearing used for the direct comparison of the two technologies exercise can be found in Table 7.

Because of the unique, but complex design of the performance test rig, fitting of the porous bearings was a complex and time consuming procedure. This, in addition to the thoroughness of the testing programme, limited the number of SC journal bearings which were tested to three, in addition to the conventional hydrostatic journal bearing used for the above mentioned comparison.

Results are presented in the following sections, and these were expressed in relation to either their correspondent operational parameter or their dimensionless porous hydrostatic bearing design parameters. The latter have been discussed in the literature review chapter in more depth. Additional results from previous research [3] for porous-ceramic journal bearings, of similar characteristics, have been used here in order to broaden the scope of the discussion. Table 27 shows these bearings characteristics.

Specimen	Permeability (m^2)	Bearing radial gap (μm)	β (dimensionless)
A50	6.50×10^{-14}	25	3.88
A53	8.60×10^{-14}	19	10.68
A71	3.40×10^{-14}	18	3.73
A88	1.6×10^{-14}	18	1.82
A100	6.0×10^{-15}	21	3.08
A109	1.30×10^{-14}	19	1.3
A110	6.0×10^{-15}	15	1.0

Table 27-Previous research bearings' characteristics.

Oil, *DIE 180*, was used as lubricant during the performance testing programme. This represents a novelty in relation to the performance measurement of porous-ceramic bearings, as only water and air have been used previously. DIE 180's density and viscosity charts as well as the manufacturer's datasheet charts can be found in the appendices. As previously mentioned, in previous porous-ceramic journal bearing research [3], water has been used as lubricant. However, conventional hydrostatic theory [37] indicates that the choice of lubricant plays no part in the determination of static stiffness, hence validating the comparison between the results of the previous and present porous-ceramic journal bearing research.

5.3.2 Porous-ceramic hydrostatic journal-bearing experimental performance results and discussion

Static stiffness with bearing gap and permeability

Figure 72 illustrates the static stiffness results with supply pressure and gap for the SC bearings. Results from bearings from previous research have been added as reference in Figure 72.

SC bearings SC-3 and SC-4, were manufactured with the same processing conditions, but were processed separately. Because of this, their permeability coefficients are very close to each other (difference is 0.39 m^2), and because their nominal size and shape was identical, it allowed a direct comparison, assuming that the resulting differences in the static stiffness were mainly attributable to the bearings' radial gap. In this particular case, bearing SC-3 had a radial gap of 19.5 μm, whereas bearing SC-4 had a radial gap of 13.35 μm.

As seen in Figure 72, SC-4 exhibited an increasingly higher stiffness across the supply pressure (Ps) range, for a maximum stiffness difference of 86 N/μm at the higher end of Ps. This was not surprising, as it is observed in conventional hydrostatic bearings, a reduction in the bearing gap results in an increase in the lubricant film pressure, which in turn maximises the bearing stiffness. The third

trend-line in Figure 72 belongs to the observed static stiffness of shell SC-3/40. This shell had a higher permeability than the previous examined shells, but it also had a larger radial gap (see Table 26). Because of these differences, a direct comparison would not yield very useful information at this stage. Nonetheless, SC-3/40 exhibits a similar trend, showing an increasing stiffness with an increasing pressure.

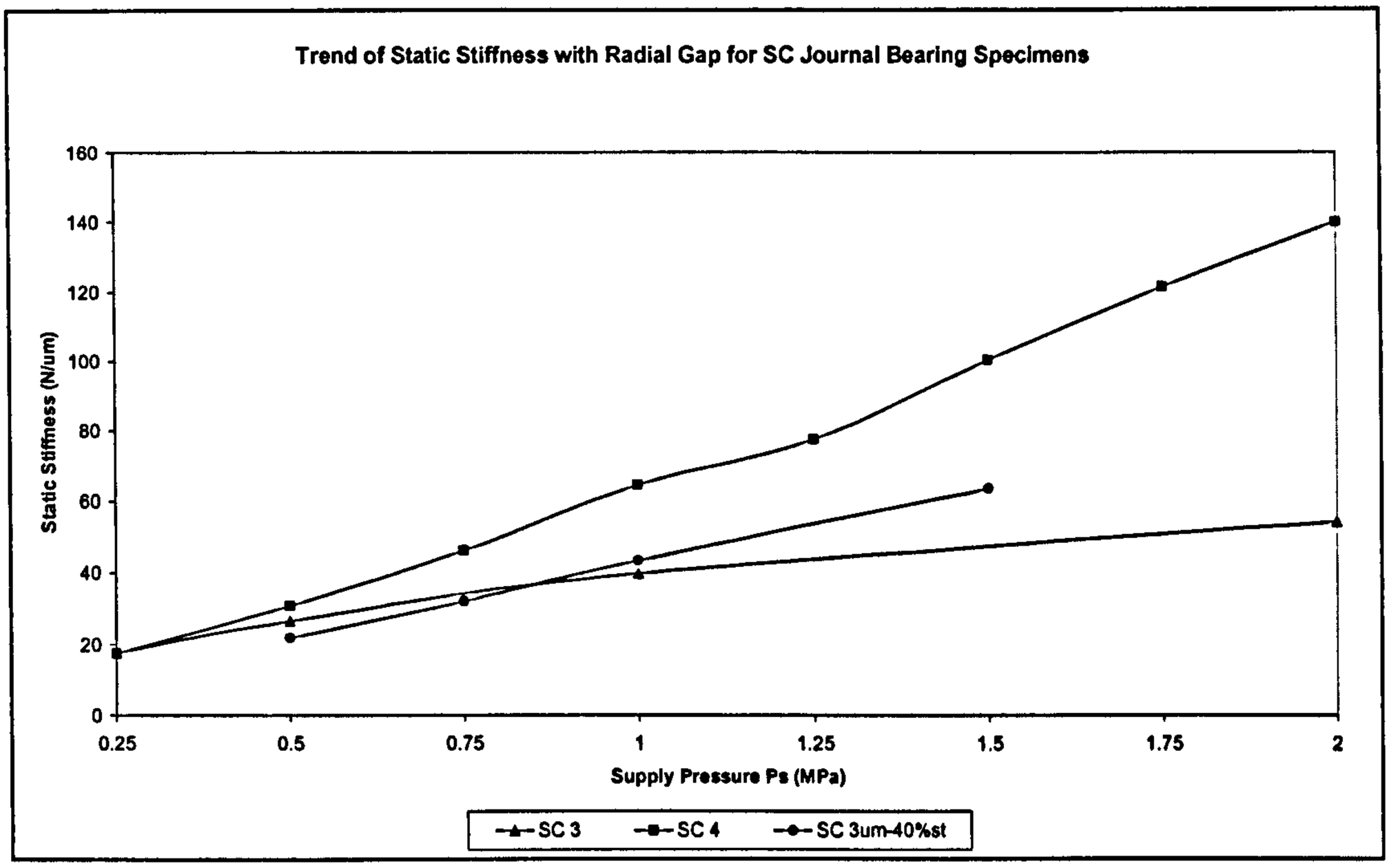

Figure 72- Trend of static stiffness with supply pressure and radial gap.

In order to make a more useful comparison, the static stiffness performance results of some bearings tested in previous research have been added in Figure 73. These bearings, A-100 and A-71, are of particular interest because of their permeability coefficient and/or bearing gap. A-100 has a very similar permeability to SC 3 and 4, the difference in permeability being 0.69 and 1.04, respectively (see Table 26 and Table 27). Hence, the difference in stiffness would be mainly attributable to the bearing gap. As can be observed in Figure 73, the static stiffness behaviour of A-100 is similar to that previously seen by SC-3 and 4. SC-4, however, exhibited a higher stiffness than the other two bearings because of its smaller gap (13.35μm); again this was expected from the increasing film pressure. However, although SC-3 had a smaller gap than A-100, 19.5 as opposed to 21μm, SC 3 did not outperform A-100.

SC 3 behaves similarly to A-100 through the range of Ps; however at the maximum pressure A-100 behaviour is better (approximately 20 N/μm). The results for these two bearings oppose the conventional hydrostatic theory [37]. Almond [3] observed a similar behaviour that resulted in his best bearing being one with a 19 μm radial gap over bearings with similar permeability and smaller gaps. For the particular case of SC 3, however, it is believed that the poorer behaviour of SC-3 is due to the limited number of data points, only four as opposed to eight for the other tested bearings, as well as experimental error. Unfortunately, at this stage it was not possible to repeat the experimental set for SC-3, due to an incident that resulted in the breaking of bearing SC 3. Further details of this are given in the following sections.

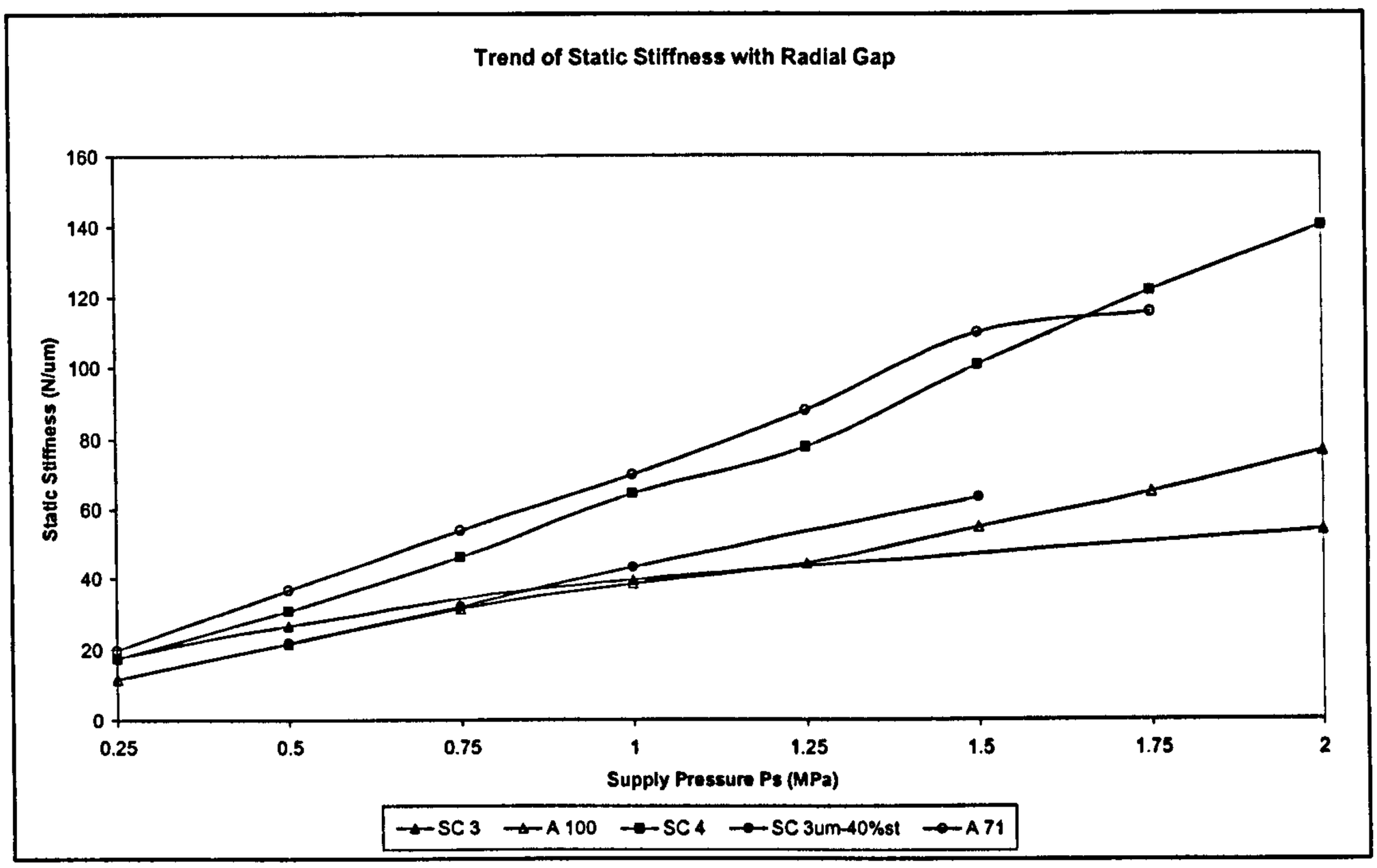

Figure 73- Trend of static stiffness Vs supply pressure with radial gap, including bearings from previous research.

On the other hand, previous research indicated that A-71 is relatively similar in permeability to SC-3/40, the difference between the two being 0.74 m^2. However, the radial gap observed by A-71 is smaller to the one observed by SC-3/40 by 8.5 μm, and this is reflected in its static stiffness results (Figure 73). The maximum difference occurring at the maximum recorded pressure of 1.5 MPa was 46 N/μm.

Again this was mainly a result of the smaller bearing gap for A-71, in accordance with the conventional hydrostatic theory and with the observed behaviour during the previous comparison of SC-3 and SC-4 Vs A-100 noted above. This second set of comparative data permits one to establish that indeed the effect of the smaller bearing gaps seems to increase the bearing static stiffness. However, in light of the behaviour observed by SC-3 and by Almond's shell 109 [3], more precise data was required to categorically confirm this.

Overall, A-71 exhibited the highest stiffness and this was a result of both, its highest permeability and its reduced gap that account for a higher lubricant film pressure. Because of the limited amount of data it was difficult to discern which of these parameters was the most influential. Alternatively, a useful approach is to observe the static stiffness in relation to the bearing feeding parameter, where both parameters interact.

Static stiffness and bearing feeding parameter

The bearing feeding parameter is a porous hydrostatic bearing design parameter that amalgamates the bearing's geometry and dimensions, gap and permeability. In this section, static stiffness is presented in terms of non-dimensional static stiffness in order to examine it in relation to the results presented by Almond [3], as well as reference for future numerical analysis.

Non-dimensional static stiffness can be defined as:

Equation 38

$$\overline{K}_{static} = \frac{4 \cdot C}{L \cdot D \cdot P_s} \cdot K_{static}$$

$\overline{K}_{static}$	non-dimensional static stiffness
K_{static}	static stiffness (N/μm)
C	bearing radial clearance (μm)
L	bearing length (m)
D	bearing diameter (m)
P_s	supply pressure (Pa)

Figure 74 shows the non-dimensional static stiffness of shells SC-4 and SC-3/40 at several supply pressures ranging from 0.25 to 2 MPa, in relation to the bearing feeding parameter (β).

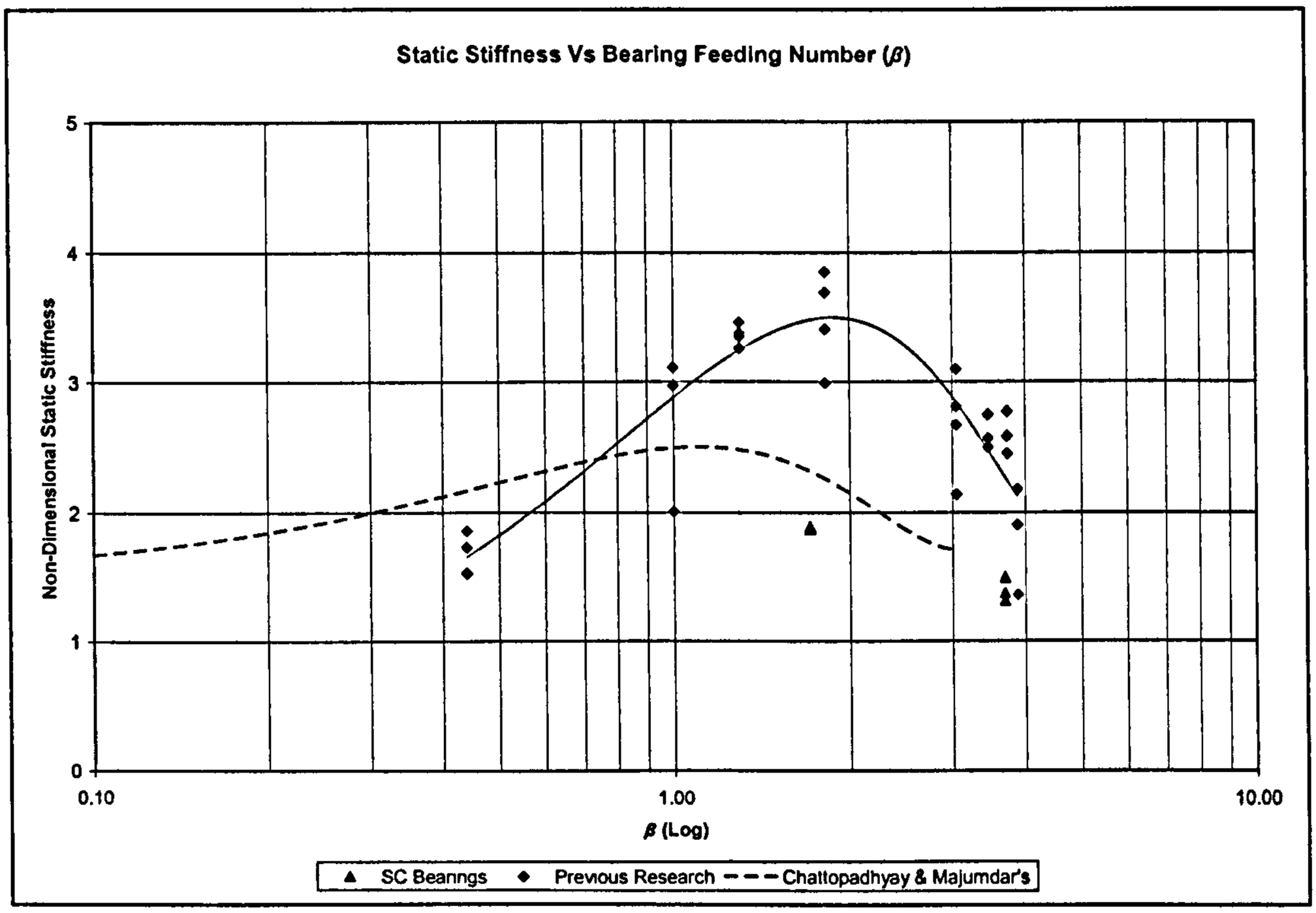

Figure 74-Dimensionless static stiffness Vs bearing feeding number.

Figure 74 also illustrates results from previous research [3] for the same range of supply pressures. The addition of these data points helped to visualize more clearly the trends followed by the non-dimensional static stiffness. As can be observed, the peak of the curve is reached at a β value near 1.8. Almond fitted a curve of the form:

Equation 39

$$\overline{K}_{stat} = a \cdot \beta^3 + b \cdot \beta^2 + c \cdot \beta + d$$

$\overline{K}_{static}$	non-dimensional static stiffness
β	bearing feeding parameter
a	empirical constant
b	empirical constant
c	empirical constant
d	empirical constant

Almond [3] validated the static stiffness Vs bearing feeding parameter curve by comparing it against the results of Chattopadhyay and Majumdar's [50] dynamic model for the direct stiffness coefficient K_{rr}, also shown in Figure 74. Attention is drawn to the fact that this theoretical set of results was originally calculated for a rotational study. Nonetheless, Almond acknowledged this and stressed this comparison was taken on a qualitative level with regard to the shape of the curves and the numerical methods.

However, despite the limited number of data points, the SC bearings' results seem to follow the Chattopadhyay and Majumdar's [50] theoretical curve, as opposed to the results from previous empirical research. In this regard, it was felt more data was required to establish whether the observed trend would hold over a wider set of testing conditions.

Nonetheless, in the interest of expanding the pool of experimental data for future reference, Almond's analysis has been broadened out by adding the current research results, resulting in a very similar curve fitting with some minor changes in the constant values, as indicated in Table 28.

Constants' origin	a	b	c	d
Almond's research [3]	0.1364	-1.4587	4.0454	0.15
Almond's research [3] + present research results	0.1059	-1.1574	3.2387	0.531

Table 28-Dimensionless static stiffness empirical constants.

The validity of Equation 39 is limited to the range of bearing feeding parameters observed, which cover the expected values for most practical designs.

However, caution should be exercised over the fair degree of scatter observed. Almond argues this is in part caused by the differences observed for each bearing permeability factor. The permeability factor is another dimensionless parameter introduced by Chattopadhyay and Majumdar [48], involving the bearing's permeability and gap.. The dimensionless permeability factor can be defined by Equation 40:

Equation 40

$$\sigma_y = \frac{C}{\sqrt{\psi v}}$$

σ_y dimensionless permeability factor

C bearing radial clearance

ψ_v viscous permeability

In general, for practical values of C and ψ_v, an increase in permeability results in a decrease of σ_y. In their theoretical analysis, Chattopadhyay and Majumdar [48] also observed the load capacity to vary with the variation of σ_y. As a consequence, the optimum value for β also varied, ranging from 1 to 3, with generally the lowest values of β for the highest values of σ_y. This noted variation provides some level of justification to the assumption made by Almond for the data scattering.

Static stiffness and eccentricity ratio

Figure 75 and Figure 76 illustrate the results of the static stiffness measurement against the observed eccentricity ratio. Eccentricity ratio (ε_0) is another porous hydrostatic bearing design parameter, and it is defined by:

Equation 41

$$\varepsilon_0 = \frac{e}{C}$$

ϵ_0	eccentricity ratio (dimensionless)
e	eccentricity (μm)
C	radial clearance (μm)

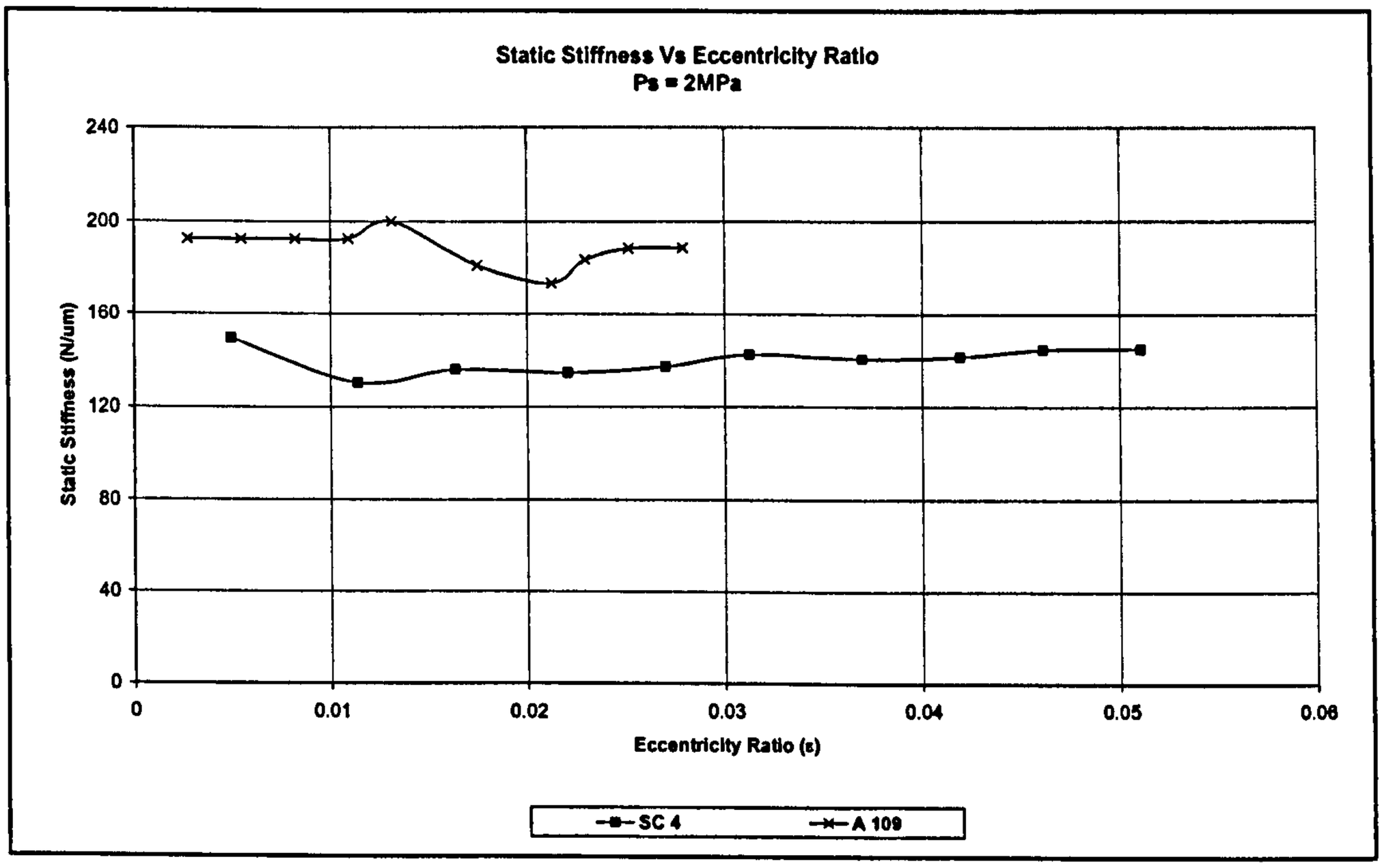

Figure 75-Static stiffness Vs eccentricity ratio, Ps=2 MPa.

Results expressed in relation to the eccentricity ratio permits comparison with the previous research results, as well as with the published analysis. In addition to the results from SC journal bearings, SC-4 and 3/40, Figure 75 and Figure 76 also illustrate the results of shell A-109 and A-50, respectively, from previous research [3].

As can be seen from Figure 75, the eccentricity ratios are relatively low for both bearings, indicating a relatively high overall stiffness. However, A-109 exhibited the highest static stiffness, averaging 188 N/μm across the range of applied loads. On the other hand, SC-4 had an average stiffness 140 N/μm. The higher stiffness of A-109 was expected as it possessed a bearing feeding number (β) value of around 1.3, near to the peak of the curve shown in Figure 74. In contrast, SC-4 had a β value of 3.69, for a combination of the bearing's geometrical dimensions, permeability and gap, all of which account for the lower stiffness performance.

Figure 76 illustrates the static stiffness results Vs eccentricity ratio for SC-3/40 and A-50 at a Ps of 1 MPa.

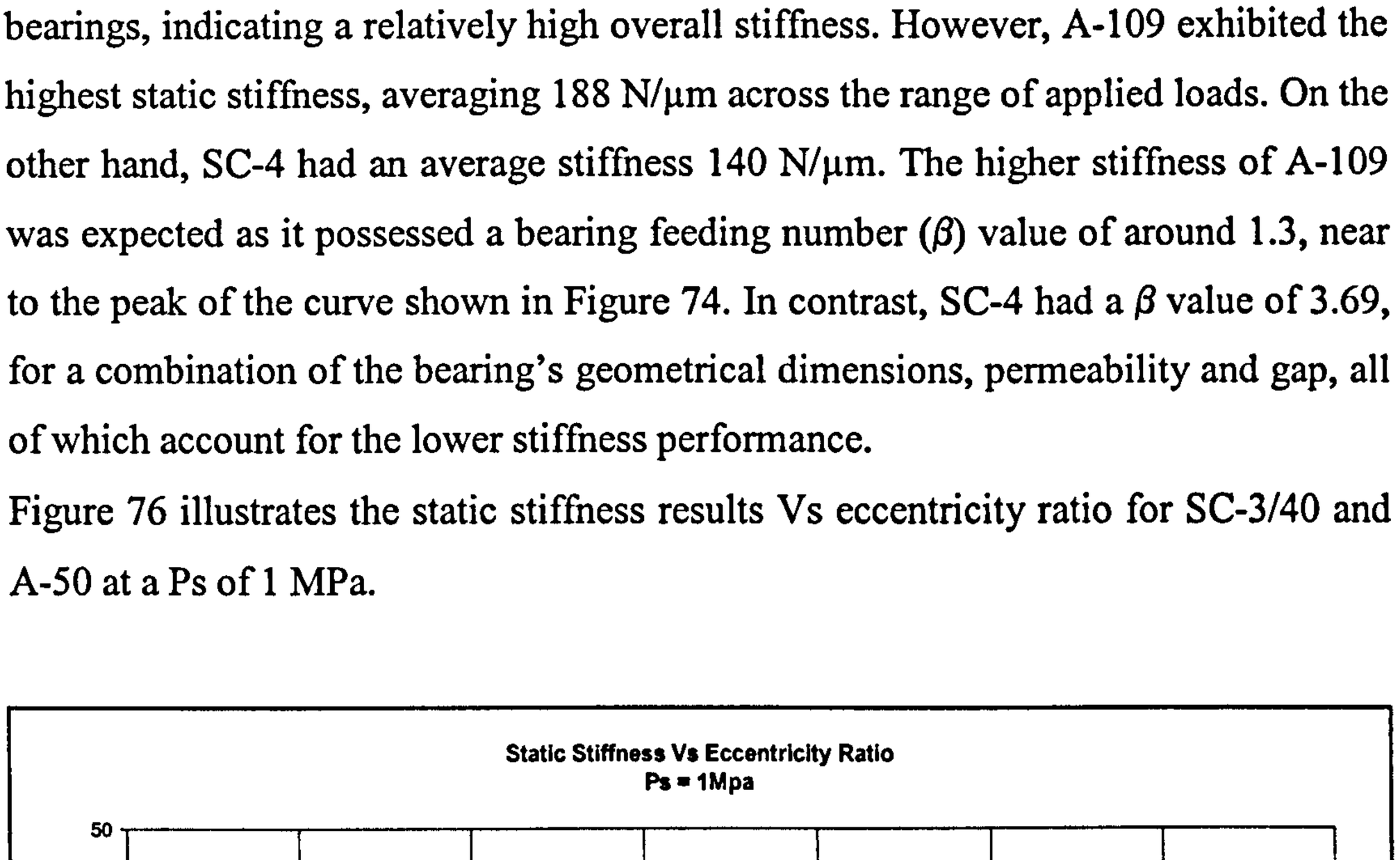

Figure 76-Static stiffness Vs Eccentricity ratio, Ps=1MPa.

As with the previous comparison, the bearing with a combination of geometrical dimensions, permeability and gap closest to the optimum β value, exhibited the highest stiffness. In this particular case, SC-3/40 has a β value of 1.71, closer to the optimum value observed in the previous static stiffness Vs the bearing feeding number experimental results analysis (Figure 74). Its average static stiffness was 43 N/μm. Conversely, A-50's β value was 3.88 and its average stiffness was 30 N/μm.

Unfortunately, no more information was available at this stage on the static stiffness Vs eccentricity ratio behaviour from either the previous or the present research.
Considering the limited amount of experimental data, it was believed that, overall, the static stiffness exhibited by the SC journal bearings was comparable to the static stiffness exhibited by the bearings produced in previous research [3], reflecting the properties and characteristics of each individual bearing tested.

Static flow rate measurement results and discussion

Flow rate with permeability and gap

The lubricant flow rate was measured over a supply pressure range of 0.25 to 2.0 MPa, in 0.25 MPa increments. Figure 77 illustrates the flow rate results for SC-3 and SC-4. Because of these two bearings similar permeability (Table 26), it can be assumed that the differences in flow rate can be the result mainly of the bearings' gap.
Figure 77 illustrates the plot of the flow rate and shows an expected linear increase as supply pressure is raised from 0.25 up to 2.0 MPa.

As shown in Figure 77 the difference in flow rate between both SC bearings in relation to their radial gap is not very significant. The maximum difference observed, 0.044 lpm, was observed in favour of SC-4, which possessed a marginally higher permeability. This observation agrees well with the trend noted by Almond [3] for a similar study in previous research. Almond's results are also shown in Figure 77.

The differences observed in relation to Almond's results arise from the different set of experimental data he used, for which the average viscous permeability was 1.2 x 10^{-14} m^2 with the bearings' gap ranging from 19 to 25 μm.

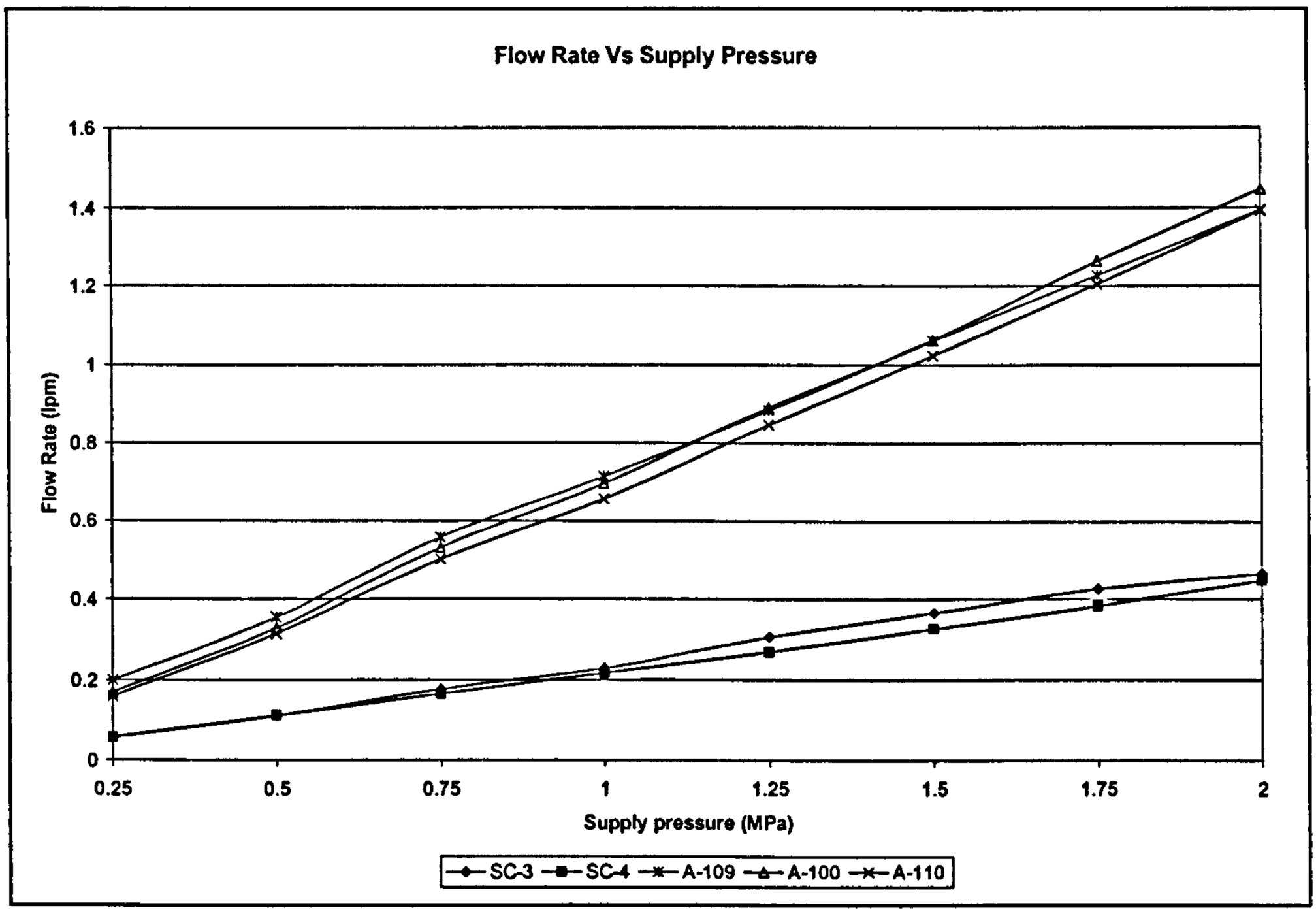

Figure 77- Flow rate Vs supply pressure for bearings with similar permeability.

The results for the set shown in Figure 77 indicate a fundamental deviation from the conventional hydrostatic theory as explained by Stansfield [37]. In his treatise, Stanfield defines flow to be proportional to the third power of the radial gap. Almond [3] acknowledged this, and suggested this difference could be a consequence of the extended land observed by the porous bearing, as well as the increasing number of feeding restrictors, causing a proportion of the flow at the bearing extremities to pass directly into the gap's exit point. Conversely, in a hydrostatic bearing, flow passes through the gap space over a fixed smaller land length. From this assumption, Almond highlights the importance of the permeability as a flow rate control parameter. With regard to the present investigation, it was thought that Almond's explanation adequately describes the observed flow trend for the SC bearings with similar permeability. Almond's assumption with regard to the marginal gap effect, is

in part supported by Chattopadhyay and Majumdar's theoretical investigation [48]. Chattopadhyay and Majumdar established that the dimensionless permeability factor (σ_y) had only a marginal effect on the bearing's final flow for a given β value. As previously reviewed in the present chapter, σ_y is expressed as the ratio of the bearing's gap to the square root of permeability.

A second study was conducted by Almond [3], looking at the most permeable HIPed bearings and limiting the bearing gaps to between 22 and 24 μm. Besides noting once again a linear response of the flow with the supply pressure, Almond also observed that increasing the permeability increased the bearing's flow. The bearings with the highest permeability, and consequently higher β values, reached higher flow rates for a given supply pressure, agreeing well with Chattopadhyay and Majumdar's theoretical investigation [48].

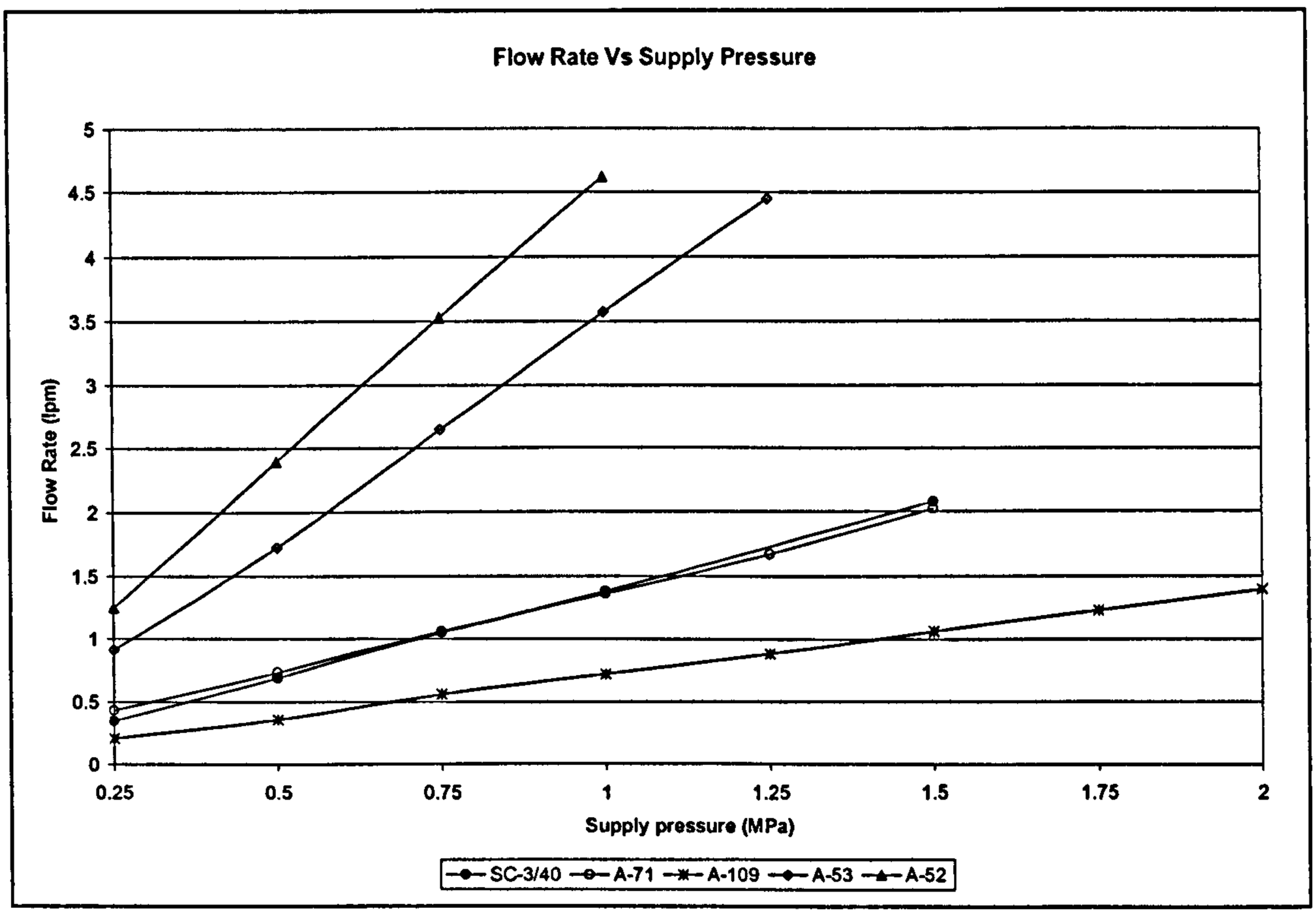

Figure 78- Trend of flow rate with permeability.

Figure 78 illustrates Almond's results for this exercise, together with the new results for SC-3/40. SC-3/40 has a permeability value within the range Almond studied

(Table 26 and Table 27), and it follows the trends he observed, despite having a slightly larger radial gap (< 2.5 μm). SC-3/4 was more permeable than A-109 and consequently had a higher flow rate. At the same time, SC-3/40 had a lower permeability than A-52 or A-53 and a lower flow rate. On the other hand, the permeability values for SC-3 and A-71 were very similar, resulting in very similar flow rates, despite the larger radial gap observed by SC-3/40 (26.5 Vs 22), confirming the trends observed in the previous exercise.

Flow rate and bearing feeding parameter

Flow rate results were also studied in relation to the bearing feeding parameter, in order to provide an application-independent account of flow characteristics. The results from 21 data points obtained during the flow rate testing were plotted against the bearings' correspondent β values. A log-log diagram, Figure 79, permitted a direct comparison with Almond's [3] experimental work, as well as with Chattopadhyay and Majumdar's theoretical analysis [48]. In this non-dimensional form, experiments conducted over a range of supply pressures were grouped together and best curve fitting resulted in a power law equation of the form:

Equation 42

$$\overline{Q} = a \cdot \beta^{b}$$

$\overline{Q}$	dimensionless flow rate
a	empirical constant
β	dimensionless bearing feeding parameter
b	empirical constant

The constants' values are shown in Table 29. Almond fitted a similar curve, and the constant values he observed are also shown in Table 29. As seen in Figure 79 both

data sets are very similar. By compounding Almond's and the present research data a new set of empirical constants is obtained for an equation of the same form as Equation 42. These new constants are shown in Table 29.

Constants origin	a	b
Almond's research [3]	1.0619	0.6407
Present research	0.8066	0.8822
Almond's + Present research	0.9886	0.8196

Table 29-Empirical constants for flow rate-bearing feeding parameter equation.

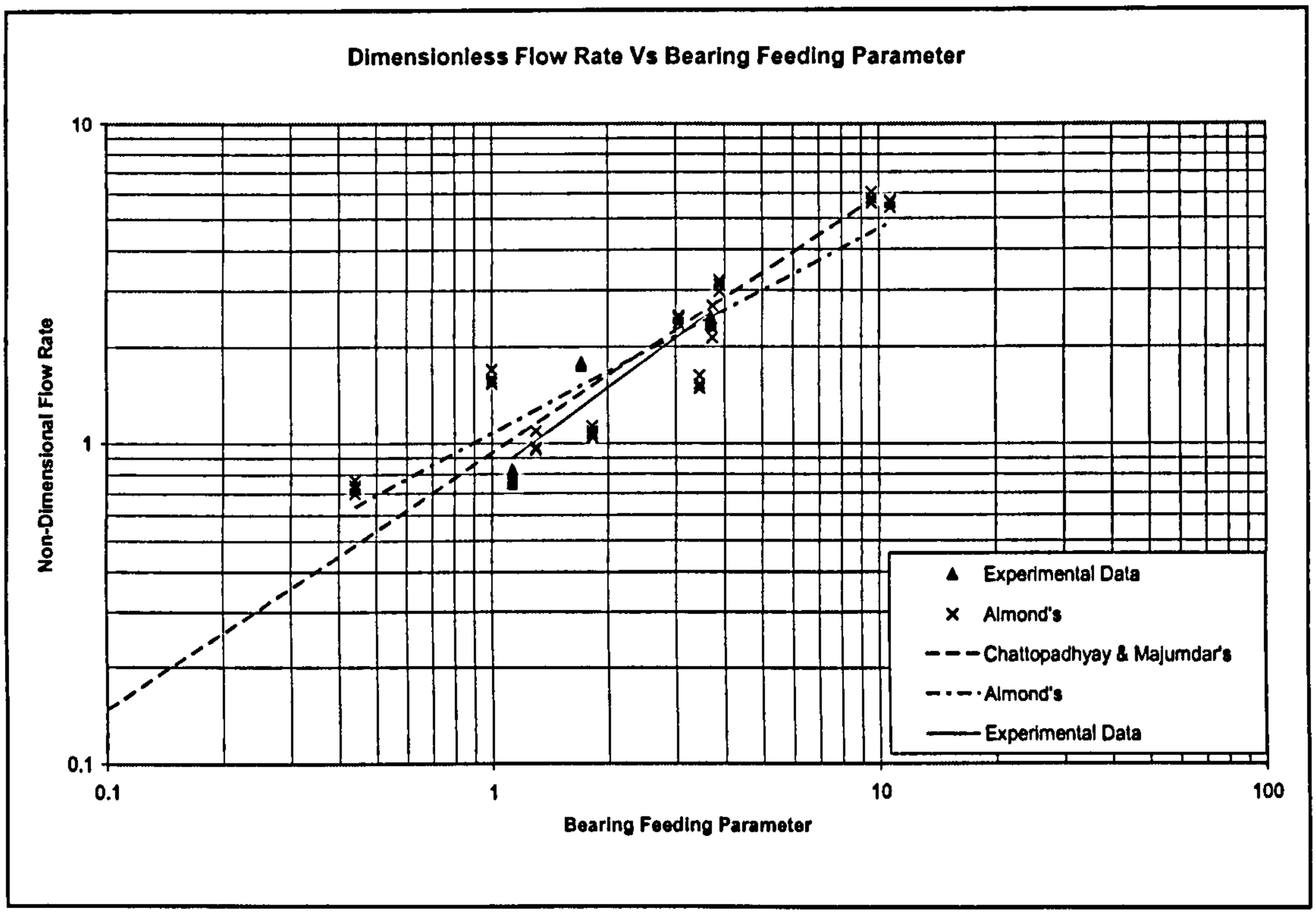

Figure 79- Dimensionless flow rate Vs bearing feeding parameter results.

As observed in Figure 79 a very good correlation is observed between the empirical and the theoretical values modelled by Chattopadhyay and Majumdar's [48]. Almond [3] observed the same correlation, and noted that in view of the close relationship between the experimental and the theoretical results, the experimental results were interpreted as a full confirmation of the theoretical trend presented by Chattopadhyay

and Majumdar. The minor differences between these trends have been attributed to the variation in the bearing end sealing techniques used.
The present research results represent the second empirical account of the flow rate-bearing feeding number for porous hydrostatic journal bearings, and this relationship has been maintained in accordance with both empirical and theoretical research.

As indicated before, the current research bearings have been lubricated with oil DIE 180, whereas the ones previously studied by Almond [3] were lubricated with water. From this fundamental difference, the present set of empirical results has confirmed another relevant aspect of the porous hydrostatic journal bearings theory [48]. This is that the influence of the lubricant's viscosity and density are not relevant for the theoretical determination of $\overline{Q}$.

In comparison with previous research [3], the minor discrepancies in flow rate in relation to the theoretical set observed here, are mainly attributable to experimental error, as an optimized sealing bearing-end technique determined by Almond [3] has been used throughout.

Based on the observed experimental results derived from both previous [3] and the present research, and their correlation with the theoretical studies by Chattopadhyay and Majumdar [48], the appropriateness of flow estimation by Equation 42 can be established, for future design applications.

Flow rate and pumping power

The power absorbed in pumping is a simple product of lubricant flow rate and supply pressure (Equation 14, previous chapter).
Figure 80 illustrates the pumping power-supply pressure relationship as supply pressure was increased from 0.25 up to 2.0 MPa for shells SC-3, SC-4 and SC-3/40. In addition Figure 80, also illustrates the results for shells A-50 and A-109, using previous research [3] as reference. These shells represent the extremes of the

stiffness range, with values ranging from 30 N/μm for shell A-50 up to 188 N/μm for shell A-109.

As a consequence of being a product of the flow rate, the pumping power varies linearly with the bearing's permeability, with an almost negligible effect of the bearing gap. This is clearly illustrated by the pumping power results for SC-3 and SC-4. These shells possess very similar permeability values but different radial gaps. As observed, the pumping power is very similar.

On the other hand, the results shown in Figure 80 also demonstrate that the higher permeability shells exhibit a greater flow rate and a correspondingly higher pumping power requirement, which is not necessarily accompanied by a higher stiffness (see previous static stiffness section). In contrast, the high stiffness shells, A-109 and SC-4, posses a lower permeability; and hence a more economic performance. This observation accentuates the importance of adequate design procedures, followed by a processing technique that is able to deliver the required bearing properties.

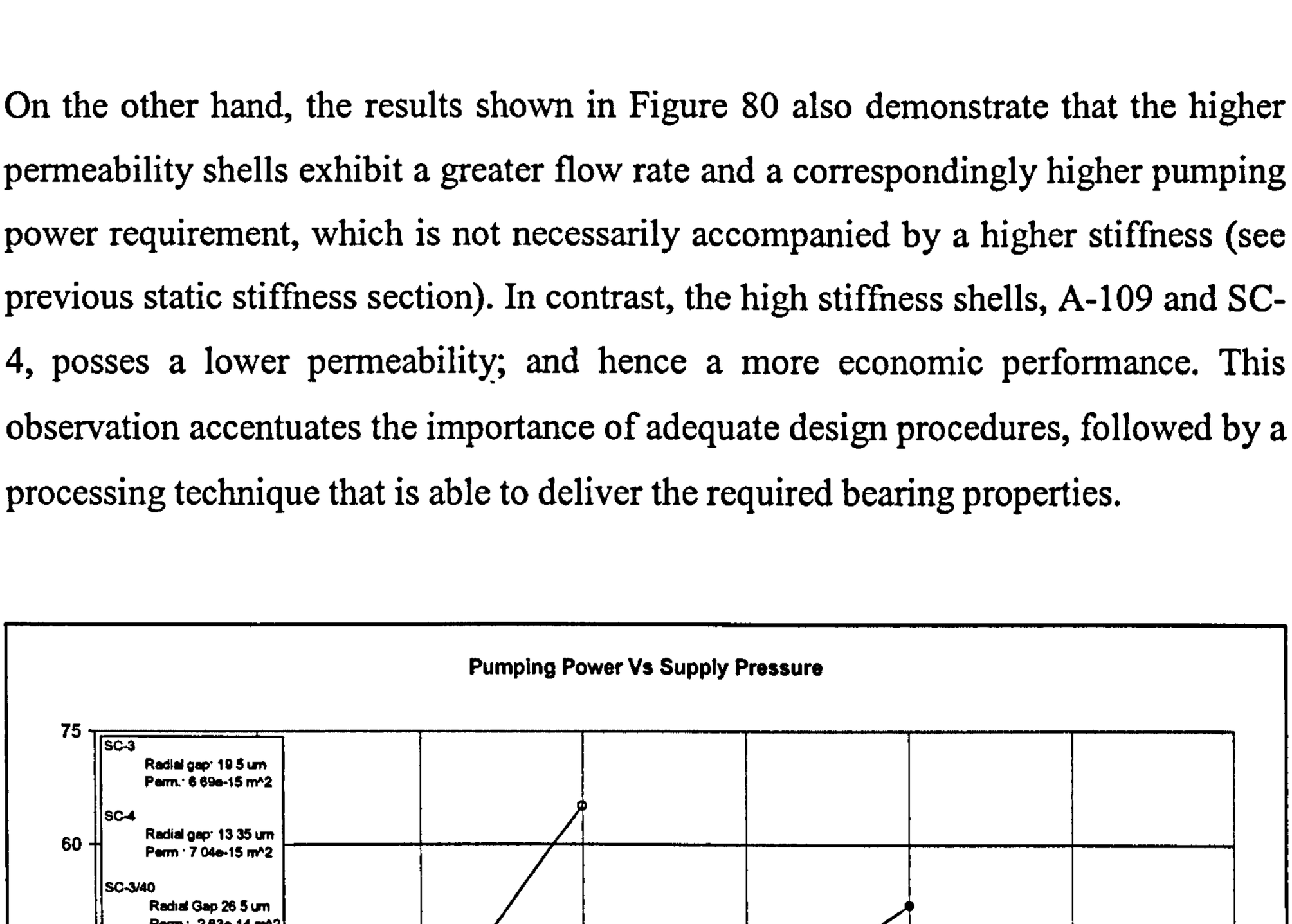

Figure 80-Pumping power Vs supply pressure.

Hydrostatic pressure distribution maps

In previous research [3], pressure maps have been envisaged as a means of providing rigorous experimental verification for existing and future mathematical models. The fluid pressure maps were produced at twenty different operating conditions for each bearing tested.

At the time of writing no theoretical verification was known to have been undertaken. However, in the interest of these theoretical analyses a similar study has been conducted in the present research for shell SC-3.

Figure 81 and Figure 82 illustrate the hydrostatic pressure maps for bearing SC-3; supporting a load of 100 N and at supply pressures of 2 and 1 MPa, respectively.

The pressure maps produced for the bearing SC-3 are of the same uniform and consistent nature as those previously studied by Almond [3], which indicates the consistency of the porous-ceramic hydrostatic bearing principle, regardless of the manufacturing method.

An obvious decrease in the range fluid film pressures can be observed by comparing Figure 81 and Figure 82, and this is due to the supply pressure observed in each case. For a Ps of 2 MPa, the maximum measured film pressure was 0.77 MPa, whereas for a Ps of 1 MPa, the maximum fluid film pressure was 0.33 MPa. Both pressure film maps, however, describe similar behaviour, which reflects the consistency of the procedure.

For a standard hydrostatic bearings design, a pressure drop of about 50 % of the supply pressure is usually acknowledged for optimum load capacity and stiffness performance [133]. In this sense, Almond [3] demonstrated that for porous-ceramic bearings of identical geometry and shape, it was possible to optimize stiffness performance by varying the bearing's permeability and gap to achieve a higher range of fluid film pressures, demonstrating the porous-ceramic bearing technology capability of tailoring the bearings' properties to suit a particular application.

Almond's fluid film pressure maps with the highest range of pressures and consequently higher stiffness, possessed fluid film pressure values of up to 70 % the Ps (2MPa) for a bearing with a β value of 1.8, which supported the results of the

previously reviewed static stiffness Vs bearing feeding parameter relationship (Figure 74), for which the optimum β value was found to be 1.9.

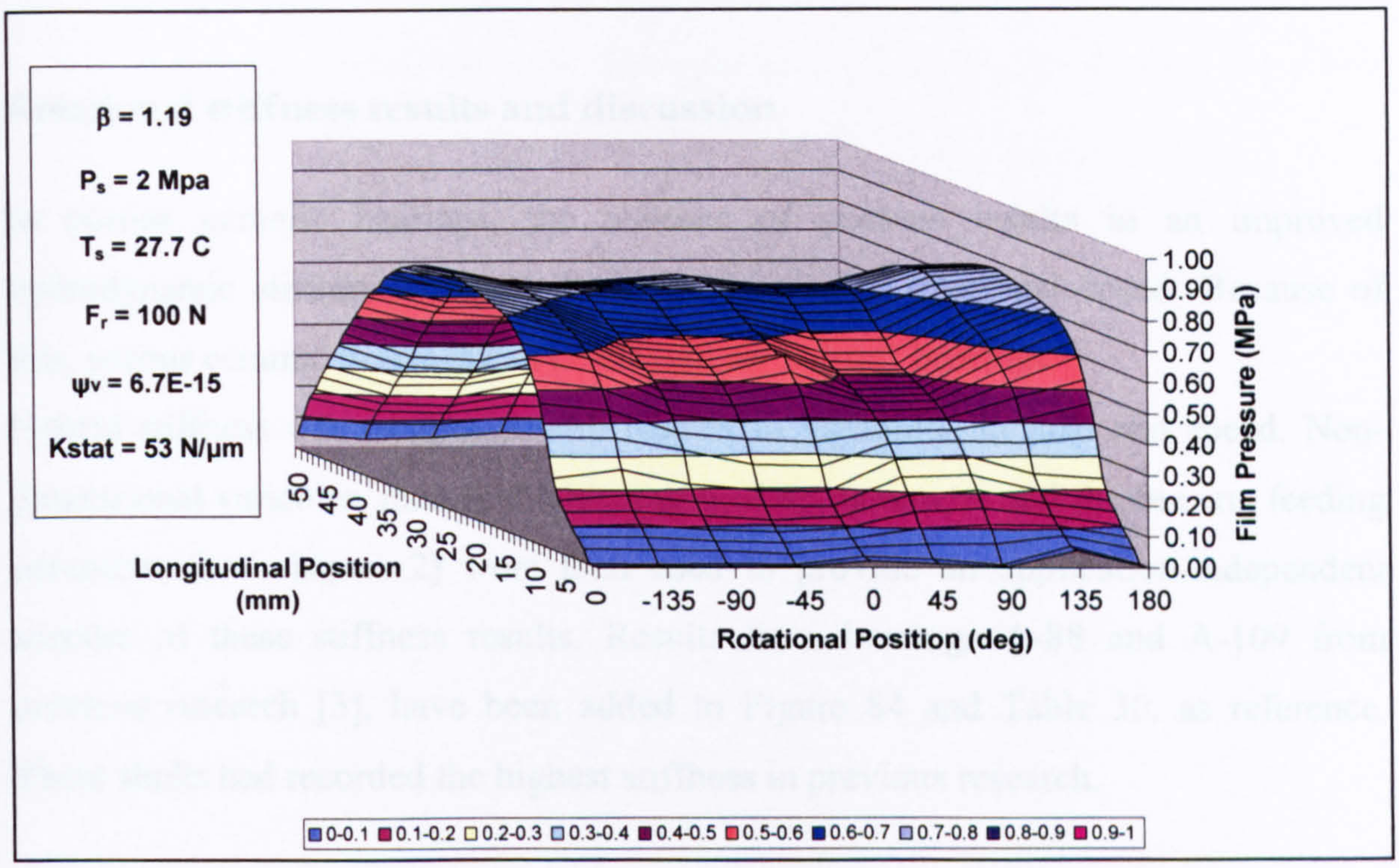

Figure 81- Hydrostatic pressure distribution map, Ps= 2 MPa.

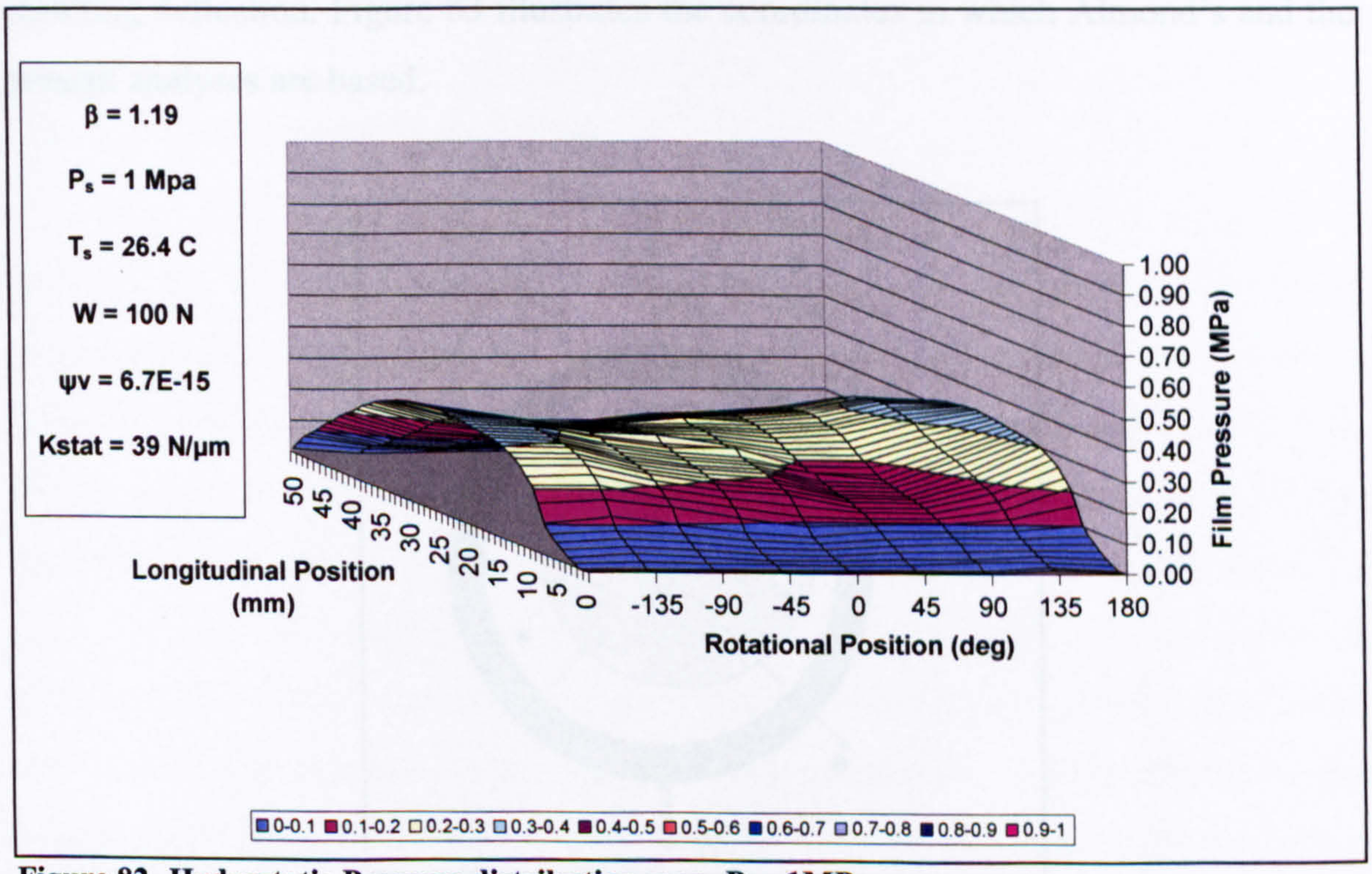

Figure 82- Hydrostatic Pressure distribution map, Ps= 1MPa.

As with the pressure maps presented by Almond, the present maps have served a qualitative purpose, providing a visual picture of the pressure distribution within a working porous hydrostatic journal bearing.

Rotational stiffness results and discussion

In porous ceramic bearings, the absence of pockets results in an improved hydrodynamic stiffness component for an increasing rotational speed. Because of this, porous ceramic bearings can be classed as 'hybrid' bearings.

Hybrid stiffness was examined with respect to variations in load and speed. Non-dimensional variables, mainly the bearing feeding parameter and the bearing feeding parameter (see chapter 2) were then used to provide an application-independent account of these stiffness results. Results from bearings A-88 and A-109 from previous research [3], have been added to Figure 84 and Table 30, as reference. These shells had recorded the highest stiffness in previous research.

Stiffness results were reported in terms of its 'r' (K_{rr}) component, in order to comply with Almond's [3] analysis. The direct stiffness Krr acts in the same direction as the resulting deflection. Figure 83 illustrates the coordinates in which Almond's and the present analyses are based.

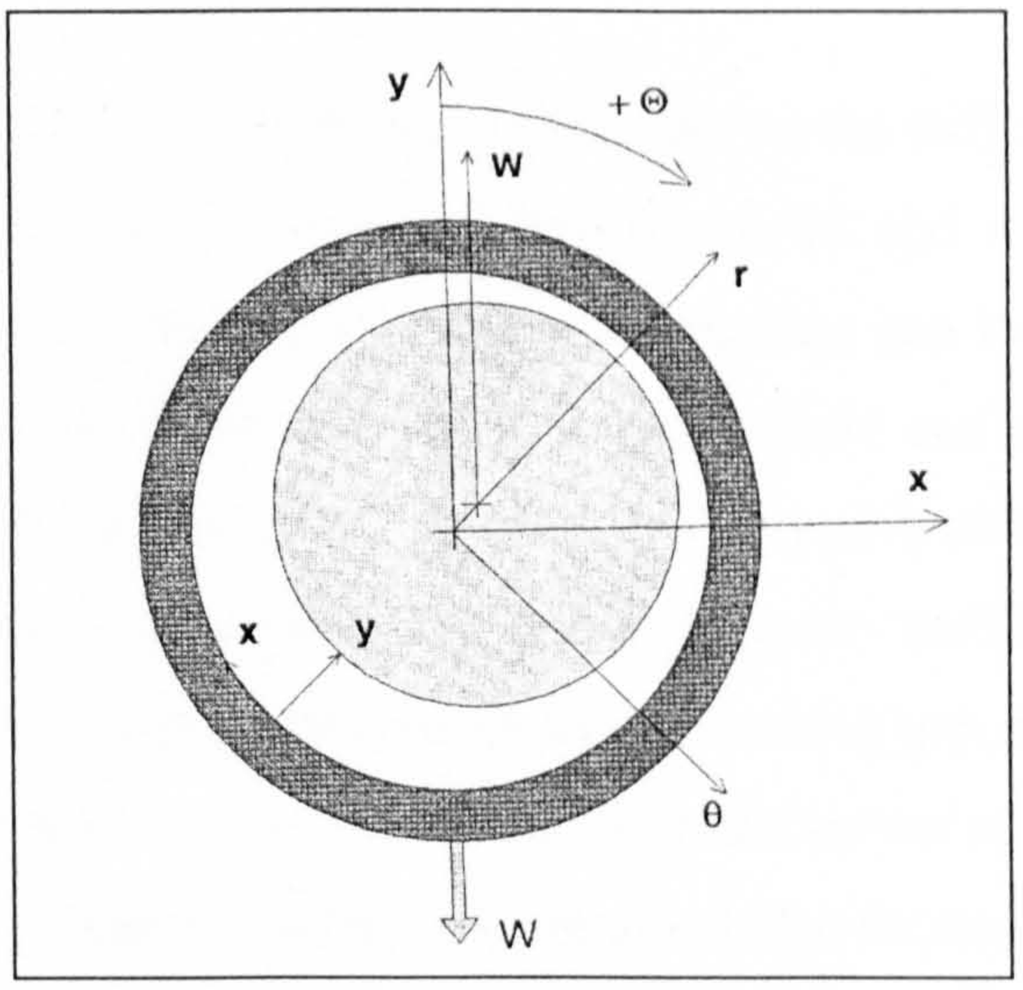

Figure 83- Almond's co-ordinates system for bearing analysis.

Hybrid stiffness Vs rotational speed

Figure 84 illustrates the measured K_{rr} Vs the shaft speed at a Ps of 2 MPa. As can be observed, hybrid stiffness rapidly increases with the shaft speed for all bearings. This was expected, as it was noted in the literature review chapter, the absence of pockets maximises the hydrodynamic stiffness component.

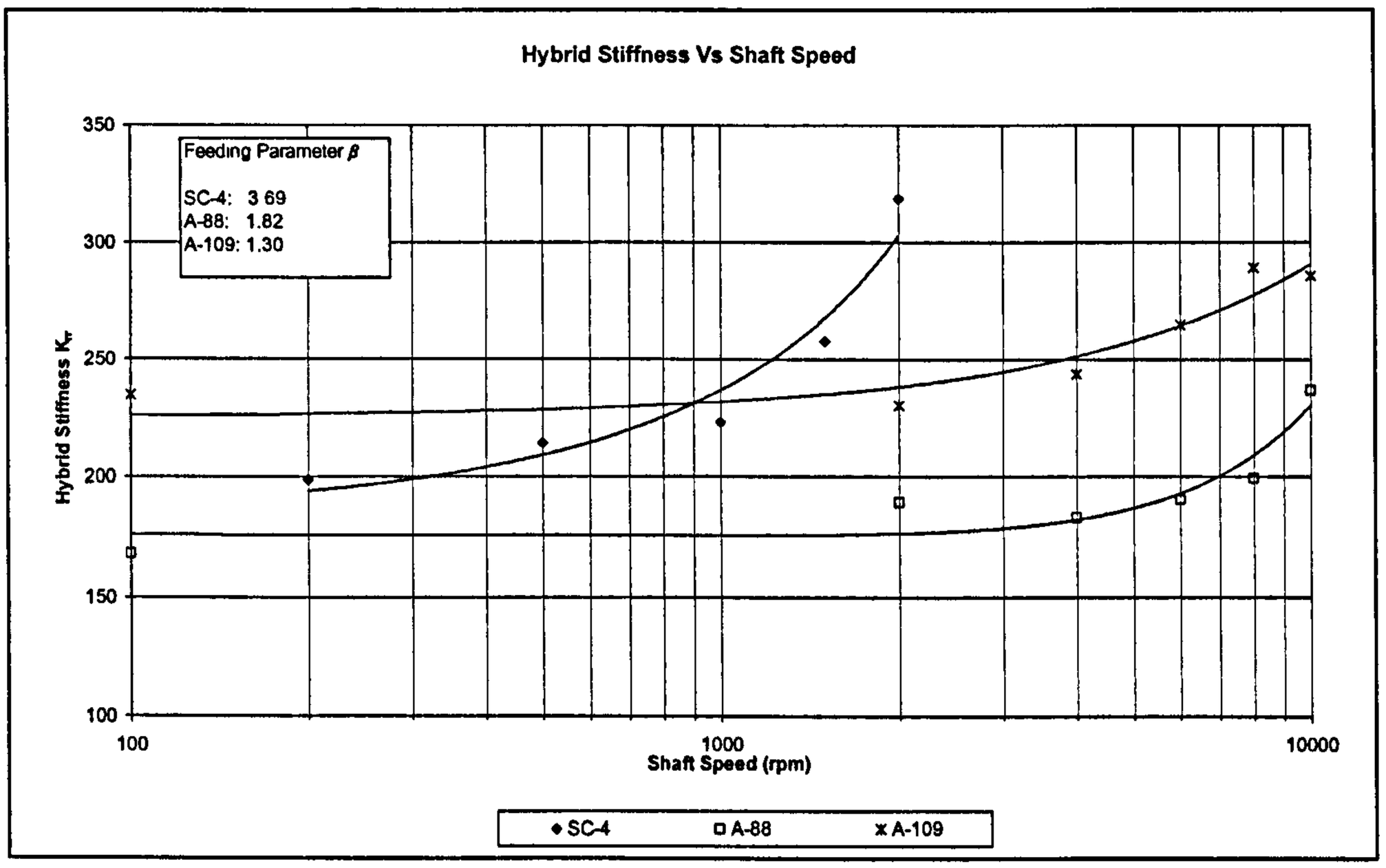

Figure 84- Hybrid stiffness Vs shaft speed.

From Figure 84, it is also evident an abrupt increase in the stiffness curve for SC 4, in comparison with the previous research bearings A-88 and A-109. This effect is believed to be mainly in response to the smaller bearing gap that this bearing had, 13.35 μm, as opposed to 18 and 19 μm for bearings A-88 and A-109, respectively. As noted by Stansfield for hydrostatic bearing technology (reference [37], equation 5.6), the critical speed at which the hydrodynamic stiffness component is increasingly dominant is directly influenced by the bearing gap, and its effect causes the critical speed threshold to vary exponentially to the power of 2. Furthermore, the magnitude of the hydrodynamic stiffness component also increases by the increasing rotational speed, as noted for conventional hydrostatic bearing technology [37], hence the continual stiffness-curve growth for bearing SC-4.

On the other hand, the effect of the lubricant's viscosity on the resulting stiffness was considered secondary at this stage, as the viscosity values for the thin oil (SC-4) and water (A-88 and A-109) were relatively close to each other at the observed test temperatures ($\eta_{abs} = 1.6 \times 10^{-3}$ and 9.87×10^{-4} Ns/m^2, for oil and water, respectively).

Conversely, for bearings A-88 and A-109, the hydrodynamic stiffness component exerts a lower influence, until the bearing speed reaches higher speeds. As seen in Figure 84, at around 5000 rpm the curve starts showing a higher gradient for both bearings.

In this sense, at the present time, an equation that is equivalent to Stansfield's equation 5.6 [37] specifically developed for the calculation of the critical speed value for porous ceramic journal bearings applications is not available. However, a similar bearing gap-critical speed relationship to that presented by Stansfield is likely to be found, as it can be inferred by Figure 84.

Above all, the most interesting aspect revealed by Figure 84 is the verification of the existence of an advantageous hydrodynamic component, as it was first experimentally demonstrated by Almond [3]. The benefits of this, in terms of stiffness from the recorded static stiffness are shown in Table 30.

Bearing	Lubricant used	Static stiffness (N/μm)	Hybrid stiffness (N/μm)	Improvement (%)	Rotational speed (rpm)
SC-4	DIE 180	140	318.5	128	2, 000
A-88	Water	170	237	40	10, 000
A-109	Water	188	276	47	10, 000

Table 30- Hydrodynamic component benefit for porous ceramic shells, at Ps= 2.0 MPa.

Another aspect of this investigation worth highlighting is the marked effect of the bearing gap upon the critical speed and the magnitude of the hydrodynamic stiffness component. In Almond's investigation [3], the gap effect on these was masked by the selection of analysed bearings, which had a very similar bearing gap.

Non-dimensional hybrid stiffness Vs bearing speed parameter (λ_s)

The bearings speed parameter is a dimensionless porous hydrostatic journal bearing design parameter. This has been already reviewed in chapter two. As with the bearing feeding number, the bearing speed parameter (λ_s) is used in theoretical analyses as the independent variable to investigate certain aspects of bearing performance.

On the other hand, non dimensional stiffness values were calculated by using Equation 37.

Figure 85 illustrates the non-dimensional hybrid stiffness results Vs the bearing speed parameter for SC-4 at a Ps of 2 MPa. In addition, Figure 85 also illustrates the non-dimensional hybrid stiffness results for bearings A-88 and A-109, at the same pressure supply.

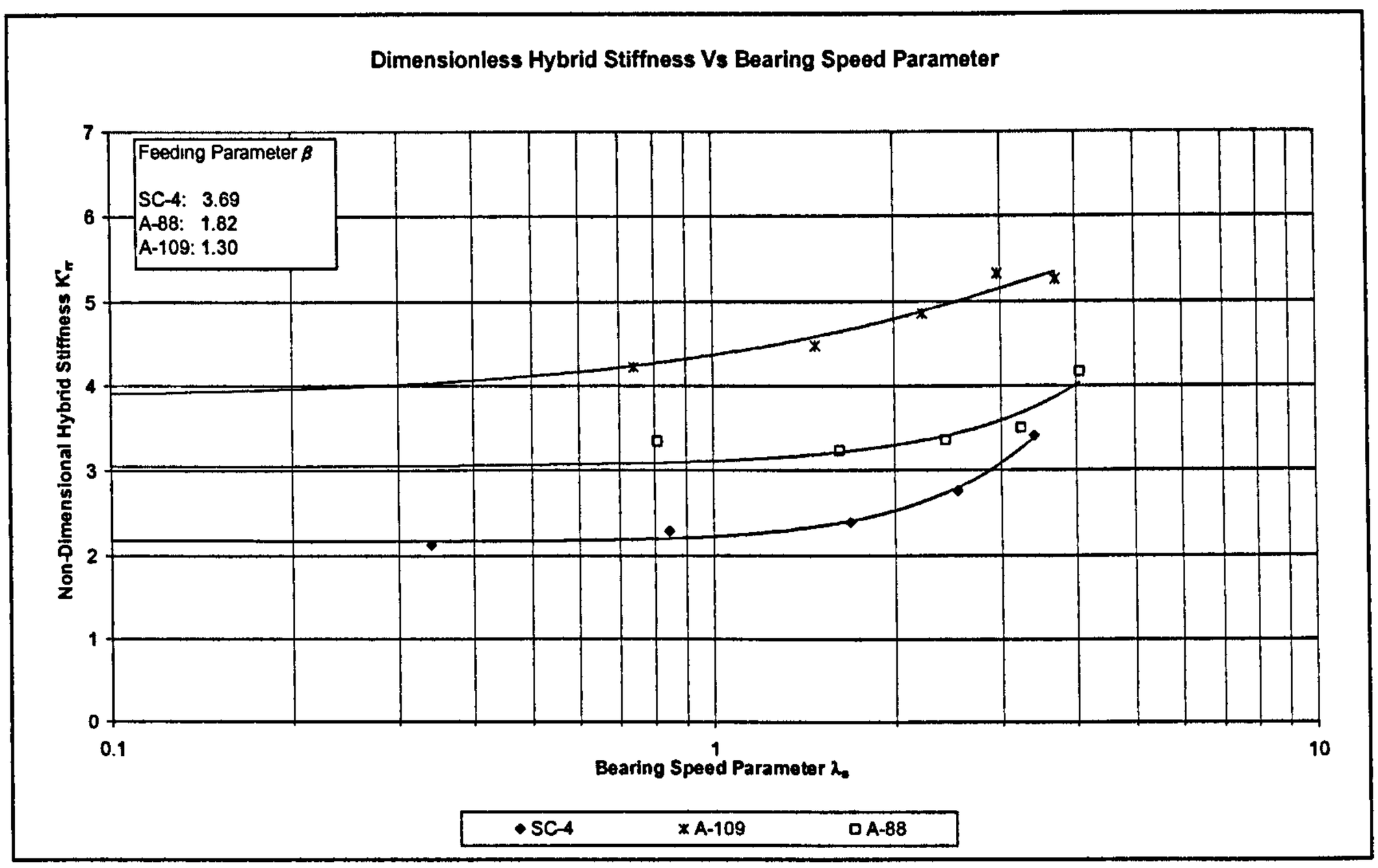

Figure 85- Dimensionless hybrid stiffness Vs bearing speed parameter.

As seen in Figure 85, the sharp effects of the gap and lubricant viscosity are masked by using the non-dimensional porous hydrostatic journal bearing design parameters. It is interesting to note that despite the lower speeds at which SC-4 was tested, the

resulting λ_s values were very similar to the ones calculated by Almond [3] for shells A-88 and A-109. Once again, this is a result of the variables input for the calculation of λ_s, particularly the bearing gap (to the power of two), as well as the lubricant viscosity and the range of rotational speeds.

By curve fitting of his results, Almond found a set of equations that along with charts similar to the one shown in Figure 85 were intended to provide design guidelines. Almond's equations are of the following form:

Equation 43

$$\overline{K}_{rr} = a \cdot \lambda_s^2 + b \cdot \lambda_s + m$$

$\overline{K}_{rr}$	non dimensional hybrid stiffness
λ_s	dimensionless bearing speed parameter
a	empirical constant
b	empirical constant
m	empirical constant

Table 31 illustrates the constant values for bearings A-88 and A-109, as well as the values for the current research's bearing SC-4.

Bearing	a	b	m
SC-4	0.1307	-0.0969	2.19
A-88	0.0261	-0.228	4.19
A-109	0.0697	-0.048	3.10

Table 31- Hybrid stiffness Vs bearing feeding parameter empirical constants.

The validity of the equations shown above extends over the rational values used during experimentation.

An additional plot is presented in Figure 86, and this illustrates the change in attitude angle with the bearing speed parameter for bearing SC-4 and for bearings A-88 and A-109 from previous research. In addition, Figure 86 includes a comparison against the results of a theoretical model by Majumdar and Rao's [47].

For this part of the analysis, Almond [3] reported some scatter in his experimental data, and this was mainly for bearing A-109. Almond also reported a general poor correlation with the theoretical model of Majumdar and Rao, although he also noted that this was originally intended for a bearing with a β value of 5.0. However, once the data points for SC-4 were overlaid in Almond's 7.20, originating Figure 86, it was noticed that in fact SC-4 and A-88 exhibit similar results, and these in fact seem to resemble Majumdar and Rao's curve, although the new curves would be offset in relation to the λ_s axis from the theoretical one. By curve fitting, Almond presented a curve and an equation that is intended to provide some design guidelines. This equation form is shown below.

Equation 44

$$\phi = 6.88 \cdot \lambda_s + 5.4$$

ϕ	attitude angle (deg)
λ_s	dimensionless bearing speed parameter

Almond's results [3] have been broadened out by including the results from SC. However by doing so, the form of the previous equation changed to a power law form:

Equation 45

$$\phi = 12.381 \cdot \lambda_s^{0.7039}$$

The validity of this equation extends over the rational values used during experimentation. The change in the equation form responds to the addition of the new data points, which also tend to smooth away the scatter observed for bearing A-109.

With regard to the observed differences with the theoretical analysis trend for the attitude angle, it was felt that a greater number of data points were required to in order to reach a more meaningful conclusion. However, it was also felt that despite the observed differences, the experimental attitude angle trend is of similar nature as to that of the theoretical curve.

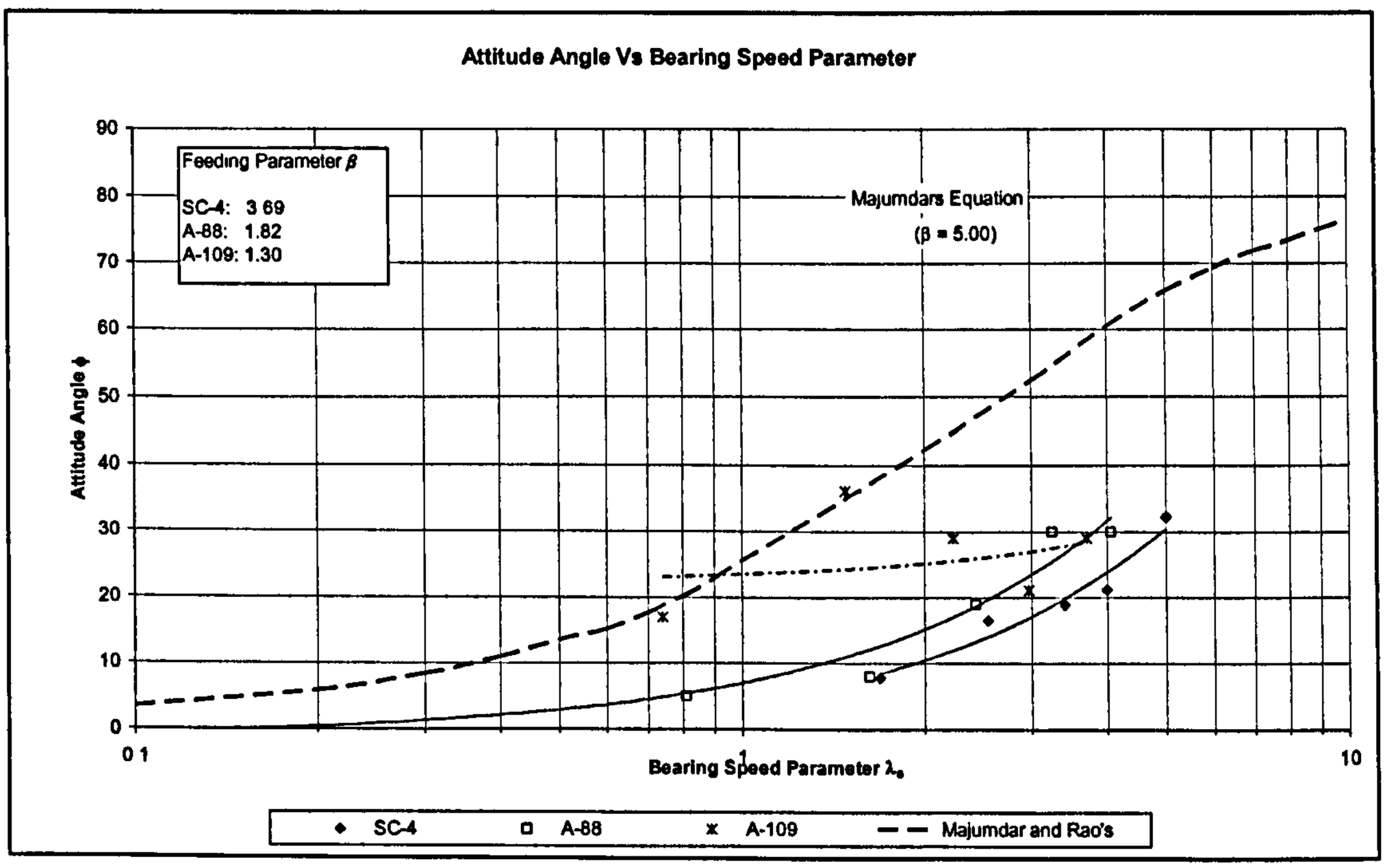

Figure 86- Attitude angle Vs bearing speed parameter.

Rotational flow rate results and discussion

The results obtained by observing the flow rate Vs the shaft rotational speed illustrate the specific effect of the angular velocity on the flow rate through the porous bearing. During these tests, supply pressures of 1.0 and 2.0 MPa were used, while the flow was measured under no load conditions. Results are shown in Figure 87, in the form of a simple plot of flow Vs the shaft rotational speed. Bearing SC-3/40 had a higher permeability than SC-3 (see Table 26), and as a result of that it exhibited a higher flow rate. This relationship, permeability Vs flow rate, has been further discussed in a previous section of this chapter.

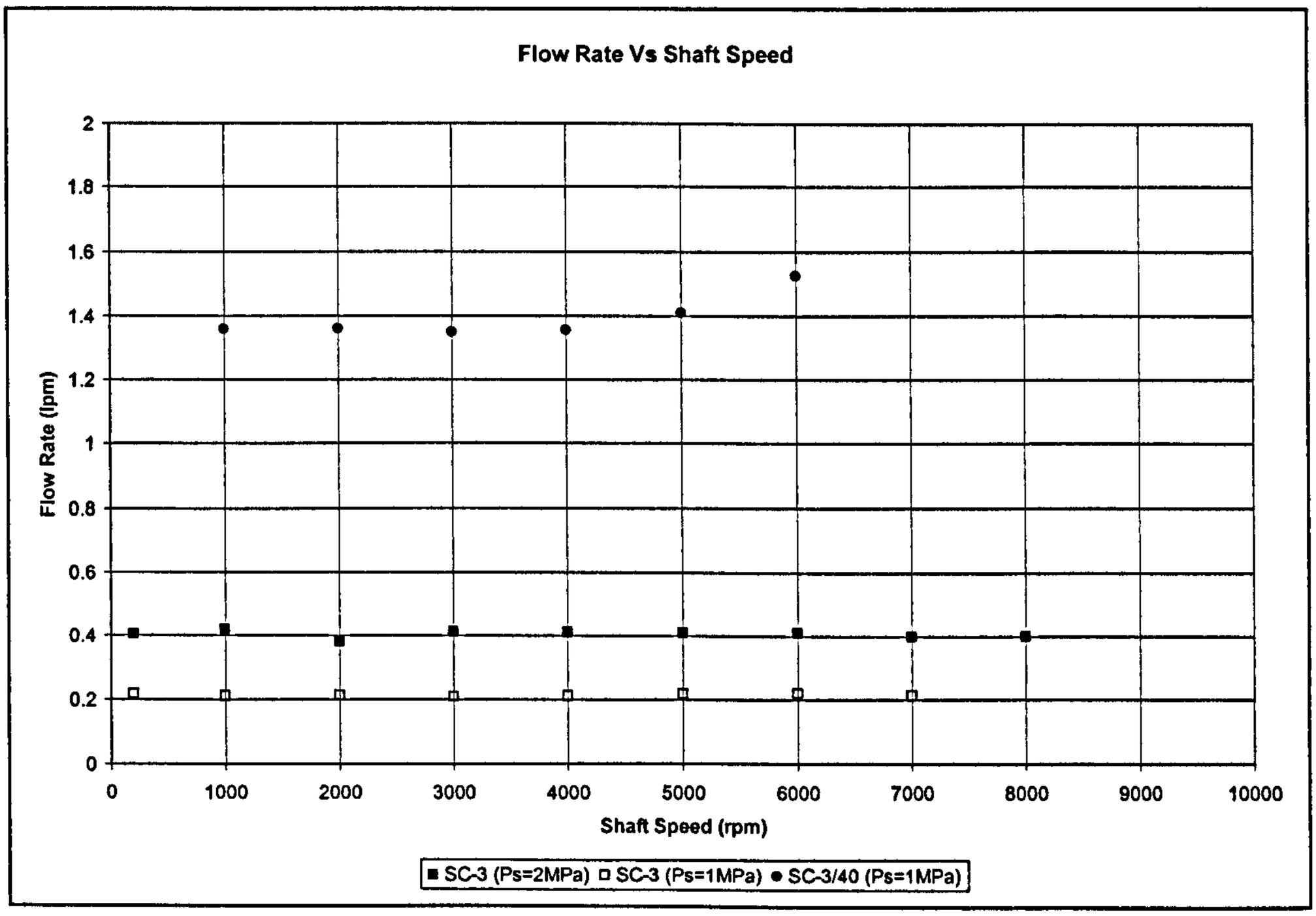

Figure 87- Flow rate Vs shaft rotational speed.

In order to achieve a comparison with the previous analyses of Almond [3] and Chattopadhyay and Majumdar[48], the observed results are expressed in terms of non-dimensional flow Vs the bearing speed parameter. Figure 88 illustrates the results for starch consolidation SC-3 and SC-3/40. In addition, Figure 88 also shows

results from previous research bearing A-109, as well as the values derived from Chattopadhyay and Majumdar's [48] model for β values of 1 and 2.

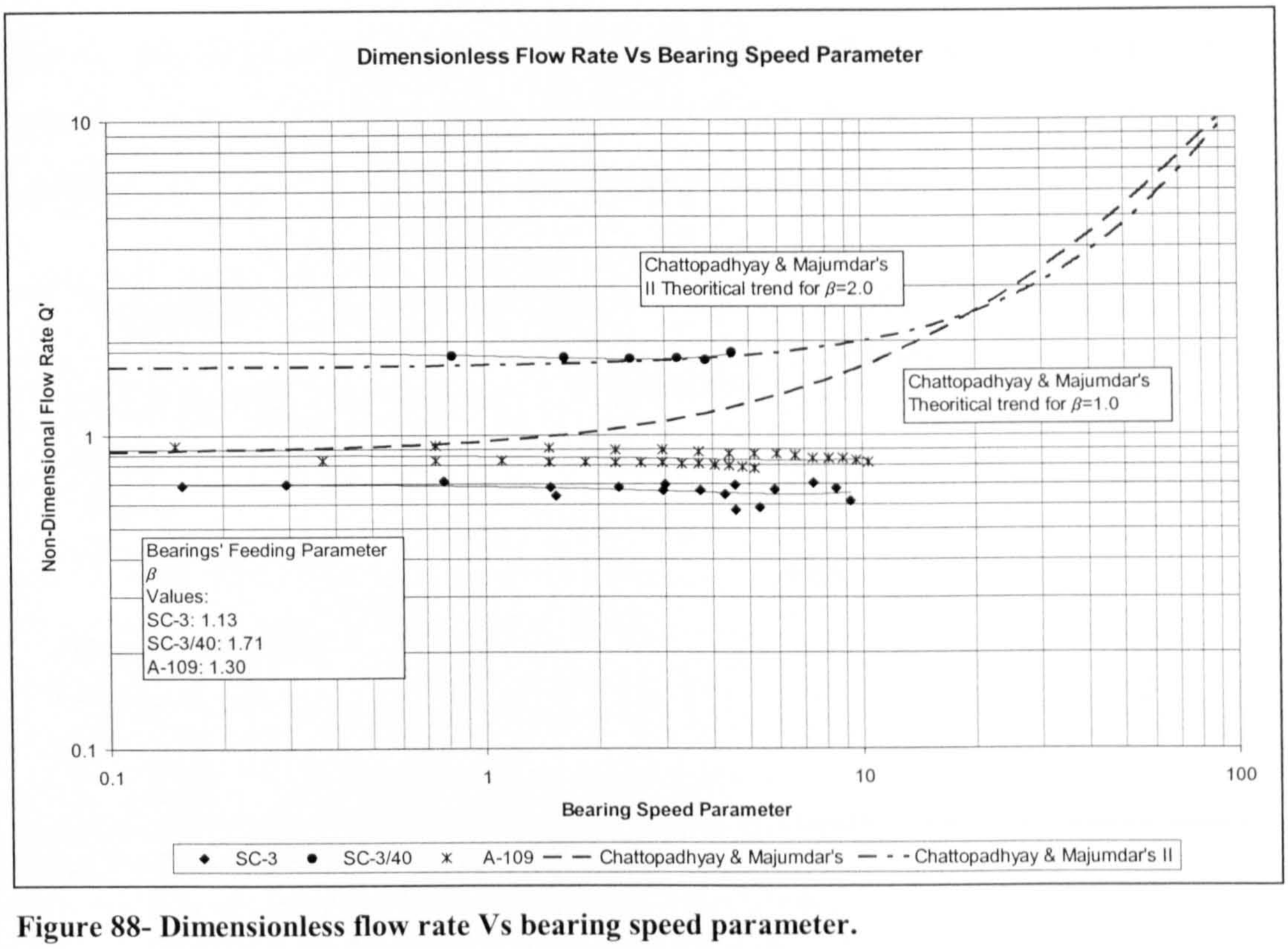

Figure 88- Dimensionless flow rate Vs bearing speed parameter.

As seen in Figure 88, a reasonable correlation is observed between the obtained results and the two previous analyses, considering the differences in the β value observed. Bearing SC-3/40, however, shows an extremely good correlation with the theoretical trend for $\beta = 2$.

As with the results observed by Almond [3], after the bearing speed parameter value exceeds a certain value, the trend lines for the theoretical results tend to break away from both experimental set of results, observing a step flow increase for higher λ_s values. The reasons for this trend behaviour are not quite clear. Almond argues the unlikeness of these flow conditions, even under hypothetical fluid film turbulence. In this sense, both sets of experimental results seem to confirm this assertion. Unfortunately for the present application, to further experimentally explore flow conditions for larger λ_s values, the shaft speed needed to be increased to a range superior to 16,000 rpm, which was considered an unsafe operation.

Summary of performance tests conducted

During this part of the experimental performance, the most relevant aspects of bearing performance have been examined. Table 32 details on the procedures conducted here as well as the SC bearings examined in those tests.

Performance parameter	SC-3 @ Ps= 2 MPa	SC-4 @ Ps= 2MPa Rot. tests @ 2000 rpm	SC-3/40 @ Ps= 1MPa Rot. tests @ 6000 rpm
Static stiffness (N/μm)	49.31	140	43
Rotational radial stiffness (N/μm)	--	376	167
Lubricant flow rate (lpm)	0.46	0.44	1.35
Pumping power (W)	15.4	14.8	23
Temperature rise (°C)	--	--	1.22
Hydrostatic pressure maps	Yes	--	--

Table 32- Summary of test conducted for SC bearings.

As mentioned before, during the course of the experimental performance an incident occurred that resulted in SC-3 seizing. As a consequence of this incident bearing SC-3 shattered and the shaft was also damaged. The causes originating this incident are not quite clear. With the porous-ceramic broken in several dozen pieces it was difficult to recreate a hypothetical scenario, although some evidence of rubbing was present. The most likely causes considered were lubricant starvation or the spindle operation near its critical speed.

The test rig was repaired and a new shaft was fitted and balanced, in accordance with the procedures laid down by Almond [3]. A capacitive gauge kit was borrowed from the industrial sponsor and set to monitor the shaft dynamic run-out, as a precautionary measure.

Unfortunately, the in-shaft instrumentation was also damaged during the incident and it was not impossible to re-install its components, due to time constraints. As a result,

hybrid pressure and hybrid temperature distribution maps were not conducted here. These maps are were intended to serve as verification of mathematical models, but so far they have served only a qualitative purpose, for illustrating the interaction of pressure and temperature within an operating porous-ceramic hydrostatic bearing.
However, hydrostatic pressure maps were produced for bearing SC-3 before the above mentioned incident, and they showed a marked similarity with the ones produced by Almond [3], despite the differences in the manufacturing process. This suggested that the similarities should also extend to hybrid pressure and temperature maps.

Performance testing with water lubrication

Towards the final stages of the present project, water lubrication was reinstated in the porous-ceramic hydrostatic journal bearing test-rig. This presented an opportunity for validating the obtained results for SC-3/40 with oil as lubricant by comparing them to results with water as lubricant.

The first set of static stiffness results showed a remarkably lower stiffness for the water lubrication set, as shown in Figure 89. From the available theoretical literature [37] [48] it can be reasoned that the lubricant's viscosity does not play part in the determination of the static stiffness, hence prompting an investigation into other possible sources for the discrepancies observed in the experimental results.
It was found that during the change of lubricant from oil to water, bacterial colonies grew in the lubricant reservoir within a few days (Figure 91), resulting in the formation of an 'algae' skin on the top layer of the water, and although this was drained following by thoroughly cleaning of the hydraulic tanks and filters, and fresh water replenishing, it is though the algae had survived and blocked some of the porous bearing pores, seriously affecting its performance.

A flow rate test was prepared to verify the previous hypothesis and it was found the flow had drastically reduced, hence accounting for the lowest stiffness performance. Figure 90 illustrates the results from this test. In this figure, predicted flow rate results from the Chattopadhyay and Majumdar [48] theoretical models have been

added as guidance. These models had shown previously a close agreement with both previous research [3] (water lubrication) and the present research (oil lubrication, section 5.3.2) experimental results.

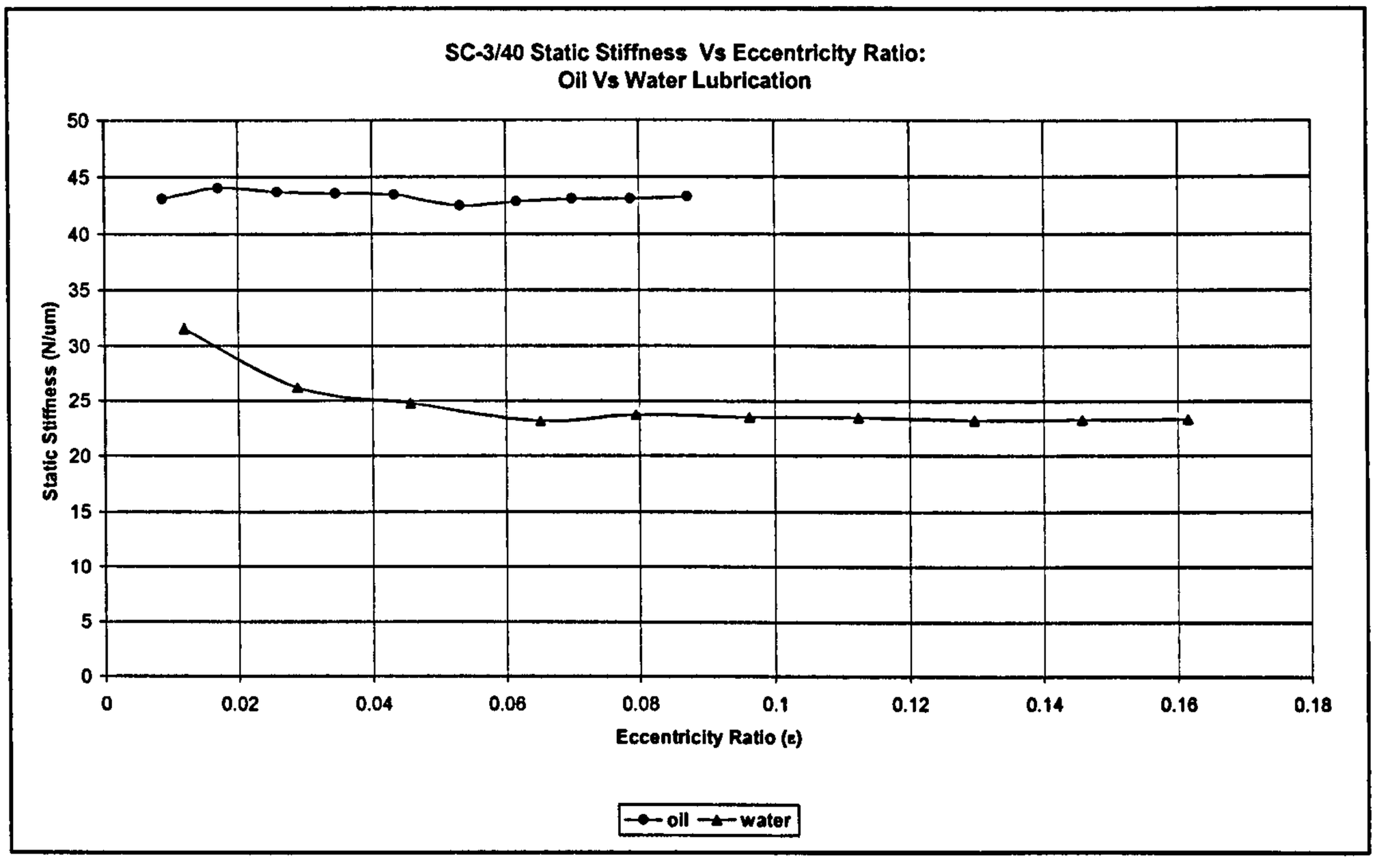

Figure 89- SC-3/40 static stiffness Vs eccentricity ratio: oil and water lubrication.

The algae growth was equivalent to the effect of the porous bearing reducing its permeability. As reviewed before (section 5.3.2), a lower permeability reduces the β value, and hence the bearing's static stiffness and in general, most aspects of bearing performance. Because of time constraints, it was not possible to physically measure permeability on bearing SC-3/40. However, it was possible to estimate its permeability by using the results from the present flow rate test, together with Chattopadhyay and Majumdar's [48] design charts. It was found that permeability of this bearing drop from 2.7×10^{-14} to 7.4×10^{-15}, with the bearing feeding number (β) also dropping from 1.71 to approximately 0.5, which in accordance with the previous static stiffness analysis (Figure 74), results in a static stiffness loss of approximately 58 %, which correlates well with measured results in Figure 89 (53 % loss).

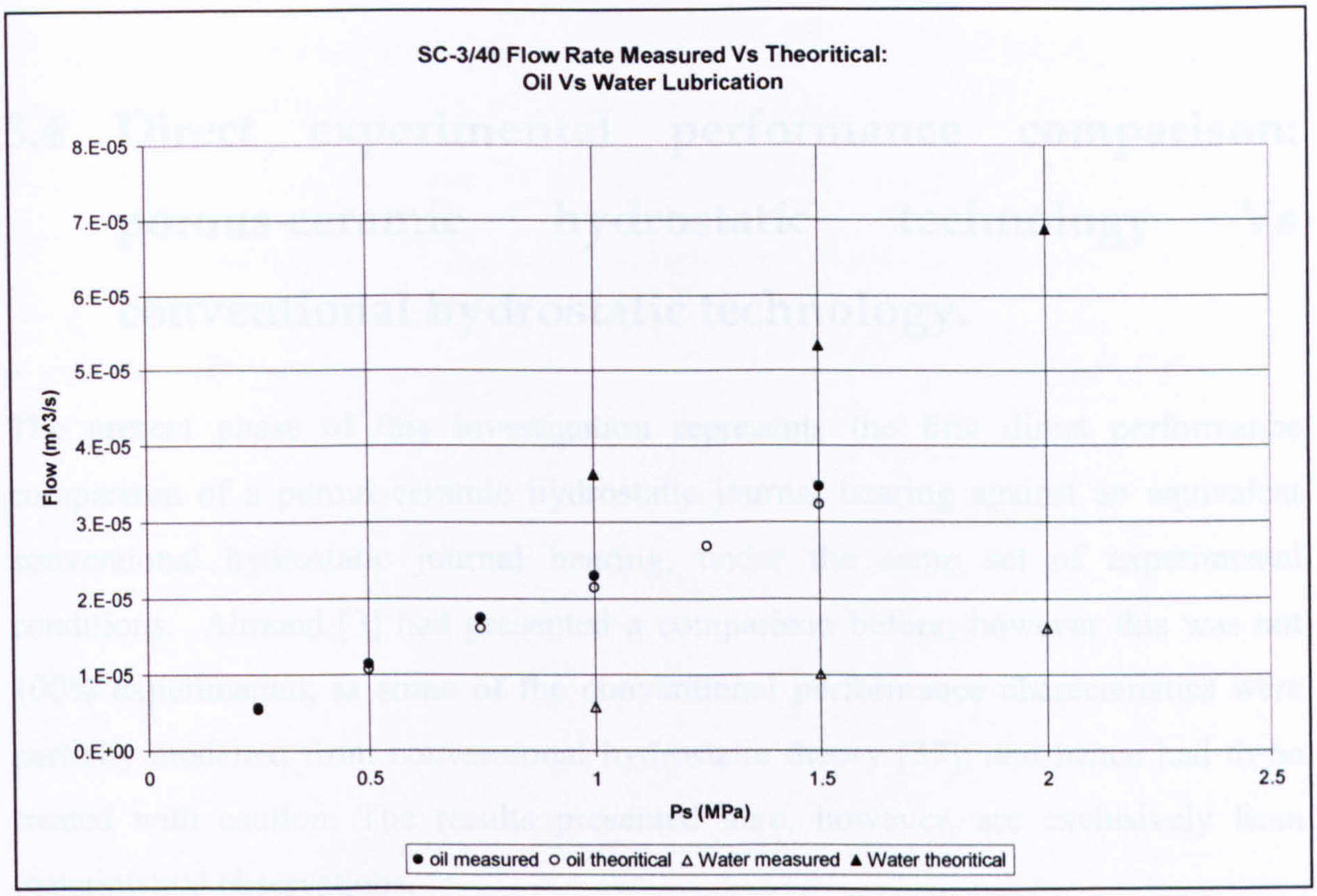

Figure 90- SC-3/40 flow rate comparison: measured Vs theoretical, for oil and water.

The most important aspect highlighted by this part of the investigation is the potential risk of pore clogging by bacterial growth. As observed, the consequences of this are very serious with regard to bearing performance. Bacterial growth is intrinsic to any water based system. The implementation and strict following of monitoring and maintenance programmes are of major importance. In this sense, water based bearing lubrication should be restricted to applications where the cost-benefit of such stringent programmes is justified.

Figure 91- 'Algae' formation in plain water. Sample taken from test rig reservoir.

5.4 Direct experimental performance comparison: porous-ceramic hydrostatic technology Vs conventional hydrostatic technology.

The present phase of this investigation represents the first direct performance comparison of a porous-ceramic hydrostatic journal bearing against an equivalent conventional hydrostatic journal bearing, under the same set of experimental conditions. Almond [3] had presented a comparison before, however this was not 100% experimental, as some of the conventional performance characteristics were partially modelled from conventional hydrostatic theory [37]; and hence had to be treated with caution. The results presented here, however, are exclusively from experimental observations.

Oil DIE-180 was used as lubricant in both cases. Further details of both bearings design characteristics, as well as details of the testing procedures can be found in section 4.3 and 4.4.

Static stiffness results and discussion

Figure 92 illustrates the experimental static stiffness results for the porous ceramic bearing SC-3/40 Vs a conventional hydrostatic journal bearing of equivalent size and the same bearing gap. From this investigation, as seen in Figure 92, the average conventional bearing stiffness measured 22 N/μm operating at a supply pressure of 1 MPa. In contrast, the stiffness for the starch consolidation bearing SC-3/40 was 43 N/μm for the same supply pressure.

The observed experimental results confirmed the well known hydrostatic porous bearings theoretical assertion that indicate that a more uniform pressure distribution is created by the multitude of small feeders distributed along the bearing's porous wall, which in turn results in an improved bearing performance. In addition, the

porous ceramic bearing had a β value of 1.71, which is near the experimentally-observed optimum β value of 1.9, for static stiffness (section 5.3).

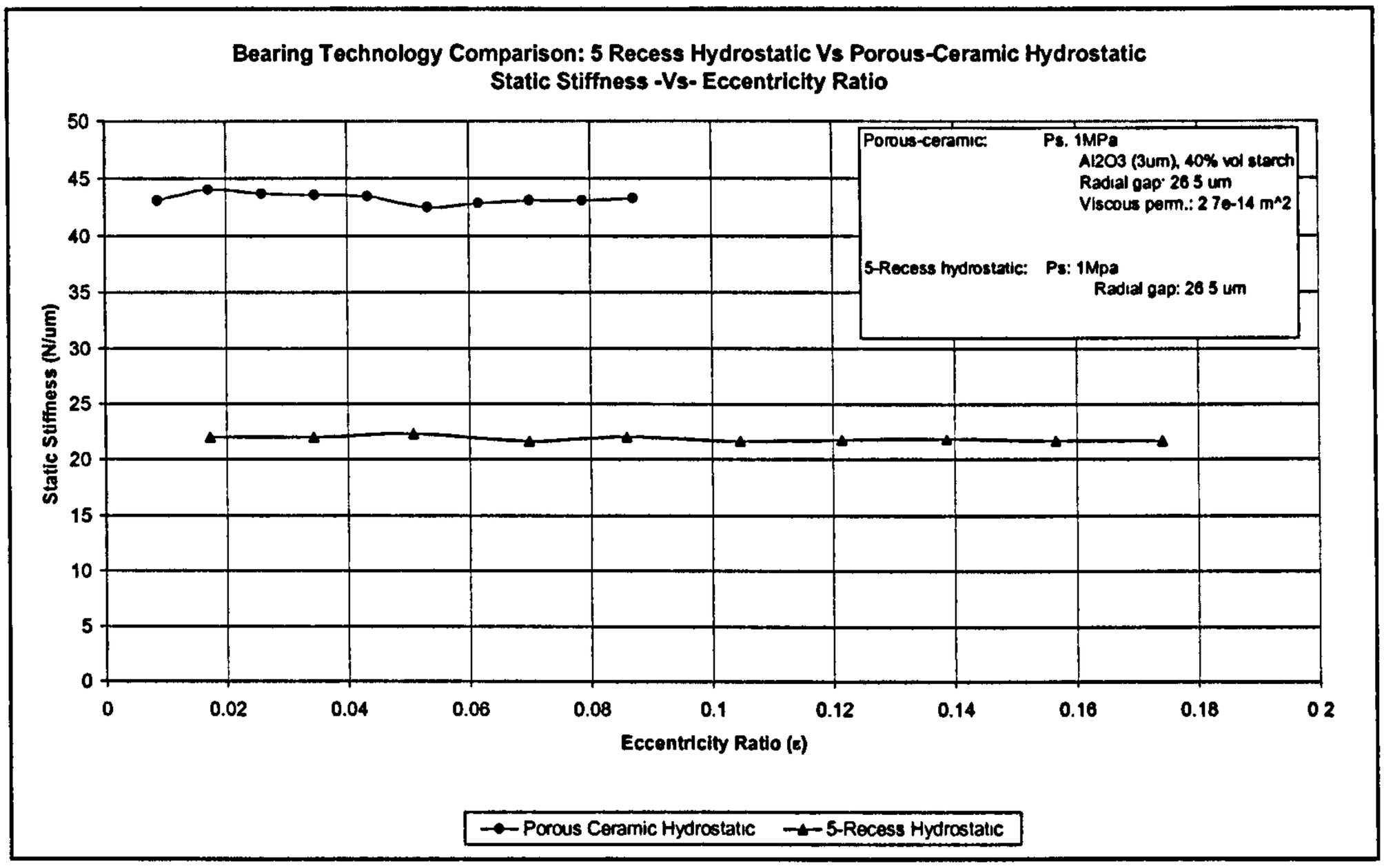

Figure 92- Bearing technology comparison: static stiffness Vs eccentricity ratio.

Rotational stiffness results and discussion

Figure 92 illustrates the results of the measured rotational stiffness for the porous-ceramic bearing and for the conventional 5-recess hydrostatic bearing.
Once again, as observed in Figure 92, the porous-ceramic bearing outperforms the conventional hydrostatic bearing.

Here, it is interesting to note the very rapid growth of the porous ceramic bearing static stiffness curve, which is more noticeable after 2000 rpm. This growth is directly associated to the improved hydrodynamic effect particular to this technology, which results from the absence of bearing pockets. At 4000 rpm, the stiffness hydrodynamic-component contribution is of 37 N/μm (46 %) on top of the observed static stiffness. In contrast, the hydrostatic displays a slowly growing curve, demonstrating a poorer hydrodynamic component. At 4000 rpm, the stiffness

hydrodynamic-component contribution is of a meagre 6 N/μm (21 %) on top of the observed static stiffness.

From Figure 92, the stiffness benefit of the porous-ceramic hydrostatic is self evident.

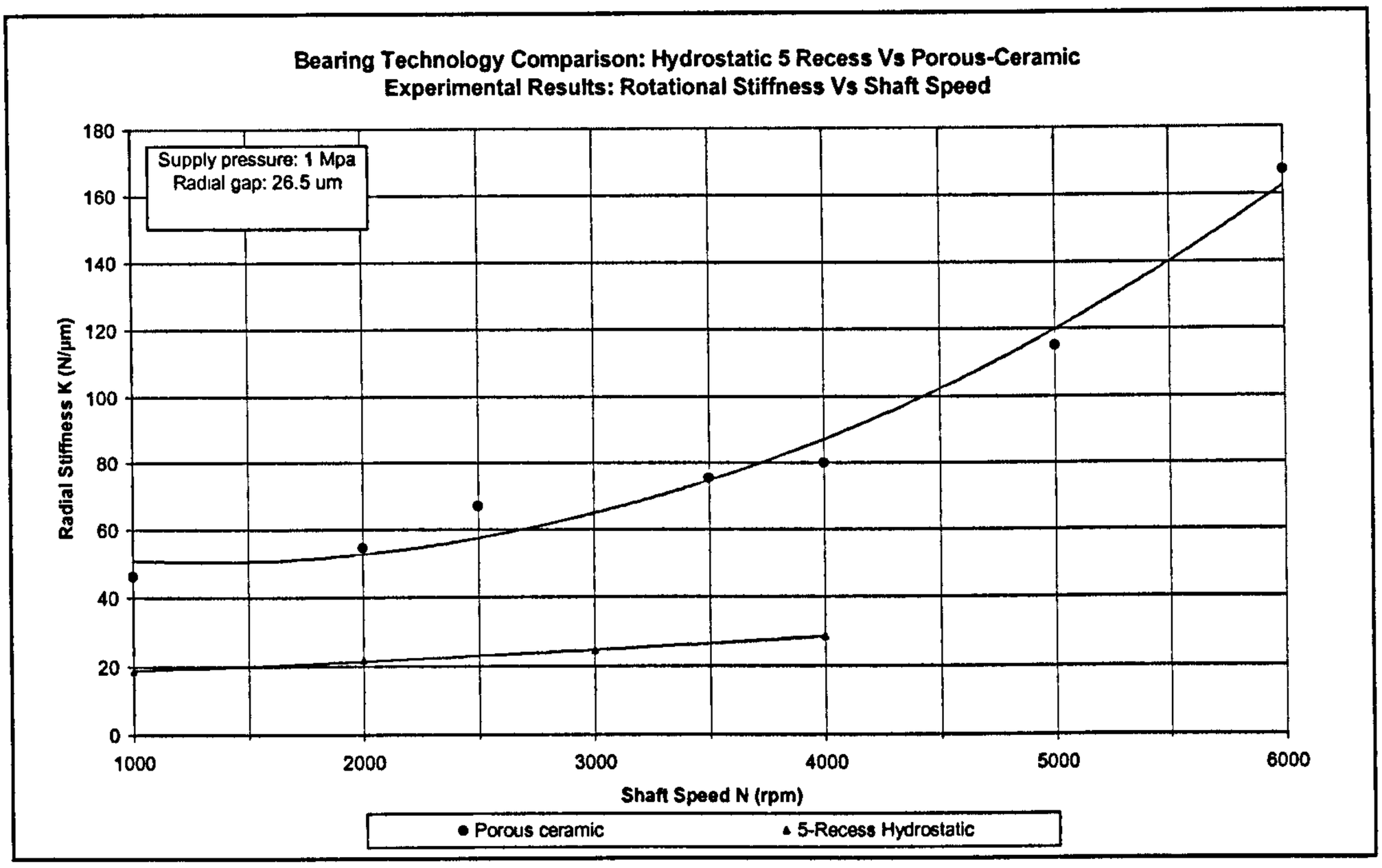

Figure 93- Bearing technology comparison: Rotational stiffness Vs shaft speed.

Pumping power results and discussion

Pumping power was calculated as a product of flow rate and pressure supply (Equation 13). Figure 94 illustrates the measured flow rate for both the porous-ceramic bearing and the conventional 5-recess hydrostatic bearing with the supply pressure. As can be observed in the figure, the hydrostatic bearing flow rate is higher than the porous bearing. Factors influencing this are the bearing's resistance radial gap and resistance ratio [37]. Conversely, the lower flow of porous bearing is mainly influenced by the bearing's permeability, as observed in section 5.3.2. In this sense, Figure 94 is not considered a direct comparison. However, it serves to illustrate the range of flows for both bearings, as well as to calculate the pumping power.

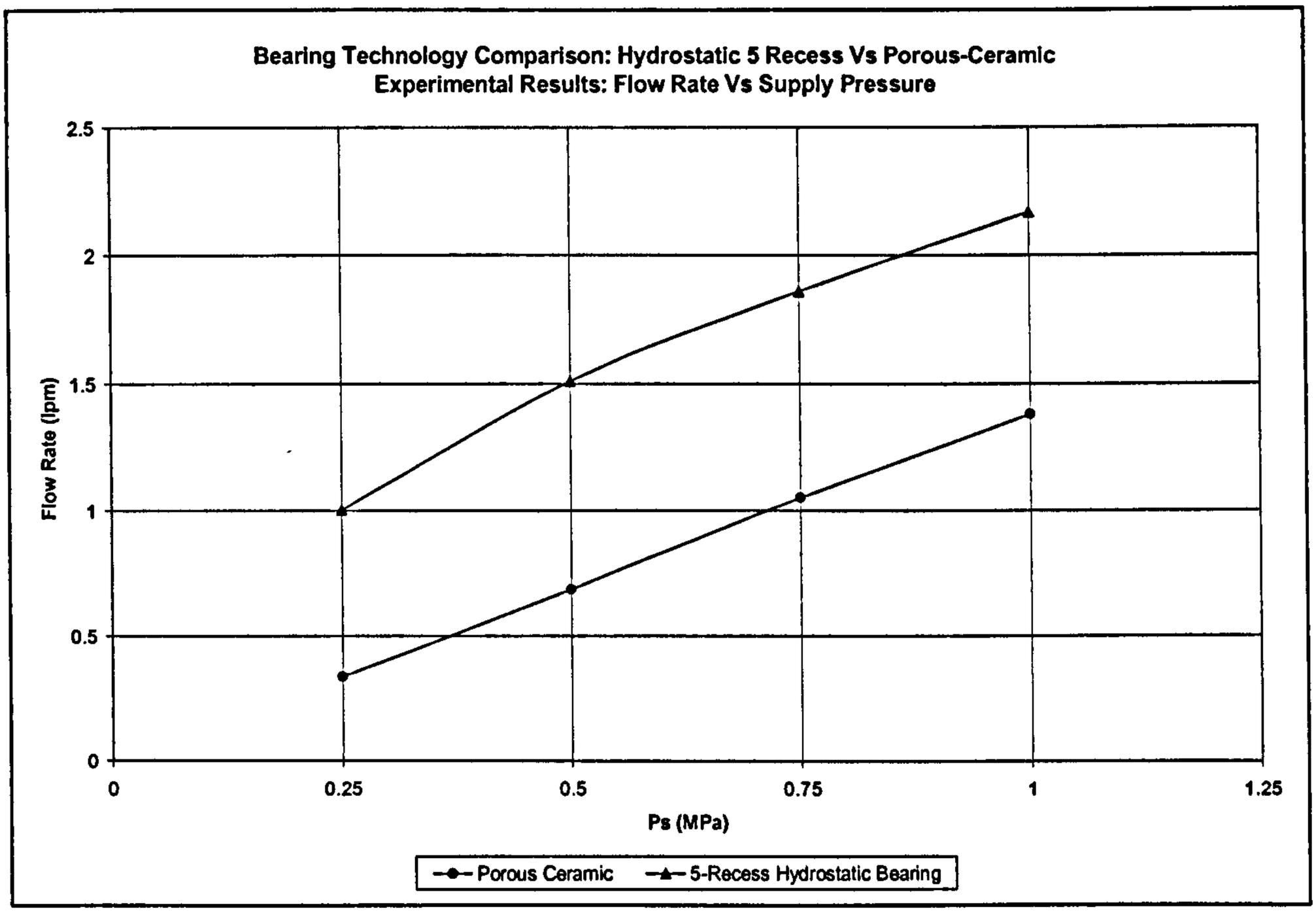

Figure 94- Bearing technology comparison: flow rate Vs supply pressure.

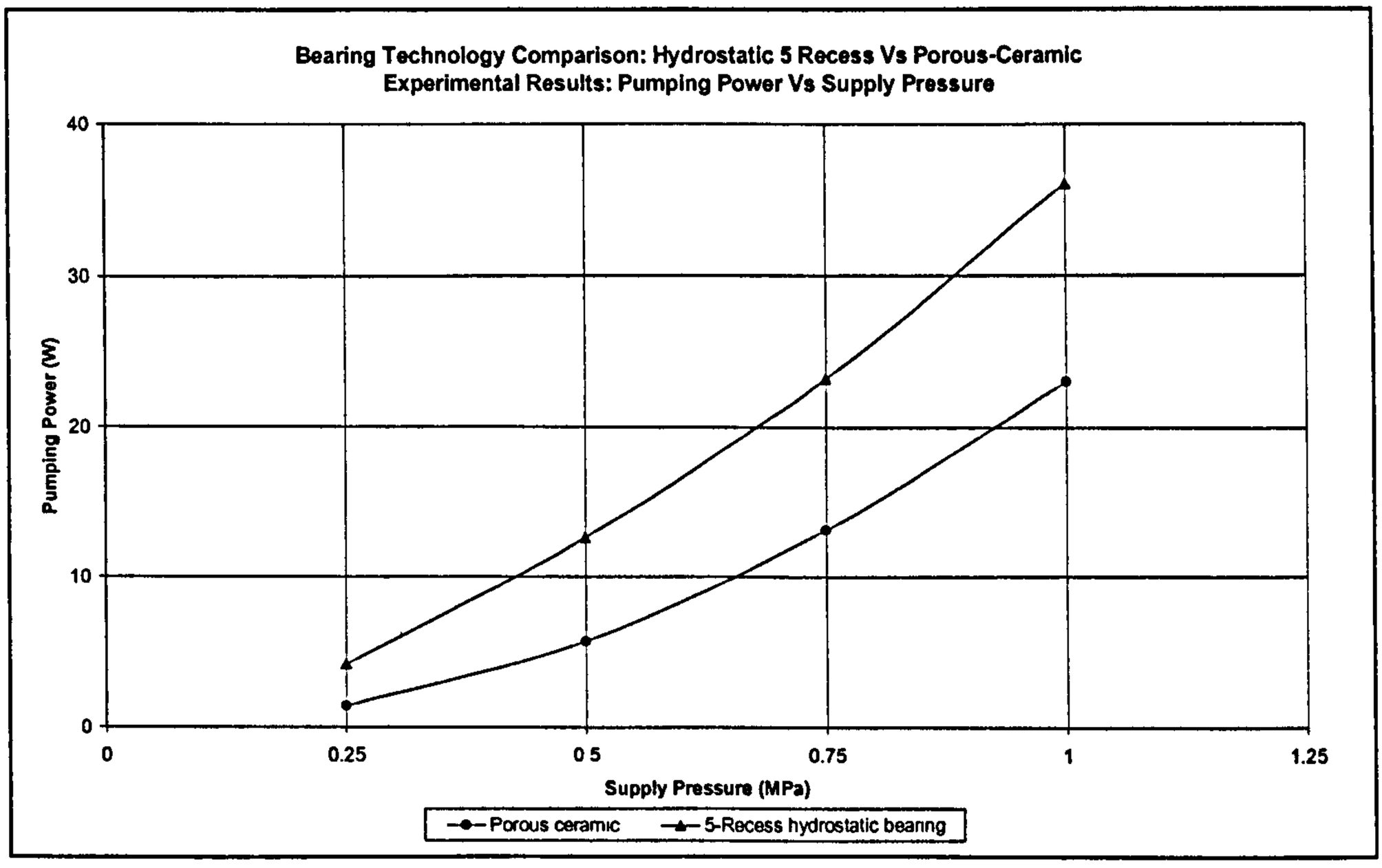

Figure 95- Bearing technology comparison: pumping power Vs supply pressure.

From the observed flow rates in Figure 94, it follows that the pumping power consumed by the conventional hydrostatic is higher. Figure 95 illustrates the calculated pumping power for each bearing at varying supply pressures. As can be observed from Figure 95 the conventional 5-recess hydrostatic bearing in effect consumes more power. The difference in power consumed between the two bearings at a Ps of 1 MPa is 13 W (56 % higher).

Temperature rise results and discussion

Figure 96 illustrates the temperature rise results for both bearings against the shaft rotational speed. The higher temperature rise exhibited by the conventional hydrostatic bearing it is immediately noticeable, for a maximum of 1.6 ˚C at 4000 rpm. In contrast, the porous-ceramic bearing temperature rise at the same speed was 0.8 ˚C.

Since the same oil was used to lubricate both bearings, the higher temperature exhibited by the conventional hydrostatic bearing was mainly attributable to the effect of re-circulating type of flow of the lubricant within the pockets (Figure 97), which gives rise to greater frictional drag over the area of the pockets This type of flow and its effect is particular of this technology. In contrast, in the operation of porous-ceramic hydrostatic bearings, the lubricant directly escapes the bearing in a less turbulent manner.

Another possible source of frictional drag might be encountered in the nature of the hydraulic circuit for each bearing. In the porous-ceramic housing, the lubricant is more efficiently feed into the bearing gap via an annular cavity, fed by two inlets ports (see Figure 27 and Figure 28 in chapter 4). The lubricant fills this cavity and then flows through the ceramic bearing into the gap. In contrast, in conventional hydrostatic bearings the lubricant is 'channelled' to each of the pockets via a more complex hydraulic circuit, that generates more friction. A typical hydraulic circuit for conventional hydrostatic bearing is shown in Figure 97.

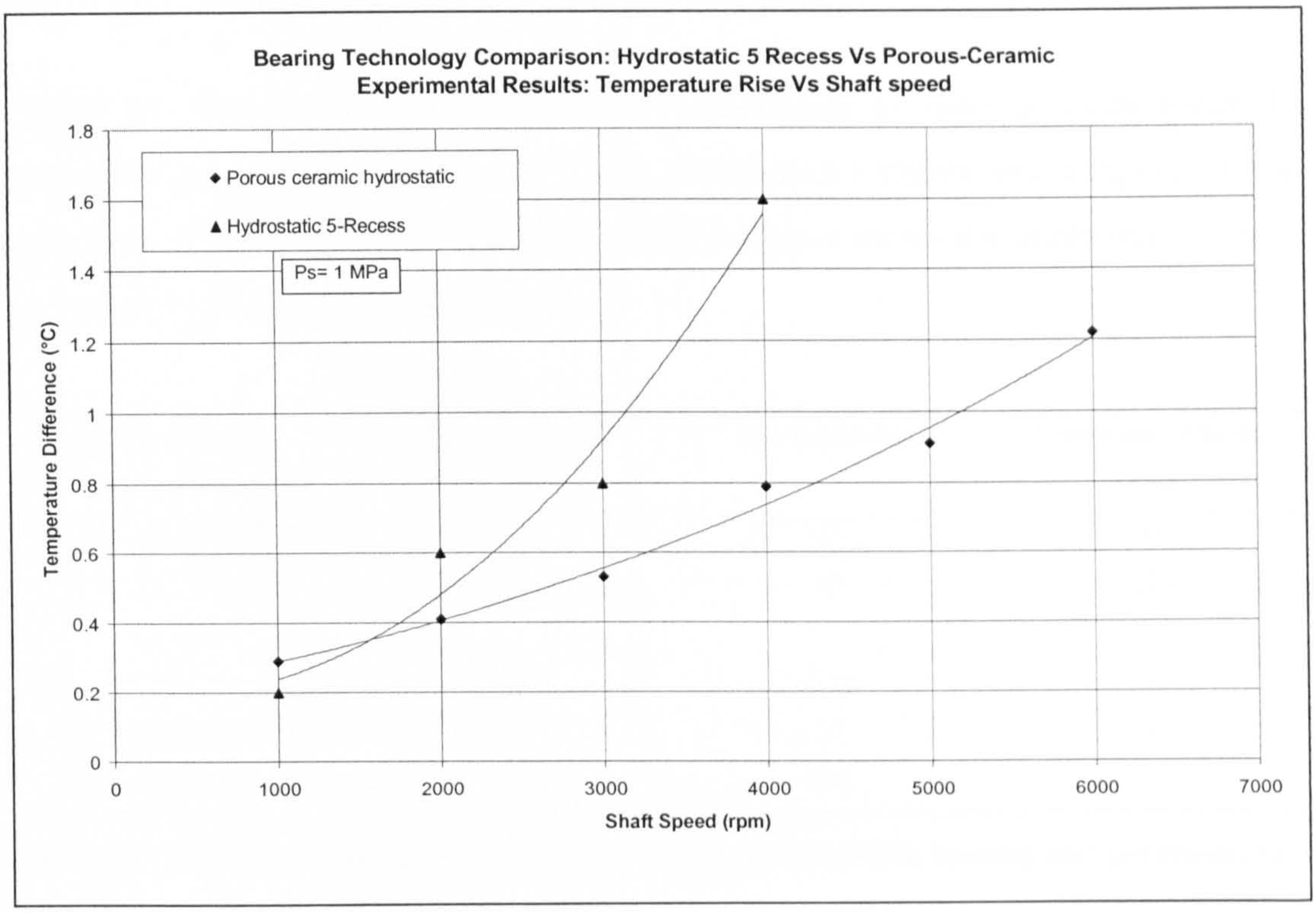

Figure 96- Bearing technology comparison: temperature rise Vs rotational speed.

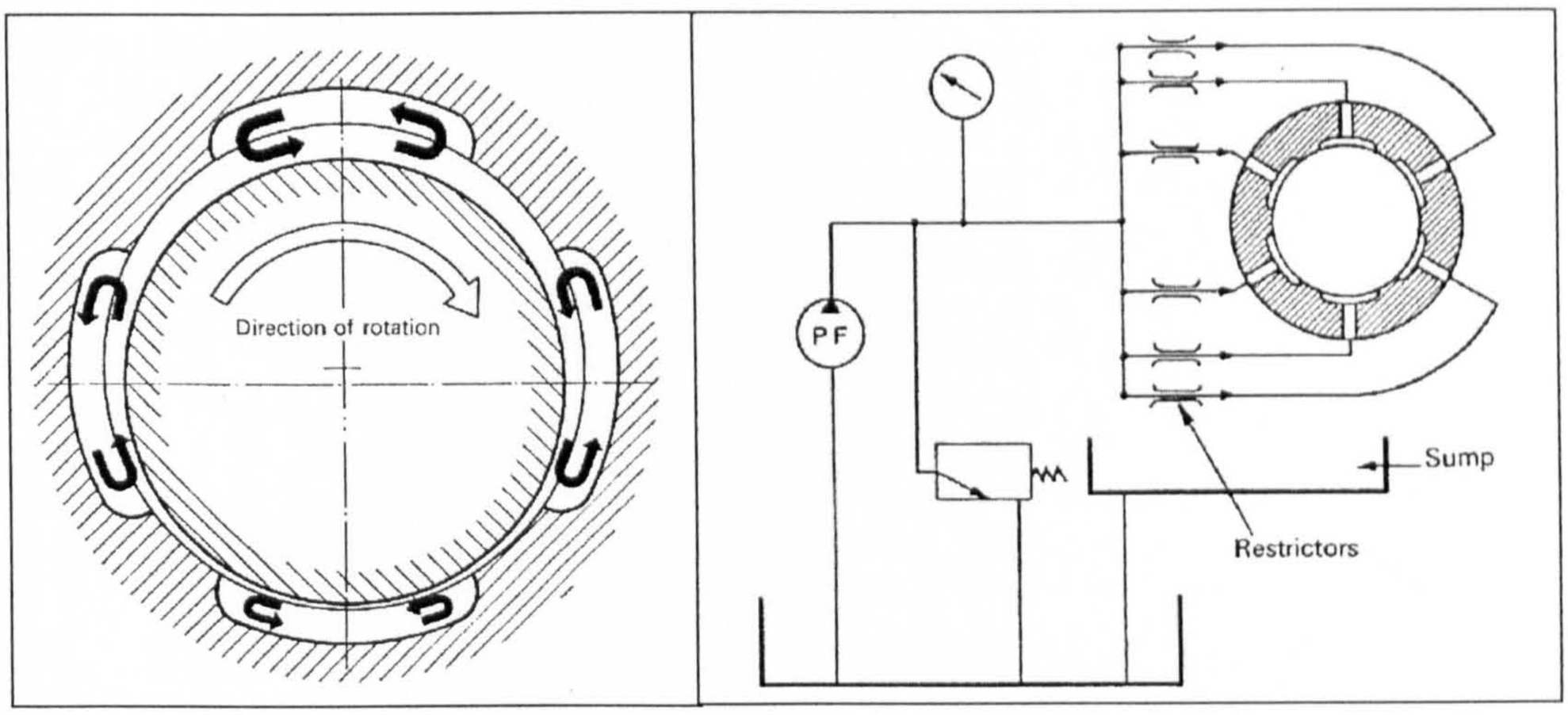

Figure 97- Conventional hydrostatic journal bearing, from reference [37]. Left side: re-circulation of the lubricant within the pockets. Right side: typical hydraulic circuit.

Bearing technology comparison: summary of results

Table 33 illustrates the results for the comparison of bearing technologies by parameter investigated at a Ps of 1 MPa. Rotational stiffness and temperature rise tests were conducted at 4,000 rpm. The fourth column shows the improvement factor in favour of the porous ceramic bearing.

Performance parameter	Conventional Hydrostatic	Porous ceramic .	Improvement factor (%)
Static stiffness (N/μm)	22	43	95
Rotational stiffness (N/μm)	29	80	175
Lubricant flow rate (lpm)	2.17	1.38	64
Pumping power (W)	36	23	64
Temperature rise (°C)	1.6	0.8	50

Table 33- Comparison between conventional 5-recess hydrostatic bearing and porous-ceramic bearing.

5.5 Water lubrication: investigation into the corrosion, foaming and air release characteristics for porous-ceramic hydrostatic bearing systems

5.5.1 Corrosion test results

Initial experimental runs

The initial corrosion experimental runs were conducted without any inhibitor and only plain water, in order to determine the factors that have more impact on the corrosion resistance of cast iron. This test conditions are more thoroughly detailed in section 4.5.1.

The test exposure times were initially set to 120h and this was established in accordance with the standard NACE procedure [112] and with the results of preliminary corrosion tests. The Temperature of the solution was monitored at random times throughout the testing to ensure proper control of this variable. This was regularly seen to vary within ± 2°C of the corresponding experimental setting.
In all experimental runs, duplicate test specimens were exposed, observing a corrosion rate of ± 10% between them, as recommended by the standard [112].

Corrosion products did form on the surfaces of the cast iron coupons immersed in plain water. The conditions that promoted this were the stirring and the deionised warm water, which occurred in run 4 Table 34. Figure 101 illustrates this run's exposed corrosion test coupons
However, on closer inspection of the analysis sheet (Table 34), the results from this test revealed that the only variable that to have a major influence in the corrosion rate observed was the stirring speed. Additionally, it was also found that the water temperature had only a secondary effect and that the water type plays a marginal role

at most. Presumably, the agitation caused by the stirring is turbulent enough to remove corrosion products formed at the coupons' surfaces while immersed, as well as possibly causing the aeration of the solution, leading to further corrosion.

Run	Water type	Temperature	Stirring Speed	Corrosion rate (mm/y)
1	-	-	+	0.86485847
2	+	-	-	0.08930049
3	-	+	-	0.19025858
4	+	+	+	0.96926727
∑+	1.058568	1.159526	1.834126	
∑-	1.055117	0.954159	0.279559	2.11368481
Net total	0.003451	0.205367	1.554567	
Effect	**0.001725**	**0.102683**	**0.777283**	
1/2 effect	0.000863	0.051342	0.388642	

Table 34- Corrosion test experiment's analysis sheet.

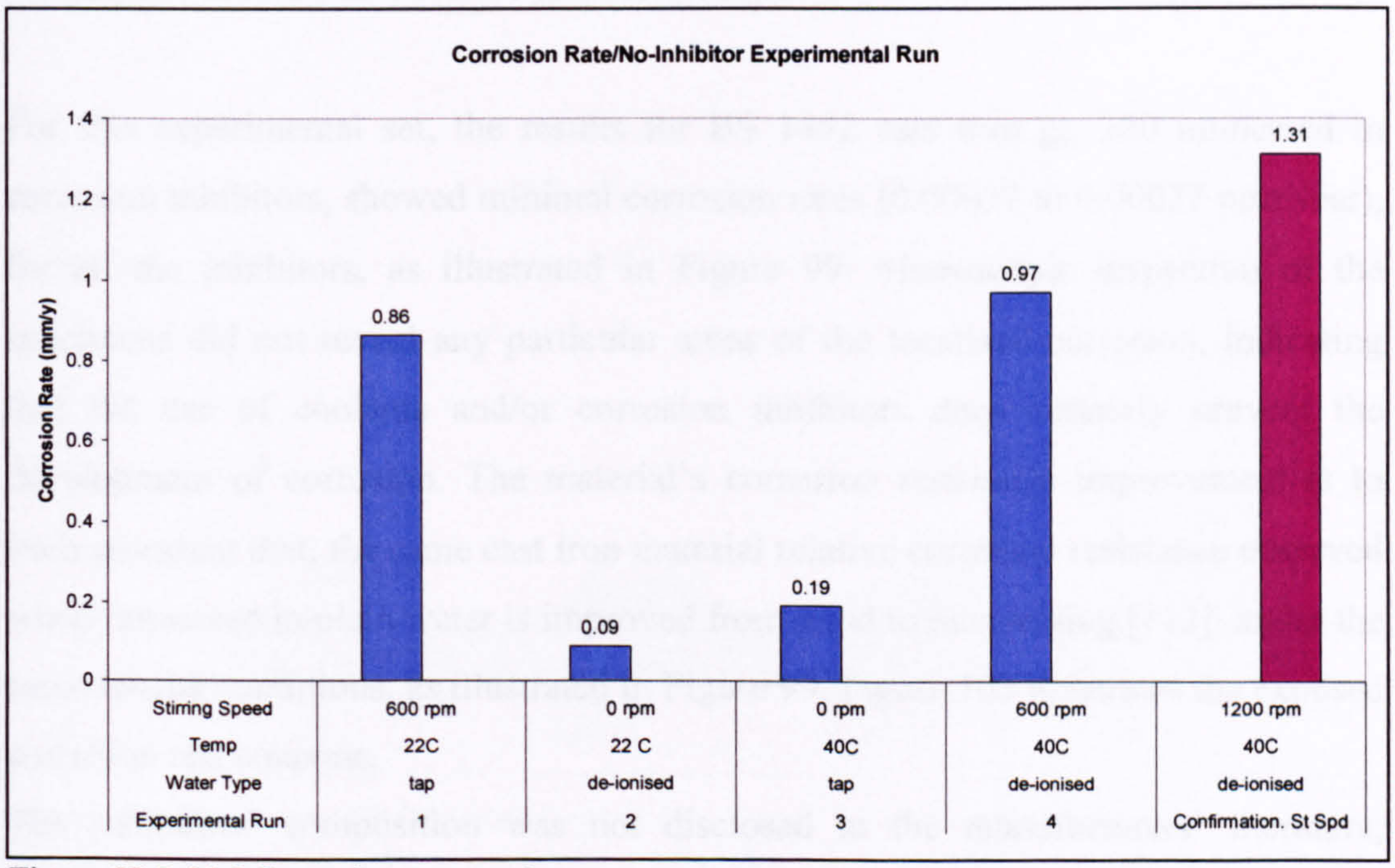

Figure 98-Initial Corrosion test results.

A confirmation run was prepared with the resulting worst case conditions at an increased stirring speed of 1200 rpm. The results are shown in Figure 98, clearly confirming the test findings. Because of the nature of the application, the relevance

of the turbulence effect should not be overlooked. Turbulences of this nature are likely to be found not only in the spindle itself but in the auxiliary equipment required for the bearing system such as feeding and auxiliary pumps.

It is worth noting, however, that in relation to the level of the corrosion rates observed here, the relative corrosion resistance of cast iron immersed in water is considered from fair to good for this type of material and testing, according to Fontana [113].

Experimental results for runs with machining coolants and corrosion inhibitors

Once the effect of the variables was identified, a series of experimental runs adding the corrosion inhibitors to the water under the most severe conditions was prepared using the same test equipment and procedures as before. Details of the inhibitors and the dilution used are in Table 10 (previous chapter).

For this experimental set, the results for BS 1452 cast iron gr. 250 immersed in corrosion inhibitors, showed minimal corrosion rates (0.00037 to 0.00027 mm/year), for all the inhibitors, as illustrated in Figure 99. Microscopic inspection of the specimens did not reveal any particular areas of the localized corrosion, indicating that the use of coolants and/or corrosion inhibitors does certainly prevent the development of corrosion. The material's corrosion resistance improvement is to such an extent that, the same cast iron material relative corrosion resistance observed when immersed in plain water is improved from good to outstanding [113], under the same testing conditions, as illustrated in Figure 99. Figure 102 illustrates the exposed corrosion test coupons.

The inhibitors' composition was not disclosed in the manufacturers' literature; therefore the occurring inhibition process was not completely explained. In this sense, Fontana [113] acknowledged the lack of a thorough understanding of the inhibition mechanism due to commercial sensitivity; nonetheless he presents a thorough classification according to their basic inhibition mechanism and composition.

However, towards the end of the present experimental set, a set of specimens belonging to an aborted run that were left by the test-area started developing corrosion rusting stains within a few days, as shown in Figure 103. The previous experiment had indicated that corrosion did not develop when the specimens remained immersed. However this incident highlighted the potential corroding of machine components exposed to an intermittent water/inhibitor exposure.

An obvious method for protecting a ferrous material is to cover it with a layer of a more resistant material, such as hard chrome plating, although this is often a more expensive solution.

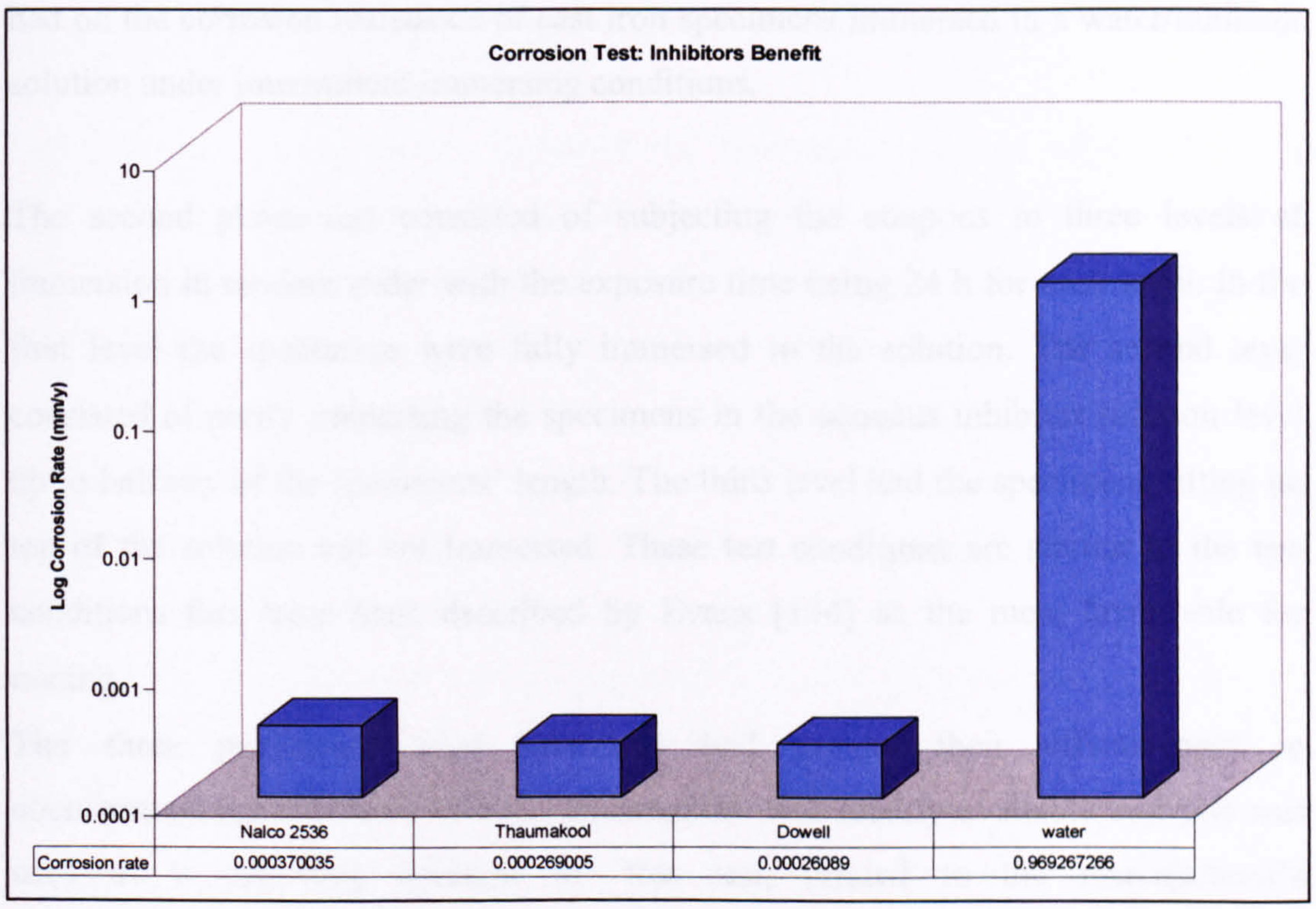

Figure 99-Corrosion rate: Inhibitors benefit.

An alternative solution to alleviate the intermittent exposure problem was to provide a simpler surface coating or heat treatment to the specimens, and this led to a second phase of the present corrosion study.

Certain coatings and heat treatment processes are known to enhance a material's corrosion resistance. Tufftriding is particularly well suited for the cast iron type studied here. Tufftride is a relative simple and cheap salt-bath nitriding process; it can be carried out for most ferrous materials and it is main benefits include the increase of wear, fatigue and corrosion resistance [64] . The tufftride process typically produces a thin (10-20 μm) outer iron nitride compound with a deeper diffusing nitrogen layer underneath.

Intermittent exposure corrosion test

A number of corrosion test coupons were sent off to a heat treatment specialist for tufftriding, and a corrosion test was prepared to observe the effect this processing had on the corrosion resistance of cast iron specimens immersed in a water/inhibitor solution under intermittent immersing conditions.

The second phase test consisted of subjecting the coupons to three levels of immersion in random order with the exposure time being 24 h for each level. In the first level the specimens were fully immersed in the solution. The second level consisted of partly immersing the specimens in the aqueous inhibitor solution level up to halfway of the specimens' length. The third level had the specimens sitting on top of the solution but not immersed. These test conditions are similar to the test conditions that have been described by Evans [134] as the most favourable for rusting.

The three previously used inhibitors had proved their effectiveness in counterattacking corrosion effects. Thaumakool was readily available and this was used as a corroding solution for this test, diluted to the manufacturer's recommendation. A further advantage of aqueous metal working solutions is their convenience, as these could be used for both metal cutting coolants and corrosion inhibitors. The solution temperature and stirring speed were set to 40 °C and 600 rpm, respectively, which were the settings at which the most severe corrosion occurred previously.

In view of the very low corrosion rates observed in the previous test, the present test duration was extended from 120 to 336 h. At the end of the exposure cycle the samples were cleaned and weighed to detect any mass changes. The sample was then left to dry and rest at room temperature and exposed to the general conditions of the laboratory for another 30 days (no immersion). Cleaning and re-weighing of the specimens after this 30-day period was then conducted to detect any subsequent mass changes, followed by microscopic inspection.

Although the testing conditions do not duplicate entirely the conditions observed in a spindle system, it was thought that these simulate adequately the operation conditions and levels of immersion for a given machine tool spindle and auxiliary equipment components.

Intermittent exposure test results

The tufftride coating further improved the corrosion resistance of the cast iron specimens. The specimens' change of mass was not measurable and, in addition, microscopic inspection revealed no signs of corrosion development. This meant that the coating of the specimen effectively counterattacks the effects of intermittent corrosion. The overall benefits of both corrosion inhibitors and surface coating are shown in Figure 100. Figure 104 shows one of the corrosion test coupons exposed during this test.

At this stage, the industrial sponsor proposed to extend the corrosion test to include another material commonly used in precision engineering machine building, providing a sample of B01 alloy tool-steel (BS 4659). The material sample was machined to produce a number of corrosion coupons, similar in dimensions and surface finish (see corrosion test procedures) to the ones produced with the cast iron material. The samples were then heat treated (hardened) according to the industrial sponsor's material specification. This basically involved preheating up to 500° C, further heating up to 820°C and oil quenching, followed by tempering to approximately 150 ° C.

After heat treatment, a corrosion test was prepared with the observed worst case conditions for plain water, which included the following settings: solution temperature 40° C, stirring speed 600 rpm and de-ionized water.

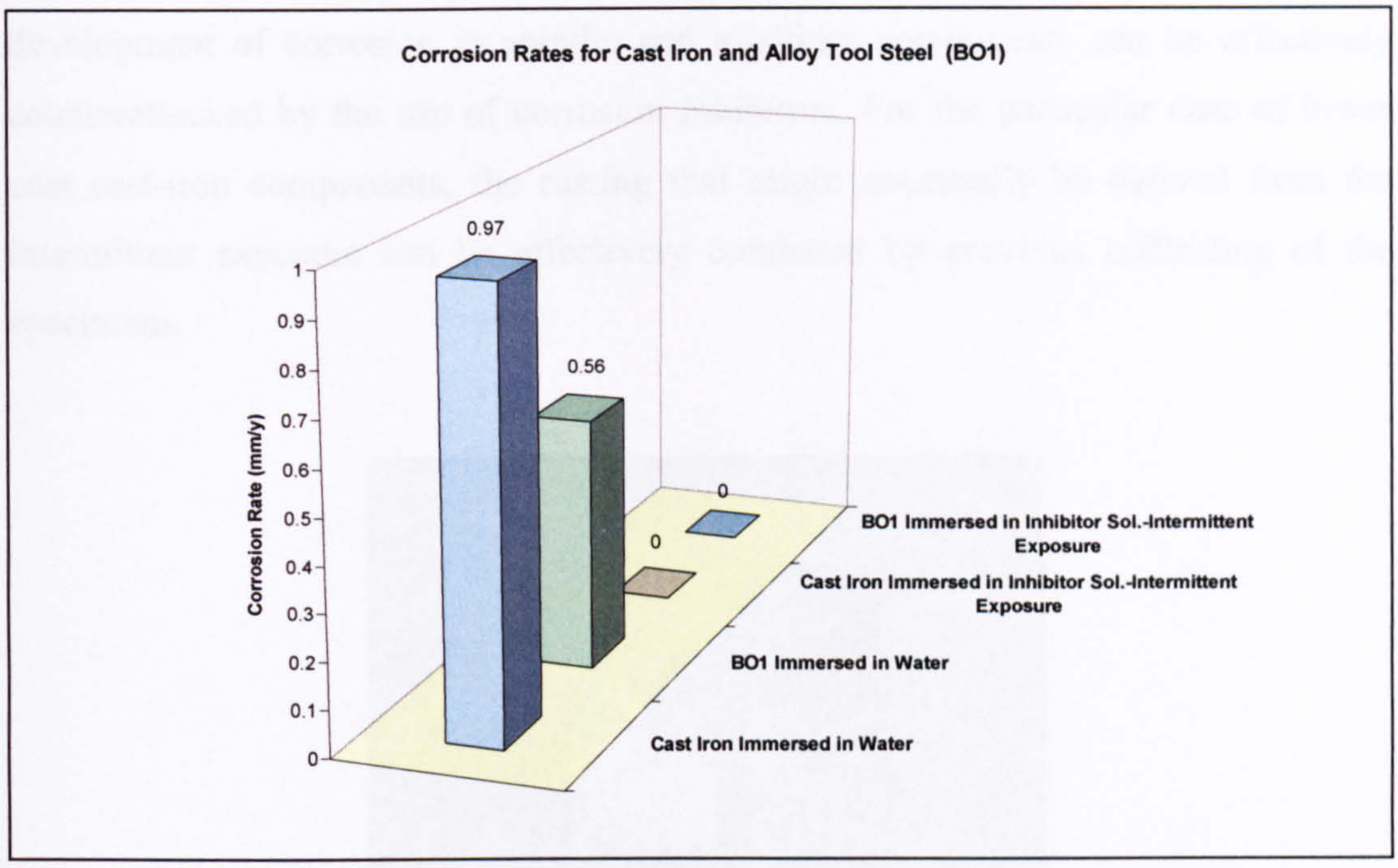

Figure 100- Corrosion rates for cast iron and alloy tool steel.

The results from this test provided a basic benchmark value for a subsequent test, in which corrosion inhibitors were added; as well as the previous material tested. Figure 100 illustrates the results from this test.

As observed in Figure 100, alloy tool steel B01 exhibits a lower corrosion rate than the cast iron specimens. This material typical composition includes a small amount of chromium (0.40-0.65%), that it is thought accounts for its better performance.

Heat treated alloy tool steel samples were then subjected to an intermittent exposure test, which replicated the test conditions described above. The results from this test are also shown in Figure 100. As observed in this figure, the corrosion rate of alloy tool steel samples was negligible and the microscopic inspection did not reveal any sign of corrosion. Again, it is thought that the alloy elements within this material provide a corrosion resistance which is at least equal to the one observed by the cast

iron specimens after tufftriding. Figure 105 shows two corrosion test coupons exposed during the B01 experimental set.

Based on the present investigation results, it can be established that the potential development of corrosion in spindle and auxiliary components can be effectively counterattacked by the use of corrosion inhibitors. For the particular case of lower cost cast-iron components, the rusting that might potentially be derived from the intermittent exposure can be effectively combated by previous tufftriding of the specimens.

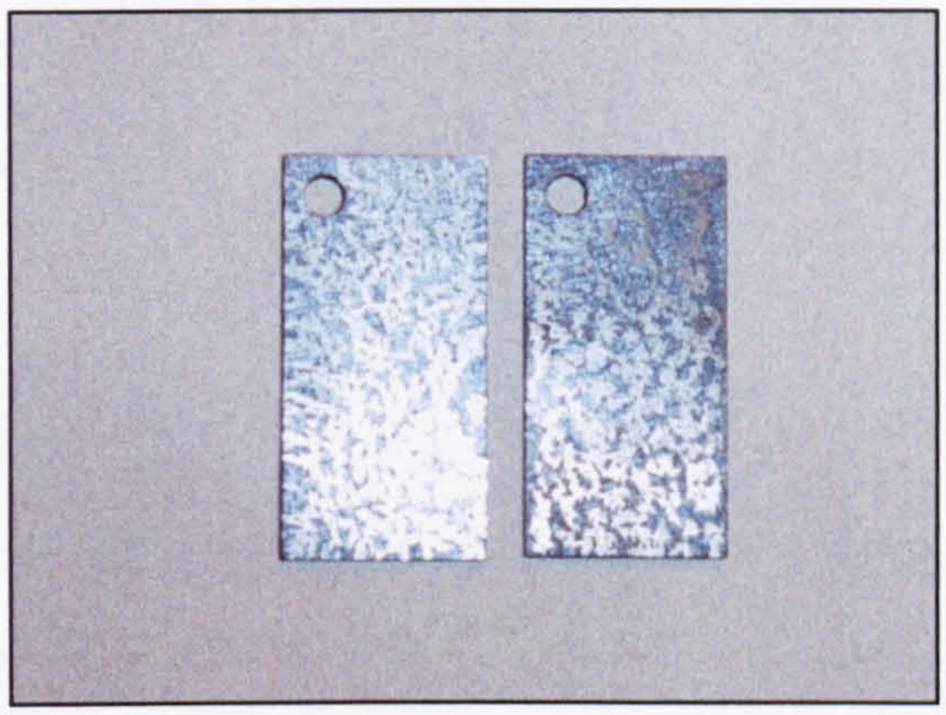

Figure 101-Cast iron corrosion test coupon immersed in plain water, 40°C and 600 rpm.

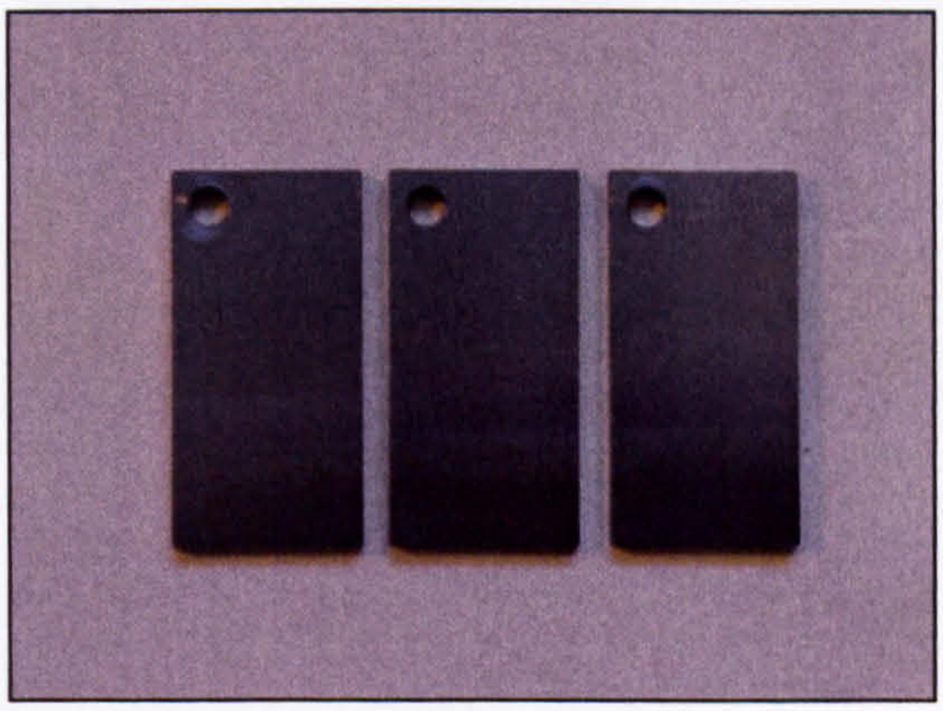

Figure 102- Cast iron corrosion test coupons immersed in inhibitors. From left to right Dowell, Thaumakool and Nalco immersed.

Figure 103- Cast iron corrosion test coupons rusted from an aborted inhibitor run (intermittent exposure).

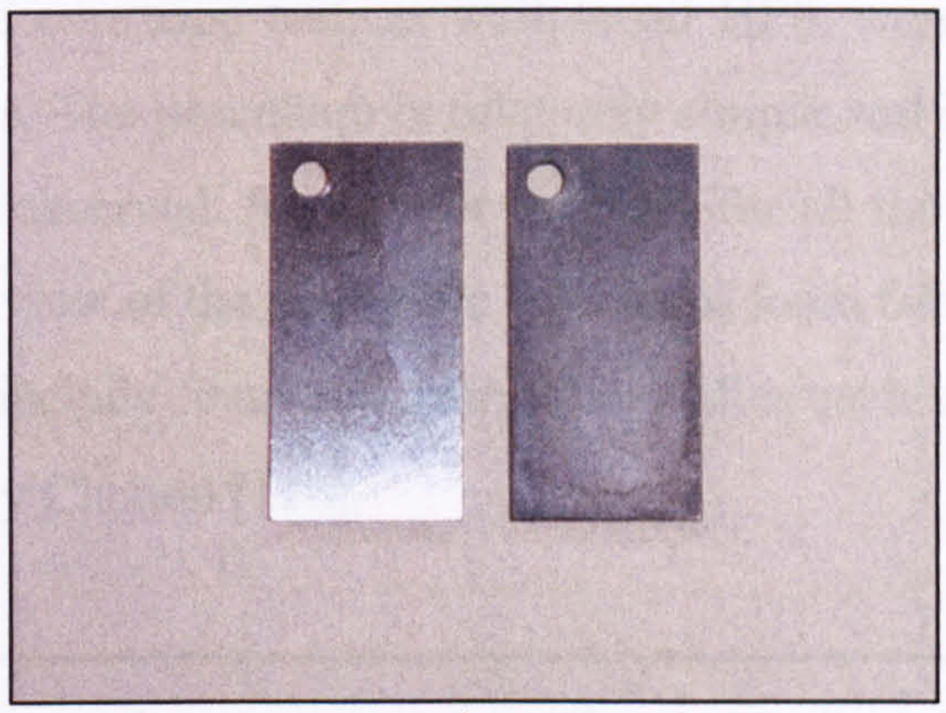

Figure 104- Cast iron corrosion test coupons immersed in Thaumakool. Left side: corrosion inhibitor run. Right side: Intermittent immersion run, tufftride coated.

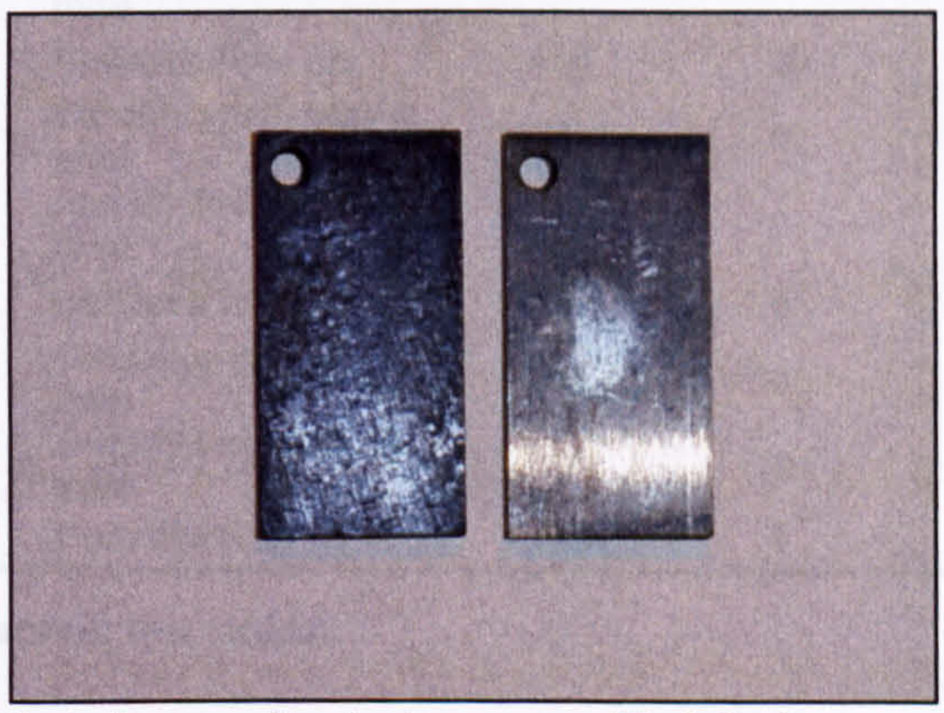

Figure 105- B01 alloy tool steel corrosion test coupons. To left: immersed in plain water. To the right: intermittent exposure in Thaumakool.

From these tests it not clear which of these two materials possess the highest corrosion resistance to intermittent exposure. Longer term tests would be required to

be able to specifically determine this, which are out of the scope of the present investigation.

5.5.2 Foaming and air release test results

Foaming test results and discussion

The foaming test was conducted in accordance with ASTM D892 [118]. Further details of the procedures can be found in section 4.4. The three corrosion inhibitors previously used in the corrosion test, as well as oil HP0, were examined for their foaming characteristics. The procedure is relatively simple and in general very rapid collapsing times were observed. Results for this test, for all the lubricants tested are shown in Table 35. In view of the negligible volume of foam formed, the reporting of these test results also include foam collapsing times after each shutting off of the air supply, as proposed by Claxton [116].

		HP0	Dowell	Thaumakool	Nalco 2536
Sequence 1 (at 24˚C)	*Tendency* (ml, after 0 min)	40	0	0	0
	Stability (ml, after 10 min)	0	0	0	0
	Collapse time (s)	146	6	3	5
Sequence 2 (at 94˚C)	*Tendency* (ml, after 0 min)	10	0	0	0
	Stability (ml, after 10 min)	0	0	0	0
	Collapse time (s)	140	4	1	4
Sequence 3 (at 24˚C after 94˚C)	*Tendency* (ml, after 0 min)	40	0	0	0
	Stability (ml, after 10 min)	0	0	0	0
	Collapse time (s)	145	4	1	4

Table 35-ASTM D892 foaming test results.

Very little foam formed during the testing of the inhibitors. This generally did not fully cover the surface of the lubricant, so the volume was recorded as negligible for the three inhibitors in all three foaming sequences. The quickest collapsing times were observed for Thaumakool, although not by much difference from the others. In

contrast, oil HP0 exhibited a relatively inferior performance, with a maximum volume of foam of 40 ml at sequences 1 and 3; however, after the ten minutes standing period no foam was present. With the second sequence the foam volume was reduced to 10 ml, again completely collapsing before the end of the ten minute standing period.

In order to put these test results into context, they are compared to previously published results for similar tests, although these are relative scarce. Table 36 illustrates typical foam test results presented by Claxton [116] and also by Nemoto *et al* [135] for turbine base and crankcase oils, respectively.

		Turbine base oil	Turbine base oil+ 0.10 % wt of pure calcium sop of a turbine oil rust inhibitor	SG ECII oil
Sequence 1 (at 24˚C)	*Tendency* (ml, after 0 min)	250	645	0
	Stability (ml, after 10 min)	0	600	0
	Collapse time (s)	150	-	-
Sequence 2 (at 94˚C)	*Tendency* (ml, after 0 min)	30	635	10
	Stability (ml, after 10 min)	0	250	0
	Collapse time (s)	20	-	-
Sequence 3 (at 24˚C after 94˚C)	*Tendency* (ml, after 0 min)	250	705	0
	Stability (ml, after 10 min)	0	630	0
	Collapse time (s)	177	-	-

Table 36-Typical foam test results, from references [116] and [135].

By way of comparison (Table 35 and Table 36), the obtained results for the lubricants tested here were considered satisfactory for the present application.

Because of the nature and the number of lubricants studied (commercially developed water based metal working liquids and a thin mineral oil), it cannot be categorically established whether any of the lubricants' physical properties exert a dominant influence. In this sense Tourret and White [136] indicate that viscosity is a major factor in the formation of foam formation of engine oils, which may offer some level of justification over the observed relative poorer performance of oil HP0 in comparison to the water based lubricants. Other factors investigated by Tourret and White influencing foaming are surface tension, vapour pressure, temperature and

oxidation. In addition, other authors like Nemoto *et al* [135], found the foaming characteristics of crankcase oils to be dependent on the oil formulation, with regard to antifoaming additives, while Claxton [116] found that oil contaminants create an adverse effect upon foaming.

Air release test results & discussion

Air release testing, in accordance with ASTM D3427 [119], did not produce any measurable results for any of the lubricants employed in the present investigation. It was observed that the entrained air was rapidly released before the sinker was re-hung (step 5 and 6 of the procedure, section 4.5.2). Another problem encountered included the spillage of the lubricants at the start of the air supply due to the initial air blow. Although this was remedied by extending the test vessel's vent tube, it did not change the outcome of the tests.

Similar results were reported by Claxton [119], for rust inhibitors and turbine oil anti-oxidant additives. In this sense, the almost instantaneous release of the entrained air might be related the low viscosity of the lubricants tested here. Fowle [117] demonstrated that the influence of the oil viscosity on the air release properties of oils may be represented by the following equation:

Equation 46

$$v = \frac{2 \cdot r^2 \cdot g}{9 \cdot \mu k}$$

v	terminal rate of ascent of an individual bubble (mm/s)
r	bubble radius (mm)
g	gravitational constant
μ_k	kinematic viscosity of the oil (mm^2/s)

From Equation 46 it is clear that the lower viscosity lubricants would posses more rapid air release times. Fowle's [117] experimental verification is shown in Figure 106. From Fowle's results, the air release value (*arv*) for HP0 was projected, resulting in an *arv* of 0.256 min at 25 °C, which is a credible figure. In practice, however, the observed arv was faster than this (3 to 4 s). This difference might originate from the type and the range of viscosity of the oils analysed (turbine oil) by Fowle.

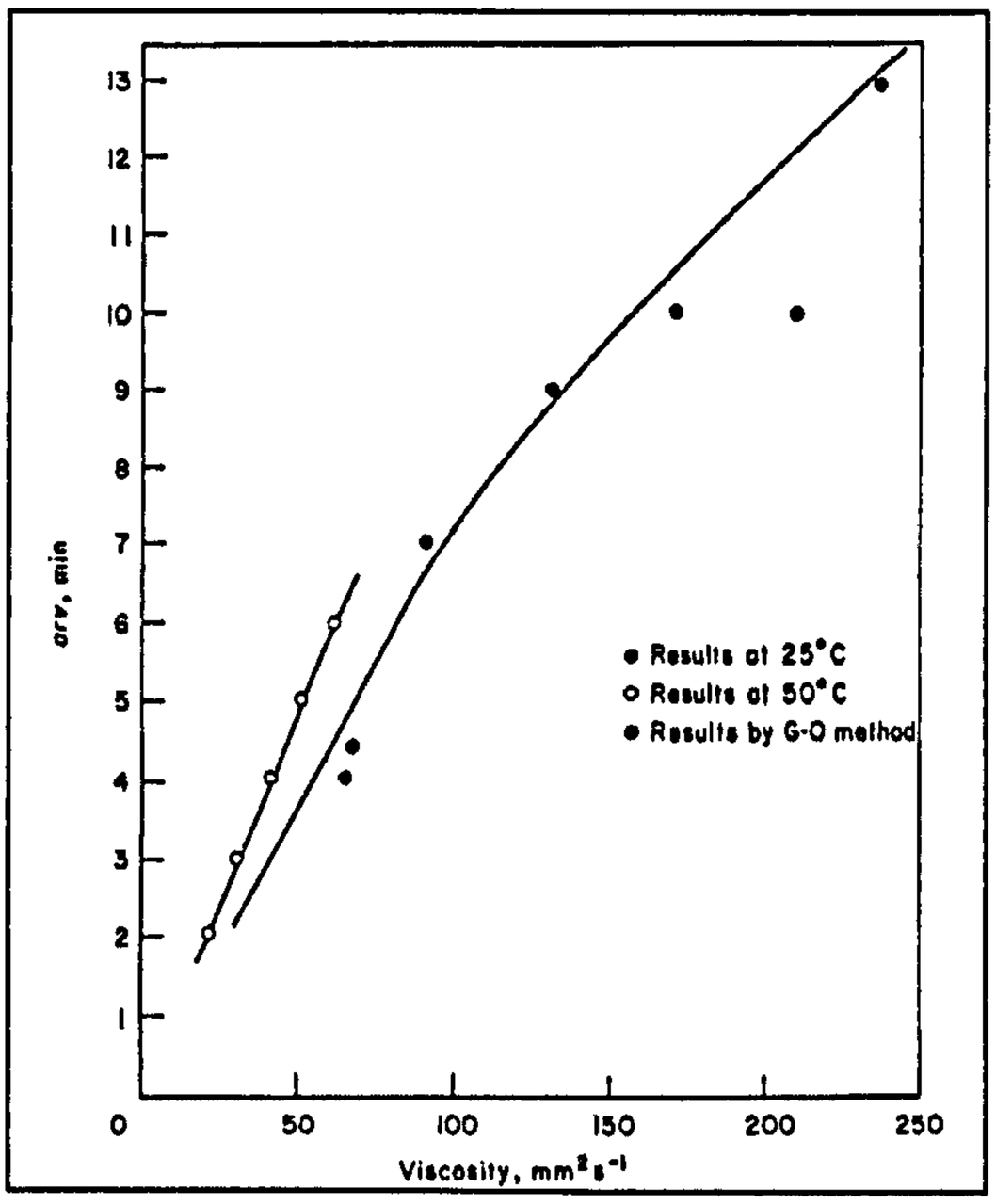

Figure 106- Fowle's ASTM D3427 air release value Vs oil viscosity, from reference [117].

Beyond considering the present test results, the deficiencies of the procedure for the air release properties of thin oils and water based lubricants are highlighted. Much of this problem may originate from the fact that the original purpose of the ASTM D3427 [119] procedure was to measure air release properties of turbine oils, and in the absence of more of more universally used methods, ASTM D3427 has been embraced by other disciplines.

Custom foaming test results & discussion

Foam formation

For the first part of the custom foaming test, the test rig's bearing housing air seal pressure was set to 2 PSI, in order to avoid the aeration of the lubricant. The purpose of this seals is to prevent the lubricant escaping from the bearing housing through the shaft. The air flow also helps to maintain the displacement sensors free of lubricant. By trial and error it was found that at 2 PSI pressure these seals were able to operate successfully. As reference, Almond's [3] recommends this to be set at 10 PSI, to ensure proper performance in all conditions.
The lubricant supply pressure was set to 2 MPa, and this flowed through a bearing with a permeability of 1.5×10^{-14} m^2.

From these experimental settings it was observed that foam started forming basically the moment the spindle reached above 1000 rpm. At approximately 2000 rpm the formation of foam becomes more uniform and constant. In general, it was observed that increasing the spindle speed increased the amount of foam and its thickness.
In samples taken at different rotational speeds, starting at 1000 rpm up to a maximum of 8000 rpm, foam thickness ranged from 4 to a maximum of 15 mm, while the time taken to clear the sample surface ranged from 5 to 14 minutes. On the other hand, the settling tank surface cleared totally in times ranging from 35 to 82 minutes, after stopping the spindle.

However, towards the end of this test it was also noticed that increasing the air supply pressure to the seals had a greater impact over the foam formation, which led to second experiment, to observe the impact of the air flow pressure in the formation of foam.

The second test consisted of shutting off the air supply, and once again observing the formation of foam at different rotational speeds. From these experimental settings, it was observed that foam only formed in negligible amounts at speeds ranging from 1000 to 3500 rpm. Running the spindle at higher rotational speeds was not possible

due to massive lubricant leaking from the seals. However, these observations meant that the main factor originating the formation of foam was indeed the compressed air supplied for the bearing housing seals operation. Rotational speed, on the other hand, was found to be a secondary factor in this sense. However, once foam formation was initiated, rotational speed exerts an important influence on the volume of foam formed, as seen in the previous experiment. Tourret and White [136] present a similar case for a gear oil. Here, the foaming increases with increasing agitation speed, until a point is reached at which the agitation itself serves to collapse the foam.

The spindle was further run for 1h periods at 2000 and 3500 rpm, and for longer periods of 3h at 2500 rpm, observing only small and dispersed amounts of foam. This served to confirm that the major influence in the foam development is exerted by the housing seal operation. Figure 107 illustrates the settling tank after 3-h operation at 2500 rpm.

Figure 107- Settling tank after 3h operation at 3500 rpm, without air flowing to the seals.

As mentioned before, this part of the investigation revealed that a great proportion of the foam formed is originated by the action of the bearing housing seals air flow,

which is consistent with the conclusions of previous published lubricant analyses. In these analysis, the authors [116] [117] [136] generally emphasize that a major proportion of the foaming and aeration problems that arise in the field have mechanical or hydraulic circuit design origins, and in general have little association with the lubricant quality.

For the particular case of the porous-ceramic hydrostatic journal bearing test-rig, the bearing housing seals are essential for its adequate performance. Alternative sealing should be considered where possible in future water based lubricants applications, in order to prevent the formation of foam and the entrainment of air. In this sense, adequate sump design, the installation of baffle plates and wire gauze screens are some of the countermeasures proposed by Hayward [137] to keep air out of hydraulic circuits.

Foam collapsing & air release times

Foam collapsing and air release times were investigated from the previous test's observed worst-case conditions. The spindle was run at 8000 rpm and a sample was then taken (approximately 160 ml) from the discharge tube in the settling tank.

A sequence of photos (Figure 108) was taken to illustrate how the air release and foam collapsing developed. It took slightly less than 2 minutes to clear out all the air bubbles entrained in the lubricant. On the other hand, the foam layer formed at the sample's surface had a thickness of approximately 15 mm, taking approximately 14 minutes to clear.

Foam collapsing and air release times for oil DIE-180

Towards the end of this research, aqueous metal-working fluids lubrication was changed to oil lubrication at the industrial sponsor's request. DIE-180 oil was subsequently used in the performance testing of the SC bearings and its foaming and air release characteristics were investigated in a similar manner to the previous investigation for aqueous metal-working fluids. Once again a sequence of photos was

taken to observe the foam formation and development. This time, supply pressure was set to 1 MPa and the rotational speed was set to a maximum of 6000 rpm, which were the conditions for the performance testing of shell SC-3/40. The housing seals' air supply was set to 2PSI, as before.

Figure 108- Dowell's sample, foaming and air release characteristics observed in porous-ceramic hydrostatic journal bearing test rig at 8000 rpm, 2.0 MPa lubricant supply pressure and an air supply pressure of 2PSI. In order from top-left to bottom-right: sample after 2 s, after 30s, after 1 min and sample after 2 min.

From the present experimental settings, very quick air release times were observed. Air bubbles entrained in the lubricant were cleared in less than 10 s. The foam layer thickness was approximately 23 mm (Figure 108). However, this collapsed and cleared in approximately 2 min, which was much quicker in comparison with the water based lubricant.

In comparison with the previous test, it is evident that the lubricant supply pressure influences its foaming behaviour. As the lubricant supply pressure is increased the

flow of lubricant increases accordingly, giving place to a more turbulent flow, and vice versa. In accordance to this, it was observed that the water based lubricant developed a greater volume of foam. However, it was also observed that the foam formed in the water based lubricant and the oil DIE-180 samples were physically different. The foam formed in the water based lubricant was bubblier and of a long lasting consistency type. Conversely, the DIE-180 foam was thinner and more unstable, accounting for a more rapid clearing.

It was thought that the observed foam consistency might be a result of each lubricant's components. Evidence of this has been presented in a previous lubricant analysis [116]. For this particular case, the addition of one of the components of a rust inhibitor (pure calcium soap) to turbine oil was found to excessively promote the development of foam, as illustrated in Table 36.

Figure 109- Oil DIE-180 foaming test sample. Foaming and air release characteristics observed in the porous-ceramic hydrostatic journal bearing test rig at 6000 rpm, 1.0 MPa lubricant supply pressure and an air supply pressure of 2PSI. In order from top-left to bottom-right: sample after 2 s, after 30s, after 1 min and sample after 2 min.

Foaming & aeration test concluding remarks

The results from the standard tests yielded negligible and non-measurable results for foaming and air release characteristics, respectively. However, the results from the custom test revealed that both phenomena are in fact present. In this sense, other authors [116] [117] have emphasized the need for more realistic and informative foaming and aeration tests.

However, the current levels of foaming and air release found in the custom test might be considered adequate, as the foam collapsing and air release times were relatively short when compared to previous investigations [116] [117]. This might a consequence of the sound design of the test-rig's hydraulic circuit, which already incorporates some of the recommendations for counterattacking the development of foam and air entrainment reviewed by Hayward [137].

Microbial growth

Approximately five months after the initial addition of the corrosion inhibitor, to the bearings performance test-rig, it was observed that this (Dowell, a cutting fluid) had decomposed, leading to the formation of 'algae' in the lubricant stored in the reservoir.

In standard metal-working applications, degradation of metal-working fluids might be considered more of an inconvenience, as replenishing is still a relatively cheap manoeuvre. For this particular technology application, however, ensuring the bacteria colonies do not proliferate is of major importance, as 'algae' formations could well lead to bearing pore-blockage. In addition, the effects of the lubricant degradation upon its ability to inhibit corrosion are not clear.

Microbial growth in water based metal working fluids is a complex phenomenon, and several factors intervene [138]: oxygen, temperature, the solution pH and the quantity and type of nutrients. Adequate maintenance and monitoring routines might prolong the useful life of these fluids [139]. However, because of its complex nature

and the obvious abundance of water, it is difficult to eradicate microbial growth in metal-working fluids.

At this stage, in order to comply with the industrial sponsor's request for oil lubrication, it was not possible to investigate further potential solutions to this problem. However, robust mechanisms for the monitoring and maintenance of this type of inhibitor need to be investigated and implemented with regard to their usefulness for the present application requirements.

5.5.3 Porous-ceramic bearing technology precision engineering applications

Towards the end of this project, porous-ceramic bearings started gaining interest within the industrial precision engineering realm. Looking for superior performance than it can be obtained by conventional technologies two reputable precision engineering companies, approached Cranfield University's precision engineering group, opening themselves to the possibility of embracing this technology for two different high precision applications.

Case 1

The industrial sponsor to this project required larger bearings for their incorporation in a precision spindle system for one of their customers. This resulted in an order for the manufacture of the required bearing sets. The bearing set and was produced via SC technique developed here and comprised a pair of journal bearings, one of which had an ID of 150 mm (Figure 110), and a pair of thrust bearings with a maximum diameter of 180 mm.

However, because of their size, these bearings could not be fully processed in Cranfield University's furnaces, and the bearing castings had to be sent to a ceramic specialist for the binder burnout and sintering operations. This presented some problems related to the transference of technology from Cranfield University

laboratory to industry. For example, some the journal bearings over-shrunk rendering them useless. The thrust bearings, on the other hand, developed some cracks that are probably related to the binder burnout operation. It was thought that the difference in furnace processing caused these problems. Cranfield University laboratory furnaces are electrical type, with a more controlled temperature profile, whereas the ceramic specialist's were gas-combustion type. At the time of writing, a solution to this problem was being sought.

This experience, nonetheless, highlighted the need for a thorough transfer of the technology from the laboratory to the precision engineering field.

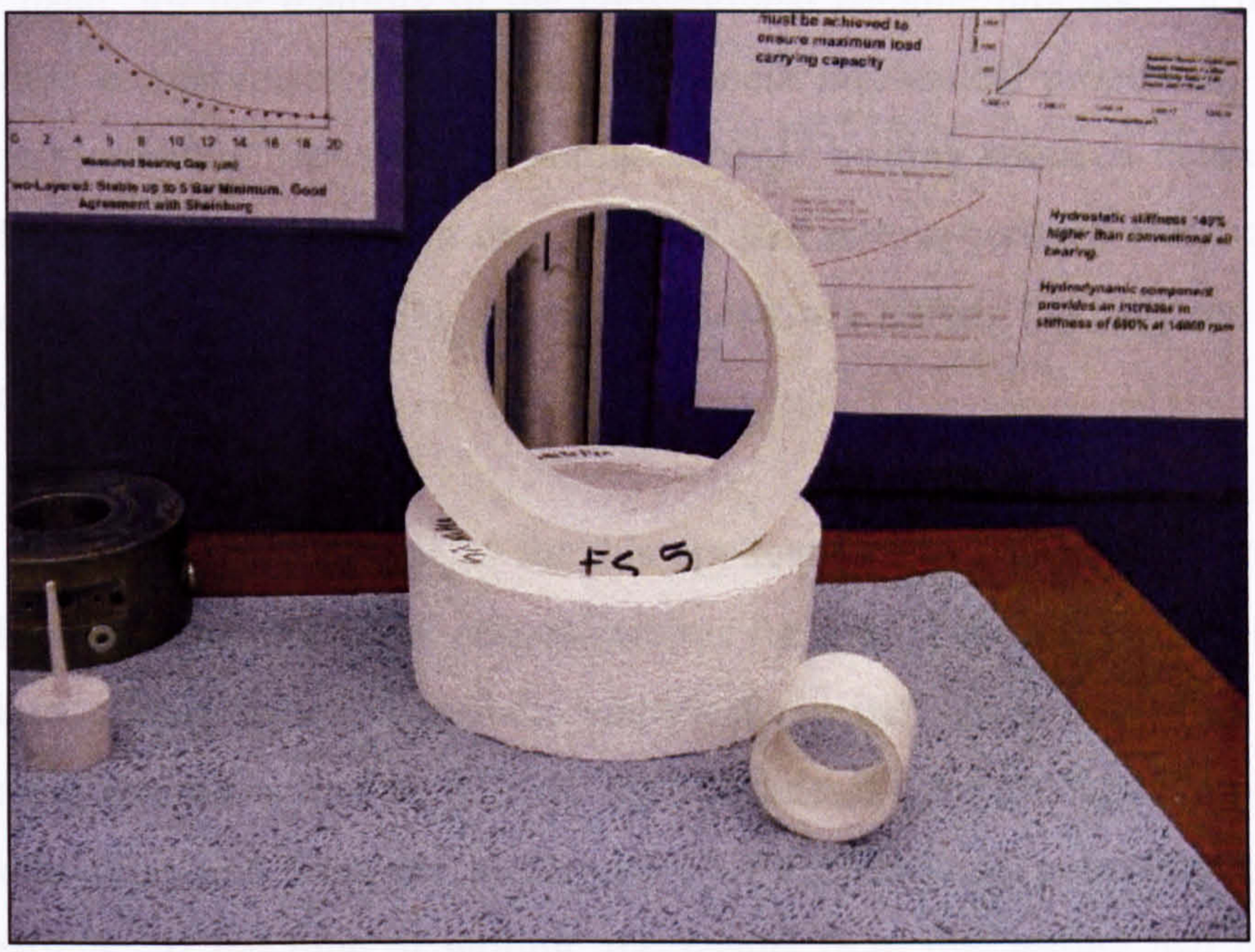

Figure 110- Larger journal bearings (ID 150 mm), produced by the SC technique.

Case 2

A second precision engineering company was considering the introduction of porous-ceramic aerostatic technology to their range of products. This company had, in fact, previously contacted a ceramics specialist to manufacture a few prototype bearings. After some load testing, they observed a very poor performance on the part of the ceramic bearings in comparison with their standard conventional-technology

opposite. At that point, this company requested technical support from Cranfield University's precision engineering group, to understand the unexpected bearing performance.

After examining the ceramic bearings for the density and permeability, it was determined that the ceramic bearings did not posses the required porosity to allow the necessary flow of air into the bearing gap. The high density of the bearings suggested they were manufactured via conventional ceramic techniques, with little observance of the porosity achieved. This case illustrated the need for ceramic techniques that yield a controlled level of porosity.

Conventional ceramic applications usually require the highest density attainable. On the other hand, for the majority of the conventional ceramic processes, a decrease density often compromises the ceramic component mechanical properties, such as the Young's modulus. However, in porous-ceramic bearing research conducted at Cranfield University, it has been demonstrated that porous-ceramic materials with relatively high Young's modulus can be produced, via HIPing [3] [30] and the SC technique.

In order to tackle the requirements for this application, the bearings' performance was modelled via the traditional porous-ceramic theories [140], in conjunction with the previous porous-ceramic aerostatic empirical research. As a result, several SC consolidation thrust bearings (ø 62 x 10 mm thickness) were produced to be tested and directly compared with the performance of conventional precision aerostatic thrust bearings. At the time of writing, the results from this testing had not been produced. Figure 111 shows the thrust bearings produced and sent to the customer.

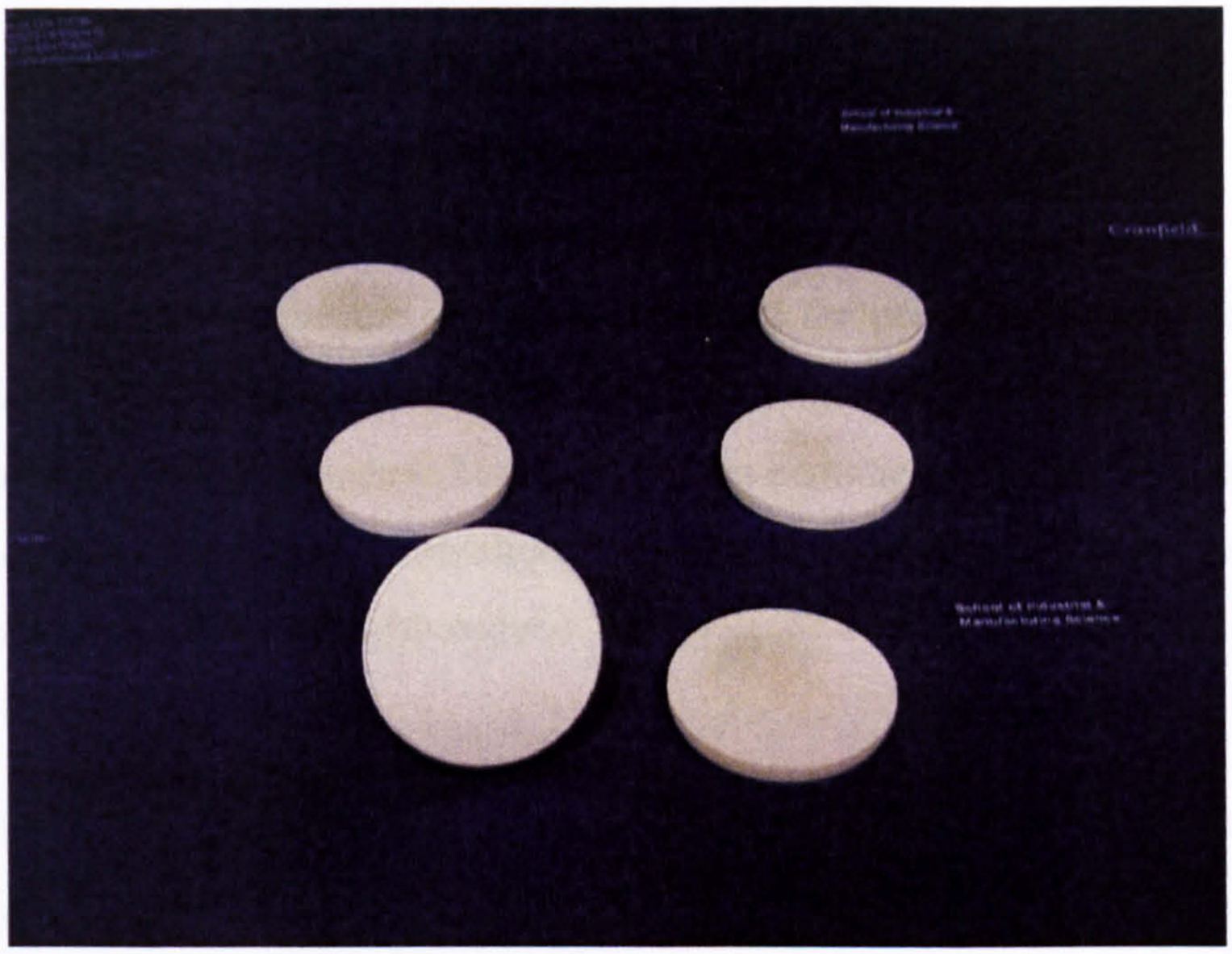

Figure 111- SC porous-ceramic aerostatic thrust bearings (ø 62 mm x 10 mm thickness).

6 Conclusions

Several important conclusions can be drawn from the present research programme. These have been organized in three main headings that are concerned with the manufacture of porous-ceramic bearings, porous-ceramic bearings performance and the study of the effects of corrosion, foaming and air release in porous-ceramic bearing systems lubricated with water.

Materials processing/Manufacture of porous-ceramic hydrostatic bearings

- A new method for the manufacture of porous-ceramic hydrostatic bearings has been successfully developed. This new method is based on the starch consolidation technique and has demonstrated to be a cost effective, flexible and reproducible manufacturing method for both, journal and thrust bearing geometry.

From the development of the new processing technique, the following conclusions can be drawn:

- The SC technique proved to be up to 36 % more economical per bearing than HIPing. Further savings can be made by optimizing the processing for mass production.

- The SC technique proved to be environmental sound. Sintering temperatures proved to be sufficiently low to conduct this operation using atmospheric furnaces. In addition, no harmful substances have been used or resulted from the processing of bearings.

- The SC technique proved to be shape/size flexible. Bearings of various shapes and sizes were produced including hollow cylinders with IDs ranging from 50 up to 150 mm, as well as discs of up to 200 mm in diameter.

From the bearing characterization, the following conclusions can be drawn:

- Uniform density and porosity values were produced repetitively, regardless of the specimens' shape and size (up to journal bearings of 80 mm ID). The maximum variation in density measured along the bearings' walls was 1.71 %. In contrast, previous research HIPed bearings maximum measured variation was 6.21 %.

- Linear shrinkage is mostly dependant on the Al_2O_3 particle size. The effect of the starch content is only noticeable for the 0.5 μm Al_2O_3 size, for which increasing the starch volumetric content, from 40 to 60 % of the solids volumetric content, increases the linear shrinkage.

- Porous ceramic bearings' porosity ranged from 19 up to 49 % of the total volume. Specimens' porosity/density showed to be first influenced by the alumina particle size. A second influence is the amount of starch and this can further increment porosity an additional 20-25 %.

- Bearings produced exhibited well defined, reliable and reproducible permeability values ranging from 1.18×10^{-16} up to 1.31×10^{-13} m^2.

- Permeability-measurements proved permeability to be independent of the specimen's shape as well as the fluid used.

- For alumina particle sizes ranging from 2-4 μm, 40% starch vol. of the solids loading, proved to be the maximum starch amount for producing reliable and reproducible ceramic bearings.

- The SC bearings structural properties measurement results (flexural and shear moduli) proved to be well defined and reproducible, as well as directly dependant on the specimen's porosity, with the measured elastic modulus ranging from 57 to 177 GPa.

- The results from flexural and shear moduli measurements performed on thrust bearings are comparable to those performed on a previous research programmes manufactured via HIPing, and higher than bearings manufactured via slip casting and injection moulding, for the same range of porosity.

SC porous ceramic bearing performance and comparison with a conventional hydrostatic bearing

- The performance of bearings manufactured by the starch consolidation technique is comparable to those manufactured in a previous research project by HIPing techniques, following similar trends for the various parameters measured, such as static and rotational stiffness, flow rate and pumping power.

- SC porous-ceramic journal bearings hydrostatic pressure maps are of the same uniform and consistent nature as those from previous research, indicating the consistency of the porous-ceramic hydrostatic bearing principle, regardless of the manufacturing method.

- It has been demonstrated that oil (low viscosity) lubrication is suitable for porous-ceramic hydrostatic bearings.

- The dimensionless flow rate Vs bearing feeding number relationship, proposed in porous hydrostatic journal bearing theoretical models, and verified in previous research, correlates very well with the results obtained in the present research.

- In direct comparison with a 5-recess hydrostatic bearing of the same dimensions, under identical performance testing conditions, a porous-ceramic bearing produced in present research project demonstrated:

- 95 % higher static stiffness. Resulting from a more uniform hydrostatic pressure distribution and near optimum permeability value.

- 175 % higher rotational stiffness (at 4000 rpm). Resulting from an optimized hydrodynamic effect, due to the absence of pockets.

- 64 % lower pumping power requirement. Resulting from lower flow rate, due to the near to optimum permeability value.

- 50 % lower lubricant temperature rise (at 4000 rpm). Resulting from a less intricate in and out lubricant flow, due to the absence of pockets and a simpler feeding hydraulic circuit.

The effects of water lubrication in porous-ceramic bearing systems

Corrosion

- Corrosion in conventional machine-tool construction materials such as cast irons & alloy tool steels can be effectively counterattacked and prevented by adding conventional aqueous metal-working fluids as well as corrosion galvanic inhibitors to the lubricating water.

- The effects of intermittent exposure to corrosive environments effects on cast iron can be successfully prevented by a low cost coating (tufftride).

Foaming and air release characteristics

- Standard ASTM procedures for foaming and air release properties indicated that the foaming and air release properties of all inhibitors examined, as well as oil HP0, were satisfactory and non-measurable, respectively. However, a custom more realistic test demonstrated than foam and air entrainment, did in fact occur for both water based lubricants and oil. In this sense, the need for the development of new standard test for foaming and air release properties for low viscosity lubricants, under dynamic lubricant flow conditions is noted.

- The main factor causing the formation of foam and air entrainment in an operational porous-ceramic spindle system proved to be the bearing-housing air pressurized seals. A second cause was the spindle rotational speed. In this sense, the levels of foaming and air entrainment should be restricted to an extend that it will not affect the performance of the bearing at the operational spindle speeds, and beyond, to a level that should be established

Microbial growth

The proliferation of bacterial colonies on both plain water and aqueous metal-working fluids, proved to alter significantly the porous bearing performance by pore blockage. Because of the obvious abundance of water in a water-based lubricated spindle system, preventing the proliferation of bacterial colonies is a complicated matter, requiring the implementation of monitoring and preventive maintenance routines. In this sense, water and water based lubrication of porous-ceramic bearing systems should be restricted to applications where the cost-benefit of such stringent programmes is justified.

7 Suggestions for future work

As with the conclusions of this work, the suggestions for future work are arranged under similar headings.

Materials processing/Manufacture of porous-ceramic hydrostatic bearings

- The further optimization of SC processing parameters. Current ball-milling and furnace processing times (24 and 44 h, respectively), are relatively long times. Further studies should be conducted to determine if these operations can be simplified. In addition, the ceramic/starch slip solids-loading and its effect on the bearings properties should be further studied to determine optimized processing conditions.

- The SC consolidation bearing processing technology transference from the laboratory to industry manufacturing needs to be addressed. The effects of larger powder batches and multiple sintering operations require quantification in terms of bearing properties. Alternatively, the implementation of starches into mass production ceramic techniques, such as injection moulding and extrusion, in order to control the ceramic body porosity

SC porous ceramic bearing performance

- Static stiffness performance testing for SC aerostatic thrust bearings. So far, only journal bearings (50 mm ID) have been tested.

- Dynamic and stability characteristics testing of porous ceramic journal bearings. This requires the current test rig upgrading and the developing of a porous-ceramic journal bearing testing programme.

- A more comprehensive set of performance data needs to be obtained, in order to provide commercial data for general publication.

References

[1] Slocum AH. Precision machine design. New Jersey: Prentice-Hall, 1998.

[2] Weck M., McKeown P., Bonse R., Herbst U. Reduction and compensation of thermal errors in machine tools. *Annals of CIRP* 1995; 44(2):589-98.

[3] Almond RJ. The development of a porous ceramic water hydrostatic bearing for ultra high precision applications. PhD theses. Cranfield, U.K.: Cranfield University, 1999.

[4] Kumar A., Rao N.S. Stability of a rigid rotor in turbulent hybrid porous journal bearings. *Tribology international* 1994; 27 no. 5:299-305.

[5] IMTR-Manufacturing process & equipment workshop group. Integrated manufacturing technology road-mapping project report- *Manufacturing process & equipment.* http://imtr.ornl.gov (June 2000). Oak Ridge, Tennessee: Integrated manufacturing technology road-mapping initiative (IMTR), 1999.

[6] Taniguchi N. The state of the art of nanotechnology for processing of ultra precision and ultrafine products. *Precision engineering* 1994; 16(1):5-24.

[7] Subramanian K, Hitchiner M, Redington P, Gobain S. Grinding is well and alive. *Manufacturing engineering* 2002; 128(5):91-7.

[8] Shore P. Fixed abrasive machining grinding processes. McKeown P.A., editor. An introduction to precision engineering-Lecture notes for MT1 lecture. Cranfield, U.K.

[9] Salmon SC. Justifying creep-feed grinding and assesing creep-feed machine tool design . 26th. abrasive engineering society conference, the new growth in abrasives. 20-25. 1988.

[10] Mckweon P, Carlisle K. Revolutionary machining of revolutionary materials. Autotech 1995. 41-54. IMechE.

[11] Shore P. ELID for efficient grinding of supersmooth surfaces . *Industrial diamond review* 1993; 6(93):318-22.

[12] Corbett J. Precision machine tools and nanotechnology . ESPRC 1st. International conference on responsive manufacture. 143-154.

[13] Durazo I. S. Development of porous ceramic hydrostatic bearings- 9-month report. Cranfield, U.K.: Cranfield University, 2000.

[14] Weck M, Koch A. Spindle-bearing systems for high speed applications in machine tools. *Annals of CIRP* 1996; 45(1):445-8.

[15] Anon. Speed and power-Editorial note. Machinery market . 29 March 2001. U.K.

[16] Dowson D. History of tribology. 2nd edn. London: IMechE, 1998.

[17] Childs P.R.N. Mechanical design. Great Britain: Arnold, 1998.

[18] Weck M, Luderich J, Wieners M. Influence of aerostatic, hydrostatic and rolling element spindles and guideways on the machining accuracy. Weck M, Kunzmann H, editors. Proceeding of the 3rd international conference on ultraprecision in manufacturing engineering. Aachen, Germany. May 1994. 94-100.

[19] Cundill R. Light-weight material for the rolling elements of aircraft bearings. *Ball bearing Journal* 1983; 216.

[20] Robinson E.Y. Silicon nitride hybrid bearing fatigue life comparisons. *NASA 19990316062-Aerospace report TR-99(8565)-1* 1999.

[21] Powell J.W. Design of aerostatic bearings. *The machinery publishing co. Ltd.*

[22] Stout K.J., Rowe W.B. Externally pressurized bearings design for manufacture. Part 1 Journal bearing selection. *Tribology international.* 1974; 7, no.3:98-106.

[23] Stout K.J., Rowe W.B. Externally pressurized bearings design for manufacture. Part 2:

design of gas bearings. *Tribology international.* 1974; 7, no.4:169-79.

[24] Sheinberg S.A., Shuster V.G. Resistance to vibrations of a hydrostatic thrust bearing. *Machines and tooling* 1960; 31 no. 11:24-9.

[25] Muskat M. The flow of homogeneous fluids through porous media. Ann Arbor, Michigan: J.W. Edwards, Inc., 1946.

[26] Sneck H.J. A survey of gas-lubricated porous bearings. *Journal of the lubrication technology* 1968;804-9.

[27] Majumdar B.C. Gas lubricated porous bearings: a bibliography. *Wear* 1976; 36:269-73.

[28] Kwan Y.B.P., Corbett J. Porous aerostatic bearings: an updated review. *Wear* 1998; 222:69-73.

[29] Kilmister G.T.F. The use of porous materials in externally pressurised gas bearings. *Powder metallurgy* 1969; 12 no.24:400-9.

[30] Kwan Y.B.P. Processing and fluid flow characteristics of hot isostatically pressed porous alumina for aerostatic bearing applications. PhD thesis. Cranfield U.K.: Cranfield University, 1996.

[31] Roach C.J. Development of porous ceramic air bearings. PhD thesis. Cranfield U.K.: Cranfield University, 2001.

[32] Khonsari M.M., Booser E.R. Applied tribology: bearing desing and lubrication. New York : John Wiley & Sons., 2001.

[33] Summers-Smith J.D. Plain bearings-problems and failures. IMechE seminar publication. Fluid film bearings, recent advances in design and performance. 77-103. IMechE, 2000.

[34] Reynolds O. On the theory of lubrication and its application to Mr. B. Tower's experiments, including an experimental determination of the viscosity of olive oil. *Philosophical*

transactions of the royal society 1886; 177, part 1:157-234.

[35] Tower B. First report on friction experiments. *Inst. Mech. Engs.* 1883;632-59.

[36] SKF-Revolve. www.revolve.com/applications. March 2003.

[37] Stansfield F.M. Hydrostatic bearings. Brighton, UK.: The machinery publishing co. ltd., 1970.

[38] Cameron A. The principles of lubrication. London G.B.: Longmans Green and Co. LTD, 1966.

[39] Morgan V.T., Cameron M. Mechanism of lubrication in porous metal bearings. Proceedings of the 1957 conference on lubrication and wear. 151-157. IMechE.

[40] Murti P.R.K. Hydrodynamic lubrication of short porous bearings. *Wear* 1972; 19:17-25.

[41] Conry T.F., Cusano C. On the stability of porous journal bearing. *Journal of engineering for industry.* 1974;585-90.

[42] Cusano C., Phelan R.M. Experimental investigation of porous bronze bearings. *Journal of lubrication technology.* 1973;173-80.

[43] Braun A.L. Porous bearings. *Tribology international* 1982;235-42.

[44] Morgan V.T. Tribology in powder metallurgy-conference report. *Tribology* 1970;111-2.

[45] Howarth R.B. Optimum performance of externally pressurized porous thrust bearings. *ASLE transactions* 1974, 17 no.2:127-33.

[46] Howarth R.B. Externally pressurized porous thrust bearing. *ASLE transactions* 1976, 19 no.4:293-300.

[47] Majumdar B.C., Rao N.S. On the analytical solution of hydrostatic oil porous journal bearings . Proceedings of the national conference on Indian tribology . 1, 70-80. 1979.

[48] Chattopadhyay A.K., Majumdar B.C. Steady state solution of finite hydrostatic porous oil journal bearings with tangential velocity slip. *Tribology international* 1984; 17 no. 6:317-23.

[49] Beavers G.S., Joseph D.D. Boundary conditions at a naturally permeable wall. *J Fluid Mech.* 1967; 30 part 1:197-207.

[50] Chattopadhyay A.K., Majumdar B.C. Dynamic characteristics of finite hydrostatic porous oil bearings considering tangential velocity slip. 1984.

[51] Chattopadhyay A.K., Majumdar B.C., Rao N.S. Stability of a rigid rotor in finite externally pressurized oil journal bearing with slip. *Journal of tribology* 1987; 109:301-6.

[52] Kumar A., Rao N.S. Turbulent hybrid journal bearings with porous bush: a steady state performance. *Wear* 1992; 152:23-35.

[53] Stephenson D.J., Alcock J.R., Corbett J. Ceramic injection moulding for porous ceramic bearing applications. *Cranfield University research proposal* Unpublished.

[54] Sheppard L.M. Fabrication of ceramics: the challenge continues. *Ceramic bulletin.* 1989; 68, no.10:1815-20.

[55] Kriegesmann J. Fundamentals of ceramic engineering. Processing of advanced bulk ceramics materials. Essex, UK.: Elsevier Science Publishers., 1991.

[56] Kyung H.K., Seong J.C, Kyung J.Y. Centrifugal casting of large alumina tubes. *The American ceramic bulletin.* Nov. 2000;54-6.

[57] ASM. Engineering materials handbook vol.4: ceramic and glasses. U.S.A.: ASM International, 1991.

[58] Nanko M., Ishizaki K., Takata A. Sintering of porous materials by a capsule free HIP process. Ceramics transactions vol. 31- Porous materials. Niigata, Japan. 28-29 September 1992. 1993. The American ceramic society.

[59] Takata A., Ishizaki K., Okada S. Improvement of a porous material mechanical property by hot isostatic process. Materials research society symposium proceedings vol. 207-Mechanical properties of porous and cellular materials. Boston, U.S.A. 26-27 November 1990 . U.S.A., Materials research society.

[60] Maziarz J.L., Isaacs J.A. Economic assessment of HIPed powder processing and conventional processes. 2001 International conference on powder metallurgy and particulate materials. New Orleans, LA. 13-17 May 2001. 50-63.

[61] Mashl S.J., Hebeisen J.C., Hjorth C.G. Producing large p/m near-net shapes using hot isoststic pressing. *JOM* 1999;29-31.

[62] Rahaman M.N. Ceramic processing and sintering. U.S.A: Marcel Dekker, Inc., 1995.

[63] Reed J. S. Principles of ceramics processing. 2nd. edn. U.S.A.: John Wiley & Sons, 1995.

[64] ASM. Source book on heat treating -1 Materials and processes . U.S.A.: American society for metals, 1975.

[65] Benbow J.J., Lawson T.A., Oxley E. W., Bridgwater J. Prediction of paste extrusion pressure. *Ceramic bulletin* 1989; 68, no.10:1821-4.

[66] De Jong R., Visser H.H. Ceramic membranes for industrial applications. 3rd European ceramic society conference. 663-668.

[67] Terpstra R., Pex P.P.A.C., De Vries A.H. Ceramic processing. Great Britain: Chapman & Hall, 1995.

[68] Saggio- Woyansky J., Scott C.E., Minnear W.P. Processing of porous ceramics. *American ceramic society bulletin.* 1992; 71, no.11:1674-82.

[69] Sepulveda P. Gelcasting foams for porous ceramics. *The American ceramic society bulletin* 1997; 76, no. 10:61-5.

[70] Lyckfeldt O, Ferreira J.M.F. Processing of porous ceramics by starch consolidation. *Journal of the European ceramic society.* 1998; 18:131-40.

[71] Omatete O.O., Janney M.A., Nunn S.D. Gelcasting: from laboratory development towards industrial production. *Journal of the European ceramic society.* 1997; 17:407-13.

[72] Janney M.A., Omatete O.O., Wall C.A. *et al.* Development of low toxicity gel-casting systems. *Journal of the american ceramics society.* 1998; 81, no.3:581-91.

[73] Gauckler L.J., Graule T.J., Baader F.H., Will J. Enzime catalysis of alumina forming. *Key engineering materials.* 1999; 159-160:135-50.

[74] Kosmac T., Novack S., Sajko M. Hydrolysis assisted solidification (HAS): a new setting concept for ceramic net shaping. *Journal of the European ceramic society.* 1997; 17:427-32.

[75] Rak Z.S. Advanced shaping techniques in advanced ceramics. *Ceramic forum int/ber.* 2000; 77 no.6:6-16.

[76] Bonekamp B.C., Schoute M.J., Goris M.J.A.A. Pore properties of ceramics porous media prepared by slip casting of starch filled a-alumina suspensions. *Euro-ceramics.* 1989; 1:223-7.

[77] Lyckfeldt O., Liden E., Carlsson R. Processing of thermal insulation materials with controlled porosity. Ceramic transactions vol. 52- low expansion materials symposium. Indianapolis 25-27 April 1994. 1994. the American ceramic society.

[78] Costa A.C., Santana L., Madeiros V.M., Costa R.V. Influéncia de alguns ligantes sobre a porosidade de corpos de alumina compactados por prensagem á seco. *Ceramica* 1996; 42 no.278:829-32.

[79] Brant J., Carlström E., Kristoffersson A., Lyckfeldt O., Lindsten G. Forming ceramics with biopolymers. Ceramic processing '97. Ceramic processing science.

[80] Lyckfeld O. Novel water-based shaped of ceramics. 6th Conference & Exhibit of the

european ceramic society. Brighton, UK. 20-24 June 1999. 219-221.

[81] Bowden M.E., Rippey M.S. Porous ceramics formed using starch consolidation.

[82] Pabst W., Tynova E., Mikac J., Gregorova J., Havrda J. A model for the body formation in starch consolidation casting. *Materials science letters* 2002; 21:1101-3.

[83] Tynova E., Pabst W., Gregorova E., Havrda J. Starch consolidation casting of alumina ceramics- body formation and microestructural characterization. Key Engineering materials. 206-213, 1969-1972. 2002.

[84] Alves H.M, Tari G., Fonseca A. T., Ferreira J.M.F. Processing of porous cordierite bodies by starch consolidation. *Materials research bulletin* 1998; 33(10):1439-48.

[85] Lemos A. F., Ferreira J.M.F. Porous bioactive calcium carbonate implants processed by starch consolidation. *Materials science and engineering c* 2000; 11:35-40.

[86] Vasconcelos P.V. Permeability of diatomite layers processed by different colloidal techniques.

[87] British standards institution. Powder metallurgical materials and products. Part 3. Methods of testing sintered metal materials-Determination of fluid permeability. BS 5600:Part 3: Section 3.6: 1988(ISO 4022: 1987).

[88] Lemmens J.W. Operating instructions for the Grindosonic MK5 industrial instrument. *Grindosonic machine manual.*

[89] The American society for testing and materials. Standard test method for drying and firing shrinkages of ceramic whiteware clays. Designation: C 326-82 .

[90] British standards institution. Sintered metal materials, excluding hardmetals- permeable sintered metal materials- determination of density, oil content and open porosity. BS EN ISO 2738:2000:1-9.

[91] Cliffel E. M., Smith W.E., Schwope A.D. Theory and appliations of controlled permeability. *Modern developments in powder metallurgy* 1966; 3:114-28.

[92] Dullien F. A. L., Batra V.K. Determination of the structure of porous media. Flow through porous media symposium. 62 no.10, 25-53. Oct. 1970.

[93] Robens E., Unger K.K., Kumar D. Survey on porosity determining methods. *Powder & bulk magazine. TIZ international.* 1991; 115, no. 9:352-7.

[94] Scheidegger A. F. The physics of flow through porous media. Great Britain: University of Toronto Press, 1957.

[95] Clemens J.F., Vyse J. A comparison of methods od measuring pore-size distribution in refractories. *Transactions of the british ceramic society.* 1968; 67, no.7:285-317.

[96] British standards institution. Permeable sintered metal materials- determination of bubble test pore size. BS EN 24003:1993(ISO 4003: 1977).

[97] Gelinas C., Angers R. Improvement of the dynamic water expulsion method for pore size distribution measurements. 1968; 65, no. 9:1297-300.

[98] Richardson. Modern ceramic engineering: properties, processing and use in design. 2nd edn. New York: Marcel Dekker, 1992.

[99] Munz D., Fett T. Ceramics-Mechanical properties, failure behaviour, materials selection. Germany: Springer, 1999.

[100] Morrell R. Selection of equations for elastic modulus measurement of advanced technical ceramics using resonant and impulse excitation methods-NPL report DMM (A) 62. The National Physical Laboratory, 1992.

[101] Davis W. R. Measurement of the elastic constants of ceramics by resonant frequency methods. *Transactions of the British ceremic society* 1968; 67:515-41.

[102] Yu CJ, Henry R.J., Prucher T., Parthasarathi S., Jo J. Resonant frequency measurements for the determination of elastic properties of powder metallurgy components. Powder metallurgy congress. San Francisco CA. 21-26 June 1992. 319-332.

[103] Hendrix M, De With G., Morrell L. *et al.* Young's modulus of ceramic materials-an intercomparision of methods. Sixth conference and exhibition of the European ceramic society. Brighton, UK. 20-24 June 1999. 565-566.

[104] Lemmens J.W. Impulse excitation: a technique for dynamic modulus measurement. Dynamic modulus measurement . 1990, American society for testing and materials.

[105] Chang L.S., Chuang W.J., Wei W.J. Characterization of alumina ceramics by ultrasonic testing. *Materials Characterization* 2000; 45:221-6.

[106] Lemmens J.W. EMOD Version 9.17. Program for elasticity modulus calculation. Users guide.:59-70.

[107] British standards institution. Methods for determination of density or relative density of petroleum or petroleum products (pyknometer method). BS 4699.

[108] British standards institution . Methods for determination of the viscosity of liquids. BS 188: 1977:1-14.

[109] Institute of petroleum (IP). Water mix metal working fluid corrosion of cast iron. Test method IP 125/82.

[110] Menke J. Corrosion of steel surfaces on machining equipment. Corrosion 98- National association of corrosion engineers conference. Issue 601, 1-17.

[111] The American society for testing and materials. Standard practice for operating salt spray (fog) testing apparatus. Designation B 117- 94.

[112] NACE international standard test method. Laboratory corrosion testing of metals. TMO 169-95.

[113] Fontana MG. Corrosion engineering. 3 edn. Singapore: McGraw-Hill international editions, 1987.

[114] British standards institution. Flake graphite cast iron. BS 1452: 1990.

[115] Box G.E.P., Hunter W.G., Hunter J.S. Statistics for experimenters- An introduction to design, data analysis, and model building. U.S.A.: John Wiley & sons, 1976.

[116] Claxton P.D. .Aeration of petroleum based steam turbine oils. *Tribology* 1972;8-13.

[117] Fowle T.I. Aeration in lubricating oils. *Tribology international* 1981; 14(3):151-7.

[118] The American society for testing and materials. Standard test method for foaming characteristics of lubricating oils. designation D 892-97.

[119] The American society for testing and materials. Standard test method for air release properties of petroleum oils. D 3427-96.

[120] McGeary R.K. Mechanical packing of spherical particles. *Journal of the American ceramic society* 1961; 44(10):513-22.

[121] German R. M. Powder metallurgy science. Princeton, New Jersey: Metal powder industries federation , 1984.

[122] Robinson A.T. Permeability of tungsten matrices as a function of density, particle size and shape. *Transactions of the ASM* 1964; 57:650-7.

[123] German R.M. Porosity and particle size effects on the flow characteristics of porous metals. *Powder Technology* 1981; 30:81-6.

[124] The American society for testing materials. Apparent porosity, water absorption, apparent specific gravity, and bulk density of burned refractory brick and shapes by boiling water. C20-87.

[125] Greskovich C., Lay K.W. Grain growth in very porous $Al_2 O_3$ compacts. *The American*

ceramic society 1972; 55 no.3:142-6.

[126] Gassner R.H. Resonant frequency testing. Eight international symposium on non-destructive characterization of material. 277-284. 1998. Plenum press.

[127] Allison R.J. Non-destructive determination of Young's modulus and its relationship with compressive strength, porosity and density. *Deformation of sediments and sedimentary rocks-Geological society special publication* 1987;(29):63-9.

[128] Oberg E., Jones F.D., Horton H.L., Ryffel H.H. Machinery's handbook 25. 25 edn. U.S.A.: Industrial press, 1914.

[129] Duckworth W. Discussion of the Ryshkewitch. *Journal of the American ceramic society* 1953; 36(2):68.

[130] Spriggs R.M. Expression for effect of porosity on elastic modulus of polycrystalline refractory materials, particularly aluminium oxide. *Journal of the American ceramic society* 1961; 44(12):628-9.

[131] Wagh A.S., Poeppel R.B., Singh J.P. Open pore description of mechanical properties of ceramics. Journal of materials science 26, 3862-3868. 1991.

[132] Costa Oliveira FA, Fernandes J.J., Paiagua P., Guerra Rosa L. The influence of forming methods on the flexural strength of a porous cordierite-based ceramic. Galassi C., editor. Fourth euro-ceramics. Vol. 1, 389-396. Italy, Gruppo editoriale Faenza editrice. 1997.

[133] Stout K.J., Tawfik M. Externally pressurized bearings for systems leading to nanometer technology. *Scanning microscopy technologies and applications* 1988; 897:144-53.

[134] Evans U.R. The rusting of iron: causes and control. Great Britain: Edward Arnold, 1972.

[135] Nemoto S., Kunihiko K., Kuribayashi T. *et al.* A study of oil engine aeration. *JSAE Review* 1997; 18:271-6.

[136] Tourret R., White N. Aeration and foaming in lubrication oil systems. *Aircraft engineering* 1952;122-37.

[137] Hayward A.T.J. How to keep air out of hydraulic circuits-A practical booklet for the engineer. Scotland: National engineering laboratory , 1963.

[138] Hill E.C. Microrganisms- Number, types, significance, detection. Chater K.W.A., Hill E.C., editors. Monitoring and maintenance of aqueous metal-working fluids. London U.K. April 1983. 97-112. 1984. Great Britain, John Wiley & sons.

[139] Lloyd G. Microbial monitoring services and corrective procedures for small users. Chater K.W.A., Hill E.C., editors. Monitoring and maintenance of aqueous metal-working fluids. London, U. K. April 1983. 141-146. 1984. Great Britain, John Wiley & sons.

[140] Gargiulo E.P., Gilmour P.W. A numerical solution for the design of externally pressurized porous gas bearings: thrust bearings. *Journal of lubrication technology- transactions of the ASME* 1968; October.

Appendix 1

Detail Drawings

DRAWING NO.	
MD 212 A601 A3	

ISSUE	MODIFICATION
A	.

ALL DIMENSIONS IN MILLIMETRES UNLESS OTHERWISE STATED

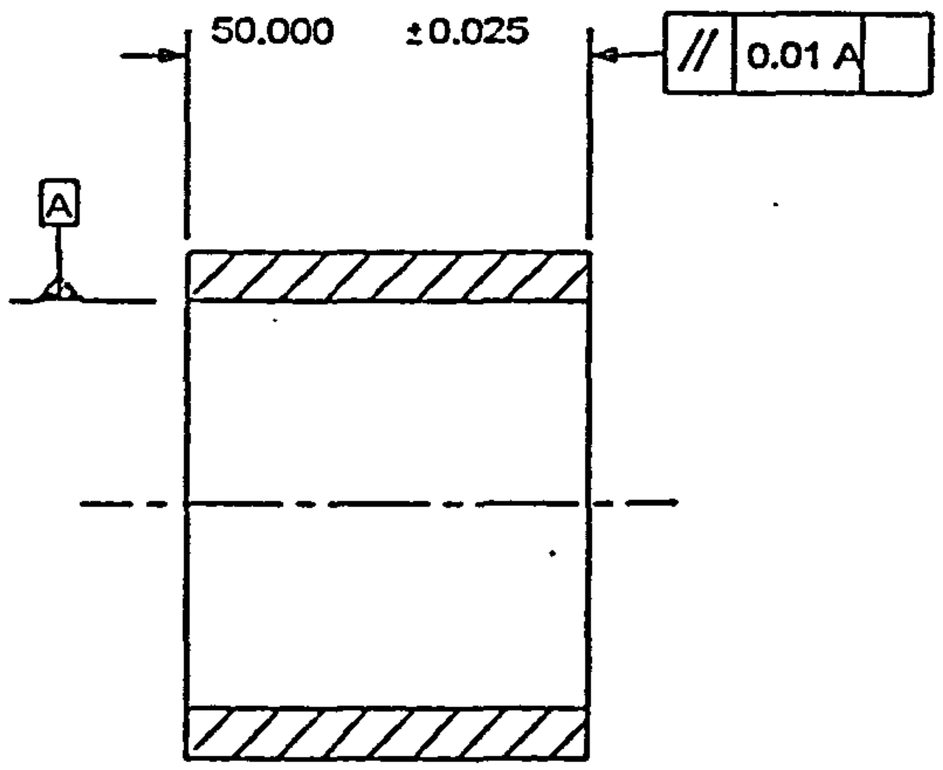

SECTION A-A

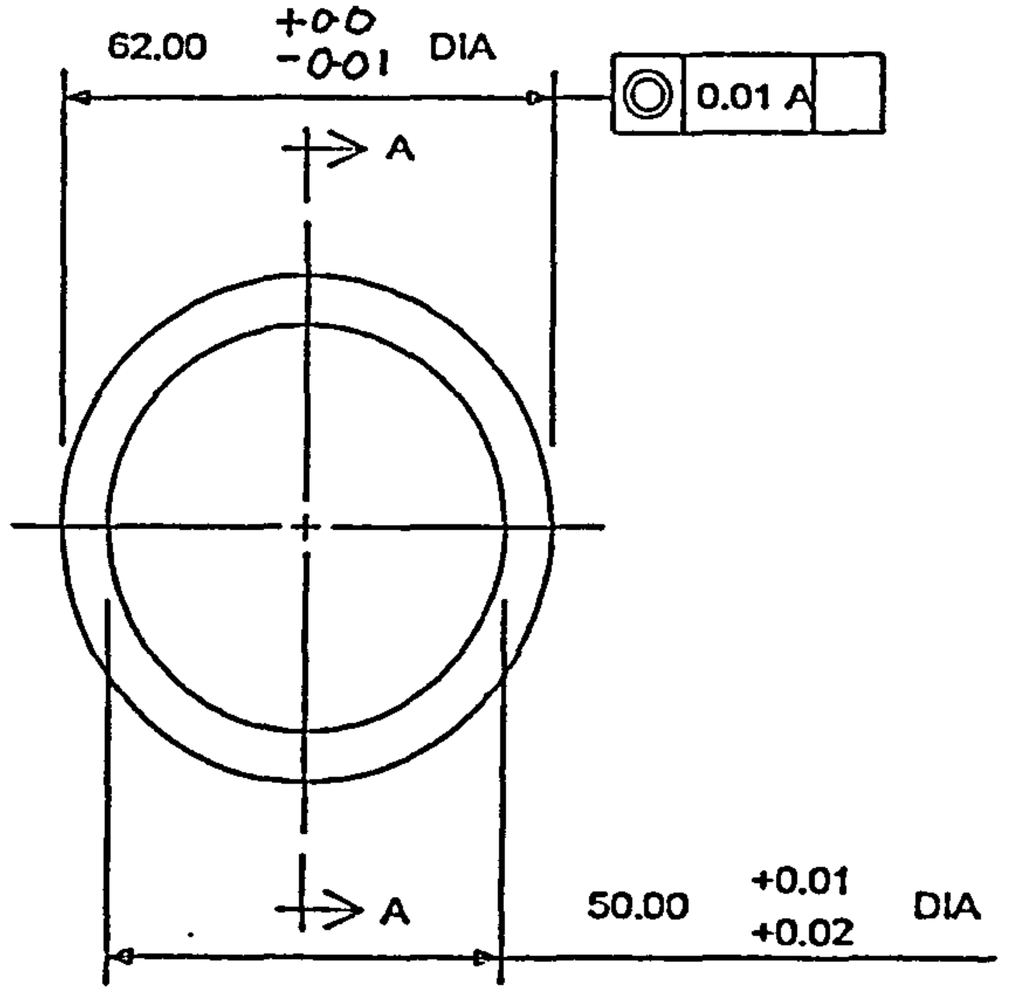

THIRD ANGLE PROJECTION

A 3

ITEM	PART NO.	DESCRIPTION	NO. OFF	MATL.	SPEC.	REMARKS
1	A601		1	ALUMINA		

GENERAL TOLERANCE ON DIMENSION	JOB NO.	NO. OF SETS REQD.	SCALE	DRAWN	CHKD	APPVD	
MACHINED			1/1				
UNMACHINED							
OTHER DIMENSION AS STATED			FINISH				
WELD WHERE SHOWN THUS ⌒ L							
MACHINE WHERE SHOWN THUS ✓	USED ON DRG.						

TITLE CERAMIC BEARING

ISSUED BY SCHOOL OF INDUSTRIAL & MANUFACTURING SCIENCE

CRANFIELD UNIVERSITY
CRANFIELD, BEDFORD, MK43 0AL.

DRAWING NO. MD 212 A601 A3

SHT. OF SHEETS

DRAWING No

ISSUE	MODIFICATION

ALL DIMENSIONS IN MILLIMETRES UNLESS OTHERWISE STATED. IF IN DOUBT ASK.

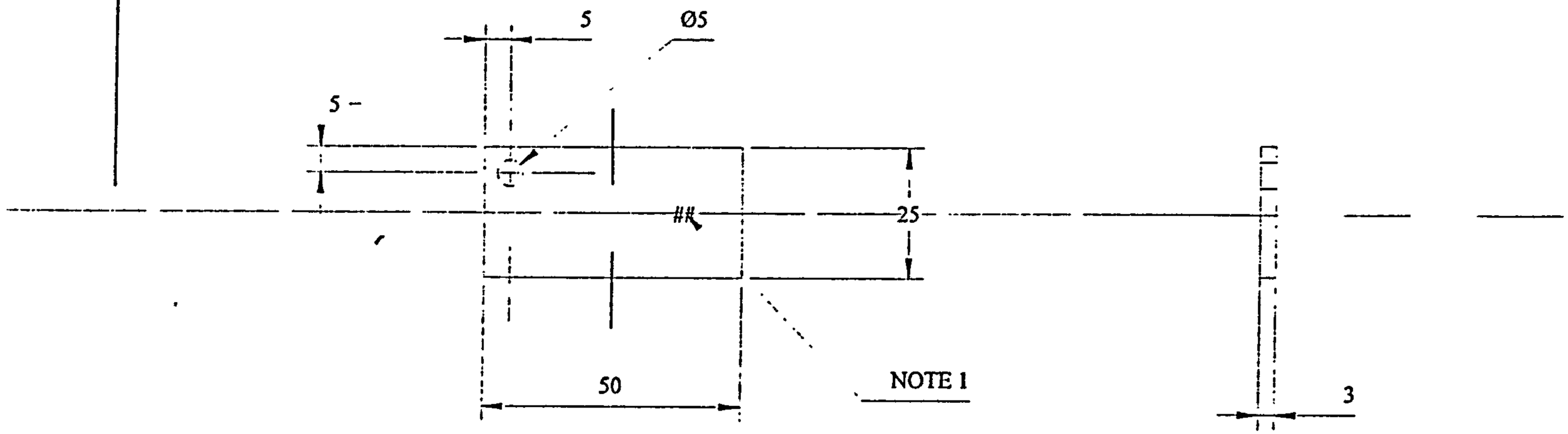

NOTE 1: STAMP CONSECUTIVE NUMBERS
NOTE 2:

THIRD ANGLE PROJECTION

SHEET SIZE A3
SCALE 1:1
FINISH

ITEM	PART No.	DESCRIPTION	No. OFF	MATL. (AS SUPPLIED)	SPEC.	REMARKS

GENERAL TOLERANCE ON DIMENSIONS MACHINED UNMACHINED OTHER DIMENSIONS AS STATED	JOB No.	No. OF SETS REQ.
WELD WHERE SHOWN THUS		
MACHINE WHERE SHOWN THUS		

DRAWN	CHK	DATE
I.S. DURAZO		14-06-00

TITLE:- CORROSION TEST COUPON

SCHOOL OF INDUSTRIAL & MANUFACTURING SCIENCE
CRANFIELD UNIVERSITY

DRAWING No.

SHT. 1 OF 1 SHEETS

1 2 3 4 5 6 7 8

DRAWING No.	
ISSUE	MODIFICATION

ALL DIMENSIONS IN MILLIMETRES UNLESS OTHERWISWE STATED. IF IN DOUBT ASK

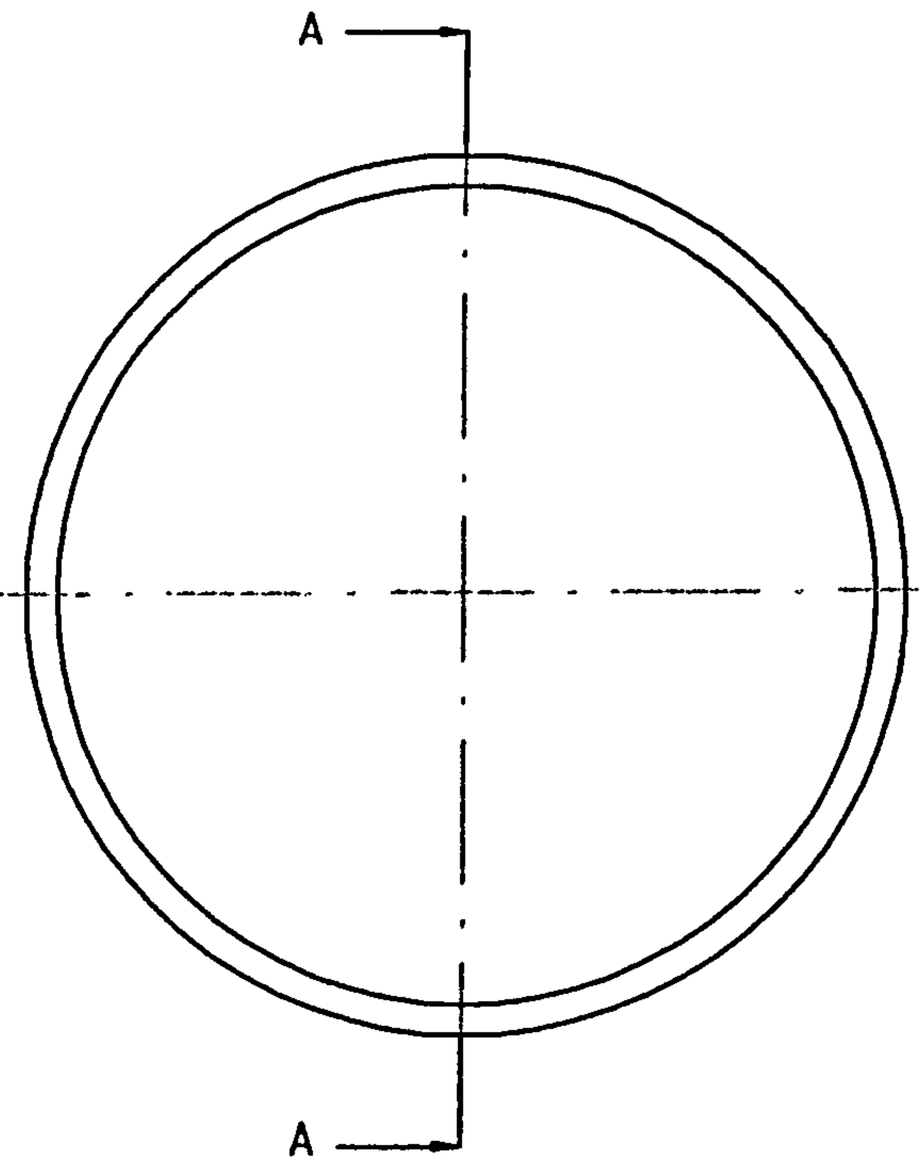

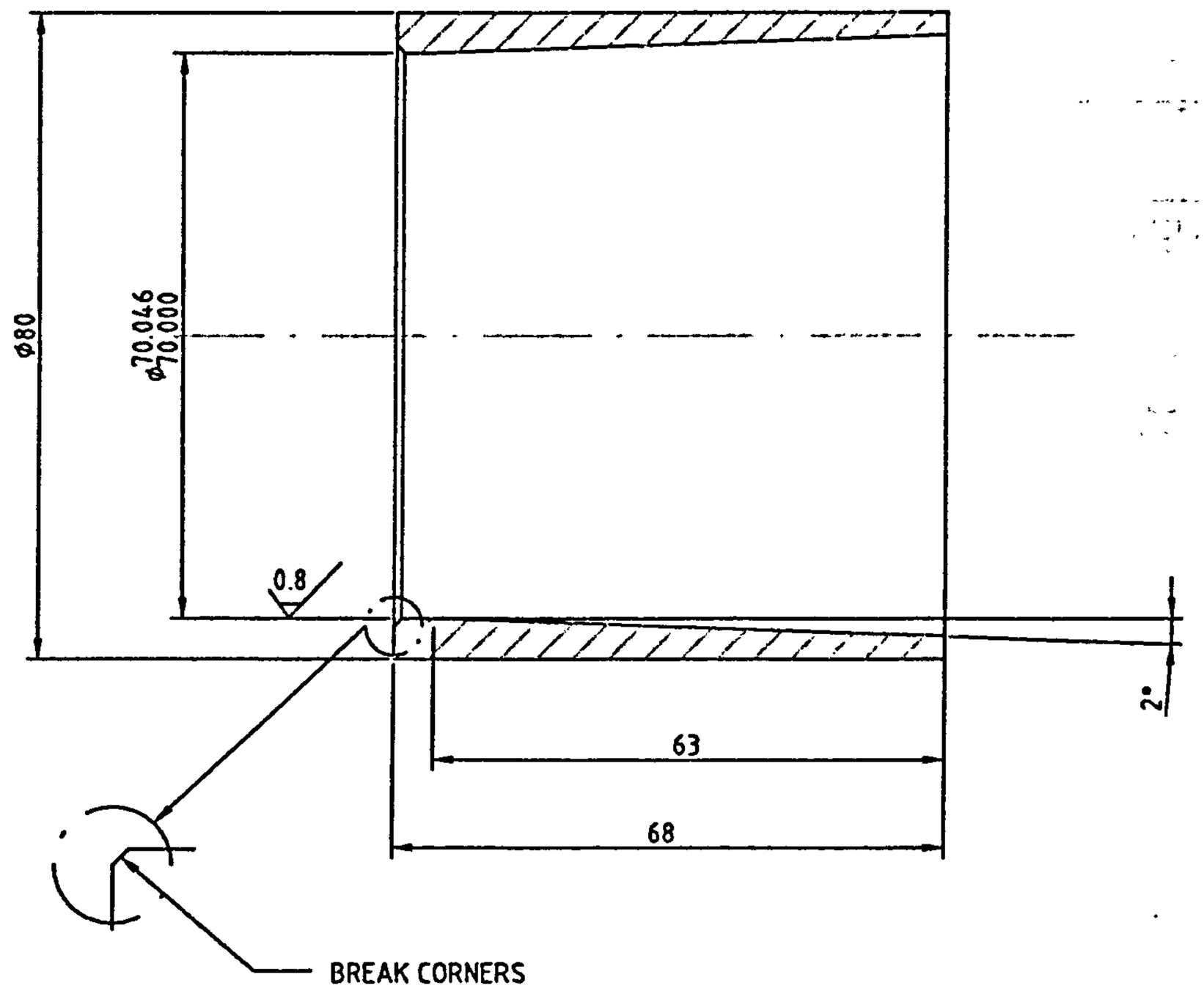

REMOVE ALL SHAPE EDGES

THIRD ANGLE PROJECTION	SHEET SIZE A4	ITEM	PART No.	DESCRIPTION	No. OFF	MATL.	SPEC.	REMARKS
						ALUM		

GENERAL TOLERANCE ON DIMENSIONS MACHINED UNMACHINED OTHER DIMENSIONS AS STATED	JOB No.	No. OF SETS REQ.	SCALE 1:1	DRAWN	CHK	DATE	TITLE: MOULD SLEEVE
				I.S. DURAZO		AUG 00	

FINISH	SCHOOL OF INDUSTRIAL AND MANUFACTURING SCIENCE CRANFIELD	DRAWING No.
		SHEET 1 OF 1 SHEETS

DRAWING No.	
ISSUE	MODIFICATION

ALL DIMENSIONS IN MILLIMETRES UNLESS OTHERWISWE STATED. IF IN DOUBT ASK

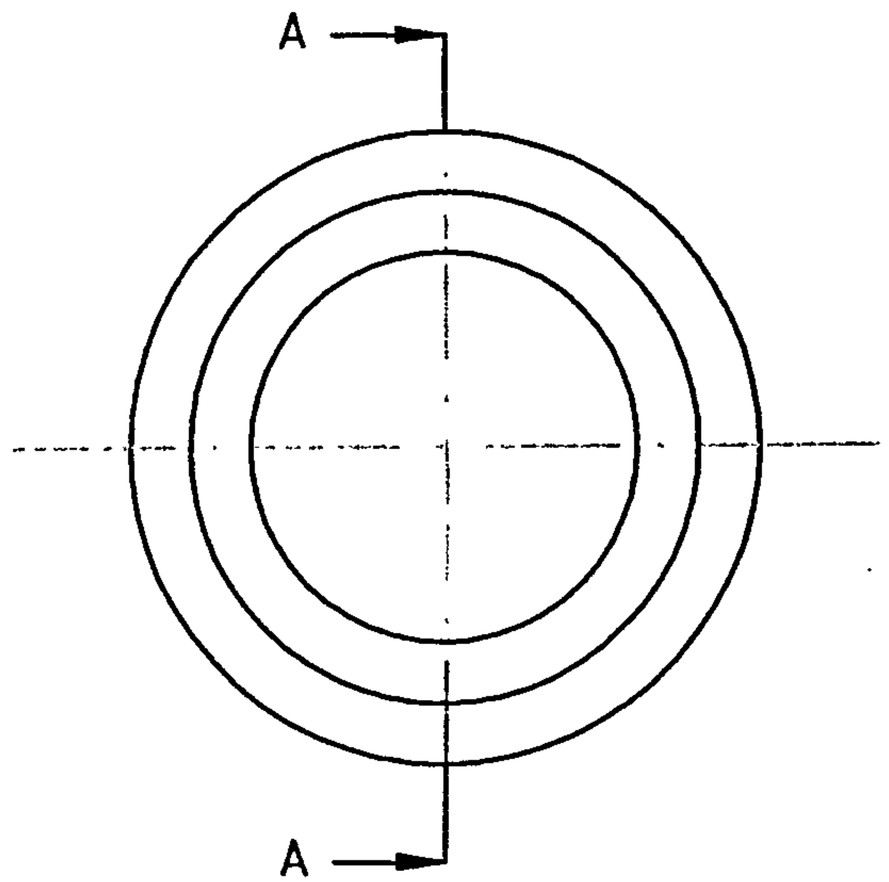

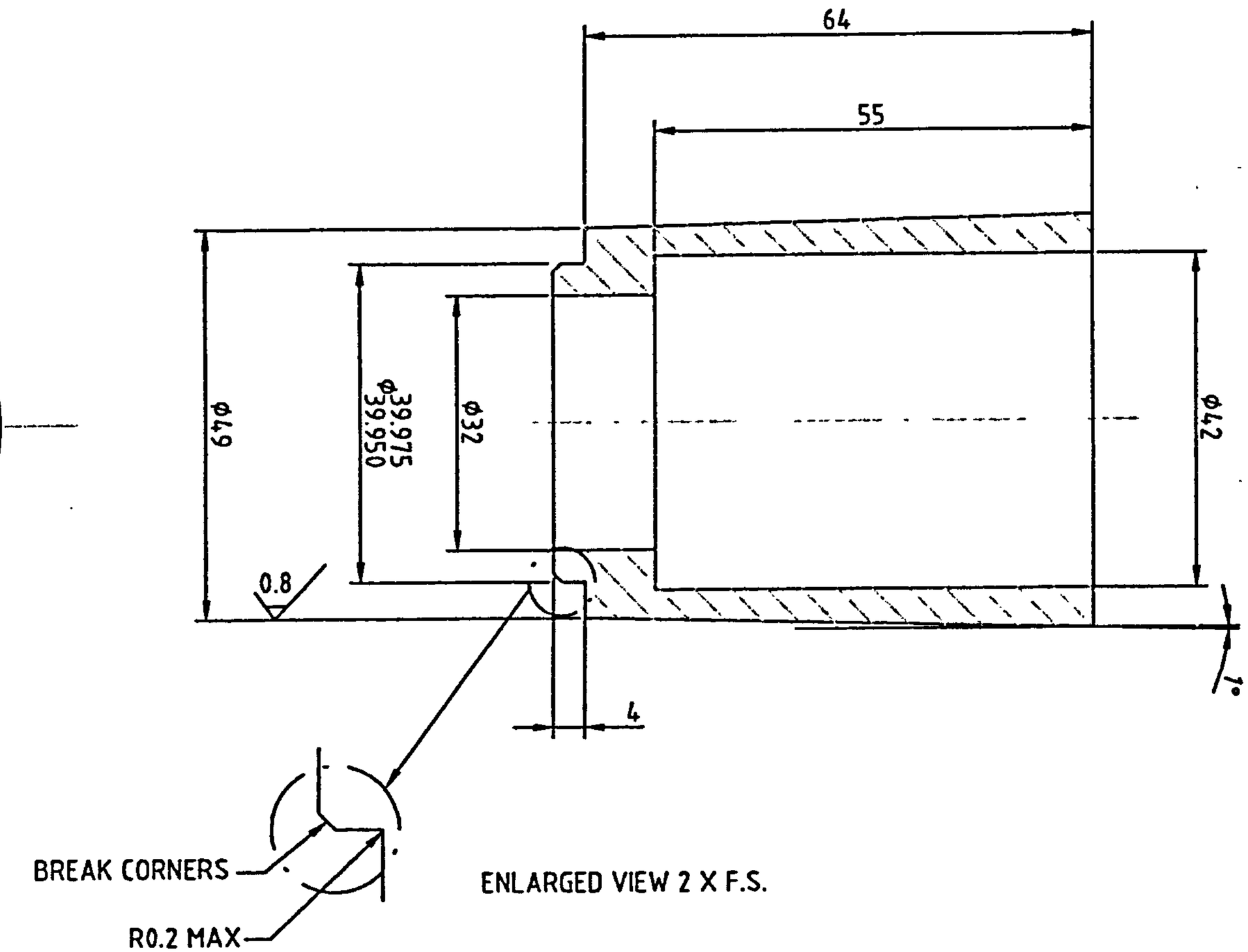

ENLARGED VIEW 2 X F.S.

REMOVE ALL SHAPE EDGES

THIRD ANGLE PROJECTION			SHEET SIZE A4	ITEM	PART No.	DESCRIPTION	No. OFF	ALUM MATL.	SPEC.	REMARKS
GENERAL TOLERANCE ON DIMENSIONS MACHINED UNMACHINED OTHER DIMENSIONS AS STATED	JOB No.	No. OF SETS REQ.	SCALE 1:1	DRAWN I.S. DURAZO	CHK	DATE AUG 00	TITLE: CORE			
			FINISH	SCHOOL OF INDUSTRIAL AND MANUFACTURING SCIENCE CRANFIELD			DRAWING No.			
							SHEET 1 OF 1 SHEETS			

DRAWING No.	
ISSUE	MODIFICATION

ALL DIMENSIONS IN MILLIMETRES UNLESS OTHERWISWE STATED. IF IN DOUBT ASK

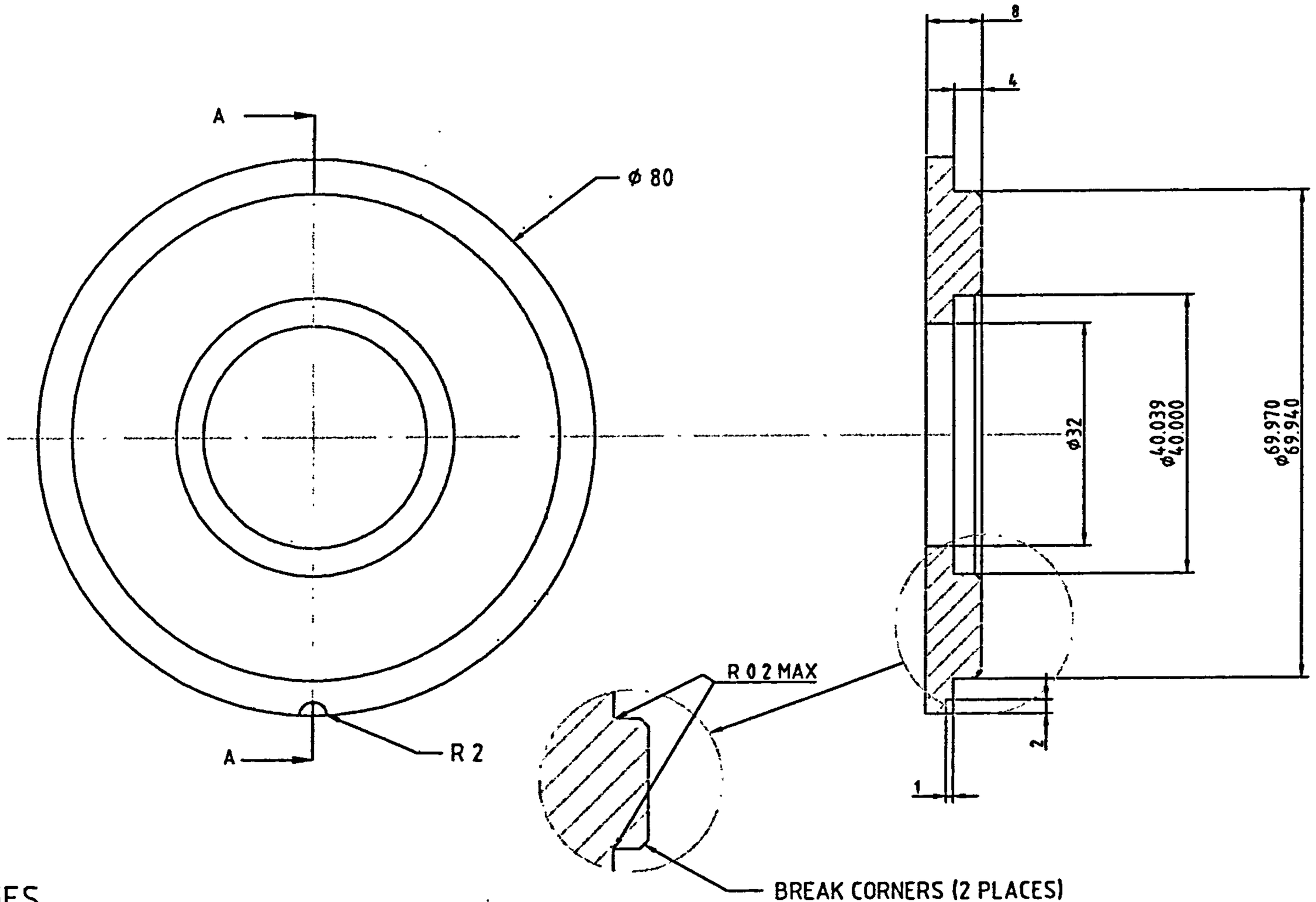

REMOVE ALL SHAPE EDGES

THIRD ANGLE PROJECTION	SHEET SIZE A4	ITEM	PART No.	DESCRIPTION	No. OFF	MATL.	SPEC.	REMARKS
						ALUM		

GENERAL TOLERANCE ON DIMENSIONS MACHINED UNMACHINED OTHER DIMENSIONS AS STATED	JOB No.	No. OF SETS REQ.	SCALE 1:1	DRAWN	CHK	DATE	TITLE: MOULD BASE
				I.S. DURAZO		AUG. 00	
			FINISH	SCHOOL OF INDUSTRIAL AND MANUFACTURING SCIENCE CRANFIELD			DRAWING No. SHEET 1 OF 1 SHEETS

DRAWING No.	
ISSUE	MODIFICATION

ALL DIMENSIONS IN MILLIMETRES UNLESS OTHERWISWE STATED. IF IN DOUBT ASK

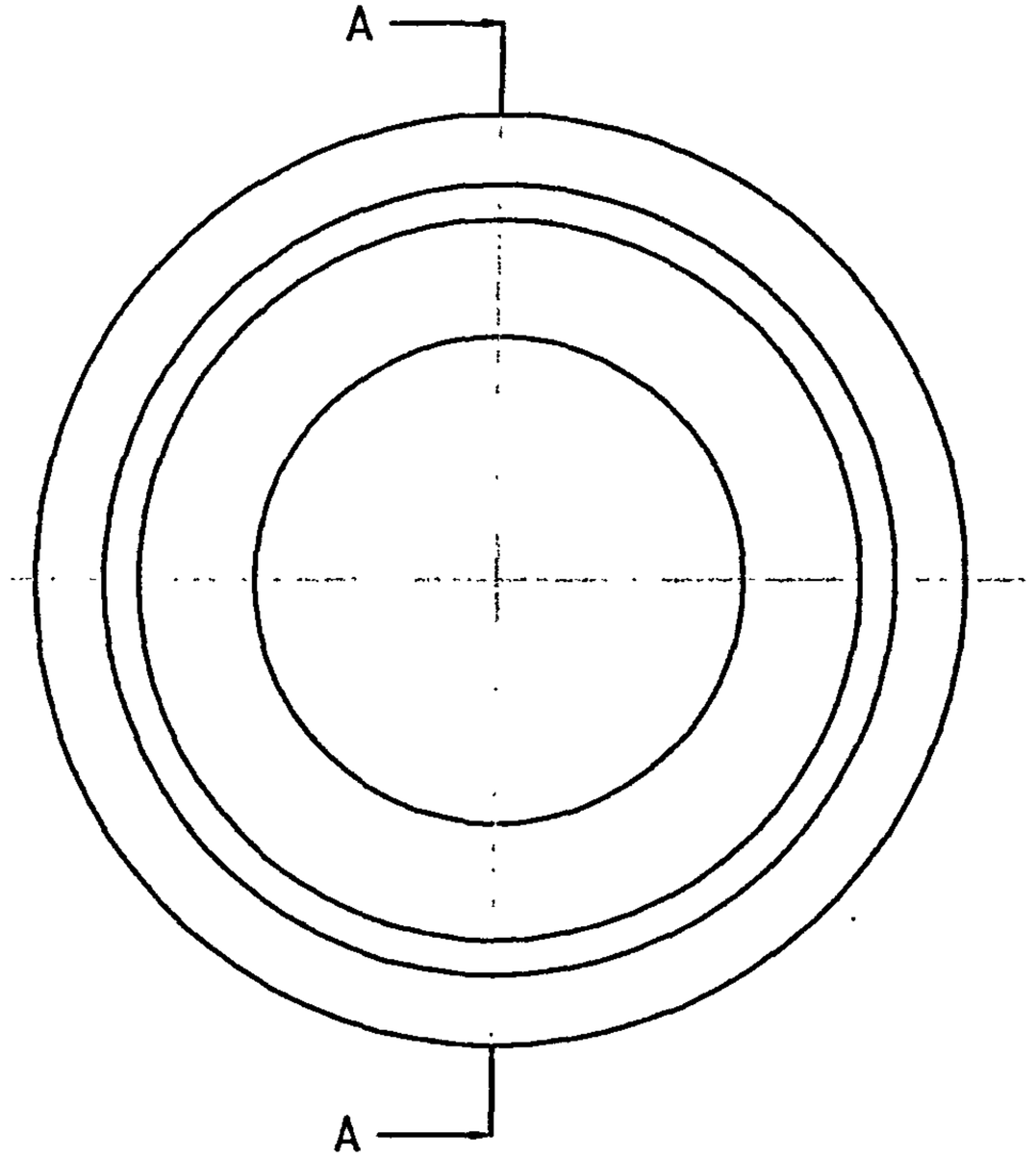

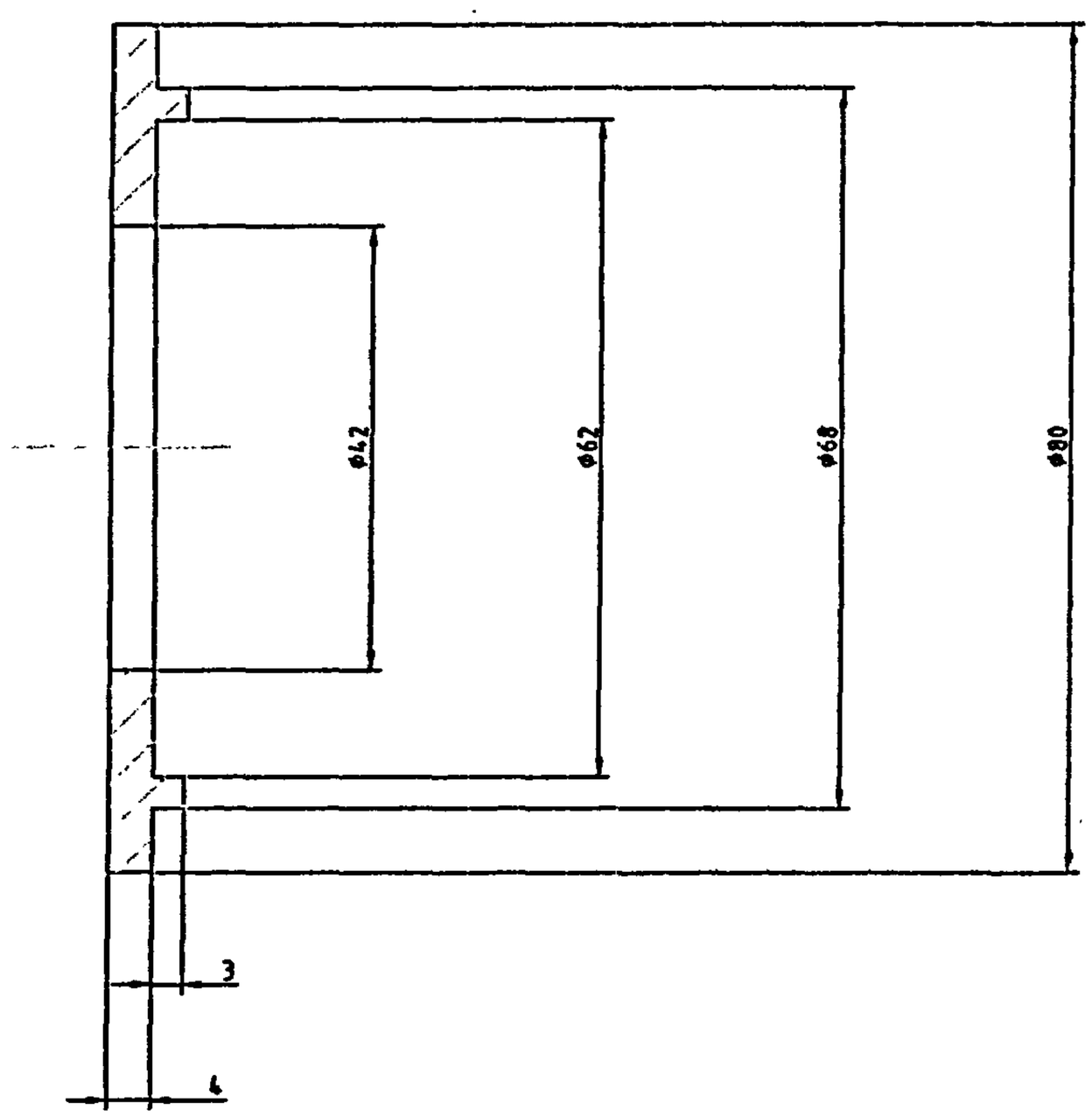

REMOVE ALL SHAPE EDGES

THIRD ANGLE PROJECTION			SHEET SIZE A4	ITEM	PART No.	DESCRIPTION	No. OFF	MATL.	SPEC.	REMARKS
								ALUM		
GENERAL TOLERANCE ON DIMENSIONS MACHINED UNMACHINED	JOB No.	No. OF SETS REQ.	SCALE 1:1	DRAWN	CHK	DATE	TITLE: MOULD LID			
				I.S. DURAZO		AUG 00				
OTHER DIMENSIONS AS STATED			FINISH	SCHOOL OF INDUSTRIAL AND MANUFACTURING SCIENCE CRANFIELD			DRAWING No.			
							SHEET 1 OF 1 SHEETS			

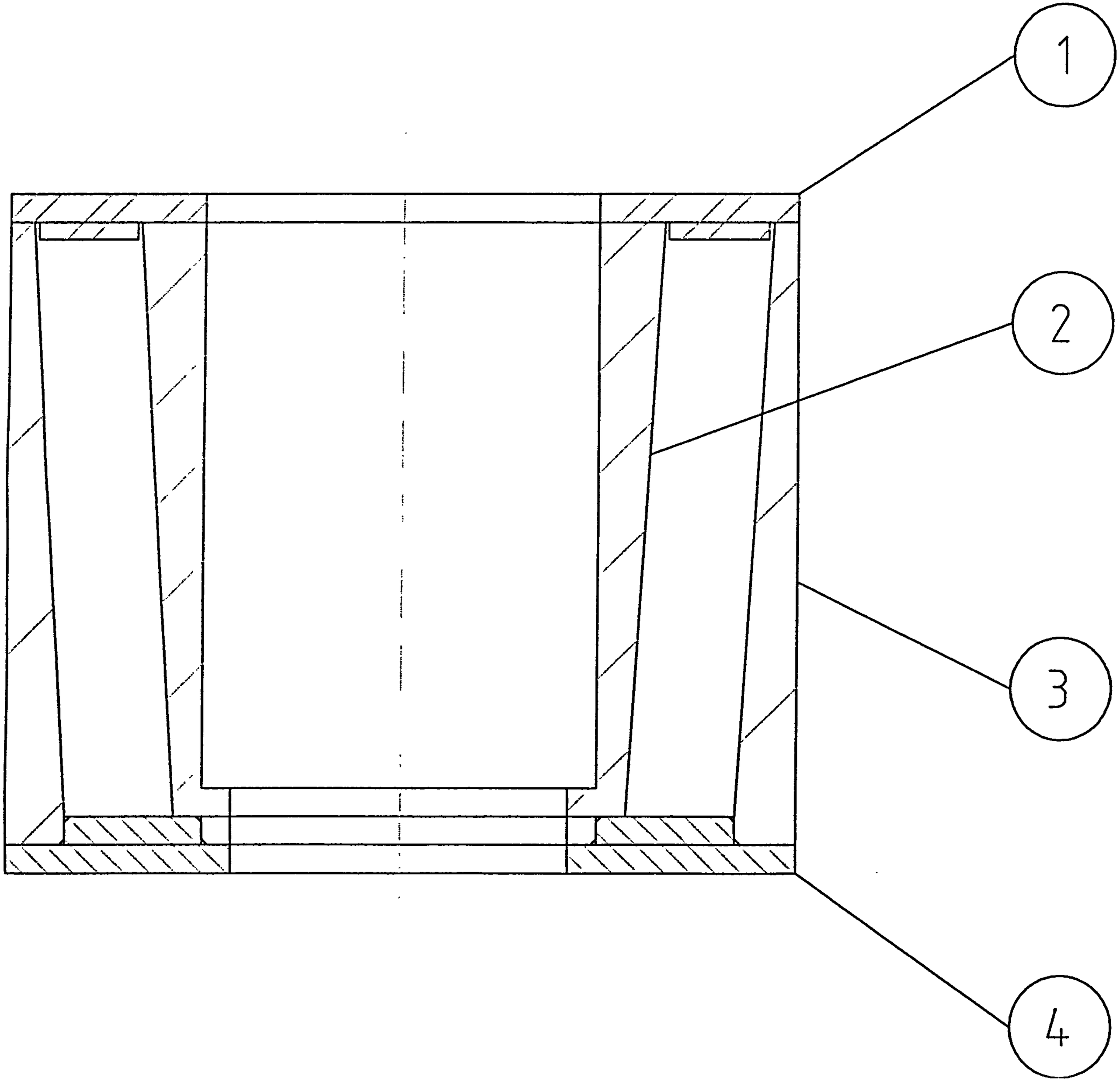

1. MOULD LID
2. MOULD CORE
3. MOULD SLEEVE
4. MOULD BASE

Appendix 2

Datasheets: Raw materials, oil and water based lubricants

Alcan Chemicals Europe

Data Sheet 570

Issue 4:10/97/570

Calcined Alumina Alcan Reactive Grades for Ceramics

The four products featured in this data sheet are low soda reactive aluminas. It can be seen from the physical properties overleaf that RA45E and RA207LS are more reactive than RA204LS and RA203LS.

These **Alcan RA** grades are white, free flowing crystalline powders with the chemical formula Al_2O_3.

All grades are recommended for use in the ceramic industry where there is a requirement for high thermal reactivity. Their reactive nature allows low porosity, high density, high alumina ceramic parts to be produced at lower firing temperatures; other benefits include high mechanical and good surface finish.

RA45E and **RA207LS** also have a controlled magnesia content which assists with the control of grain growth during the firing process.

Another important feature of the products is the low soda content which imparts excellent electrical properties to the finished ceramic products.

Applications include wear resistant ceramics, electronic substrates, engineering component, etc.

Alcan low soda reactive aluminas can be used with all conventional ceramic fabrication techniques.

Summary

- *High reactivity*
- *Low soda content*
- *Excellent sintering performance*
- *Reduced firing temperatures*
- *Controlled grain growth during firing (RA45E and RA207LS)*
- *Can be used with all conventional ceramic forming techniques*

Typical Applications

- *Wear resistant ceramics*
- *Electrical and electronic components*
- *Engineering components*

Alcan Chemicals Europe (Part of Alcan Aluminium UK Limited)
Chalfont Park, Gerrards Cross, Buckinghamshire SL9 0QB. England
Telephone: +44 (0) 1592 411000 · Facsimile: +44 (0) 1753 233444

ALCAN

Alcan Chemicals Europe

Specification

Data Sheet 570

(Typical values, unless otherwise stated)

Issue 4:10/97/570

Physical Properties

Products		RA203LS[6]	RA204LS[6]	RA207LS	RA45E
Surface area [1]	m^2/g	3	4	7.5	7.5
Screen analysis[2] Retained on 45µm	%	0.01	0.01	0.01	0.01
Particle size distribution [3] d_{10}	µm	3.3	2.8	1.2	1.5
d_{50}	µm	1.4	0.9	0.4	0.45
d_{90}	µm	0.5	0.3	0.2	0.25
Green density [4]	g/cm^3	2.2	2.25	2.1	2.18
Fired Density [5], 1500°C	g/cm^3	2.8	3.17	3.76	3.87
1550°C	g/cm^3	3.07	3.46	3.89	3.93
1600°C	g/cm^3	3.58	3.77	3.95	3.94
1650°C	g/cm^3	3.84	3.91	3.95	3.95

Packaging

Multi-ply paper sacks	kg	25	25	25	25
Weight per pallet	tonnes	1	1	1	1

Stretchwrapping of paper sacks is standard for deliveries outside the UK. Options available on request include Big-bags, bulk tanker deliveries and stretchwrapping within the UK. All paper sacks are recyclable.

Chemical analysis (%)

	RA203LS	RA204LS	RA207LS	RA45E
Al_2O_3 (by difference)	99.6	99.8	99.8	> 99.8
Na_2O (total)	≤ 0.1	0.05	0.07	0.03
SiO_2	≤ 0.1	0.1	0.04	0.01
Fe_2O_3	0.03	0.04	0.03	0.03
CaO	0.02	0.01	0.02	0.01
MgO	0.005	0.005	0.04	0.04
K_2O	0.01	0.01	0.01	0.01
Loss on Ignition (300°C - 1100°C)	0.2	0.2	0.2	0.2

Notes

1. *Micromeritics Flowsorb*
2. *Wet sieve*
3. *Micromeritics Sedigraph*
4. *Pressed at 2 tpsi*
5. *Fired at the rate of 5°C/min. (Soak time of 2 hours)*
6. *0.1% MgO added for ceramic testing*

Health and safety

Alcan Reactive Alumina Ceramic grades when properly used do not constitute a health risk, nor do they carry any fire or explosion hazard. It is recommended that ventilation and personal protection measures are taken to meet the requirements of the Guidance Note on Occupational Exposure issued by the UK Health and Safety Executive, and the American Conference of Governmental Industrial Hygienists (ACGIH) total and respirable airborne particulate of 10 and 4 mg/m^3 respectively.

Please refer to Alcan Chemicals Europe '*Material Safety Data Sheet number 2*' for more information about use and disposal.

ALCAN

BACO
REACTIVE
ALUMINAS

Data Sheet 570

Issue No. 2:8/96/570

Baco RA45E Grade

RA45E is a low soda calcined alpha alumina that has been dry ball milled to below its ultimate crystallite size to give a highly reactive product. The principle application is for high alumina technical and engineering ceramic products.

RA45E is a white, free flowing crystalline powder with the chemical formula Al_2O_3.

RA45E is used in the manufacture of ceramic components where there is a requirement for high thermal reactivity. The reactive nature of this grade of alumina allows low porosity, high density, high alumina ceramic parts to be produced at lower firing temperatures; other benefits include high mechanical strength and good surface finish. The controlled magnesia content of 0.04% assists in the control of grain growth during the firing process.

Another important feature of **RA45E** is the low soda content which imparts excellent electrical properties to the finished product.

RA45E exhibits very high density when fired at temperatures above 1550°C (see graph overleaf) making it ideal for use in the production of wear resistant ceramics, electronic substrates and engineering components. The product gives excellent results with all conventional ceramic fabrication techniques.

SUMMARY

* *Highly reactive*
* *Low soda content*
* *Excellent sintering performance*
* *Reduced firing temperatures*
* *Controlled grain growth during firing*
* *Can be used with all conventional ceramic forming techniques*

APPLICATIONS

* *Wear resistant ceramics*
* *Electrical and electronic components*
* *Engineering components*

SPECIFICATION

Typical values (unless otherwise stated)

PHYSICAL/CERAMIC PROPERTIES			RA45E
Screen analysis [1]	Retained on 45 µm (350 BSS)	(%)	0.01
Surface area [2]		(m^2/g)	7.5
Median particle size		(µm)	0.45
Green density [3]		(g/cm^3)	2.1
Fired density [3]	1550°C	(g/cm^3)	3.9
	1650°C	(g/cm^3)	3.94
Linear shrinkage	1550°C	(%)	18.5

PACKAGING		
Multi-ply paper sacks	(kg)	25
Weight per pallet	(tonnes)	1

Also available on request: Big-Bags and stretchwrapping of palleted goods (the latter is standard for export).

CHEMICAL ANALYSIS (%)					
Al_2O_3	> 99.8	Fe_2O_3	0.03	MgO	0.04
Na_2O	0.03	SiO_2	0.01	CaO	0.01

Notes:
1. *Wet sieve*
2. *Micromeritics Flowsorb*
3. *100% Al_2O_3 pellet. Fired at 5°C/min. and 2 hrs at temp.*

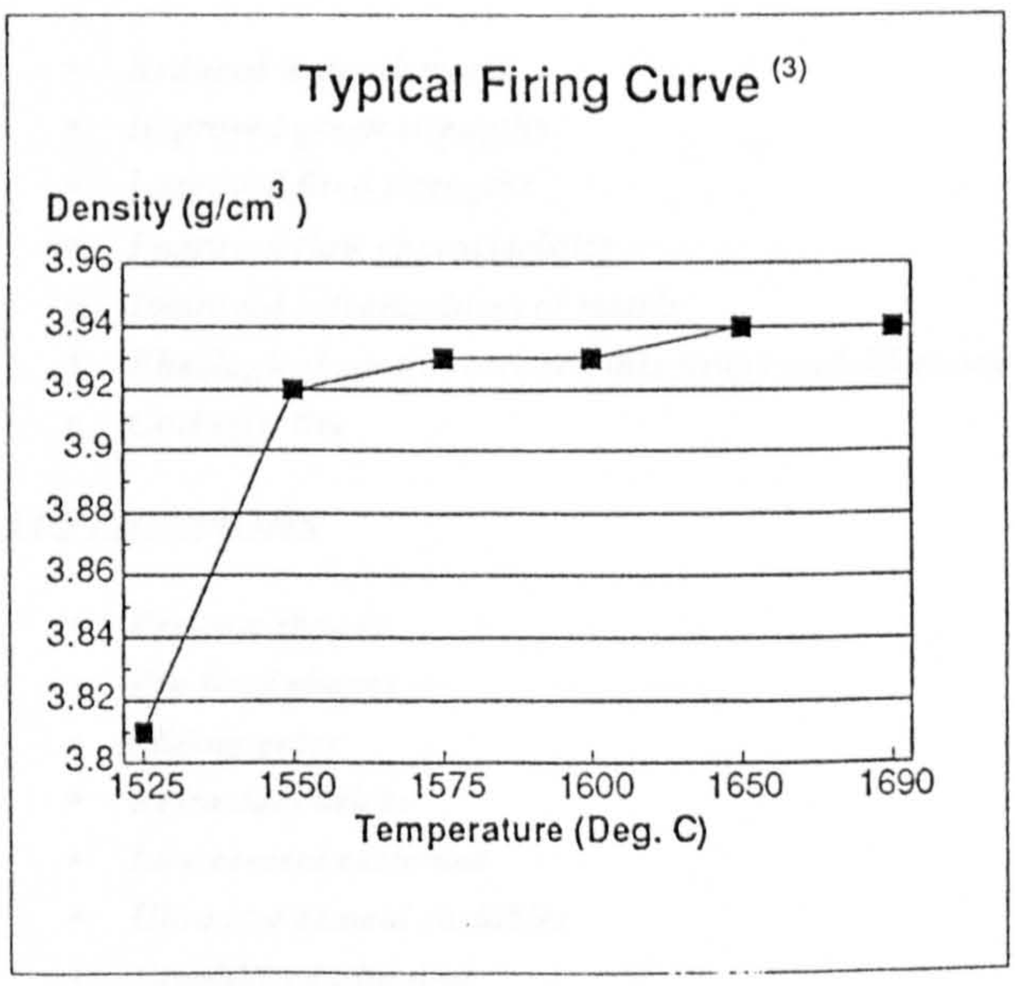

HEALTH AND SAFETY

RA45E grade when properly used does not constitute a health risk, nor does it carry any fire or explosion hazard. It is recommended that ventilation and personal protection measures are taken to meet the requirements of the Guidance Note on Occupational Exposure, issued by the UK Health and Safety Executive and the American Conference of Governmental Industrial Hygienists (ACGIH), for total and respirable airborne particulate of 10 and 5 mg/m^3 respectively.

Please refer to Alcan Chemicals Europe *Material Safety Data Sheet No. 2* for more information about use and disposal.

TTCN: 281820-00-9
CAS-RN: [1344-28-1]

BACO
REACTIVE
ALUMINAS

Data Sheet 550

Issue 3:9/94/550

Baco RA Refractory Grades

Due to the arduous performance requirements the refractory industry has found increasing use for reactive alumina grades originally developed for specialised ceramic applications. Baco RA grades of reactive alumina have been developed from this ceramic technology but with the specific requirements of the refractory industry in mind. Four grades are offered - RA 7, RA 10, RA 12 and RA15 - each with a unique combination of physical properties to meet the needs of the refractory producer.

Baco RA grades are white crystalline powders which are predominantly α-alumina (Al_2O_3). They are of high chemical purity and offer a choice of water adsorption value, surface area and particle size distribution.

The **Baco** range of refractory grade reactive aluminas, consisting of **RA7, RA10, RA12** and **RA15**, impart to refractory systems all the benefits of high quality calcined alumina including excellent refractory properties, hardness, high mechanical strength and resistance to corrosion and chemical attack. All four grades can be employed to influence the rheology of **monolithic** formulations to give thixotropic or dilatant properties.

The **Baco** refractory **RA** range of aluminas offers a choice of physical properties to meet individual requirements. These properties include water adsorption value, particle size distribution and specific surface area, all of which are controlled within tight limits.

Particular applications for these **Baco RA** grades include low and ultra-low cement castables, refractory shapes and investment casting refractories.

CHARACTERISTICS

* *Low water adsorption*
* *Reactive*
* *High tamped density*
* *Low median particle size*
* *Controlled particle size distribution*

BENEFITS IN REFRACTORY SYSTEMS

* *Reduced water demand*
* *Improved green strengths*
* *Improved fired strengths*
* *Improved flow characteristics*
* *Improved refractoriness of matrix*
* *Rheological control between thixotropy and dilatancy*
* *Cost effective*

APPLICATIONS

* *Pre-cast shapes*
* *Pre-fired shapes*
* *Sliding gates*
* *Refractory bricks*
* *Low cement castables*
* *Ultra low cement castables*
* *Graphitised alumina*
* *Investment casting*

SPECIFICATION

(Typical values (unless otherwise stated)

PROPERTIES / PRODUCTS		RA7	RA10	RA12	RA15
Surface area (1)	(m^2/g)	3	2.2	1.8	3.7
Median particle size (2)	(μm)	1.1	2.1	4	2.7
Water adsorption value	(g/100g)	15	14	12	11

PACKAGING					
Multi-ply paper sacks	**(kg)**	**25**			
Weight per pallet	**(tonnes)**	**1**			
All pallets will be shrink-wrapped and have cardboard skirts and caps.					
CHEMICAL ANALYSIS (%)					
Al_2O_3	(by difference)	99.5	SiO_2		0.04
Na_2O	(total)(RA15)	0.06	Fe_2O_3		0.02
Na_2O	(total)(other grades)	0.18	CaO		0.03
Loss on Ignition		0.2			

Notes: *(1) Flowsorb Areameter*
(2) X-ray Sedigraph

For other milled grades of **Baco** aluminas see data sheets:-

No. 450 for ***Baco MA 65, 95 and 130*** *grades*
No. 455 for Coated ***Baco MA'D'*** *grades*
No. 460 for ***Baco RMA 300*** *series*
No. 470 for ***Baco MA250*** *grades*
No. 480 for ***Baco MA*** *Refractory grades*
No. 490 for ***Baco MA-LS*** *low soda grades*
No. 576 for ***Baco RA 107 LS*** *grade*
No. 577 for ***Baco RA 207 LS*** *grade*
No. 579 for ***Baco RA 204 LS*** *grade*
No. 580 for ***Baco RA 203 LS*** *grade*

HEALTH & SAFETY

Baco RA grades when properly used do not constitute a health risk, nor do they carry any fire or explosion hazard. It is recommended that ventilation and personal protection measures are taken to meet the requirements of the Guidance Note on Occupational Exposure, issued by the UK Health and Safety Executive and the American Conference of Governmental Industrial Hygienists (ACGIH), for total and respirable airborne particulate of 10 and 5 mg/m^3 respectively.

Please refer to **Alcan Chemicals Europe** ***Safety Data Sheet No. 2*** for information about use and disposal.

TTCN: 281820-00-9
CAS RN: [1344-28-1]

Alcan Chemicals Europe

Data Sheet 550

Issue 3:9/94/550

Calcined Alumina Alcan Reactive Grades for Refractories

Due to the arduous performance requirements the refractory industry has found increasing use for reactive alumina grades originally developed for specialised ceramic applications. Alcan RA grades of reactive alumina have been developed from this ceramic technology but with the specific requirements of the refractory industry in mind. Four grades are offered - RA7, RA10, RA12 and RA15 - each with a unique combination of physical properties to meet the needs of the refractory producer.

Alcan RA grades are white crystalline α-alumina powders with the chemical formula (Al_2O_3). They are of high chemical purity and offer a choice of water adsorption value, surface area and particle size distribution.

The **Alcan** range of refractory grade aluminas, consisting of **RA7, RA10, RA12** and **RA15** impart to refractory systems all the benefits of high quality alumina, calcined alumina including excellent refractory properties, hardness, high mechanical strength and resistance to corrosion and chemical attack. All four grades can be employed to influence the rheology of monolithic formulations to give thixotropic or dilatant properties.

The **Alcan** refractory **RA** range of aluminas offers a choice of physical properties to meet individual requirements. These properties include water adsorption value, particle size distribution and specific surface area, all of which are controlled within tight limits.

Particular applications for these **Alcan RA** grades include low and ultra-low cement castables, refractory shapes and investment casting refractories.

Characteristics

- *Low water adsorption*
- *Reactive*
- *High tamped density*

Typical Applications

- *Pre-cast shapes and pre-fired shapes*
- *Sliding gates and refractory bricks*
- *Low cement castables and ultra low cement castables*
- *Graphitised alumina*
- *Investment casting*

Benefits in Refractory Systems

- *Reduced water demand and improved flow characteristics*
- *Improved green and fired strengths*
- *Improved refractoriness of matrix*
- *Rheological control between thixotropy and dilatancy*

Alcan Chemicals Europe (Part of Alcan Aluminium UK Limited)
135 Aberdour Road Burntisland Fife Scotland UK KY3 0EP
Telephone: +44 (0) 1592 411000 Facsimile: +44 (0) 1592 411111

ALCAN

BACO
REACTIVE
ALUMINAS

Data Sheet 580

Issue 3:8/96/580

RA 203LS Grade

Baco RA203LS is a white, free flowing crystalline alumina powder with the chemical formulae Al_2O_3. It is a calcined low soda grade that has been dry ball milled to below its ultimate crystal size to give a reactive product.

Baco RA203LS is recommended for use in high alumina ceramics products where there is a requirement for high thermal reactivity. Its reactivity allows low porosity, high density, high alumina ceramic parts to be produced at lower firing temperatures. The low soda content of **RA203LS** imparts excellent electrical properties to the finished ceramic product The type and amount of the added flux components can be adjusted to give products with good wear resistance, electrical properties or corrosion resistance.

Applications for **Baco RA203LS** include wear resistant ceramics, electronic substracts and engineering components.

Baco RA203LS can be used with all conventional ceramic fabrication techniques.

Summary

* *High reactivity*
* *Low soda content*
* *Good sintering performance*
* *Can be used with all conventional ceramic forming techniques*

Applications

* *Wear resistant ceramics*
* *Electrical and electronic components*
* *Engineering components*

TYPICAL PROPERTIES

CHEMICAL/PHYSICAL PROPERTIES		
Surface area [1]	(m^2/g)	2.9
Particle size distribution [2]	(µm)	
d_{10}		3.3
d_{50}		1.4
d_{90}		0.5
Al_2O_3 (by difference)	(%)	99.6
Na_2O (total)	(%)	≤ 0.1
SiO_2	(%)	≤ 0.1
Fe_2O_3	(%)	0.03
CaO	(%)	0.02
MgO	(%)	0.005
K_2O	(%)	0.01

CERAMIC PROPERTIES		
	Green Density (g/cm^3) [3]	2.2
1550°C	Fired Density (g/cm^3)	2.9
1600°C	Fired Density (g/cm^3)	3.1
1650°C	Fired Density (g/cm^3)	3.4

PACKAGING		
Multi-ply paper sacks	(kg)	25
Weight per pallet	(tonnes)	1

Also available on request: Big-Bags and stretchwrapping of palleted goods (the latter is standard for export).

Notes:

(1) Flowsorb areameter

(2) X-ray sedigraph

(3) 100% Al2O3 pellet pressed at 32 MPa (2 tsi). Fired at 10°C min^{-1}, 2 hours at temperature

HEALTH AND SAFETY

Baco RA203LS grade when properly used does not constitute a health risk, nor does it carry any fire or explosion hazard. It is recommended that ventilation and personal protection measures are taken to meet the requirements of the Guidance Note on Occupational Exposure, issued by the UK Health and Safety Executive and the American Conference of Governmental Industrial Hygienists (ACGIH), for total and respirable airborne particulate of 10 and 5 mg/m^3 respectively.

Please refer to Alcan Chemicals Europe *Material Safety Data Sheet No 2* for information about use and disposal.

TTCN: 281820-00-9
CAS-RN [1344-28-1]

Processed Food

C☆Gel [redacted]

Description

Native maize starch

Functionality

- short gel texture
- opaque gel
- relatively high viscosity
- easy dispersion in cold water
- fair resistance to shear
- poor stability to retrogradation
- poor freeze-thaw stability

Typical data

Moisture	%	12
pH		4.5
Ash	%	0.1
Bulk density (packed)	g/l	700 (560 UNPACKED)
Viscosity	see Brabender profile	

Applications

Native maize starches are multifunctional ingredients exhibiting properties that can be used in a number of food applications and manufacturing processes: texturising agents, film formers, water binders, fillers and thickeners.
C☆Gel [redacted] is applied in food products such as:

- bakery products
- pudding powders
- salad dressings
- soups and sauces
- baby and health foods
- meat products (corned beef, hams and shoulders)

Packaging

Bulk
Big bags.
Net 25 and 50 kg multi-ply white sacks with red distinguishing panels.

Storage

Best storage is realised in a cool dry place off the ground and away from chemicals and odorous materials

Legislation

The FDA has proposed to affirm native starches GRAS under § 21 CFR 184. 1847.
[redacted] 03401 should appear in the ingredients list in the EU as "starch" and as "food starch-unmodified" in the USA

CN code

1108 12 00

Safety

Dust is flammable and explosive.

Cerestar UK Ltd

Trafford Park
GB-Manchester M17 1PA
United Kingdom

Tel :#44 (0)161 872 5959
Telefax :#44 (0)161 848 9034

C☆Gel 03401

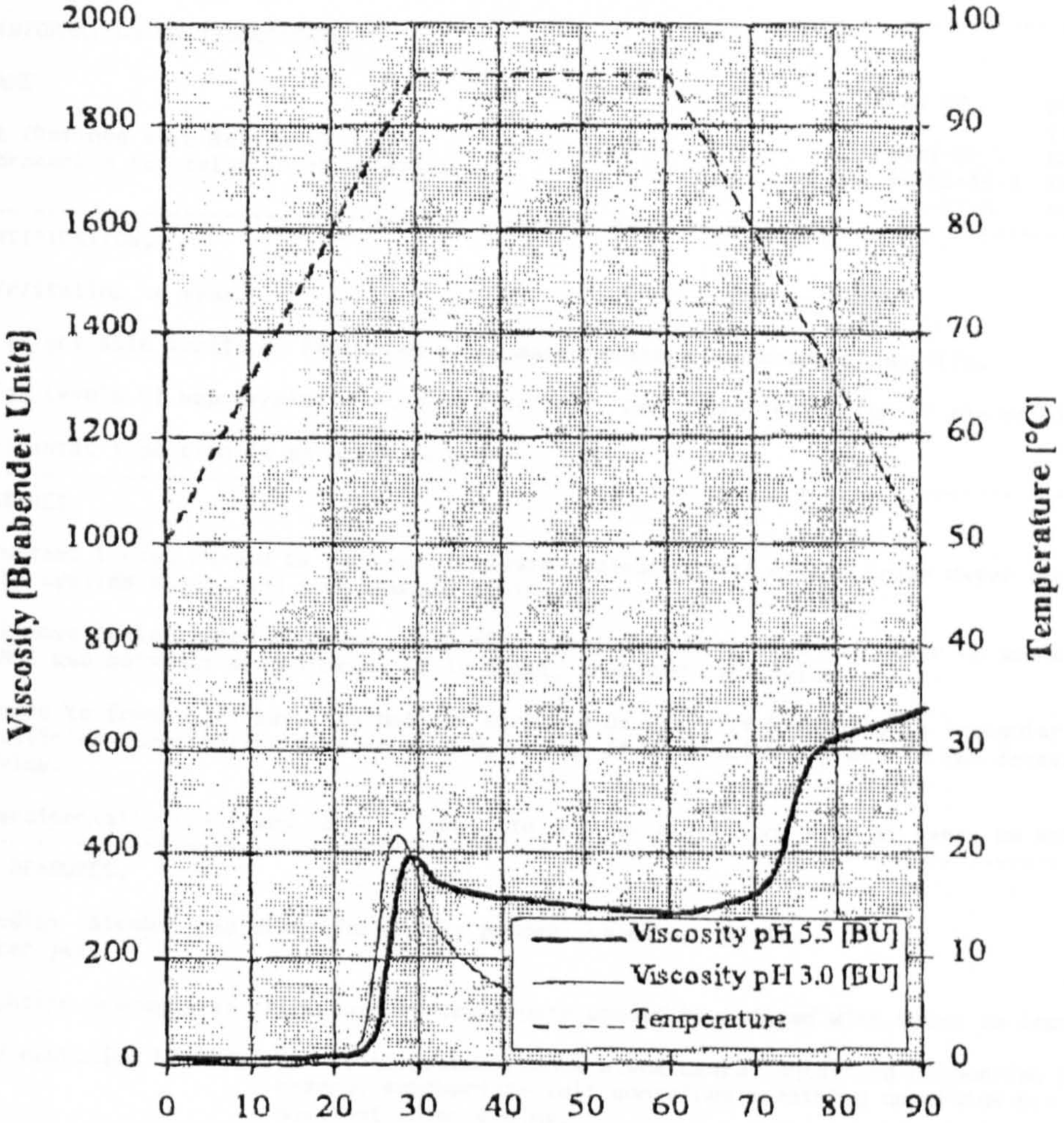

Brabender Viskograph (electronic type)
- concentration: 30 g c.p./distilled water to 480 g total
- cartridge: 350 cmg

1/98/MW

SAFETY DATA SHEET

1.IDENTIFICATION OF THE SUBSTANCE/PREPARATION AND COMPANY.

Product name: ENSNC16 NON SILICONE RELEASE AGENT
Intended use: Lubricant NICKERSON PART N° MJ 425F

Nickerson Europe Ltd
C5 Baird Court, Park Farm Industrial Estate, Wellingborough, Northants NN8 6QJ.
Tel: 01933 674144/679839 Fax: 01933 400461
E-mail: info@nickersoneurope.co.uk Website: www.nickersoneurope.co.uk

2.COMPOSITION/INFORMATION ON INGREDIENTS.

INGREDIENT NAME	CAS NO.	HEALTH (class)	RISK (R No.)	CONTENTS %
Vegetable oil (Refined Soya Bean Oil)	8001-22-7	None	None	5-10
Aliphatic hydrocarbon (contains <0.1% benzene)	64742-49-0	Xn	65	25-50
Butane	106-97-8	None	None	25-50

3.HAZARDS INDENTIFICATION.

Eye contact: Irritating to eyes.

Skin contact: Slight skin irritant. Prolonged or repeated contact can cause dermatitis.

Inhalation: High levels of vapour/mist may cause dizziness. Can cause irritation of the respiratory tract.

Ingestion: Accidental ingestion is an unlikely event.

4.FIRST AID MEASURES.

Eye contact: Contact lenses should be removed. Irrigate copiously with clean, fresh water for at least 10 minutes, holding the eyelids apart, and seek medical advice.

Skin contact: Remove contaminated clothing. Wash skin thoroughly with soap and water or use a proprietary skin cleaner. Do NOT use solvents or thinners. If in doubt, seek medical advice.

Inhalation: Remove to fresh air, keep the patient warm and at rest. If breathing is irregular or has stopped, administer artificial respiration. Give nothing by mouth. If unconscious, place in the recovery position and seek medical advice.

Ingestion: If accidentally swallowed, obtain immediate medical attention. Keep at rest. Do NOT induce vomiting.

5.FIRE-FIGHTING MEASURES.

Extinguishing media: Alcohol resistant foam; CO2; powder; water spray/mist
Do not use: Water jet.

Special fire fighting procedures: Fire exposed containers should be sprayed with water to lessen risk of explosion.

Unusual fire and explosion hazards: Fire will produce dense black smoke containing combustion products which may be a health hazard. Appropriate self-contained breathing apparatus may be required. Run off from fire must not enter drains.

6.ACCIDENTAL RELEASE MEASURES.

Procedures for leaks or spillage: Exclude sources of ignition and ventilate the area. Exclude non-essential personnel. Avoid breathing vapours. Refer to protective measures listed in Section 7 & 8. Contain and collect spillages with non-combustible absorbent materials, e.g.sand, earth, vermiculite, diatomaceous earth and place in a suitable container for disposal in accordance with waste regulations (see Section 13). Do not allow to enter drains or water courses.
Clean preferably with a detergent; avoid the use of solvents If the product enters drains or sewers, the local water company should be contacted immediately; in the case of contamination of streams, rivers or lakes, the National Rivers Authority.

7.HANDLING AND STORAGE.

Handling: Vapours are heavier than air and may spread along floors. They may form explosive mixtures with air. Prevent the creation of flammable or explosive concentrations of vapour in air and avoid vapour concentrations higher than the occupational exposure limits.
Use only in areas from which all sources of heat, sparks and open flame have been excluded.

TEXT BOUND INTO THE SPINE

NTINUED

Avoid skin and eye contact.
Avoid inhalation of vapour and spray mist.
Smoking, eating and drinking should be prohibited in areas of use and storage.

Storage: Store below 50 Deg.C in a dry, well ventilated place away from sources of heat, ignition and direct sunlight. No smoking. Observe the label precautions.
Store separately from strong oxidising agents and strongly alkaline and strongly acidic materials.

8.EXPOSURE CONTROLS/PERSONAL PROTECTION.

INGREDIENT NAME	OES/MEL	8hr TWA	15min STEL
Aliphatic Hydrocarbon solvent blend	OES	265ppm (Sup)	
Butane	OES	600ppm	750ppm

Engineering measures: Provide adequate ventilation to maintain the flammable vapour concentration well below the lower explosive limit (LEL) and ensure the airborne concentration of substances to which an OES has been assigned is below that OES (Occupational Exposure Standard).

Respiratory protection: Air-fed respiratory equipment should be worn when this product is sprayed if the exposure of the sprayer or other people nearby cannot be controlled to below the occupational exposure limit and engineering controls and measures cannot reasonably be improved.

Hand protection: When skin exposure may occur, advice may be sought from the glove suppliers on appropriate types. Barrier creams may help to protect exposed areas of the skin but are not substitutes for full physical protection. They should not be applied once exposure has occurred.

Eye protection: Eye protection designed to protect against liquid splashes should be worn.

Skin protection: Cotton or cotton/synthetic overalls are normally suitable. Grossly contaminated clothing should be removed and the skin washed with soap and water or a proprietary skin cleaner.

9..SICAL AND CHEMICAL PROPERTIES.

Physical State: Aerosol.
Appearance: Pale straw
Odour: Hydrocarbon
pH: N/A
Boiling point/boiling range: 71 Deg.C
Melting point/melting range: <0 Deg.C
Flash point: -40 Deg.C
Flammability: LEL 0.8 (% vol in air @ 25 Deg.C)
UEL 9.0
Autoflammability: 230 Deg.C
Explosive properties: None
Oxidising properties: None
Can pressure: 2.41 bar.
Relative density: N/A
VOC content: 57 g/100ml
Solubility-Water: Insoluble
Solubility-Solvent: Soluble in aliphatic hydrocarbons.
Other data:

10.STABILITY AND REACTIVITY.

Stability: Stable.

C itions to avoid: Avoid naked flames, red hot surfaces, other high temp.sources that may induce thermal decomposition

Incompatibility (Materials to avoid): Oxidising agents, strong acids, strong alkalis.

Hazardous decomposition products: In a fire, hazardous decomposition products such as smoke, carbon monoxide, carbon dioxide and oxides of nitrogen may be produced.

11.TOXICOLOGICAL INFORMATION.

INGREDIENT	LD50(Animal/oral)
Aliphatic Hydrocarbon solvent blend	>5g/Kg(Rat)

There is no data available on the product itself.
Exposure to organic solvent vapours may result in adverse health effects on the renal and central nervous systems. Symptoms can include headache, dizziness, fatigue, muscular weakness, drowsiness and in extreme cases, loss of consciousness.
Splashes in the eyes may cause irritation and reversible local damage.
Aliphatic hydrocarbon solvent in this product will cause temporary irritation to eyes. Irritation to skin caused by its defatting action may lead to dermatitis. Inhalation of high concentrations of vapour will produce headache, nausea and vomiting and in extreme cases coma. Ingestion will produce nausea and vomiting, diarrhoea, drowsiness and pulmonary oedema.

CONTINUED

12.ECOLOGICAL INFORMATION.

There is no data available on the product itself.
The product should not be allowed to enter drains or water courses or be deposited where it can affect ground or surface waters.
Aliphatic hydrocarbon solvent in this product has low bio-accumulation potential, is not acutely toxic to aquatic organisms and has good biodegradability.

13.DISPOSAL CONSIDERATIONS.

Do not allow into drains or water courses or dispose of where ground or surface waters may be affected.
Wastes, including emptied containers, are controlled wastes and should be disposed of in accordance with regulations made under the Control of Pollution Act.
Using the information provided in this data sheet, advice should be obtained from the Waste Regulation Authority whether the special waste regulations apply.

14.TRANSPORT INFORMATION.

CCCN: 3403 99 90
UN no.: 1950 AEROSOLS
IMDG: 2102
Class: 2
ICAO/IATA: 2.1
RID/ADR: 2,5'F
Packing Group: N/A

15.REGULATORY INFORMATION.

Label for supply: EXTREMELY FLAMMABLE

R phrases: None

Safety phrases:
2: Keep out of the reach of children.
16: Keep away from sources of ignition - No Smoking.
23: Do not breathe vapour/spray.
51: Use only in well ventilated areas.

Regulatory references: The Chemicals (Hazard Information and Packaging) Regulations 1994 and subsequent amendments.

16.OTHER INFORMATION.

The information contained in this data sheet is provided in accordance with the requirements of the Chemicals (Hazard Information and Packaging) Regulations. It does not constitute the user's own assessment of workplace risks as required by other health and safety legislation. The provisions of the Health & Safety at Work etc. Act and the Control of Substances Hazardous to Health Regulations apply to the use of this product at work.
The product should not be used for purposes other than those shown in Section 1 without first referring to the supplier and obtaining written handling instructions. As the specific conditions of the product are outside the supplier's control, the user is responsible for ensuring that the requirements of the relevant legislation are complied with.
OES/MEL values are obtained from the current issue of EH40 unless indicated thus (Sup) when a value has been obtained from the supplier.
Further information and advice can be found in the following publications:
The Control of Substances Hazardous to Health Regulations 1988 (SI 1988:1657)
The Environmental Protection (Duty of Care) Regulations 1992 (SI 1992:2839)
Storage of Packaged Dangerous Substances, HS(G)71
The Highly Flammable Liquids and Liquified Petroleum Gases Regulations 1972 (SI 1972:917)
Storage of Flammable Liquids in Containers, HS(G)51

Date of issue of original: 10/03/94

Revision: 3

Revision dated: 29/01/97

Items marked with a * have been amended since last revision.

This product should be stored, handled and used in accordance with good industrial hygiene practices and in conformity with legal regulations. The information contained herein is based on the current state of our knowledge and is intended to describe products from the point of view of safety requirements and thus should not be construed as guaranteeing specific properties. For further information contact the office.

Alumina-Starch Process Sheet

Alumina Qty (g)
0

Solids Content %
59.1

Starch Content %
20

Fixed Values

Starch Density=0.56 g/cm^3

Alumina Density= 3.98 g/cm^3

Alumina Particle Size: 4

Lot No:

Calculation

Per 100 Cm^3

Al2O3 vol per % (cm3)	Starch vol per % (cm3)	alumina qty (g)	starch qty (g)
59.1	47.28	11.82	188.1744	6.6192

Mixture Formulation (g)

Alumina	Starch	Water	Dispex A40
0	0.000	0.000	0.000

Actual Mixture (g)

Alumina	Starch	Water	Dispex A40

Date:_____

Ball- milling

Ball mill blg_____ From:_____ to:_____ Speed:_____

Viscosity

Date:_____ Temp Susp:_____

Ref: Oil visc:_____ Temp:_____

Consolidation Stage

Date:_____ Temp:_____ From:_____to_____

Samples:

Ambient Drying From:_____/____/____ to:_____ ____/____/____

Furnace processing

Distribution

Drying	Date	

Comments:

Binder Burnout	Date	

Comments:

Presintering	Date	

Comments:

Sintering	Date	

Comments:

bp

Dielectric

Fluids for Electro-discharge Machines (EDM)

Description; Description

The BP Dielectric range is formulated to suit spark-erosion machines of all power ratings, while providing long fluid life and meeting the demands of operator requirements regarding health and safety.

All fluids are hydrocarbon oils of low viscosity and good cooling characteristics; they flush erosion particles from the work area and provide quick and easy separation in filter systems.

Applications; Applications

- BP Dielectric 180 is designed for the finest and most delicate machining operations, particularly in small EDM units working on finishing operations where very close tolerances are important. This grade is additive-treated to avoid the generation of unpleasant odours in service and to provide long service life.

- BP Dielectric 200 is an oil of slightly higher viscosity and a grade that can be used in machines of all sizes. It is formulated for optimum metal-removal rates and low electrode wear. Its characteristics make it equally suitable for roughing and finishing operations. It is additive-treated to achieve long service life.

- BP Dielectric 250 is an oil of high viscosity and lower volatility, designed for larger electrodischarge machines and particularly suited for roughing operations where high rates of metal-removal are required. It has a high flash point, very low odour and a low level of aromatic hydrocarbons.

The BP Dielectric fluids are approved or recommended by:
- AEG-Elotherm (Elbomat)
- AGIE
- Charmilles (BP Dielectric 250)
- Ingersoll (BP Dielectric 250)

Main Benefits; Main Benefits

- High metal-removal rates and low electrode wear
- Excellent filterability with good flushing and cooling capabilities
- Resistant to oxidation, hence long service life
- Low odour and fume generation, hence pleasant in operation
- Highly refined oils with low aromatics content for safe working environment

Storage; Storage

All packages should be stored under cover. Where outside storage is unavoidable drums should be laid horizontally to avoid the possible ingress of water and the obliteration ; All packages should be stored under cover. Where outside storage is unavoidable drums should be laid horizontally to avoid the possible ingress of water and the obliteration of drum markings. Products should not be stored above 60°C, exposed to hot sun or freezing conditions.; of drum markings. Products should not be stored above 60°C, exposed to hot sun or freezing conditions.

Health, Safety and Environment; Health, Safety and Environment

Health, safety and environmental information is provided for this product in the Materials Safety Data Sheet. This gives details of potential hazards, precautions and First Aid measures, together with environmental effects and disposal of used products.; Health, safety and environmental information is provided for this product in the Materials Safety Data Sheet. This gives details of potential hazards, precautions and First Aid measures, together with environmental effects and disposal of used products.

BP Lubricants and Special Products Ltd. or its subsidiaries will not accept liability if the product is used other than in the manner or with the precautions or for the purpose/s specified. Before the product is used other than as directed, advice should be obtained from the local BP office.; BP Lubricants and Special Products Ltd. or its subsidiaries will not accept liability if the product is used other than in the manner or with the precautions or for the purpose/s specified. Before the product is used other than as directed, advice should be obtained from the local BP office.

Typical Characteristics; Typical Characteristics

	Test Methods; Test Methods	Units; Units	Grade :; Grade :		
			180	200	250
Density @ 15°C	ISO 3675, ASTM D1298	kg/m³	752	816	823
Flash Point (COC)	ISO 2592, ASTM D92	°C	78	106	125
Viscosity KV @ 20°C	ISO 3104,	mm²/s	1.9	3.6	6.0
40°C	ASTM D445		1.4	2.4	3.7
Colour	ISO 2049, ASTM D1500	-	L0.5	L0.5	L0.5
Neutralization value	ASTM D974, DIN 51 558	mgKOH/g	0.01	0.01	0.01
Boiling point: 5%	DIN 51 435	°C	180	195	230
95%		°C	240	290	340
Aromatic content	DIN 51 378	%	<0.1	<0.1	<0.1

The above figures are typical of those obtained with normal production tolerance and do not constitute a specification.

This Data Sheet and Information it contains is considered to be accurate at the date of printing. No warranty or representation, expressed or implied, is made as to the accuracy or completeness of the data and information contained in this publication.; This Data Sheet and Information it contains is considered to be accurate at the date of printing. No warranty or representation, expressed or implied, is made as to the accuracy or completeness of the data and information contained in this publication.

It is the User's obligation to evaluate and use products safely and within the scope advised in the data sheet and to comply with all applicable laws and regulations. No statement made in this publication shall be construed as a permission, recommendation or authorisation given or implied to practice any patented invention without a valid licence.; It is the User's obligation to evaluate and use products safely and within the scope advised in the data sheet and to comply with all applicable laws and regulations. No statement made in this publication shall be construed as a permission, recommendation or authorisation given or implied to practice any patented invention without a valid licence.

The Seller shall not be responsible for any loss or damage resulting from any hazards or risks identified in the data sheet and which are associated with petroleum products concerned (provided that this disclaimer shall not affect any statutory rights of the Buyer of the petroleum products concerned).; The Seller shall not be responsible for any loss or damage resulting from any hazards or risks identified in the data sheet and which are associated with petroleum products concerned (provided that this disclaimer shall not affect any statutory rights of the Buyer of the petroleum products concerned).

BP Lubricants and Special Products Limited
Witan Gate House Lubricants Helpline: 0845 - 6031080
500/600 Witan Gate Fax: 0845 - 6031070
MILTON KEYNES
MK9 1ES
Witan Gate House Lubricants Helpline: 0845 - 6031080
500/600 Witan Gate Fax: 0845 - 6031070
MILTON KEYNES
MK9 1ES

Date Created: 02/11/93 04:52:26 AM Last Modified:05/28/2002

bp

Energol HP

Machine Tool Oil

Description

A range of mineral oils for lubrication of high machinery applications. Energol HP 5 contains additives to increase resistance to oxidation, provides anti-wear properties and resistance to corrosion.

Applications

Energol HP oils are recommended for circulatory systems in particular for the lubrication of spindle bearings in precision tools and textile plant.

Energol HP 0, the lowest viscosity grade, is a specially refined oil, recommended for high speed bearings in grinding machines, automatic lathes and high-speed saws. It also has a specialised application, such as an aluminium rolling oil.

Main Benefits

- Long service life
- Effective lubrication of high speed precision equipment
- Good anti-wear properties

Storage

All packages should be stored under cover. Where outside storage is unavoidable drums should be laid horizontally to avoid the possible ingress of water and the obliteration of drum markings. Products should not be stored above 60°C, exposed to hot sun or freezing conditions.

Health, Safety and Environment

Health, safety and environmental information is provided for this product in the Materials Safety Data Sheet. This gives details of potential hazards, precautions and First Aid measures, together with environmental effects and disposal of used products.

BP Lubricants and Special Products Ltd. or its subsidiaries will not accept liability if the product is used other than in the manner or with the precautions or for the purpose/s specified. Before the product is used other than as directed, advice should be obtained from the local BP office.

Typical Characteristics

	Test Methods	Units	Grade :

HP 0
used in Flip Flop spindle

HP "0"

Energol HP
Machine Tool Oil

Typical Characteristics

	Test Methods	Units	Grade: 0	5	10
Density at 15 °C	ISO 3675, ASTM D1298	kg/m³	787	843	860
Flash Point (PMC)	ISO 2795, ASTM D93	°C	66	124	140
Viscosity KV @ 40 °C	ISO 3104 ASTM D445	mm²/s	1.45	4.63	10.6
Pour Point	ISO 3016, ASTM D97	°C	-40	-20	-14
Colour	ISO 2049	-	<0.5	<1.0	<1.0

The above figures are typical of those obtained with normal production tolerance and do not constitute a specification.

SHC J/kg.K = 2.226 @ 20°C
@ 40°C = 2.312

DENSITY ρ = 784.0 @ 20°C
= 772 @ 40°C

VISCOSITY @ 40°C = 0.00114 NS/m²

@ 20°C : 0.00268 NS/m²

BP Oil UK Limited
BP House
Breakspear Way
HEMEL HEMPSTEAD
HERTS HP2 4UL

Customers Helpline: 0345 515353
Fax: 0922 59171

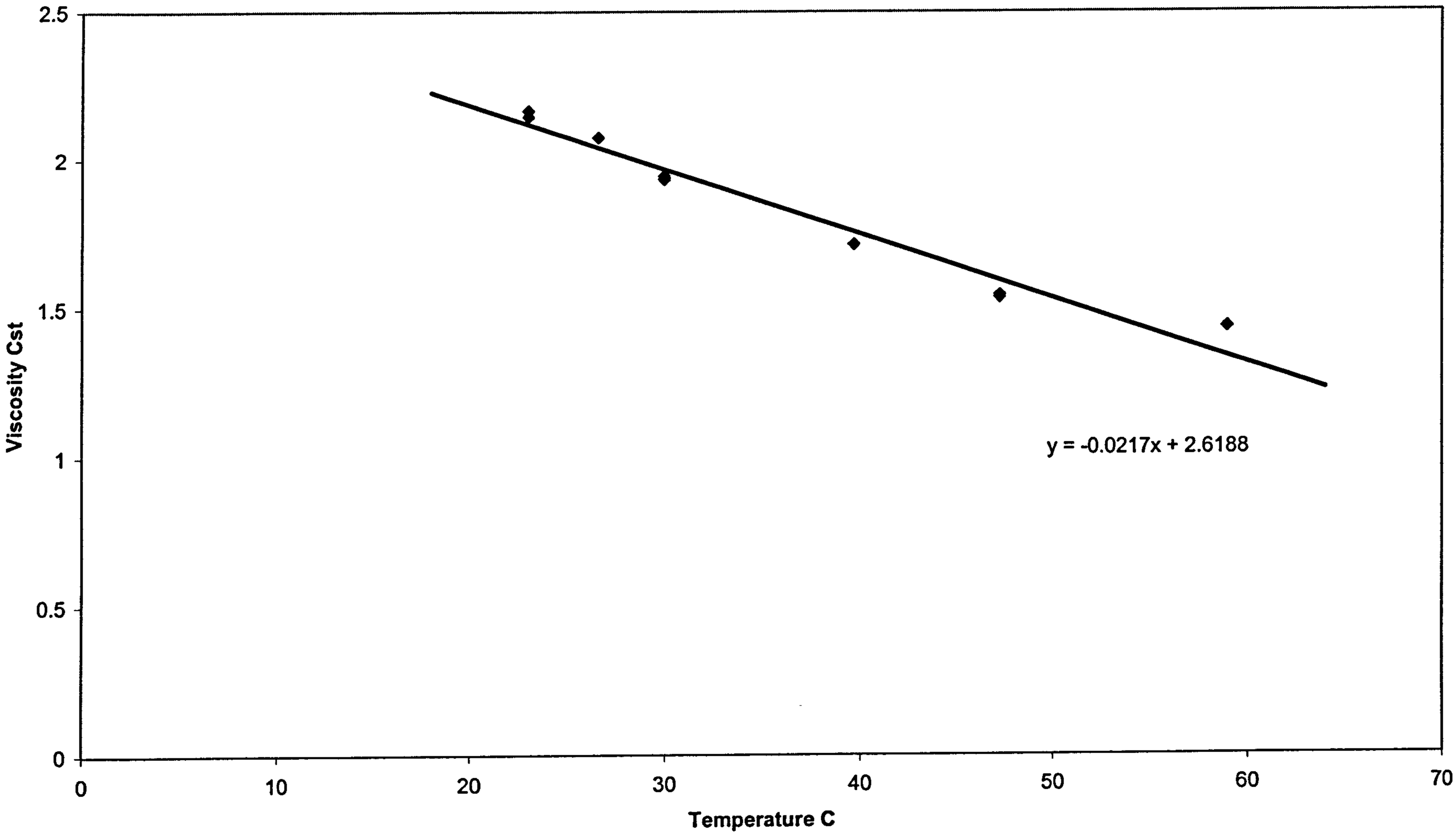
Dielectric 180 Kinematic Viscosity
Viscosity Cst
2.5
2
1.5
1
0.5
0
y = -0.0217x + 2.6188
0
10
20
30
40
50
60
70
Temperature C

Oils Density

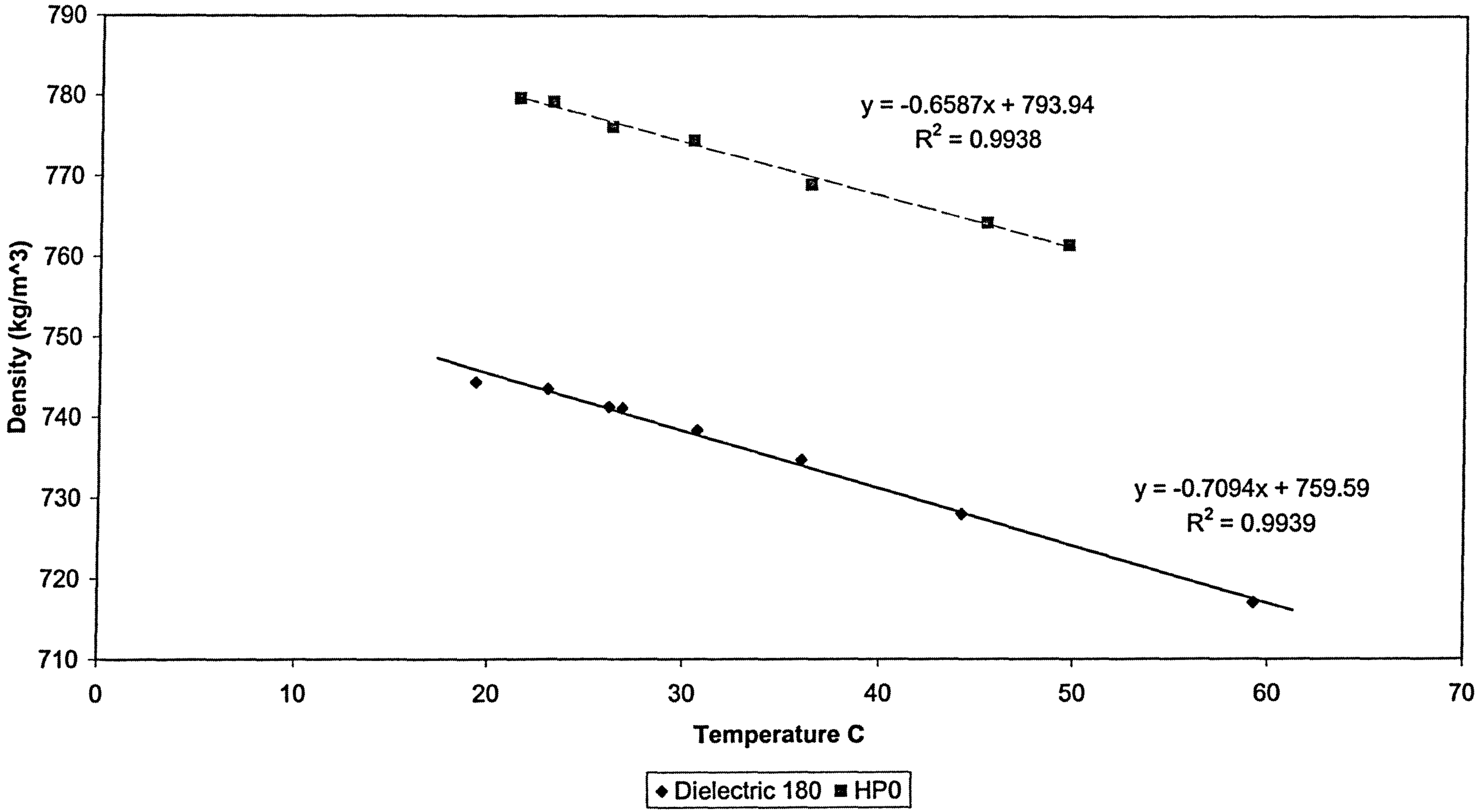

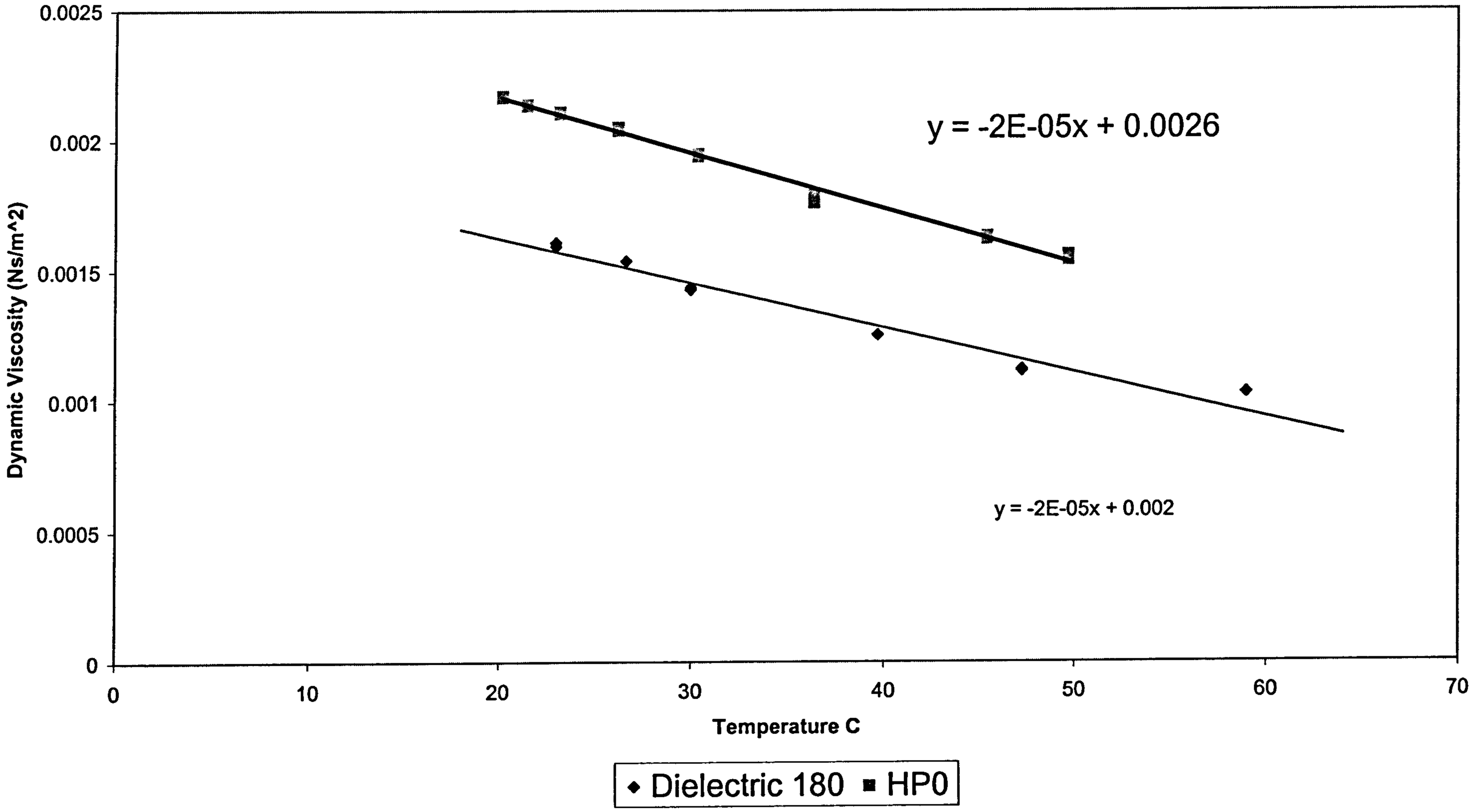
Dielectric 180 & HP0 Dynamic Viscosity
0.0025
0.002
0.0015
0.001
0.0005
0
Dynamic Viscosity (Ns/m^2)
y = -2E-05x + 0.0026
y = -2E-05x + 0.002
0
10
20
30
40
50
60
70
Temperature C
Dielectric 180
HP0

SAFETY DATA SHEET

1 - IDENTIFICATION OF PREPARATION AND COMPANY/BUSINESS

Preparation:

Name: DOWEL

Product code: 101420R1.

Company/business:

Registered company name: CHEMSEARCH

Address: Landchard House, Victoria Street, West Bromwich, West Midlands, B70 8ER

Telephone: 0121 525 1666 . Fax: 0121 500 5386 . Telex:

Emergency telephone No.: 0121 525 1666

Association/Organisation: A Division of NCH (UK) Ltd

Normal use:

..Cutting fluid

2 - INFORMATION REGARDING CONSTITUENTS

Hazardous substances present on their own.

(present in the preparation at a sufficient concentration to give it the toxicological characteristics it would have in a 100% pure state)

This preparation contains no hazardous substance in this category.

Other substances representing a hazard:

607-196-00-2 Cas 111-14-8 HEPTANOIC ACID Concentration >=2.50% and <10.00%. Symbol: C R: 34

C693.23.2 Cas 693-23-2 DODECANEDIOIC ACID Concentration >=0.00% and <2.50%. Symbol: Xi R: 36

Substances present at a concentration below the minimum danger threshold.

C7747.35.5 Cas 7747-35-5 7A-ETHYLDIHYDRO-1H,3H,5H-OXAZOLO (3,4-C) OXAZOLE Concentration >=2.50% and <10.00% Symbol: Xn R: 36/38-52/53-20/21

Other substances with occupational exposure limits.

No known substance in this category present.

3 - IDENTIFICATION OF HAZARDS

This preparation is not classed as hazardous to health by directive 88/379/EEC.

This product is not classed as flammable. Refer to the recommendations regarding the other products present on the site

4 - FIRST AID.

As a general rule, in case of doubt or if symptoms persist, always call a doctor.

NEVER induce swallowing in an unconscious person.

5 - FIRE-FIGHTING MEASURES

Not relevant.

Firefighters should wear self contained breathing apparatus and full protective clothing.

6 - MEASURES TO BE TAKEN IN THE EVENT OF ACCIDENTAL SPILLAGE

Consult the safety measures listed under headings 7 and 8.

Contain and control the leaks or spills with non-combustible absorbent materials such as sand, earth, vermiculite, diatom earth in drums for waste disposal.

Prevent any material from entering drains or waterways.

Clean preferably with a detergent, do not use solvents.

7 - HANDLING AND STORAGE

The regulations relating to storage premises apply to workshops where the product is handled.

Handling:

Prevent access by unauthorised personnel.

8 - EXPOSURE CONTROL - PERSONAL SAFETY

Technical measures.

Do not breathe spray.

Exposure limits per INRS ND 1945-153-93/(1996) and ND 2022-163-96:

Substance in this category unknown.

9 - PHYSICAL PROPERTIES

Density:	> 1
Acid/base character of preparation:	slightly basic.
Solubility of preparation in water:	Soluble.
Vapour tension at 50°C of volatile constituents:	not specified.
Physical state:	fluid liquid
Flash point interval:	not relevant.
When a pH measure is possible, it has a value of:	not stated.
Self-ignition temperature:	not relevant.
Decomposition temperature:	not relevant.
Melting temperature interval:	-5 °C.
Average distillation temperature of solvents contained:	not relevant.

10 - STABILITY AND REACTIVITY

The preparation is stable at the handling and storage conditions recommended per § 7 of the safety data sheet,

Materials to avoid: /

11 - TOXICOLOGICAL INFORMATION

12 - ECOLOGICAL INFORMATION

No ecological data on the product itself is available.

Other data:

.....All surfactants are biodegradable.

13 - DISPOSAL CONSIDERATIONS

Dispose of in accordance with local regulations.

Packaging: Can be reused after rinsing or recycled or burnt.

14 - TRANSPORT INFORMATION

Exempt from transport classification and labelling.

Transport product in compliance with provisions of the ADR for road, RID for rail, IMDG for sea and ICAO/IATA for air transport

15 - STATUTORY INFORMATION

Not relevant .

Particular hazards associated with the preparation and safety recommendations:

S 2 Keep out of reach of children.

For industrial and institutional use only

16 - OTHER INFORMATION

Since the user's working conditions are not known by us, the information supplied on this safety data sheet is based on our current level of knowledge and on national and community regulations.

The product must not be used for any purposes other than those specified under heading 1 without first obtaining written handling instructions.

It is at all times the responsibility of the user to take all necessary measures to comply with legal requirements and local regulations.

The information given on this safety data sheet must be regarded as a description of the safety requirements relating to our product and not a guarantee of its properties

Revised by: km

MATERIAL SAFETY DATA SHEET

1. IDENTIFICATION of the SUBSTANCE/PREPARATION and COMPANY

PRODUCT NAME: THAUMAKOOL
COMPANY Thaumaturgy (UK) Ltd
PO Box 37
Blackburn
BB1 3BU
TEL: 01254 680223
FAX: 01254 682378
EMERGENCY: 01333 311981
DESCRIPTION: Fully Synthetic Machine Coolant

2. COMPOSITION/INFORMATION on INGREDIENTS
Blend of synthetic surfactants and corrosion inhibitors.

Hazardous Ingredients	%W/W Range	Nature of Hazard
Diethanolamine esters	25 - 60	Irritant TWA 3ppm
Diethanolamine Glycol	1 - 10	Irritant TWA 23ppm
Hexylene Glycol	1 - 10	Irritant TWA 25ppm

3. HAZARD IDENTIFICATION
Product is classed as IRRITANT under Chemicals Hazard Information and Packaging Regulations 1993.

4. FIRST AID MEASURES
Eyes: Immediately wash eye with plenty of clean water ensuring eyelids are held open. For diluted product obtain medical attention if irritation or redness persists or as an additional precaution.
Skin: Following contact with undiluted product wash thoroughly with soap and water without delay. Remove contaminated clothing and launder contaminated clothing before reuse. If irritation persists seek medical advice. If the use of metalworking emulsions give rise to irritation or skin rashes possible contamination and or usage conditions may need to be investigated.
Inhalation: Do not induce vomiting. Wash out mouth with water and obtain medical attention. Milk or water to drink may be beneficial. Treat symptomatically if product is aspirated into the lungs e.g. through vomiting send to hospital immediately.
Ingestion: For effects produced by over exposure move to fresh air. If effects persist obtain medical advice.

5. FIRE FIGHTING MEASURES
Flammability:
This product has a significant water content and is not expected to be able to support combustion. However the residual left after water evaporation could be ignited by high energy sources.
Flash Point: >100 C Closed cup.
Extinguishing Media:

Small Fires: Foam dry powder carbon dioxide sand or earth.
Large Fires: Foam or water fog - Do not use water jet.
Product of Combustion:
Combustion can produce a variety of compounds including: Oxides of carbon and Nitrogen Water vapour and unidentified organic and inorganic compounds some of which may be Toxic.

6. ACCIDENTAL RELEASE MEASURES

Prevent entry into drains or water courses spillages can be slippery.
Small Spills:
Soak in non combustible absorbent granules sand or earth.
Large Spills:
Bund using absorbent material sand or earth. Reclaim liquid directly or soak in absorbent medium and transfer to a suitable marked container.
Disposal of Spillage:
Dispose via an authorised/licensed disposal contractor.
Disposal must be in accordance with local regulations and in the UK the Environmental Protection Act 1990 part 2 - "Waste".

7. HANDLING & STORAGE

Avoid contact with eyes wear chemical goggles when handling product. Avoid skin contact with undiluted product. The use of an appropriate barrier cream and after work creams may be beneficial.
Store in dry conditions protected from frost and elevated temperatures. Store in the original containers or in either mild steel or high density polyethylene containers which are closable and clearly labelled.

8. EXPOSURE CONTROLS/ PERSONAL PROTECTION

Exposure Limits:
The product does not have an established Occupational Exposure Limit OES, Maximum Exposure Limit MEL or Threshold Limit Value TLV. However it is derived from components which have individual established OES's/TLV's.

Eyes:	Wear chemical goggles when handling the undiluted product or if there is a risk of splashing with diluted product.
Skin:	Wear impervious gloves when handling the undiluted product. Prolonged or repeated contact with the diluted metalworking fluid emulsions is often unavoidable the use of appropriate skin protective and conditioning creams may be beneficial and gloves should be considered whenever there use is practical and safe. Change contaminated clothing and overalls as soon as possible.
Inhalation	Respiratory protection is not normally required. Work rooms should have good general ventilation but where machine guards do not adequately prevent mist/vapour reaching the general atmosphere local exhaust should be applied.
Industrial Hygiene:	Adopt normal good working practices and personal hygiene standards. Wash hands after use before eating drinking smoking and after using the toilet. Contaminated clothing should be laundered before reuse.

9. PHYSICAL AND CHEMICAL PROPERTIES

Appearance	Green liquid.
Odour	Mild
pH at 3% aq	9.5
Density at 15.5 C	1.06
Auto ignition temp	>150 C
Flash Point	>100 C
Boiling Point	>100 C
Water Solubility	Forms clear green solution

10. STABILITY AND REACTIVITY

Stability:
This product is stable and is unlikely to react in a hazardous manner under normal conditions of use.
Conditions to Avoid:
Extremes of temperature preferably store between 5 and 30 C.
Protect from frost. Do not store above 60 C.
Materials to Avoid:
Strong oxidising agents strong acids N.B. May soften some rubbers and other elastomeric sealing materials.
Decomposition Products:
Thermal decomposition can give rise to a variety of compounds the nature of which will largely depend upon the conditions bringing about the decomposition. Thermal decomposition will generate irritating fumes and may be expected to generate such materials as oxides of carbon oxides of nitrogen small amounts of hydrogen chloride and other unidentified organic and inorganic compounds.

11. TOXICOLOGICAL INFORMATION

Eyes:	Eye contact with the undiluted product may cause strong irritation and stinging. There may be a potential to cause corneal injury if treatment is not prompt. Dilute emulsions are only expected to cause slight transient irritation or redness.
Skin:	The undiluted product in brief or occasional skin contact may cause slight irritation which may become more intense if not promptly removed. Prepared emulsions are surface active and slightly alkaline and prolonged or repeated contact with undiluted or overstrengthened solutions may cause de fatting of the skin slight irritation and dermatitis.
Inhalation	This product is unlikely to present any significant inhalation hazard at ambient temperatures. High temperatures or atomising systems may lead to the generation of vapours mists or fumes which may lead to the irritation of the eye and respiratory tract. Repeated excessive exposure to oil mists may cause respiratory damage and a condition resembling pneumonia.
Ingestion:	This product is of low toxicity. Ingestion is not regarded as a significant health hazard likely to arise in normal use. Swallowing significant quantities may cause discomfort nausea irritation of the digestive tract and diarrhoea.

12. ECOLOGICAL INFORMATION

Water:

The individual components range are expected to biodegrade at low concentrations. The components are not expected to be highly toxic to aquatic life. If released in to water the product may deplete the oxygen supply to bottom dwelling organisms.

Soil:

Small quantities will be absorbed in the upper layers where biodegradation may take place. Larger quantities may penetrate the anaerobic soil layers in which some of the organic compounds may persist. Some compounds have a high soil absorption coefficient some will be capable of penetrating the soil to cause ground water contamination.

13. DISPOSAL CONSIDERATION

Dispose of according to local regulations.

14. TRANSPORT INFORMATION

Not classed as dangerous.

15. REGULATORY INFORMATION

EEC Classification Xi: Eye and skin irritant
EEC No Not applicable
Risk Phrases:
R36/38: Irritating to eyes and skin
Safety Phrases:
S25: Avoid contact with eyes.
S26: In case of contact with eyes rinse immediately with plenty of water and seek medical advice.

The above classification relates to the undiluted product as supplied. It may not apply when the product is diluted at the operating strength.

16. OTHER INFORMATION

1. Other materials should not be added to the product unless otherwise recommended.
2. Emulsions should be maintained at the recommended concentrations in order to minimise health hazards.
3. Minimise tramp oil and other contamination remove metallic swarf or other debris at frequent intervals.
4. During machining metallic particles from work pieces or tools can contaminate emulsions. These may abrade the skin with resultant increase in perceptibility to inherent irritancy effects of the emulsion.
5. Proper procedures for regular draining and cleaning of machine tool coolant systems can help obtain optimum fluid performance and reduce bacteriological degradation.

USE RESTRICTIONS / CAUTIONARY NOTICE

Cemented carbides sometimes referred to as Tungsten Carbide or Hard Metal contain significant quantities of Colbalt or Nickel and sometimes Chromium and other transition metals.
This product is not inhibited to prevent potentially hazardous levels of dissolved cobalt and other transition metals being produced during the grinding of 'Hard metal'.

The information to ensure safe working conditions within the workplace remains with the user. The health hazard and general information contained within this Material Safety Data sheet are given as a guide to the precautions required to maintain a safe work environment.

Data Issued 20/09/94

Dowel

al Fully Synthetic Coolant

Maximum protection for demanding machining jobs

Tough enough to use in place of oil soluble coolant

Dowel represents the late generation in synthetic coolants.

- ***LESS ODOUR THAN OILS (SUDS)*** – BETTER WORKING CONDITIONS FOR OPERATORS.
- ***LOW FOAMING*** – SPECIAL FORMULATION IS IDEAL WHERE EXCESSIVE FOAMING IS A PROBLEM.
- ***WATER SOLUBLE*** – GREATER ECONOMY. NO OILY MESS.
- ***CONTAINS CORROSION INHIBITORS*** – SUPERIOR CORROSION INHIBITION ON TOOLS, WAYS AND WORKPIECES.
- ***ADVANCED FORMULATION*** – NOT FORMULATED WITH NITRITES, SECONDARY AMINES OR MINERAL OIL.
- ***TRANSPARENT SOLUTION*** – WORKPIECE CAN BE SEEN EASILY.

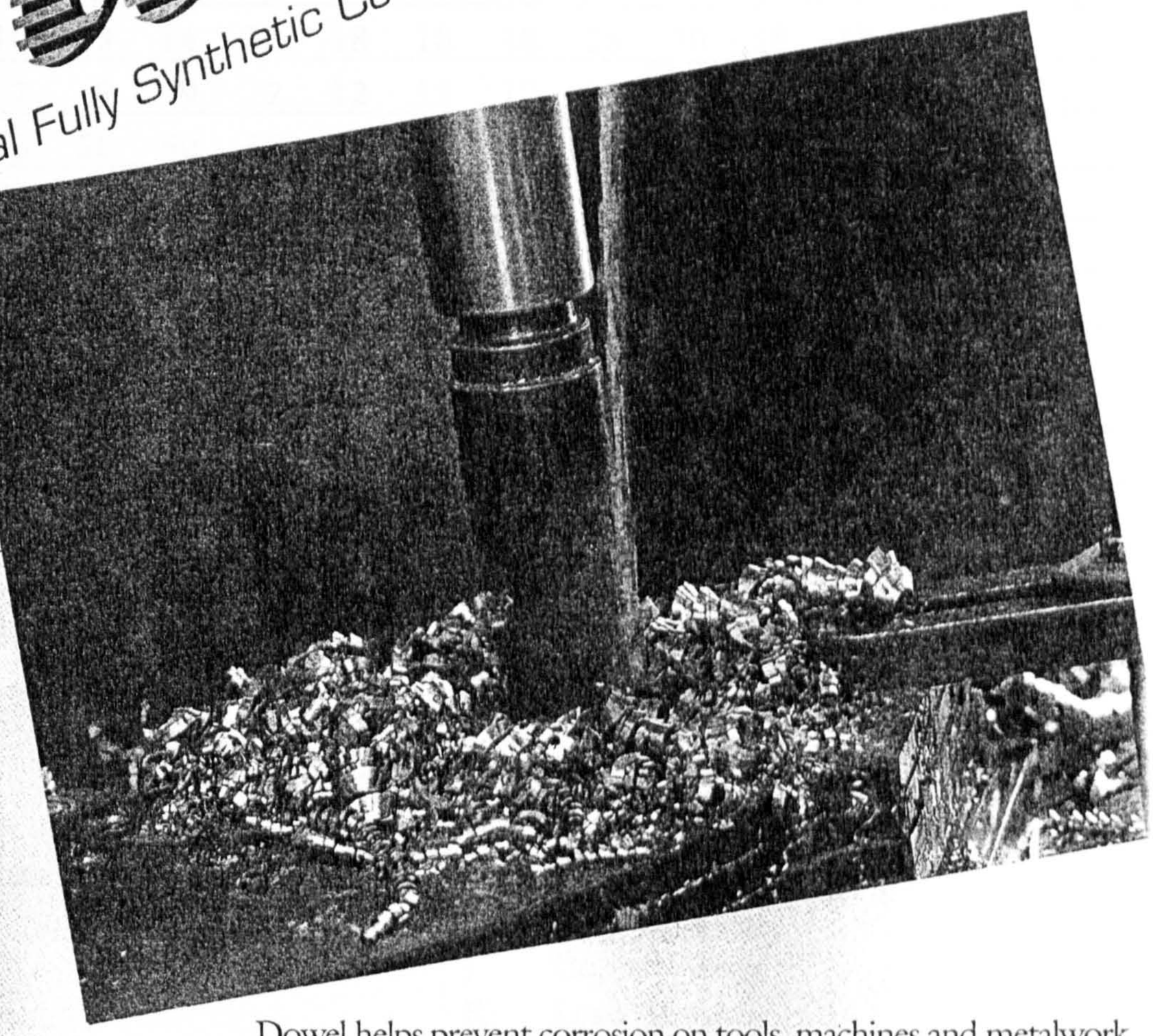

Dowel helps prevent corrosion on tools, machines and metalwork. It increases tool life, chemically cools and lubricates worked pieces for less heat distortion and less tool burning. Remains clear at any dilution for better visibility, better finishes, cleaner cutting and fewer rejects.

Recommended Uses –

Especially good for moderate to heavy duty machining operations.

Excellent For: Cast iron, steel, stainless steel, brass and aluminium (Do not use on magnesium).

Consult label for complete directions before use.

CHEMSEARCH

Division of NCH (UK) Limited
Landchard House, Victoria Street,
West Bromwich, West Midlands B70 8ER.
Telephone: 0121 525 1666
Facsimile: 0121 500 5386

Division of NCH (Ireland) Limited
Airport Industrial Estate,
Santry, Dublin 9, Ireland.
Telephone: Dublin 8425244
Facsimile: Dublin 8421221

CHP0395

Dilution Guide for Dowel

	A	B	C	D	E	F	G	H	I	J	K
Boring	12	15	16	20	20	20	20	20	30	20	20
Broaching	7	9	9	15	15	15	10	15	30	15	15
Drilling	12	15	16	20	20	20	20	20	30	20	20
Forming	10	13	14	18	18	18	18	18	30	18	18
Gear Hobbing	7	9	9	12	12	12	12	12	30	12	12
Grinding	50	50	50	50	50	50	50	50	50	50	50
Honing	9	9	9	9	9	9	9	20	30	20	20
Milling	12	15	16	20	20	20	20	20	30	20	20
Planing	12	15	16	20	20	20	20	20	30	20	20
Reaming	9	12	12	16	16	16	16	16	30	16	16
Sawing	12	15	16	20	20	20	20	20	30	20	20
Tapping	7	11	10	15	15	15	15	15	30	15	15
Trepanning	9	12	12	16	16	16	16	16	30	15	15
Threading	7	9	9	12	12	12	12	12	30	15	15
Turning	12	15	16	20	20	20	20	20	30	20	20

Key to Metals

A	Heat Resistant Alloy Steel
B	High Alloy Steel harder than Rockwell C-30
C	Titanium
D	Tool Steels
E	Carbon Steel
F	Alloy Steels softer than Rockwell C-30
G	Stainless Steel
H	Cast Iron
I	Aluminium
J	Copper Alloys
K	Lead Alloys

Note:

These coolant dilutions are given as a guide only and may require adjustment depending on specific metal characteristics, feeds and speeds, tool type and geometry and local water conditions.

Duo Cool

As a general rule, dilutions for Duo Cool are twice those for Dowel, with a dilution limit of 40:1 (for corrosion protection).

For example: Broaching Heat Resistant Steel; dilution for Dowel = 7:1, dilution for Duo Cool = 14:1.

CHEMSEARCH

Appendix 3

Calibration certificates

NOTTINGHAM GAUGE & THERMOMETER CO.

1/1a Standhill Road
Carlton Hill
Nottingham NG4 1JL
Tel. 0115 9876418
Fax 0115 9875918

CALIBRATION CERTIFICATE

01/0235

Instrument	:	63 mm Capsule Gauge.1/4" BSPT Back Entry.
Range	:	0-40 Kpa
Serial No.	:	15275/1
Temperature at test	:	17.5 Deg C.
Calibration Standard	:	Budenberg Air Deadweight Tester 18769 & 19139 Model No.239/240L Piston Cylinder Unit H736 Weight set 7002. UKAS calibration Lab 0138 Lab Ref RR0045 Cert No. 02265.(4.5.2000)

Gauge was tapped lightly before readings taken

True Pressure	Indicated Pressure-Rising	Indicated Pressure-Falling
5	4.90	5.00
10	9.85	10.00
15	14.90	15.00
20	20.00	20.01
25	25.15	25.02
30	30.20	30.30
35	35.30	35.40
40 Kpa	40.30	-----

We Certify that the above instrument has been calibrated by us with reference to BS / EN 837-3 1998 and is accurate to within ± 1.6 % of F.S.D.

Signed..... Date. 27.4.2001.....
Inspector.

NG T CO

KDG Instruments
Crompton Way Crawley West Sussex England RH10 2YZ
Tel: +44 (0)1293 525 151 Fax: +44 (0)1293 533 095
Email: sales@solartron.com www.solartron.com

Certificate No. KS002211/1

CERTIFICATE OF TEST

Date : 29-Jan-2001
CUSTOMER : CRANFIELD UNIVERSITY
METER TESTED ON : 29-Jan-2001

CUSTOMER ORDER NO : WS01371
WORKS ORDER NO : KS002211-1
METER SERIAL NO : KS002211/1

DESCRIPTION : ROTAMETER, SERIES 1100

CALIBRATED FLOW OF 10 TO 150 MILLILITRES/MINUTE (FREE VOLUMES AT 15°C, 1.01325 BAR)
FLUID : AIR
AT THE FOLLOWING CONDITIONS :
TEMPERATURE = 15 Deg C
PRESSURE = 1013.25 millibar absolute

FLOWS IN MILLILITRES/MINUTE		OBSERVED ERROR
INDICATED	OBSERVED	PERCENT
10	9.722	2.779
20	19.51	2.472
40	39.8	0.4879
60	59.91	0.1531
80	80.15	-0.187
100	100.5	-0.547
120	120.8	-0.697
140	140	-0.0192
150	149.9	0.04

MASTER USED : WM/95003
CLASS OF ACCURACY : VDI/VDE CLASS 4

CALIBRATION TRACEABLE TO NATIONAL STANDARDS

..... 29.1.01.....
FOR AND ON BEHALF OF KDG INSTRUMENTS DATE

KDG Instruments
Crompton Way Crawley West Sussex England RH10 2YZ
Tel: +44 (0)1293 525 151 Fax: +44 (0)1293 533 095
Email: sales@solartron.com www.solartron.com

Certificate No. KS002211/2

CERTIFICATE OF TEST

Date : 29-Jan-2001
CUSTOMER : CRANFIELD UNIVERSITY
METER TESTED ON : 29-Jan-2001

CUSTOMER ORDER NO : WS[illegible]
WORKS ORDER NO : KS002211-1
METER SERIAL NO : KS002211/2

solartron mobrey

DESCRIPTION : ROTAMETER, SERIES 1100

CALIBRATED FLOW OF 10 TO 150 MILLILITRES/MINUTE (FREE VOLUMES AT 15°C, 1.01325 BAR)
FLUID : AIR
AT THE FOLLOWING CONDITIONS :
TEMPERATURE = 15 Deg C
PRESSURE = 1013.25 millibar absolute

FLOWS IN MILLILITRES/MINUTE INDICATED	OBSERVED	OBSERVED ERROR PERCENT
10	9.722	2.779
20	19.95	0.2457
40	40.07	-0.167
60	59.29	1.185
80	79.31	0.8579
100	100.5	-0.547
120	117.8	1.818
140	138.1	1.323
150	147.8	1.497

MASTER USED : WM/95003
CLASS OF ACCURACY : VDI/VDE CLASS 4

CALIBRATION TRACEABLE TO NATIONAL STANDARDS

..... 29.1.01
FOR AND ON BEHALF OF KDG INSTRUMENTS DATE

KDG Instruments is an operating unit of Solartron Mobrey Limited
Registered office: Solartron Mobrey Limited Byron House
Cambridge Business Park Cambridge CB4 4WZ
Registered in England and Wales N° 293743

a Roxboro Group company

PETROLAB COMPANY
874 Albany-Shaker Road
Latham, New York 12110
Phone: (518) 783-5133
Fax: (518) 783-5185
Email: info@petrolab.com
Web: www.petrolab.com

CERTIFICATE OF CONFORMANCE

Customer: Petrolab Corp.
874 Albany-Shaker Road
Latham, NY 12110

Date: 10/24/00

Customer P.O.: 35278

P.O. Item #: N/A

Part Name: N/A

MC SO#: 54861 From Job #: 54861-01-00 Date: 10/23/00

☐ Customer Part/Drawing #: N/A Rev.: Qty.:

☐ MC Catalog #: 4000S-.812-1.050-5-AD Qty.:

☐ MC CPN: 4051511-050-TAC Rev.: Qty.: 50

Applicable Specifications:

Mott Corporation (MC) hereby certifies that MC standard manufacturing procedures designed to maintain the material analysis and dimensional requirements were followed in the fabrication of the above listed parts.

All inspection and test records for the parts are on file with MC and/or MC suppliers. The records are available for examination.

Our inspection controls are in compliance with MIL-I-45208 and our calibration system meets MIL-STD-45662. Our Quality system is in compliance with ISO 9001-1994.

Authorized Signature: Robin Moore

Carlton Hauer – Quality Manager **OR**
Roy Ouellette – Quality Supervisor **OR**
Robin Moore – Quality Analyst

CUST. NAME: Petrolab

[redacted] #15 [redacted]

[redacted] SCCM = 5050

[redacted] B.Pt. = 408.9 MMH2O ^P

[redacted] D = 21.84 [redacted]

DATE: 10-20-00 INITIALS: SV

CUST. NAME: Petrolab

[redacted] #23 [redacted]

[redacted] SCCM = 5650

[redacted] B.Pt. = 398.8 MM H2O ^P

[redacted] D = 22.39 [redacted]

DATE: 10-20-00 INITIALS: SV

Appendix 4

Journal bearings metrology records

SC-3

RESULTS TABLE

ID :

ALL PLANES

	Z (mm)	ΔRE (um)		∠ (degs)	○ (um)	↗ (um)	◎ (um)	
[*	115.0	-2.1	0.0	0	7.6	7.7	0.0	I
	130.0	-4.0	0.3	270	7.5	7.3	0.6	I
	145.0	2.1	1.4	180	7.3	9.3	2.9	I
[*	160.0	2.1	0.0	0	6.8	6.9	0.0	I

CYLINDER RESULTS

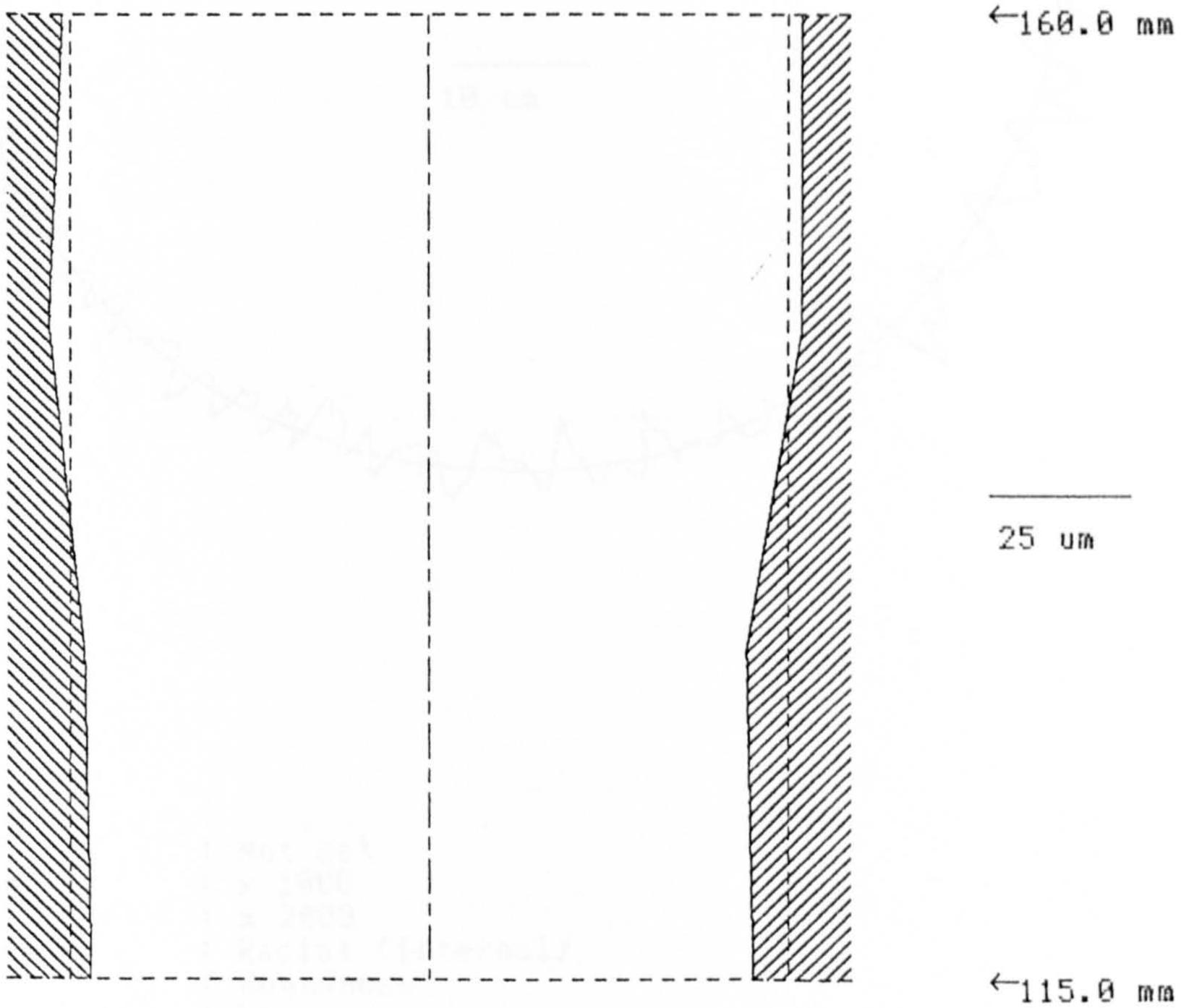

ID :

SC-3

No 3 Bottom Plot.

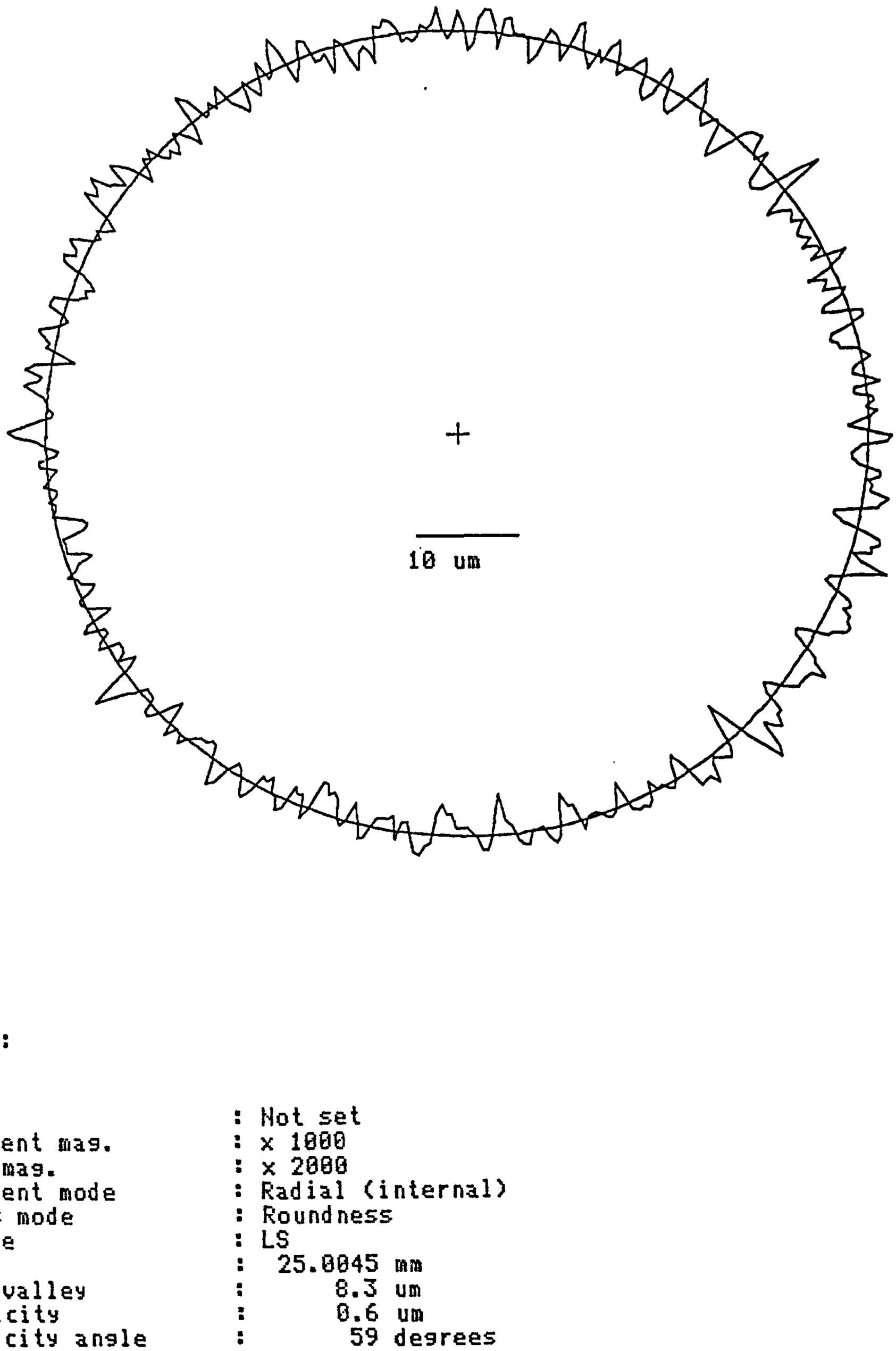

ID :

Z height	: Not set
Measurement mag.	: x 1000
Display mag.	: x 2000
Measurement mode	: Radial (internal)
Analysis mode	: Roundness
Reference	: LS
Radius	: 25.0045 mm
Peak to valley	: 8.3 um
Eccentricity	: 0.6 um
Eccentricity angle	: 59 degrees
Concentricity	: 1.2 um
Runout	: 9.1 um
Filter	: Unfiltered

SC4

RESULTS TABLE

ID :

ALL PLANES

	Z (mm)	ΔRE (um)	(um)	∠ (degs)	○ (um)	↗ (um)	◎ (um)	
[*	115.0	1.9	0.0	0	10.6	10.7	0.0	I
	130.0	0.9	2.3	27	15.1	16.8	4.6	# I
	145.0	-3.3	4.1	41	11.6	13.9	8.3	I
[*	160.0	-1.9	0.0	0	6.7	6.8	0.0	I

SC4

CYLINDER RESULTS

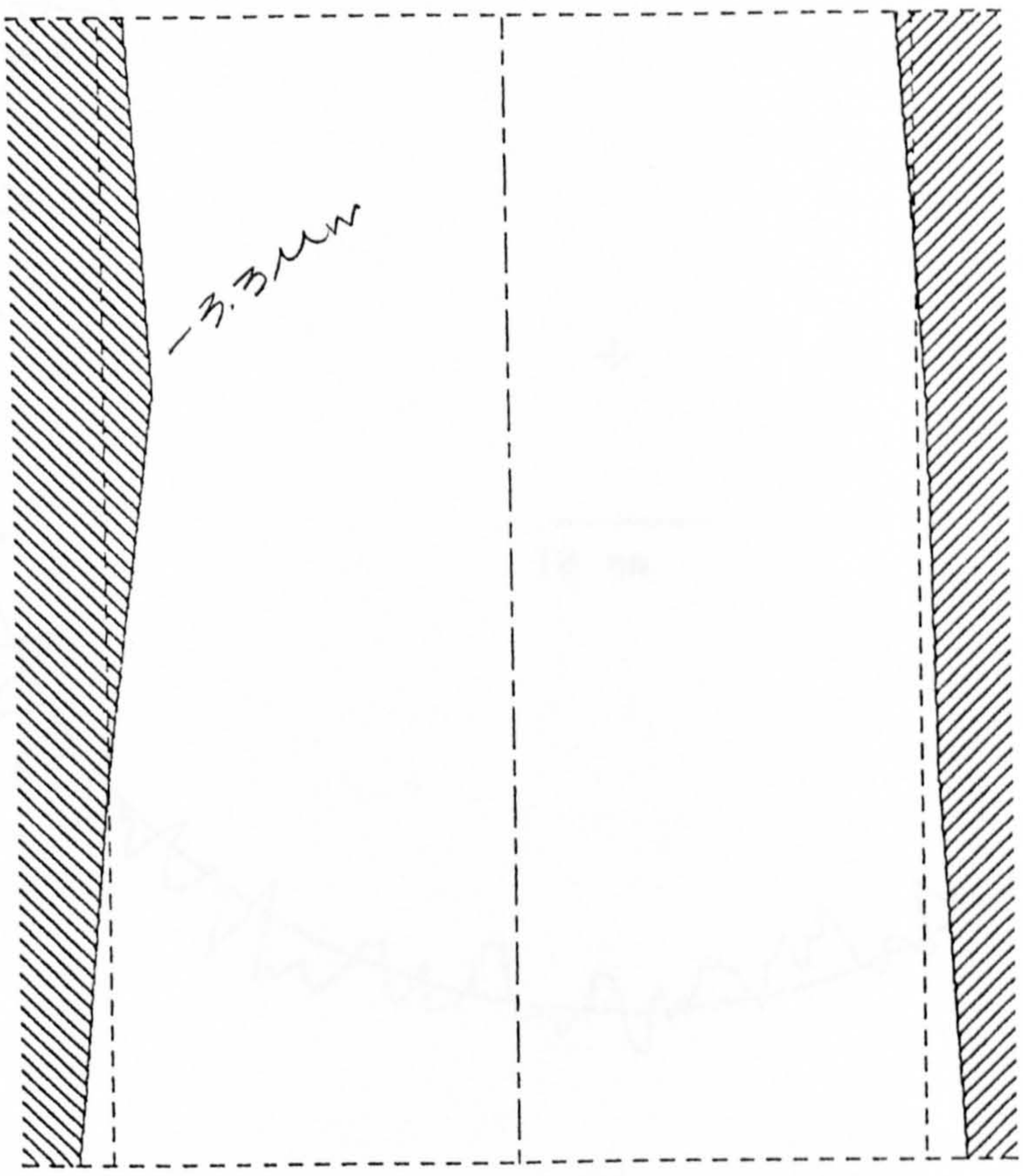

ID :

CYLINDER 1

Number of planes	:	4
Measurement mode	:	Radial (internal)
Cylinder reference	:	LS
Cylinder peak to valley	:	22.84 um
Cylinder parallelism	:	-18.10 um at 14.8 degrees
Maximum parallelism	:	-18.10 um at 14.8 degrees

SC 4

№ 4
BOTTOM

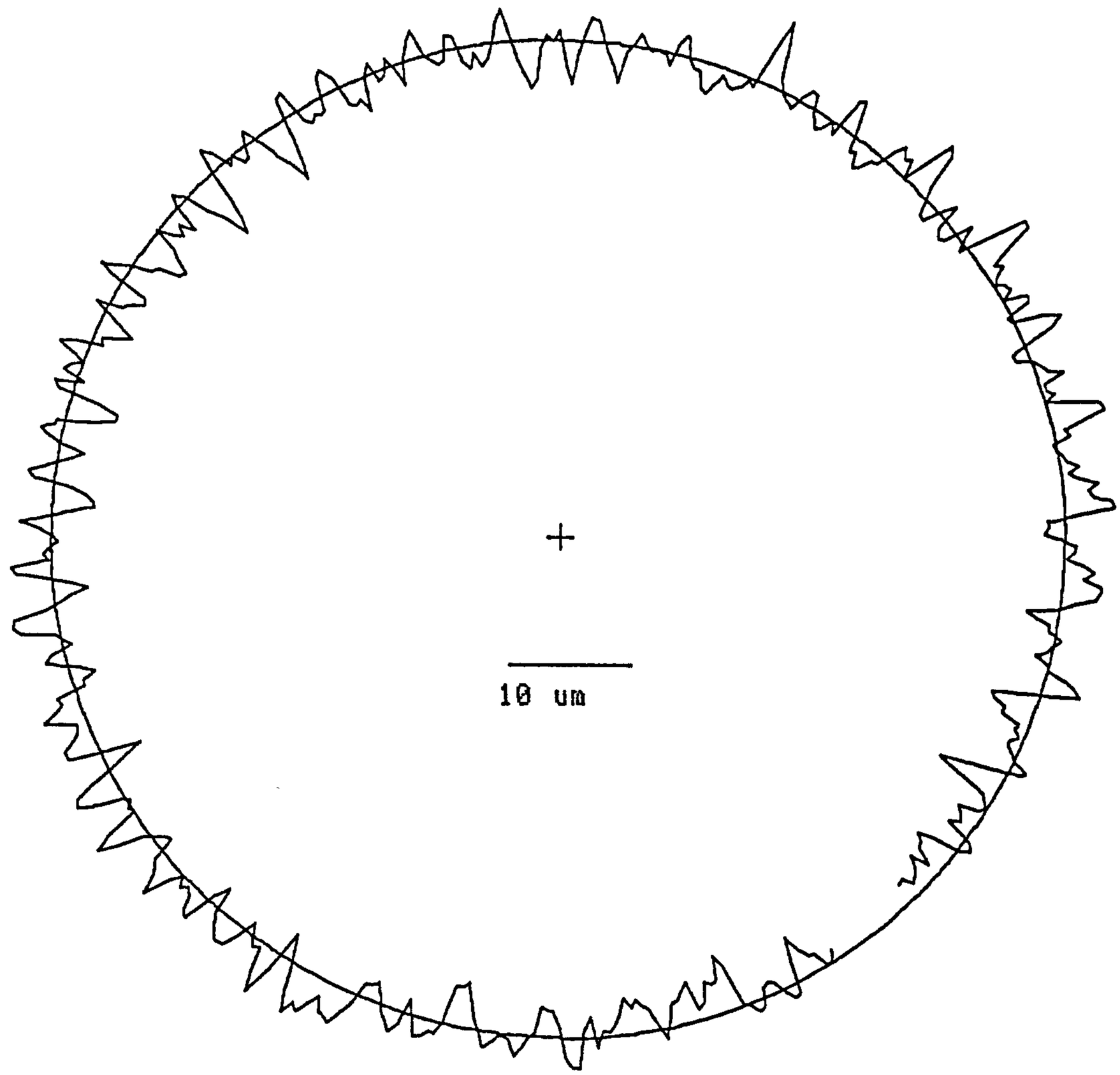

ID :

Z height	:	Not set
Measurement mag.	:	x 500
Display mag.	:	x 2000
Measurement mode	:	Radial (internal)
Analysis mode	:	Roundness
Reference	:	LS
Incomplete profile	:	5 points deleted
Radius	:	25.0064 mm
Peak to valley	:	10.1 um
Eccentricity	:	10.0 um
Eccentricity angle	:	297 degrees
Concentricity	:	20.0 um
Runout	:	26.2 um
Filter	:	Unfiltered

SC
Shell 4

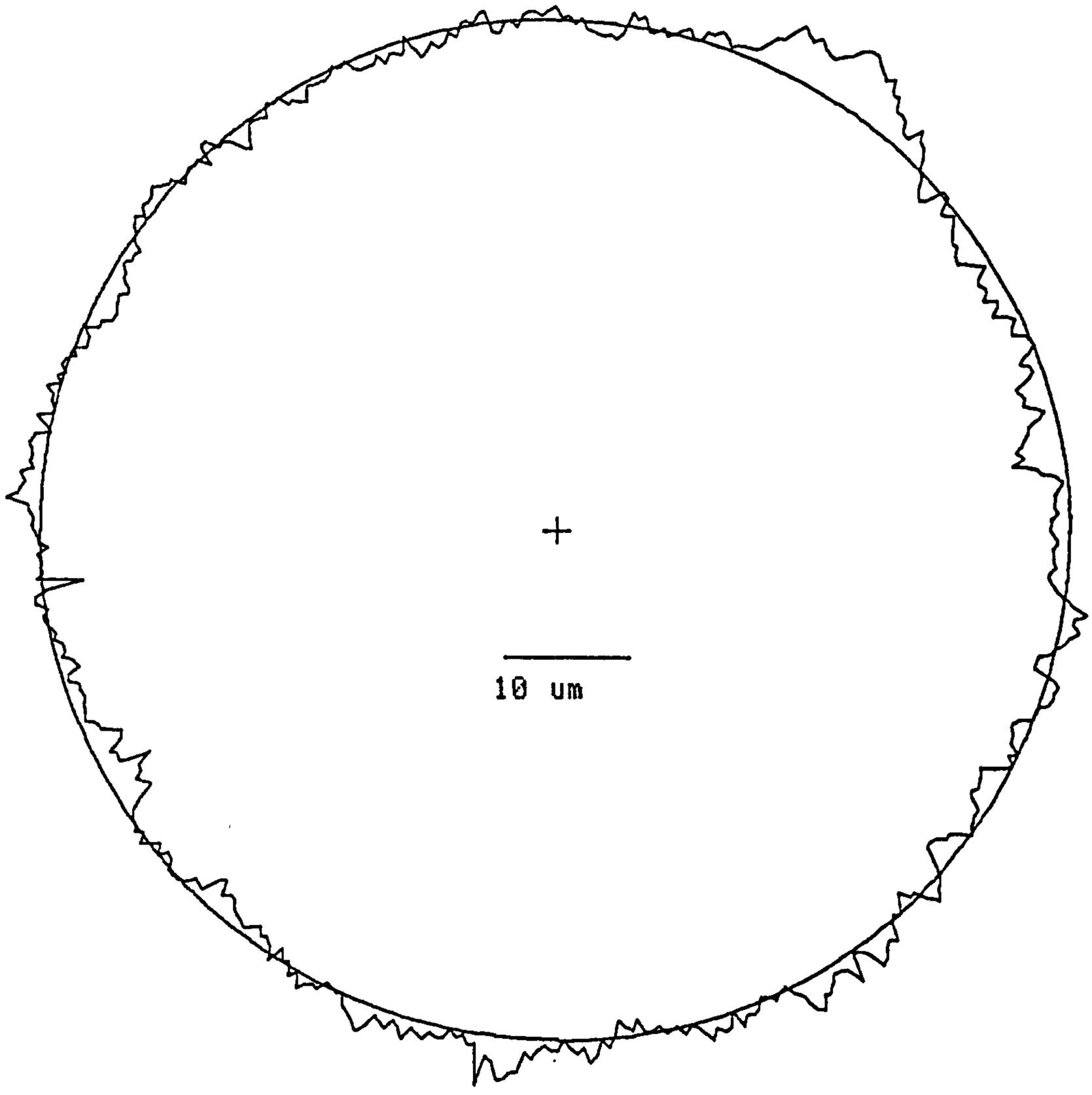

ID :

Z height	: Not set
Measurement mag.	: x 500
Display mag.	: x 2000
Measurement mode	: Radial (internal)
Analysis mode	: Roundness
Reference	: LS
Radius	: 25.0016 mm
Peak to valley	: 8.4 um
Eccentricity	: 1.7 um
Eccentricity angle	: 39 degrees
Concentricity	: 3.4 um
Runout	: 11.7 um
Filter	: Unfiltered

SL 4

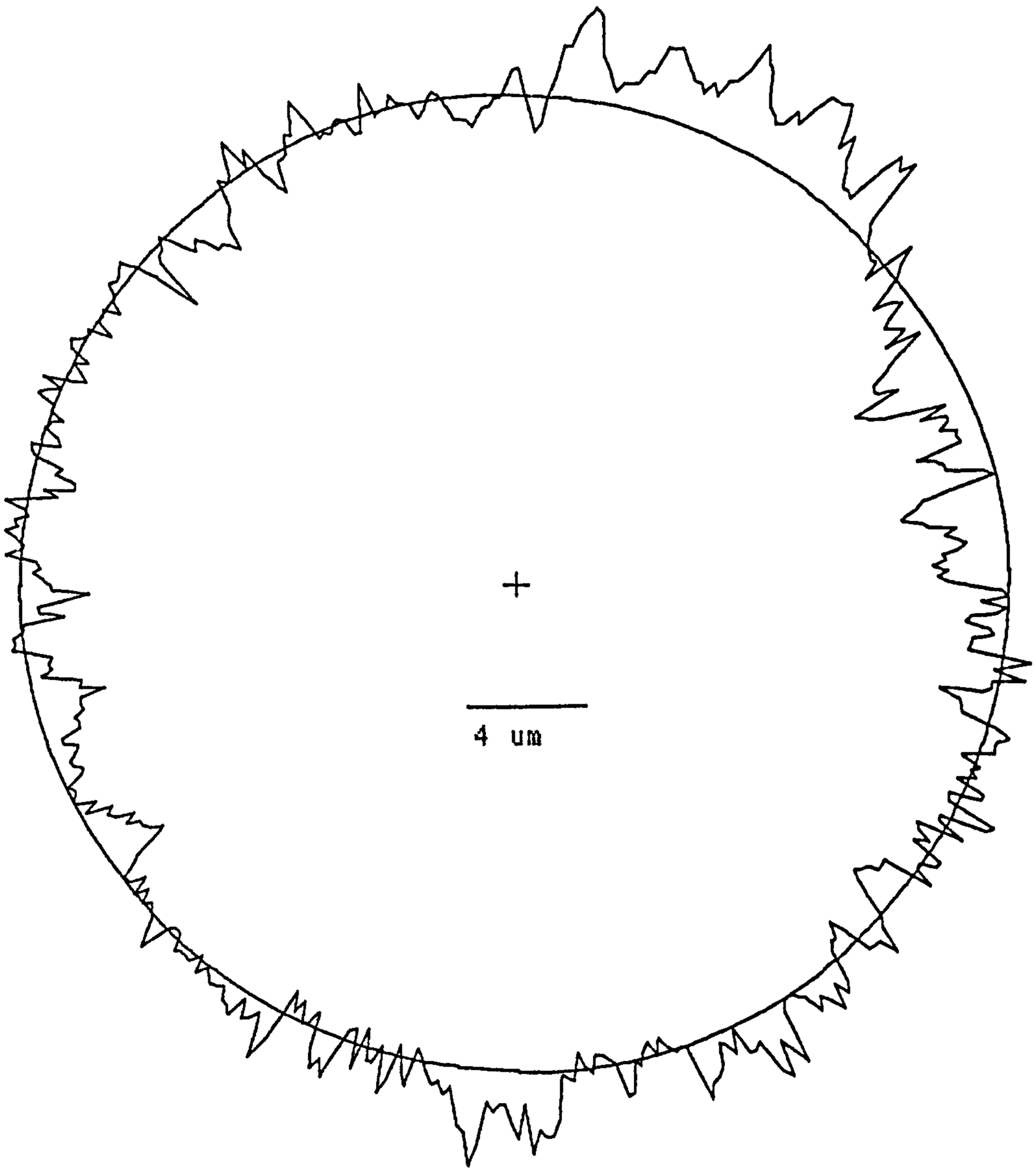

ID :

Z height	:	160.0 mm
Measurement mag.	:	x 1000
Display mag.	:	x 5000
Measurement mode	:	Radial (internal)
Analysis mode	:	Roundness
Reference	:	LS
Delta radius	:	-3.9 um
Peak to valley	:	6.7 um
Eccentricity	:	9.7 um [*
Eccentricity angle	:	111 degrees
Concentricity	:	19.3 um [*
Runout	:	21.4 um [*
Filter	:	Unfiltered

SC
Shell 4

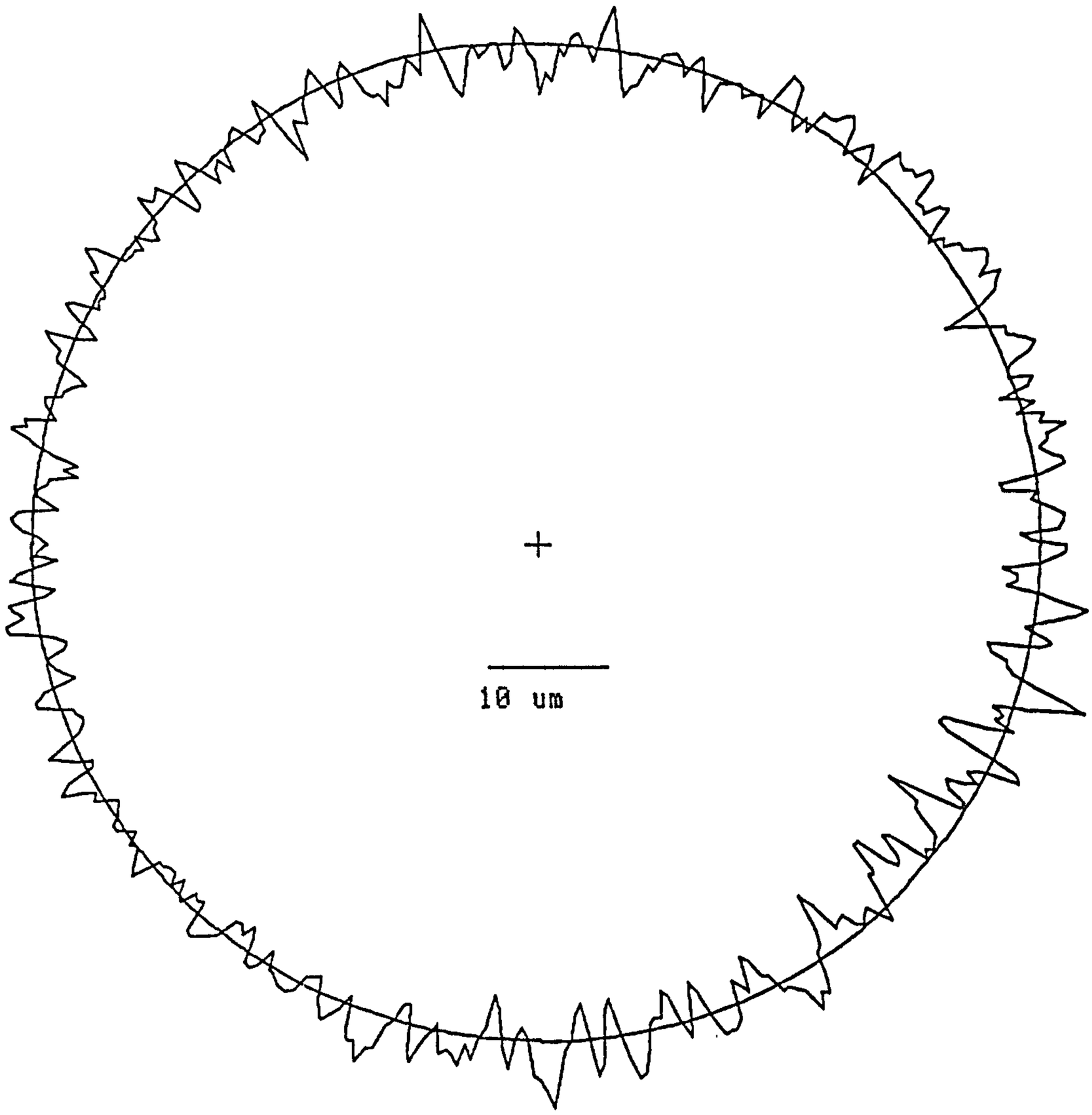

ID :

Z height	:	145.0 mm
Measurement mag.	:	x 1000
Display mag.	:	x 2000
Measurement mode	:	Radial (internal)
Analysis mode	:	Roundness
Reference	:	LS
Delta radius	:	-5.2 um
Peak to valley	:	11.6 um
Eccentricity	:	8.7 um
Eccentricity angle	:	85 degrees
Concentricity	:	17.5 um
Runout	:	24.2 um
Filter	:	Unfiltered

N°4 Bottom

SC4

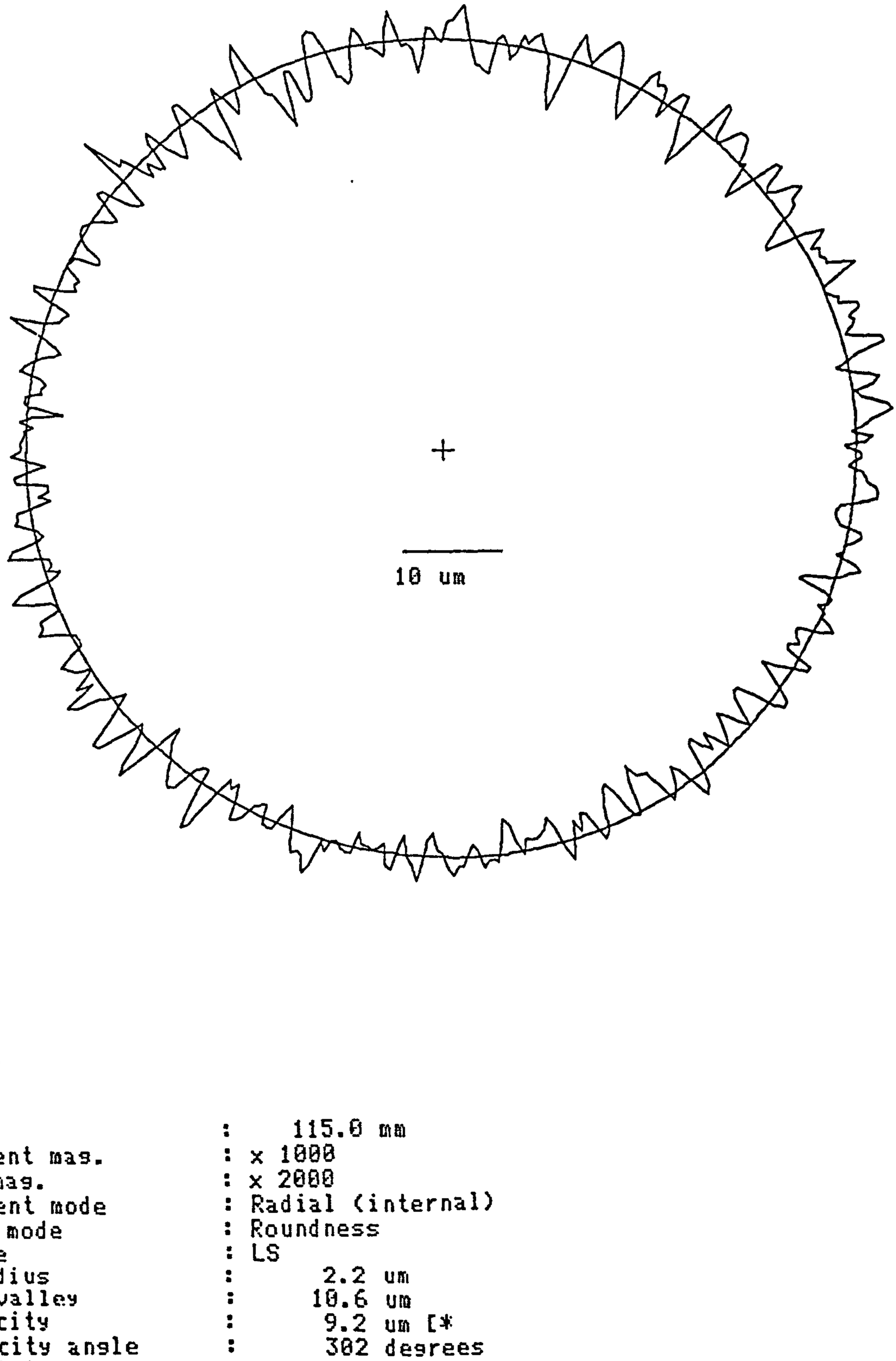

ID :

Z height	:	115.0 mm
Measurement mag.	:	x 1000
Display mag.	:	x 2000
Measurement mode	:	Radial (internal)
Analysis mode	:	Roundness
Reference	:	LS
Delta radius	:	2.2 um
Peak to valley	:	10.6 um
Eccentricity	:	9.2 um [*
Eccentricity angle	:	302 degrees
Concentricity	:	18.5 um [*
Runout	:	26.2 um [*
Filter	:	Unfiltered

5C 3Llm-40 %St

RESULTS TABLE

ID :

ALL PLANES

	Z (mm)	ΔRE (um)	E (um)	∠ (dess)	○ (um)	↗ (um)	◎ (um)	
[*	20.0	0.0	0.0	0	5.6	5.7	0.0	I
	30.0	-0.1	0.8	79	4.0	4.4	1.6	I
	40.0	-0.2	1.5	62	8.0	7.3	3.1	I
	50.0	-0.9	2.4	64	5.1	8.9	4.7	I
[*	60.0	-1.1	3.5	58	6.1	9.4	7.0	I

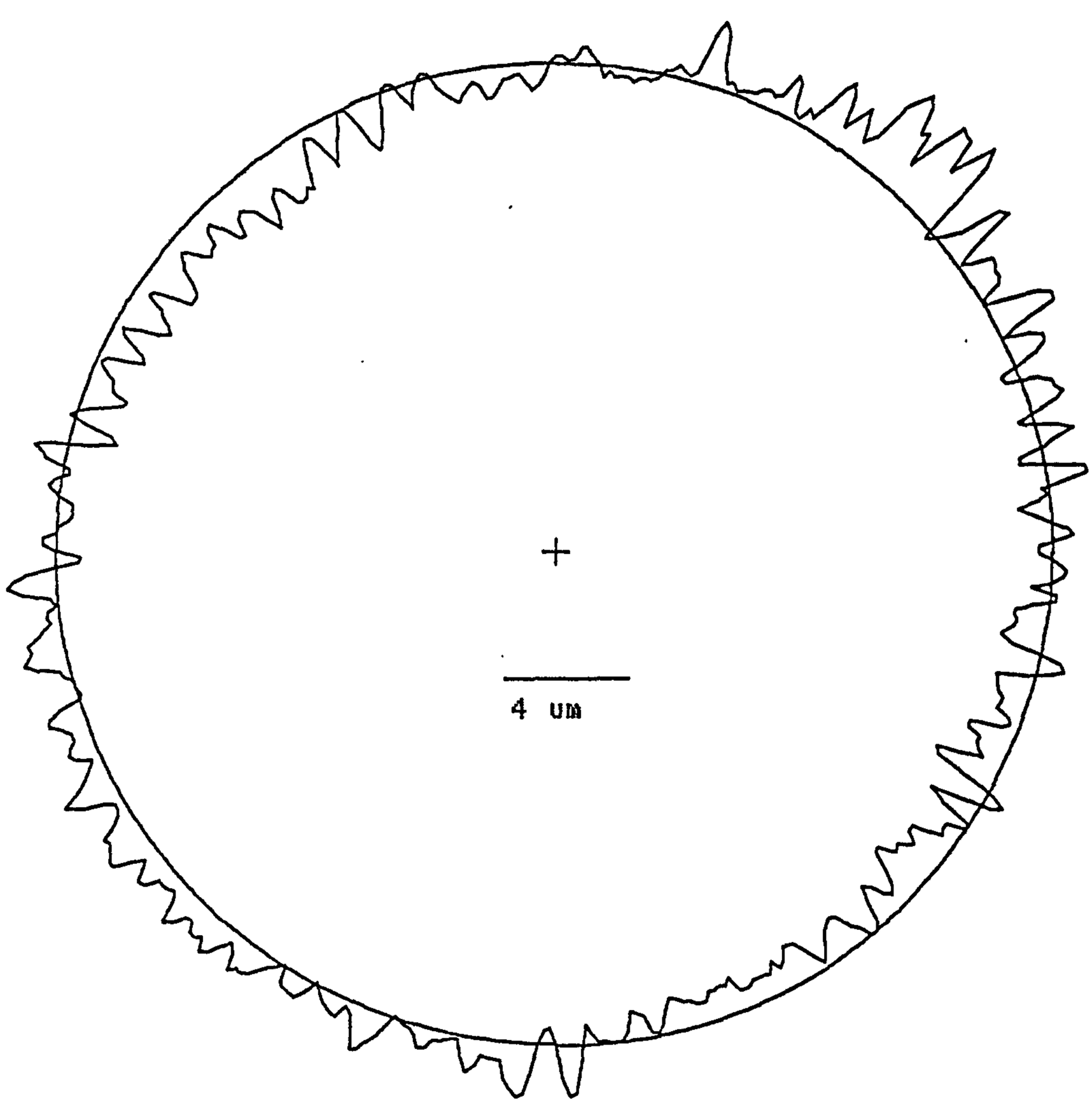

3Min - 40% St

SC 3Min-4C

L1

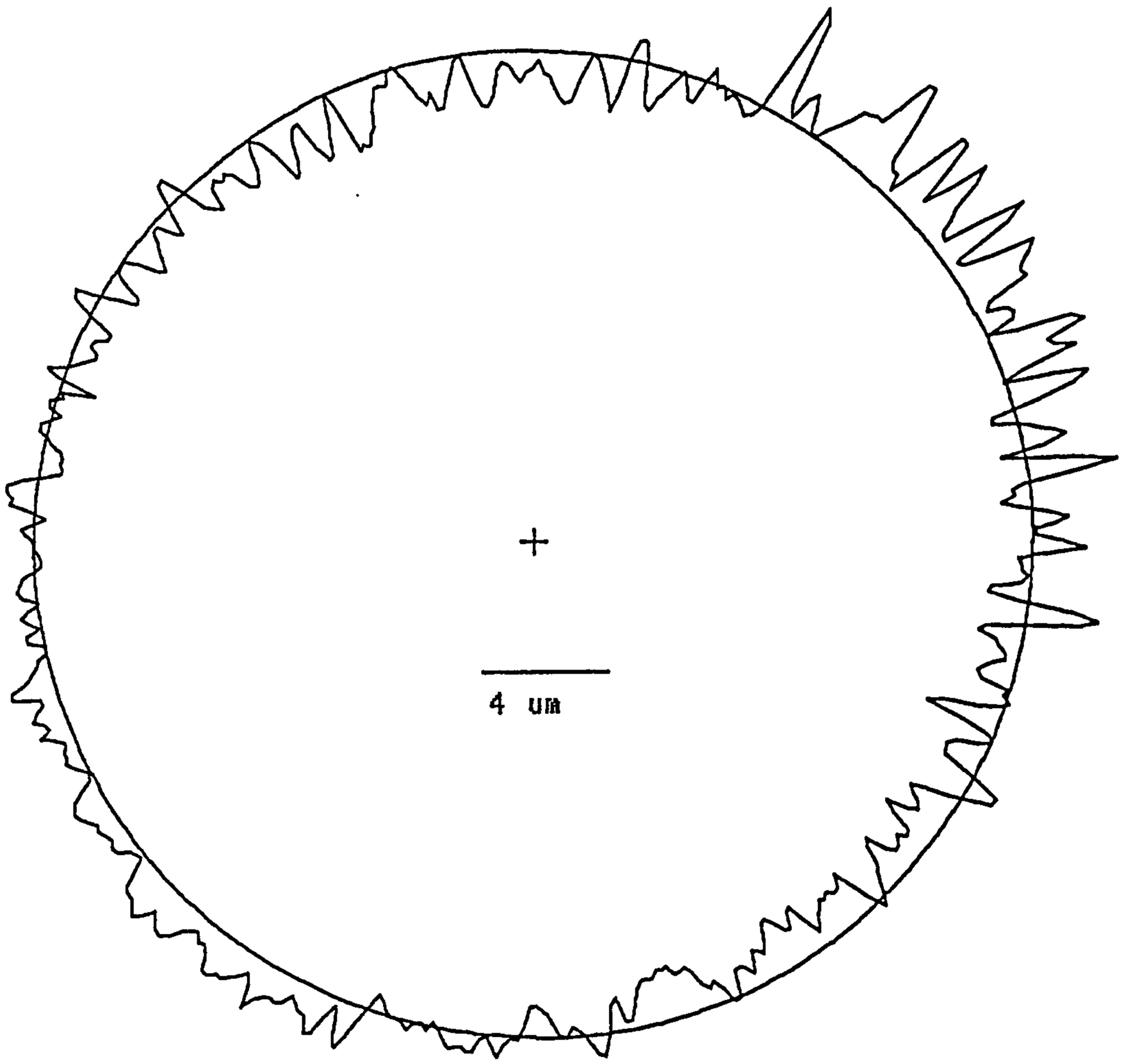

ID :

Z height	:	20.0 mm
Measurement mag.	:	x 1000
Display mag.	:	x 5000
Measurement mode	:	Radial (internal)
Analysis mode	:	Roundness
Reference	:	LS
Delta radius	:	0.5 um
Peak to valley	:	5.6 um
Eccentricity	:	1.2 um
Eccentricity angle	:	243 degrees
Concentricity	:	2.5 um
Runout	:	5.6 um
Filter	:	Unfiltered

SC 3.Um·40

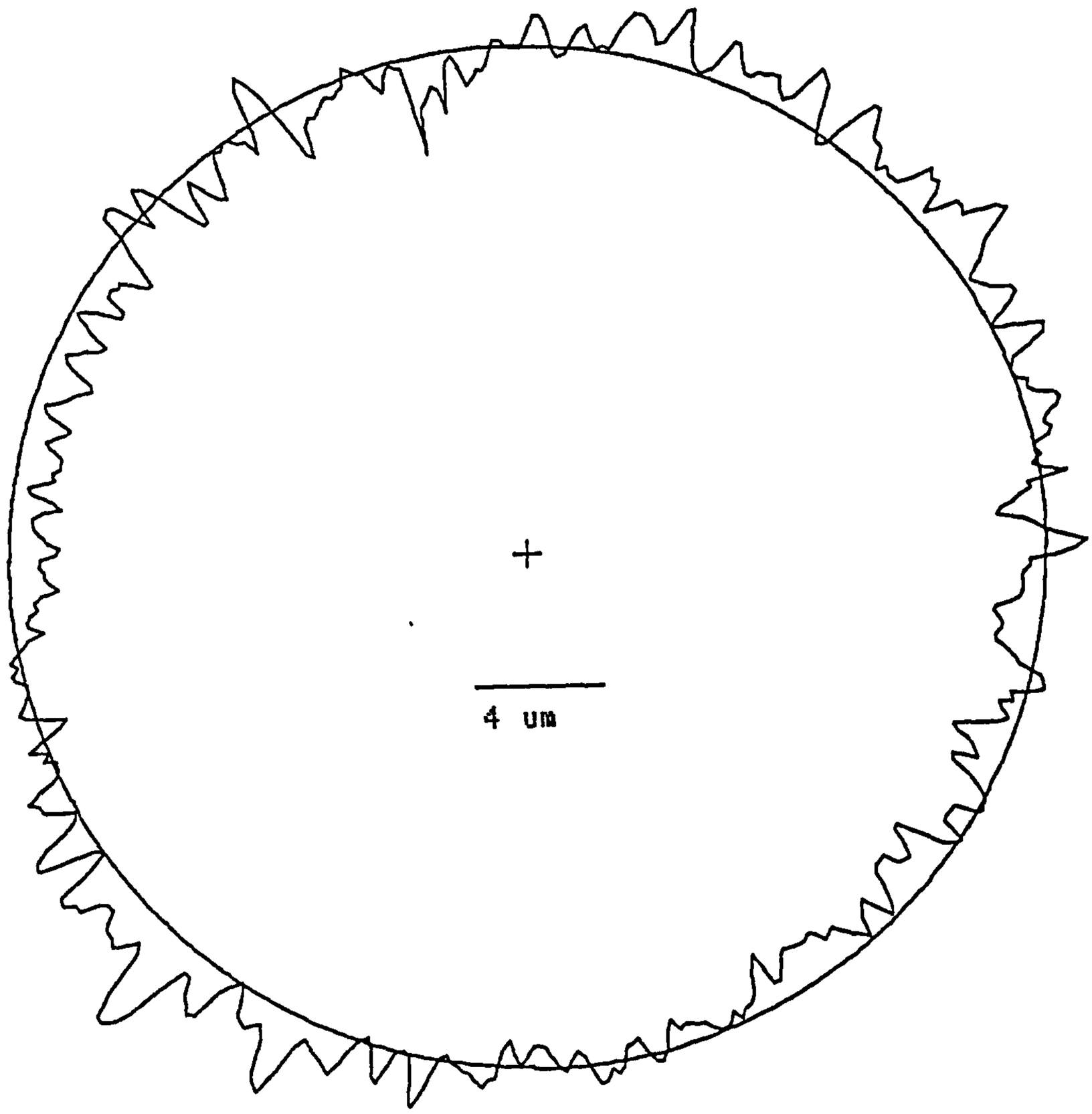

ID :

Z height	:	60.0 mm
Measurement mag.	:	x 1000
Display mag.	:	x 5000
Measurement mode	:	Radial (internal)
Analysis mode	:	Roundness
Reference	:	LS
Delta radius	:	-0.6 um
Peak to valley	:	6.1 um
Eccentricity	:	2.3 um
Eccentricity angle	:	55 degrees
Concentricity	:	4.5 um
Runout	:	7.2 um
Filter	:	Unfiltered

SC 3um-40%St

ID :

Z height	: Not set
Measurement mag.	: x 1000
Display mag.	: x 5000
Measurement mode	: Radial (internal)
Analysis mode	: Roundness
Reference	: LS
Radius	: 25.0179 mm
Peak to valley	: 5.0 um
Eccentricity	: 2.0 um
Eccentricity angle	: 228 degrees
Concentricity	: 4.0 um
Runout	: 6.1 um
Filter	: Unfiltered

Appendix 5

Journal bearing permeability calculation sheet

STARCH SHELL 4

Viscous and Inertia Permeability Calculation

Starch content: 20%vol **Powder:** 4

This spread sheet is based on the equations given in BS5600 ref {87}, and compensates for viscosity and density changes against temperature. Please refer to the standard for nomenclature.

The setup constants are:-

Brg O/D | Brg I/D | Brg length

Viscosity temperature coefficients (m and n).

Density temperature coefficients (a, b, c and d).

Average pore diameter. | Substrate fractional density

The input parameters are:-

Mass flow | Pressure diff | Temperature

Interim calculated Values are:-

Effective thickness | Kinematic Viscosity | Effective area

Absolute Viscosity | Actual Density | Volume flow

Final calculated values are:-

Viscous & Inertia Permeability | Reynolds Number in substrate

Setup Constants:

D =	6.20E-02	d=	5.00E-02	Len = 5.00E-02
Delta=	7.00E-07	f=	62	

Interim Calculated Values:

Eff A=	0.008728984	Eff e =	0.005977

From raw data (below)

M (kg/min)	dP (Pa)	T (deg C)	De(Kg/m3)	K Vis (m2/s	A Vis (Ns/n	Q (m3/s)	L	VPerm(m)	Re (ndim)
0.02109	1.00E+05	25.55	741.4648	2.01E-06	1.49E-03	4.74072E-07		4.83E-15	4.98E-05
0.056524	2.00E+05	25.45	741.5358	2.01E-06	1.49E-03	1.27042E-06		6.48E-15	1.33E-04
0.072183	3.00E+05	25.45	741.5358	2.01E-06	1.49E-03	1.62237E-06		5.52E-15	1.70E-04
0.098443	4.00E+05	25.50	741.5003	2.01E-06	1.49E-03	2.2127E-06		5.64E-15	2.32E-04
0.12754	5.00E+05	25.55	741.4648	2.01E-06	1.49E-03	2.86685E-06		5.85E-15	3.01E-04
0.158609	6.00E+05	25.65	741.3939	2.01E-06	1.49E-03	3.56556E-06		6.05E-15	3.75E-04
0.18567	7.00E+05	25.80	741.2875	2.00E-06	1.48E-03	4.1745E-06		6.06E-15	4.40E-04
0.215267	8.00E+05	26.05	741.1101	2.00E-06	1.48E-03	4.8411E-06		6.13E-15	5.12E-04
0.24513	9.00E+05	26.35	740.8973	1.99E-06	1.47E-03	5.51426E-06		6.18E-15	5.85E-04
0.27778	1.00E+06	26.80	740.5781	1.98E-06	1.46E-03	6.25142E-06		6.27E-15	6.67E-04

From raw data (below)

M (kg/min)	dP (Pa)	T (deg C)	De(Kg/m3)	K Vis (m2/s	A Vis (Ns/n	Q (m3/s)	L	VPerm(m)	Re (ndim)
0.023888	1.00E+05	25.50	741.5003	2.01E-06	1.49E-03	5.36923E-07		5.48E-15	5.64E-05
0.056524	2.00E+05	25.45	741.5358	2.01E-06	1.49E-03	1.27042E-06		6.48E-15	1.33E-04
0.072183	3.00E+05	25.45	741.5358	2.01E-06	1.49E-03	1.62237E-06		5.52E-15	1.70E-04
0.098895	4.00E+05	25.50	741.5003	2.01E-06	1.49E-03	2.22287E-06		5.67E-15	2.33E-04
0.114603	5.00E+05	25.55	741.4648	2.01E-06	1.49E-03	2.57605E-06		5.25E-15	2.71E-04
0.158609	6.00E+05	25.65	741.3939	2.01E-06	1.49E-03	3.56556E-06		6.05E-15	3.75E-04
0.186392	7.00E+05	25.85	741.252	2.00E-06	1.48E-03	4.19094E-06		6.08E-15	4.42E-04
0.215267	8.00E+05	26.05	741.1101	2.00E-06	1.48E-03	4.8411E-06		6.13E-15	5.12E-04
0.245567	9.00E+05	26.40	740.8618	1.99E-06	1.47E-03	5.52436E-06		6.19E-15	5.87E-04
0.27683	1.00E+06	26.95	740.4717	1.97E-06	1.46E-03	6.23095E-06		6.23E-15	6.66E-04

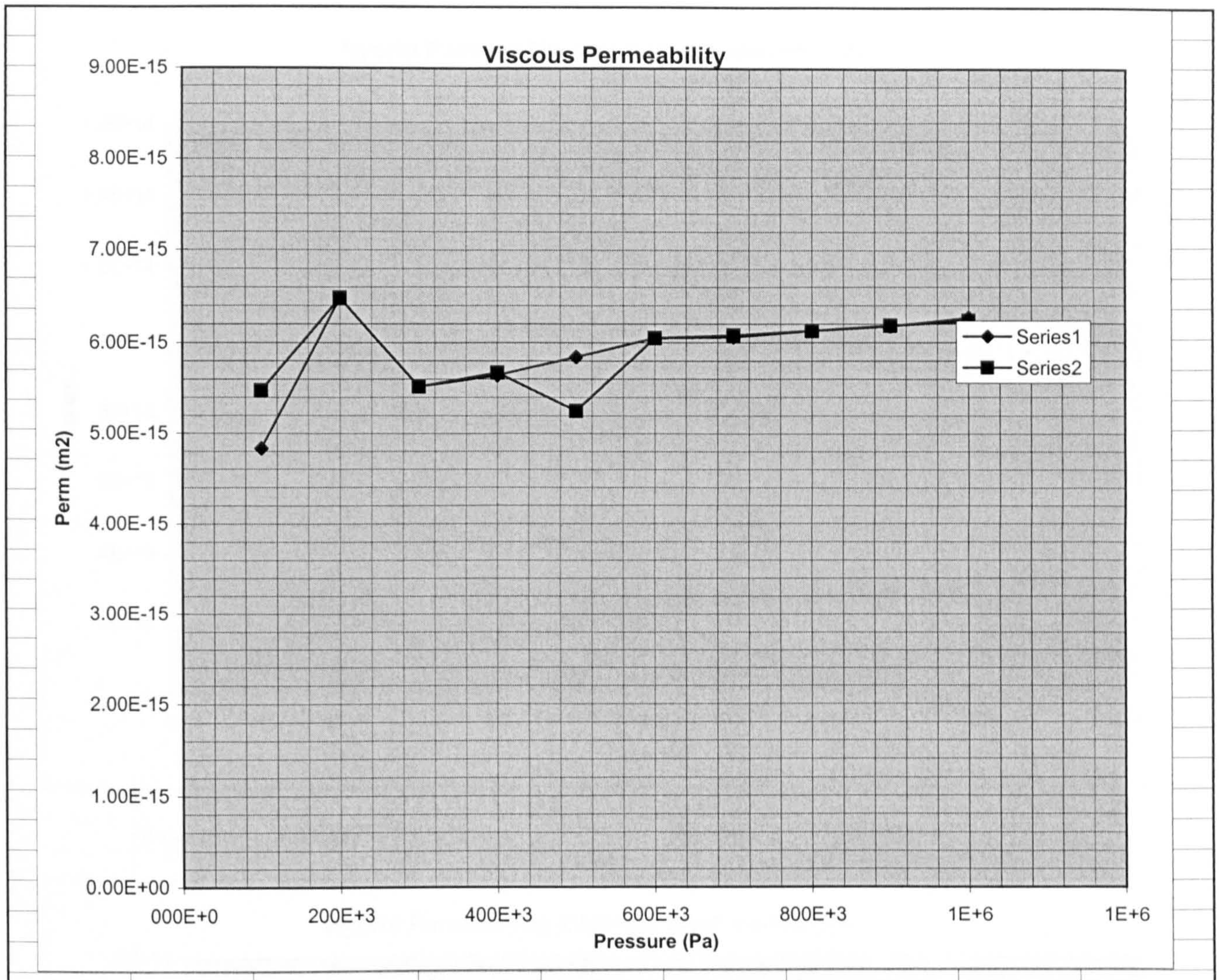

M (kg/min)	dP (Pa)	T (deg C)	De(Kg/m3)	K Vis (m2/s	A Vis (Ns/n	Q (m3/s)	Lu	x	y
0.0211	1.00E+05	25.55	777.1102	2.69E-06	2.09E-03	4.52327E-07		19.27671	1.546E+14
0.0565	2.00E+05	25.45	777.1761	2.69E-06	2.09E-03	1.21216E-06		51.61321	1.152E+14
0.0722	3.00E+05	25.45	777.1761	2.69E-06	2.09E-03	1.54797E-06		65.91193	1.354E+14
0.0984	4.00E+05	25.5	777.1432	2.69E-06	2.09E-03	2.11122E-06		89.93404	1.324E+14
0.1275	5.00E+05	25.55	777.1102	2.69E-06	2.09E-03	2.73535E-06		116.5717	1.278E+14
0.1586	6.00E+05	25.65	777.0443	2.69E-06	2.09E-03	3.40197E-06		145.1076	1.234E+14
0.1857	7.00E+05	25.8	776.9455	2.68E-06	2.08E-03	3.98291E-06		170.1101	1.232E+14
0.2153	8.00E+05	26.05	776.7809	2.68E-06	2.08E-03	4.61879E-06		197.7008	1.217E+14
0.2451	9.00E+05	26.35	776.5833	2.67E-06	2.07E-03	5.26087E-06		225.7783	1.205E+14
0.2778	1.00E+06	26.8	776.2868	2.66E-06	2.06E-03	5.96386E-06		256.9664	1.186E+14
M (kg/min)	dP (Pa)	T (deg C)	De(Kg/m3)	K Vis (m2/s	A Vis (Ns/n	Q (m3/s)	Lu	x	y
0.0239	1.00E+05	25.5	777.1432	2.69E-06	2.09E-03	5.12297E-07		21.82293	1.364E+14
0.0565	2.00E+05	25.45	777.1761	2.69E-06	2.09E-03	1.21216E-06		51.61321	1.152E+14
0.0722	3.00E+05	25.45	777.1761	2.69E-06	2.09E-03	1.54797E-06		65.91193	1.354E+14
0.0989	4.00E+05	25.5	777.1432	2.69E-06	2.09E-03	2.12092E-06		90.34732	1.318E+14
0.1146	5.00E+05	25.55	777.1102	2.69E-06	2.09E-03	2.45789E-06		104.7474	1.422E+14
0.1586	6.00E+05	25.65	777.0443	2.69E-06	2.09E-03	3.40197E-06		145.1076	1.234E+14
0.1864	7.00E+05	25.85	776.9126	2.68E-06	2.08E-03	3.99857E-06		170.8535	1.227E+14
0.2153	8.00E+05	26.05	776.7809	2.68E-06	2.08E-03	4.61879E-06		197.7008	1.217E+14
0.2456	9.00E+05	26.4	776.5503	2.67E-06	2.07E-03	5.27047E-06		226.2901	1.204E+14
0.2768	1.00E+06	26.95	776.188	2.66E-06	2.06E-03	5.94423E-06		256.4608	1.192E+14

Porous ceramic journal bearings-permeability calculation spreadsheet

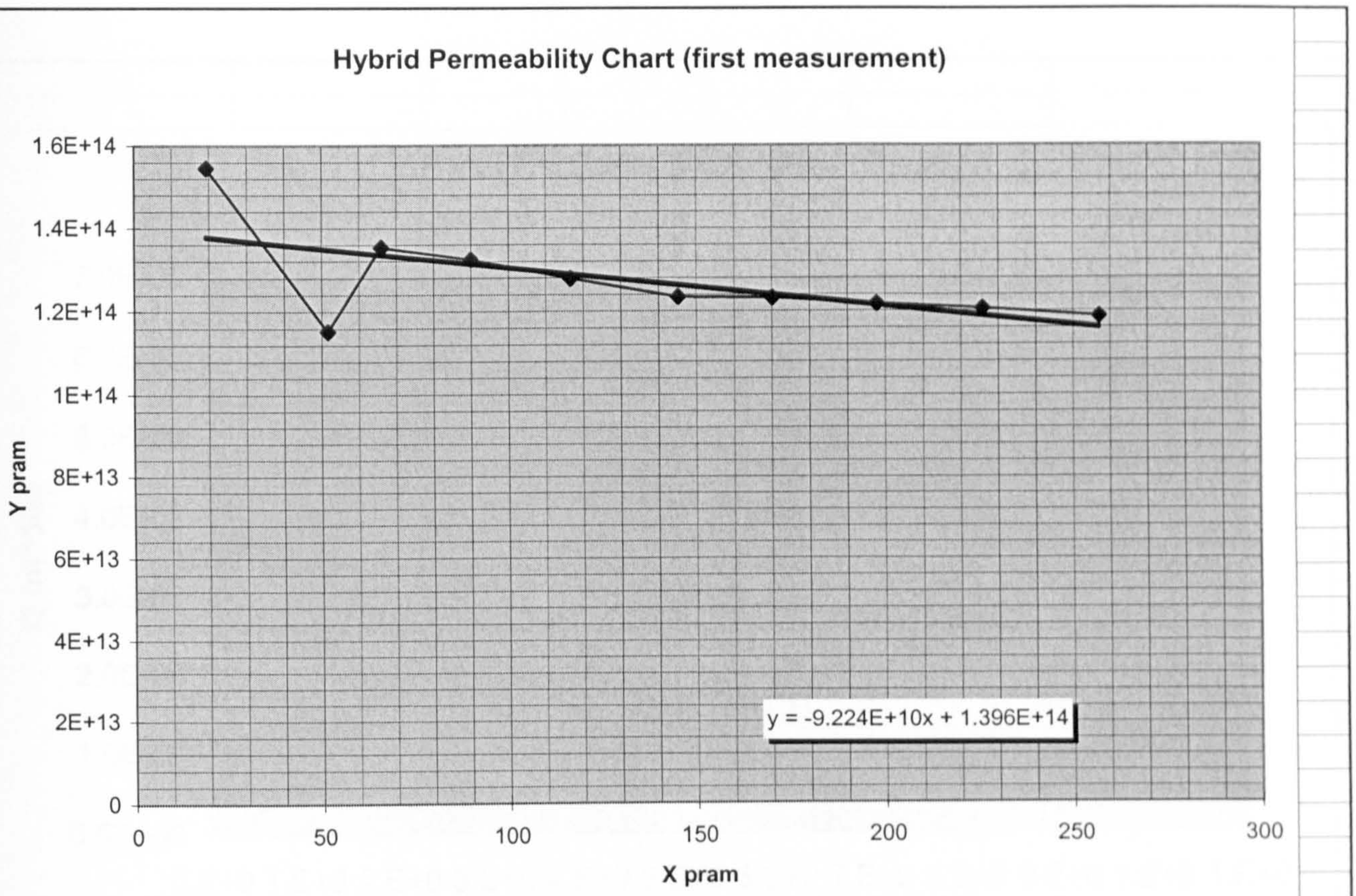

V-perm:	7.16332E-15	m^2		**I-perm:**	-1.08413E-11

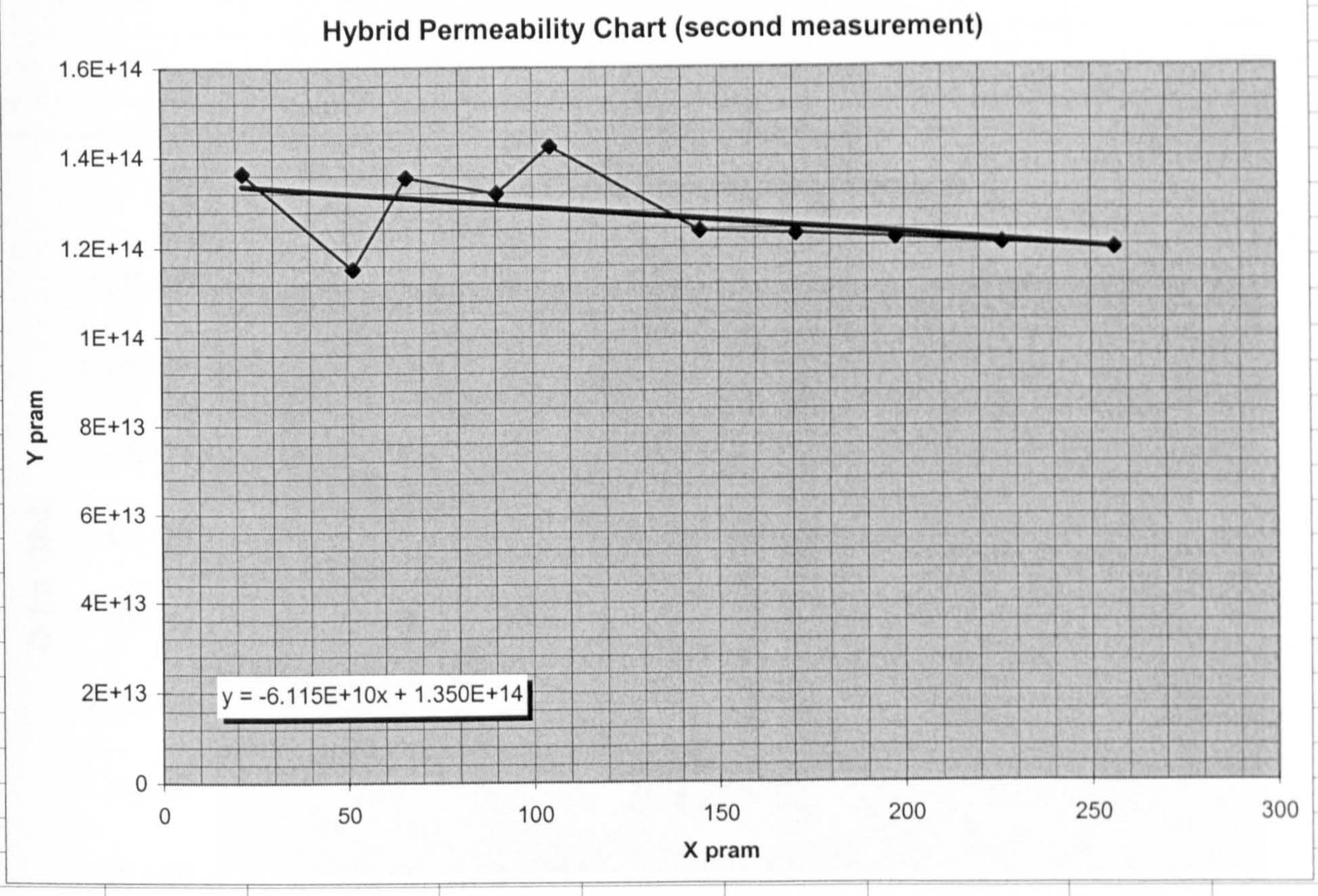

V-perm:	6.91563E-15	m^2		**I-perm:**	-1.63532E-11
				Ave Viscous perm	
				7.03948E-15	

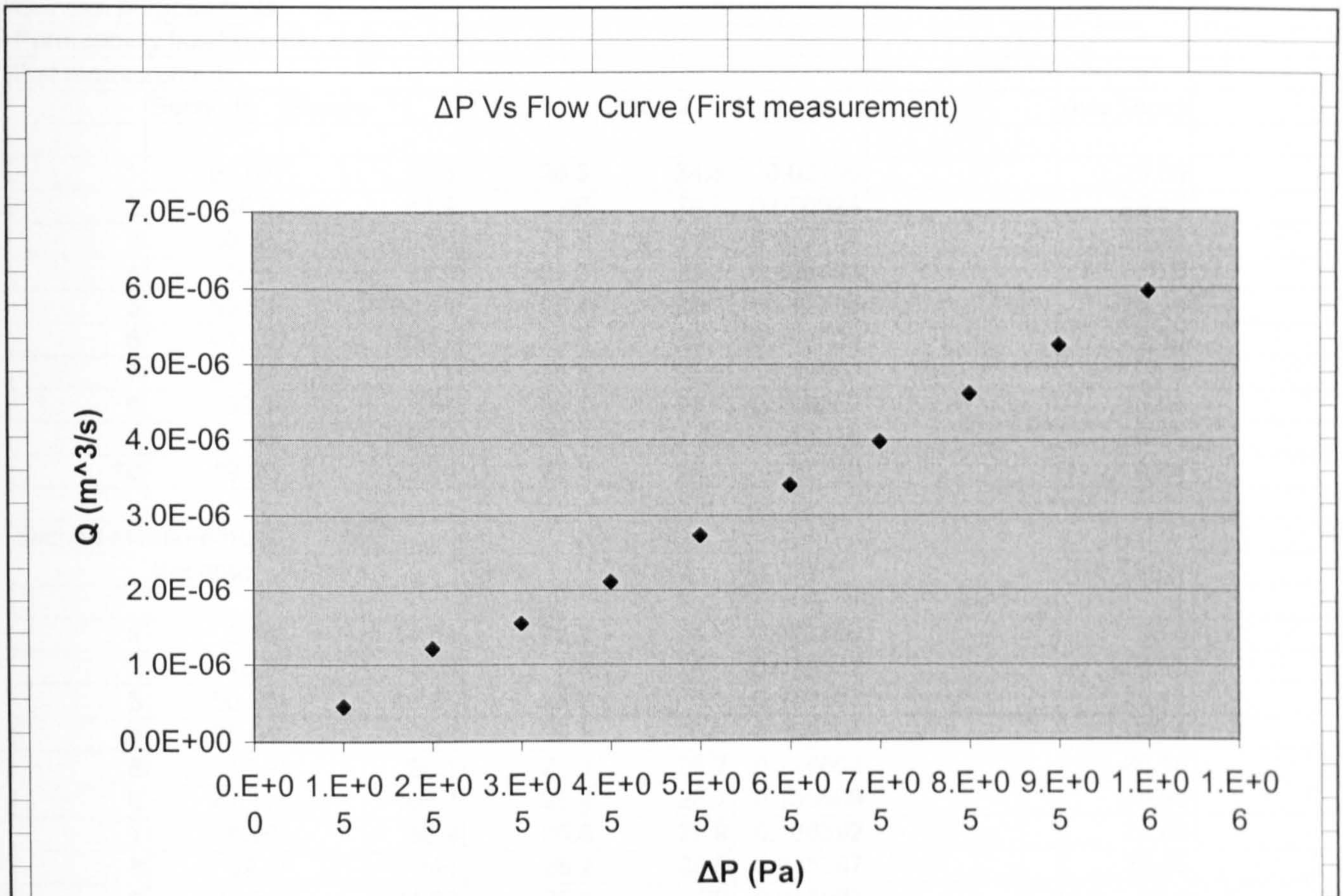
ΔP Vs Flow Curve (First measurement)
7.0E-06
6.0E-06
5.0E-06
4.0E-06
3.0E-06
2.0E-06
1.0E-06
0.0E+00
Q (m^3/s)
0.E+0 1.E+0 2.E+0 3.E+0 4.E+0 5.E+0 6.E+0 7.E+0 8.E+0 9.E+0 1.E+0 1.E+0
0 5 5 5 5 5 5 5 5 5 6 6
ΔP (Pa)

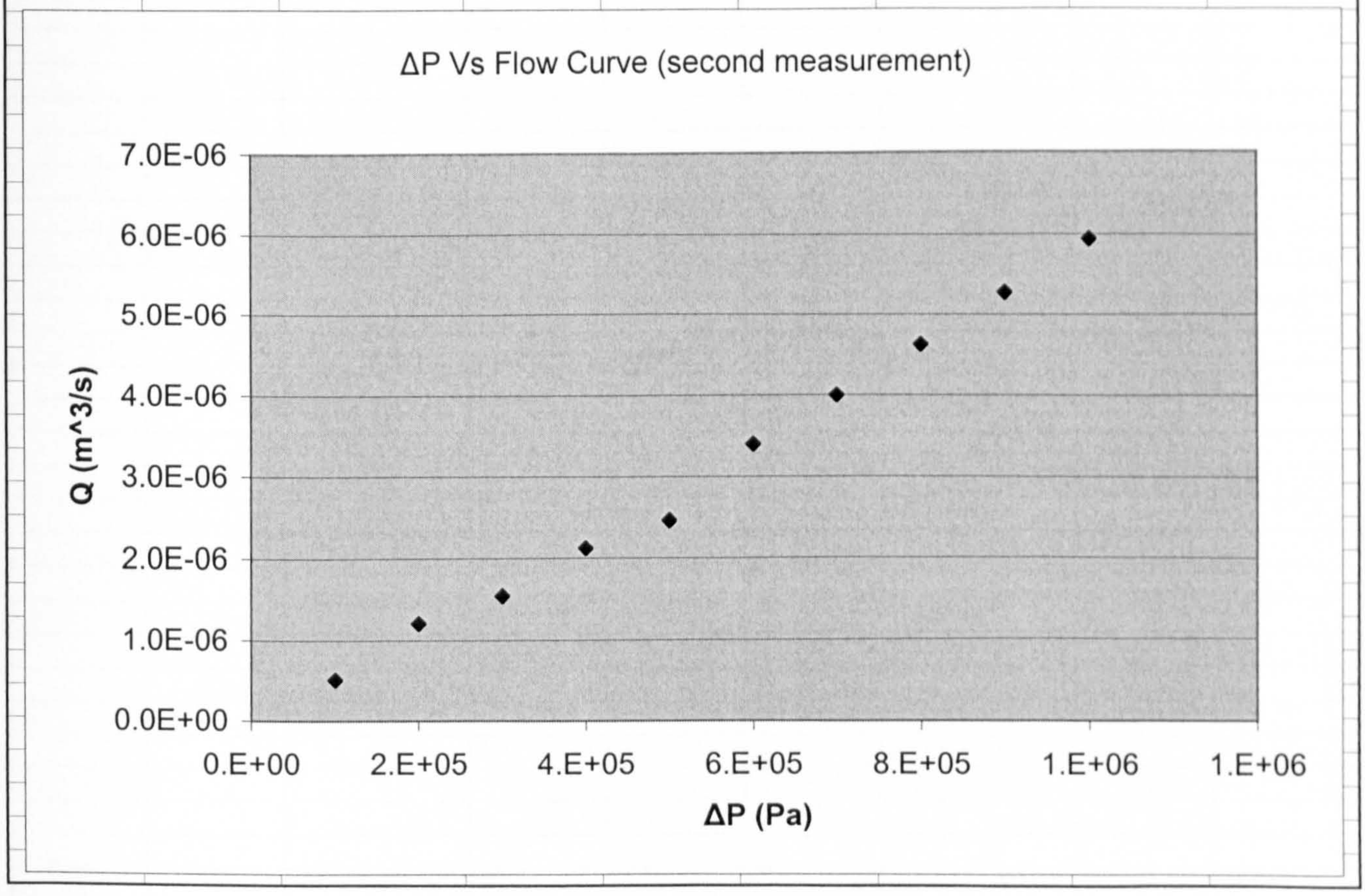
ΔP Vs Flow Curve (second measurement)
7.0E-06
6.0E-06
5.0E-06
4.0E-06
3.0E-06
2.0E-06
1.0E-06
0.0E+00
Q (m^3/s)
0.E+00 2.E+05 4.E+05 6.E+05 8.E+05 1.E+06 1.E+06
ΔP (Pa)

General purpose tools.

Permeability flow/time raw data

first measurement

	Seconds	Grams	Temp 1	Temp 2	Kg / min		Ave Temp	
1	50.07	17.6	26.3	24.8	0.02109		25.55	
2	46.6	43.9	26	24.9	0.056524		25.45	
3	50.58	60.85	25.9	25	0.072183		25.45	
4	50.1	82.2	25.2	25.8	0.098443		25.5	
5	50.53	107.41	25.4	25.7	0.12754		25.55	
6	41.12	108.7	25.6	25.7	0.158609		25.65	
7	35.87	111	25.8	25.8	0.18567		25.8	
8	39.3	141	26.2	25.9	0.215267		26.05	
9	45.38	185.4	26.7	26	0.24513		26.35	
10	49.55	229.4	27.3	26.3	0.27778		26.8	

second measurement

	Seconds	Grams	Temp 1	Temp 2	Kg / min		Ave Temp	
1	37.4	14.89	26.2	24.8	0.023888		25.5	
2	46.6	43.9	26	24.9	0.056524		25.45	
3	50.58	60.85	25.9	25	0.072183		25.45	
4	23.54	38.8	25.2	25.8	0.098895		25.5	
5	18.9	36.1	25.4	25.7	0.114603		25.55	
6	41.12	108.7	25.6	25.7	0.158609		25.65	
7	18.96	58.9	25.8	25.9	0.186392		25.85	
8	39.3	141	26.2	25.9	0.215267		26.05	
9	35.35	144.68	26.8	26	0.245567		26.4	
10	19.94	92	27.5	26.4	0.27683		26.95	